

THE IMPACT OF THALAMIC STATE ON THALAMOCORTICAL SENSORY
PROCESSING

A Thesis

Presented to
The Academic Faculty

by

Peter Y. Borden

In Partial Fulfillment
of the Requirements for the Degree
Biomedical Engineering in the
School of Georgia Institute of Technology and Emory University

Georgia Institute of Technology

May 2019

Copyright © 2019 by Peter Y. Borden

THE IMPACT OF THALAMIC STATE ON THALAMOCORTICAL SENSORY PROCESSING

Approved by:

Dr. Garrett Stanley, Advisor

Department of Biomedical Engineering

Georgia Institute of Technology

Dr. Dieter Jaeger

Department of Biology

Emory University

Dr. Bilal Haider

Department of Biomedical Engineering

Georgia Institute of Technology

Dr. Robert Liu

Department of Biology

Emory University

Dr. Biyu He

Department of Neurology

New York University School Medicine

Date Approved: January 17, 2019

To Katie

ACKNOWLEDGEMENTS

Throughout this work, I received the knowledge, support, technical skills, and friendship of many to make this thesis a reality. I would personally like to thank the past and current members of the Stanley laboratory including, Doug Ollerenshaw, Daniel Millard, Claire Gollnick, Sean Kelly, Alex Ortiz, Clarissa Whitmire, Michael Bolus, Yi Juin Liew, Adam Willats, Christian Waiblinger, Audrey Sederberg, Aurelie Pala, Caleb Wright, and Elaida Dimwamwa. Without their constant feedback, the scientific discoveries presented here would not be possible. I would also thank my thesis advisor, Garrett Stanley, who gave me the freedom to explore, and the passion to pursue greatness. Beyond my own laboratory, I have been fortunate enough to work with outstanding scientists including Craig Forest, Dieter Jaeger, and Everett Morrisette who have further aided in my growth and the work presented here. Lastly, this work could not have achieved without the sacrifices of the animals used for research.

I would like to thank my fellow graduate students and dear friends Will Stoy, Ilya Kolb, Dwight Chambers, Kyle Blum, Eric Maltbie, and Keenan May who gave me insights into worlds beyond the thalamus and laughter in times of absolute need. I would like to thank my parents Patricia and James Borden and, my brothers, David and Tim Borden, and my extended family Rachel and Kelly Borden, who gave me strength to continue my work.

Finally, I would like to thank my partner, Katie Marie Smith, who shared in my tribulations, and who gave me the support to conquer the moon.

TABLE OF CONTENTS

ACKNOWLEDGEMENTS	iv
LIST OF FIGURES	xi
LIST OF SYMBOLS AND ABBREVIATIONS	xiv
SUMMARY	xvi
CHAPTER I: INTRODUCTION	1
1.1 General Motivation	1
1.2 The Thalamus: a Critical Component of Processing.....	3
1.3 Thalamocortical Responses Are Influenced by Ongoing Thalamic State.....	4
1.3.1 Thalamic Polarization Controls Thalamic Burst and Tonic Firing Modes...	5
1.3.2 Thalamic Bursting– Regulating Sleep or Enhancing Stimulus Detection? ..	6
1.3.3 Thalamic Activity and Synchrony Shape the Thalamocortical Synapse	8
1.4 Ongoing Thalamic Polarization and State is Controlled Through Modulatory Inputs	10
1.4.1 Manipulation of Thalamic Activity Through Thalamic Reticular Nucleus and Cortical Layer VI Inputs	13
1.4.2 Neuromodulatory Control of Ongoing Thalamic Activity	15
1.4.3 Sensory Inputs and Self-Motion Alter Ongoing Thalamic State	16
1.4.4 Thalamic State Coupled to Cortical State.....	17
1.5 Dysfunction of Thalamic Activity: Insights from disease	17
1.6 GEVIs for Measuring Thalamocortical Modulation across Behaviorally Relevant Cortical Regions	18
1.6.1 Widefield Imaging of GEVIs for Measuring Voltage over Large Cortical Regions	20
1.7 General Experimental Design for Controlling Thalamic State and Measuring Effects on Thalamocortical Processing.....	20
1.7.1 Optogenetics as a tool for manipulating thalamocortical states.....	21
1.7.2 Rodent vibrissal pathway as an ideal model of thalamocortical circuits	22
1.7.3 ArcLight GEVI for Recording Cortical Layer II/III Activity	23
1.8 Organization of Thesis	23

CHAPTER II: ARCLIGHT FOR IMAGING LARGE SCALE CORTICAL ACTIVITY IN THE ANESTHETIZED AND AWAKE MOUSE	25
2.1 Introduction	25
2.2 Methods.....	27
2.2.1 AAV Delivery	27
2.2.2 Headplate and Prep	28
2.2.3 Whisker Stimulator	29
2.2.4 Cortical ArcLight and Intrinsic Imaging.....	29
2.2.5 Recording ArcLight Fluorescent Sensory Responses in the S1 Barrel Cortex	Error! Bookmark not defined.
2.2.6 Simultaneous Blood Oxygenation Measurements with Custom Monitor...	31
2.2.7 Simultaneous Local Field Potential Recordings and Analysis	32
2.2.8 Chronic Multiday Imaging Under Anesthesia	32
2.2.9 Awake Imaging.....	33
2.2.10 Histology.....	34
2.2.11 Voltage Imaging Data Analysis	34
2.2.12 Statistics:	36
2.3 Results	36
2.3.1 Experimental Setup and Histological Validation of Genetic Expression in Barrel Cortex.....	36
2.3.2 ArcLight Response to Single Whisker Deflections	38
2.3.3 ArcLight Shows Slow Rate of Photobleaching in vivo	43
2.3.4 Reducing Hemodynamic Signal With Post Hoc Off-ROI Subtraction Analysis	46
2.3.5 Comparison of ArcLight Response to Simultaneously Recorded Local Field Potential	48
2.3.6 ArcLight Cortical Response to Complex Stimuli	53
2.3.7 Stability and Variability of ArcLight as a Measure of Cortical Response .	56
2.3.8 Repeatability of ArcLight Recording over Multiple Days	59
2.3.9 Awake Recordings of Evoked ArcLight Mean and Single Trial Responses.....	64
2.4 Discussion	66
2.4.1 ArcLight Imaging as a Method for Measuring Cortical Activation on a Mesoscopic Scale.....	66

2.4.2	ArcLight Excitation Causes Substantial Hemodynamic Noise in Recordings	68
2.4.3	Limitations of the Off-ROI Subtraction Method as a Tool for Removing Hemodynamic Noise.....	69
2.4.4	Comparison of ArcLight Cortical Responses to Previously Reported Voltage Sensors	70
2.4.5	Future Applications of ArcLight and GEVI Imaging	71
2.4.6	Acknowledgements.....	72
Chapter III:	THALAMIC STATE SHAPES SPATIOTEMPORAL REPRESENTATIONS IN SENSORY CORTEX	73
3.1	Introduction	73
3.2	Methods.....	75
3.2.1	Anesthetized Electrophysiology:	76
3.2.2	Thalamic Electrophysiology:	76
3.2.3	Cortical Fluorescent ArcLight Imaging:	77
3.2.4	Functional Fluorescent Mapping of Barrel Cortex:	78
3.2.5	Simultaneous Imaging and Thalamic Optogenetic Stimulation:	78
3.2.6	Histology:.....	79
3.2.7	Thalamic Electrophysiology Data Analysis- Mean Response, Burst Ratio, and First Spike Latency:	79
3.2.8	Thalamic Electrophysiology Data Analysis: Detectability and Discriminability:	80
3.2.9	Voltage Sensitive Imaging Data Analysis:	81
3.2.10	Imaging Data Analysis – Peak amplitude, Normalized Peak, and Temporal Properties:	83
3.2.11	Imaging Data Analysis – Area Measurements:	84
3.2.12	Imaging Data Analysis– Detectability:	84
3.2.13	Imaging Data Analysis– Spatial Discriminability:	85
3.2.14	Model of Light Intensity and Optogenetic Activated Area:	85
3.2.15	Experimental Design and Statistical Analysis:	86
3.3	Results	86
3.3.1	Thalamic Hyperpolarization Increases both Thalamic and Cortical Sensory Evoked Responses	90

3.3.2	Thalamic Hyperpolarization Modulates Ongoing Thalamic and Cortical Activity	94
3.3.3	Thalamic Hyperpolarization Modulates the Thalamic Output and Downstream Cortical Response to Sensory Stimuli	98
3.3.4	Ideal Observer Detection from Single Trial Thalamic and Cortical Signals	103
3.3.5	Thalamic Hyperpolarization Modulates Cortical Detectability of Sensory Stimuli	106
3.3.6	Thalamic Hyperpolarization Increases the Sensory Evoked Active Spatial Area	109
3.4	Discussion:	114
3.4.1	Thalamic Hyperpolarization Alters Both Thalamic and Cortical Sensory Encoding Through Modulation of Thalamic Bursts	115
3.4.2	Thalamic Modulation Changes Ongoing Cortical Activity	116
3.4.3	Direct Thalamic Hyperpolarization Increases Ideal Observer Detection with No Change in Discrimination of Sensory Events	116
3.4.4	Thalamic Hyperpolarization Modulates the Spatial Activation of Cortex in Response to Sensory Stimuli	118
3.4.5	Conclusion	118
Chapter IV: THE MODULATION OF THALAMOCORTICAL STATE IN THE AWAKE AND ANESTHETIZED BRAIN.....		120
4.1	Introduction:	120
4.2	Methods	123
4.2.1	AAV Delivery:	123
4.2.2	Anesthetized Electrophysiology:	124
4.2.3	Awake Behavioral Training:	124
4.2.4	Thalamic Electrophysiology:	125
4.2.5	Intrinsic Imaging:	126
4.2.6	Awake Cortical Fluorescent ArcLight Imaging:	126
4.2.7	Functional Fluorescent Mapping of Barrel Cortex:	127
4.2.8	Simultaneous Imaging and Thalamic Optogenetic Stimulation:	128
4.2.9	Histology:	129
4.2.10	Thalamic Electrophysiology Data Analysis- Mean Response, Burst Ratio, and First Spike Latency:	129

4.2.11	Voltage Sensitive Imaging Data Analysis:	130
4.2.12	Dual Camera Imaging – Imaging analysis:.....	132
4.2.13	Imaging Data Analysis – Peak amplitude, Normalized Peak, and Temporal Properties:	132
4.2.14	Imaging Data Analysis – Area Measurements:	133
4.2.15	Awake Whisking – Data Analysis:	134
4.2.16	Experimental Design and Statistical Analysis:	134
4.3	Results:	135
4.3.1	Simultaneous Thalamic Manipulation and Cortical Recordings in the Awake and Anesthetized mouse.	135
4.3.2	Halorhodopsin Activation Transitions Awake Thalamus into a Bursting State in Awake Brain	138
4.3.3	Thalamic Halorhodopsin Activation Decreases Cortical Evoked Response in Awake Mice	143
4.3.4	Thalamic Halorhodopsin Activation Creates Opposite Cortical Effects in Awake and Anesthetized Mice	146
4.3.5	Thalamic Halorhodopsin Activation Reduces Evoked Area in Awake Animal	149
4.3.6	Internally Driven Whisking and Non-Whisking States Determine Extent of Optogenetic Manipulation	151
4.4	Discussion:	155
Chapter V: CONCLUSIONS AND FUTURE DIRECTIONS		161
5.1	Overview of Thesis Results.....	161
5.2	GEVIs as a Tool for Measuring Spatiotemporal Cortical Information	161
5.2.1	Widefield GEVI Imaging: Long-term Potential for Measuring Cortical Dynamics	162
5.3	Thalamic State Modulates Thalamocortical Function	165
5.3.1	The Dichotomy of Thalamic Hyperpolarized States	166
5.3.2	Speculation on the Interactions of Ongoing Activity on Evoked Signals	168
5.3.3	Relating Bursting States to Thalamic Function in Sensory Processing and Sleep	173
5.3.4	Relating Observations of Bursting and Enhanced Sensory Detection.....	175
5.3.5	Future Directions: Investigation of Thalamocortical Networks	176
5.3.6	Concerns and Caveats	179

5.4	Thalamus as a Dynamic Gate to Cortex	182
APPENDIX	184
A.1.	ArcLight Overlap with Hemodynamic Signals	184
A.1.1.	Removal of Hemodynamic Frequency using Notch Filtering.....	184
A.1.2.	Removal of Hemodynamic Frequency using Off-ROI Subtraction Methods:	186
A.1.3.	Non- Injected ArcLight Control	188
A.2.	ArcLight and Halorhodopsin Expression	191
A.3.	Chloride Reversal Potential and Halorhodopsin Activation	192
A.3.1.	In vitro Methods	200
A.3.2.	IF&B Model Methods	201

LIST OF FIGURES

Figure 1.1.General Project Overview.	2
Figure 1.2.Thalamic Polarization is Controlled by Modulatory and Sensory Inputs. ...	11
Figure 2.1.Experimental Setup and Histological Validation of ArcLight Expression. .	38
Figure 2.2.ArcLight S1 Cortical Response to Punctate Deflection.....	39
Figure 2.3.Post-Hoc Analytical Methods For ArcLight Widefield Imaging.....	45
Figure 2.4. Simultaneous Paired Extracellular Local Field Potential and ArcLight Fluorescent Recordings.	51
Figure 2.5.ArcLight Response to Complex Stimuli.	55
Figure 2.6.Within Experiment Variability of ArcLight Responses to Single Whisker Deflection	58
Figure 2.7. Multiday Imaging of ArcLight Cortical Response.....	63
Figure 2.8. Cortical ArcLight Fluorescent Responses in the Awake Mouse	65
Figure 3.1.Thalamic Optogenetic Hyperpolarization Increases Thalamic and Cortical Stimulus Response.....	89
Figure 3.2. Thalamic Optogenetic Hyperpolarization Modulates Ongoing Thalamic and Cortical Activity.	96
Figure 3.3. Thalamic Hyperpolarization Increases Thalamic and Cortical Velocity Response Curve.	101
Figure 3.4. Thalamic and Cortical Activity Examined With an Ideal Observer.	104
Figure 3.5. Thalamic Hyperpolarization Increases Cortical Theoretical Detectability of Sensory Responses.	107
Figure 3.6. Thalamic Hyperpolarization Increases Activated Cortical Area with no Loss in Spatial Discrimination.	112

Figure 4.1. Experimental Setup for Simultaneous Thalamic and Cortical recordings in the Anesthetized and Awake Brain.	136
Figure 4.2. Halorhodopsin Excitation Transitions Awake Thalamus into a Burst State.	140
Figure 4.3 Awake S1 Barrel Cortical Evoked Response Decreases During Periods of Thalamic Halorhodopsin Activation	144
Figure 4.4. Thalamic and Cortical Sensory Processing with Halorhodopsin Activation in Awake and Anesthetized Brain.	148
Figure 4.5. Cortical Spatial Response Across Awake and Anesthetized States.	150
Figure 4.6. Whisking States Alter the Magnitude of Thalamic Optogenetic Stimulation.	153
Figure 5.1. Theory on the Interaction of Thalamic State on Cortical Networks.....	168
Figure 5.2.Theory#1 Thalamic State Controls Cortical Excitatory and Inhibitory Networks.	169
Figure 5.3.Theory#2 Thalamic State Controls TC Synaptic Depression.	172
Figure A1.1.Notch Filtering of Fluorescence Response.	186
Figure A1.2. Reduction of Hemodynamic Noise.....	187
Figure A1.3. Effect of the Position of the Off-ROI on the Evoked Spatial and Temporal Response..	188
Figure A1.4. Non-Injected Control of Intrinsic Response during Whisker Stimulus. A. Mean Intrinsic Mapped Response (20 Trials).....	190
Figure A2.1. Example of combined Halorhodopsin and ArcLight expression in Mouse Sections	192
Figure A3.1. Figure A3.1. Halorhodopsin Activation Increases Ongoing Thalamic	

Spontaneous Firing and Bursting.....	194
Figure A3.2. Increase in Thalamic Activity During Halorhodopsin Activation Is Consistent Across the Recording..	197
Figure A3.3. Whole Cell in vitro Recordings Confirm Halorhodopsin Hyperpolarization and Thalamic Bursting.....	198
Figure A3.4. Integrate and Fire & Burst (IF&B) model neuron replicates Anesthetized in vivo responses to Halorhodopsin Input.....	199

LIST OF SYMBOLS AND ABBREVIATIONS

A1	Primary Auditory Cortex
Ach	Acetylcholine
Ca	Calcium
Cl	Chloride
CTX	Cortex
DBS	Deep Brain Stimulation
DC	Direct Current
EPSP	Excitatory Post Synaptic Potential
F	Fluorescence
Fo	Florescence baseline
FRET	Fluorescence Resonance Energy Transfer
FS	Fast Spiking interneuron
GABA	Gamma-Aminobutyric acid
GEVI	Genetically Expressed Voltage Indicator
GFP	Green Fluorescence Protein
H	Hydrogen
HEPES	4-(2-hydroxyethyl)-1-piperazineethanesulfonic acid
Hsyn1	Human synapsin promotor-1
Hz	Hertz
IF&B	Integrate Fire and Burst Neuron
IPSPS	Inhibitory Post Synaptic Potential
K	Potassium
L	Liter
LFP	Local Field Potential
LGN	Lateral geniculate nucleus Thalamus (Visual)
M	Molar
m	meter
MGn	Medial geniculate nucleus (auditory)
min	minute
mL	Milliliter
mM	milliMolar
Mm	millimeter
ms	Milliseconds
mV	Millivolts
MΩ	MegaOhm (resistance)
n	Number
nm	nanometer
NMDG	N-Methyl-D-glucamine
P	Statistics test output (p-value)

PBS	Phosphate Buffered Saline
PCA	Principle Component analysis
pH	Concentration of hydrogen
PPT	Pedunculopontine nucleus
PSP	Post Synaptic Potential
PSTH	Post Stimulus Time Histogram
R^2	Correlation coefficient (typically Pearson)
ROI	Region of Interest
s	Seconds
S1	Primary Somatosensory Cortex
S2	Secondary Somatosensory Cortex
SD	Standard Deviation
SEM	Standard Error of the Mean
SNR	Signal-to-Noise Ratio
SOM	Somatostatin interneuron
t	Time
TC	Thalamocortical
TRN	Thalamic reticular nucleus
μm	micrometer
V	Voltage (Volts)
V1	Primary Visual Cortex
V2	Secondary Visual Cortex
VIM	Ventral Intermedial thalamus
VPM	Ventral Posterior Medial Thalamus (Whisker)
VSDs	Voltage Sensitive Dyes
VSFP	Voltage Sensitive Fluorescence Protein
VT	Ventral Temporal Cortex
Δ	Delta (Change)

SUMMARY

The sensory thalamus controls the transmission of information from the periphery to the cortex and shapes our sensory percepts. While the thalamus receives prominent afferent projections from the sensory periphery via the brainstem, thalamic activity is also shaped through diverse modulatory inputs that influence a range of thalamic state properties including the time-varying baseline thalamic polarization. Although many neurological disorders including schizophrenia, and central pain syndrome are linked to thalamic dysfunction, basic information about ongoing thalamic processing is still unknown. Specifically, it is unclear how ongoing changes in membrane polarization (i.e. state) alter the transmission of information to and from the cortex.

The goal of this thesis was to develop novel techniques to measure entire cortical regions and to determine the role of thalamic state on tactile thalamocortical processing. In order to measure spatiotemporal cortical responses, we developed the techniques for recording the genetically expressed voltage indicators (GEVIs) for widefield imaging of the primary sensory cortex. We then utilized optogenetics to adjust the ongoing thalamic activity, and measured the sensory evoked cortical response using GEVIs in the vibrissa pathway of the anesthetized and awake mouse. We found that pre-stimulus modulations of thalamic polarization greatly impacted the thalamic spontaneous activity and evoked response to punctate sensory stimuli. In particular, we observed that pre-stimulus hyperpolarization controlled the level of thalamic bursting that occurred either spontaneously or was evoked by sensory inputs. Regardless of changes in the thalamus, we found that the overall neural state (anesthetized or awake) dictated the downstream cortical response to changes in thalamic polarization.

These results highlight the dynamic nature of thalamocortical processing and suggest an important role of ongoing thalamic polarization for the encoding of sensory features. Taken even further, our work suggests that state-dependent processing may play a predominate role in neural circuitry that extends beyond even thalamocortical circuits. By better understanding how thalamic state controls function of the highly complex thalamocortical circuit, it will be possible to develop better treatment options for neurological disorders.

CHAPTER I: INTRODUCTION

1.1 General Motivation

The major sensory systems of audition, somatosensation, and vision all share a common architecture and route a vast amount of sensory information through the thalamus to the primary sensory cortices¹. In addition to sensory signals, thalamic nuclei are critical for the implementation of motor commands, and for the maintenance of short term memory². Therefore, the thalamus is central in forming sensory percepts as well as processing and modulating behavior. Both the thalamus³ and cortex⁴⁻⁶ have been shown to be vital for even the most basic sensory detection tasks. Beyond the primary inputs to the thalamus originating from sensory organs, the vast majority of inputs to the thalamus (~90%⁷) are modulatory signals ranging from neuromodulatory inputs to cortical feedback. Despite the importance of the thalamus in sensory transmission^{8,9}, motor control^{10,11}, vigilance¹²⁻¹⁵, and neurological disorders^{7,11,16,17}, little is known about how ongoing thalamic activity shapes sensory transmission and sensory percepts.

The objective of this thesis is to fill this gap in knowledge, and to develop a better framework for how thalamic states modulate sensory encoding across thalamocortical structures. Thalamic nuclei receive inhibitory and excitatory inputs that combine to modulate the thalamic polarization, which dictates the ongoing thalamic firing rate, modulates thalamic synchrony, and activates dynamic thalamic firing modes (see Chapter 1.3). Here, we utilize advances in neuroscience methods to shift the ongoing thalamic polarization and apply reversible changes in ongoing thalamic polarization while measuring spatial and temporal responses in the cortex.

To accomplish these goals, I have developed three specific aims: 1) Develop novel procedures and analytical tools to measure spatiotemporal cortical dynamics in the mouse cortex using genetically expressed voltage indicators (Chapter 2). 2) Identify how thalamocortical states alter the transformation of sensory information in the anesthetized mouse (Chapter 3), and 3) Determine how thalamic polarization alters thalamocortical sensory representation in awake circuits (Chapter 4). The general outline is shown below in Figure 1.1.

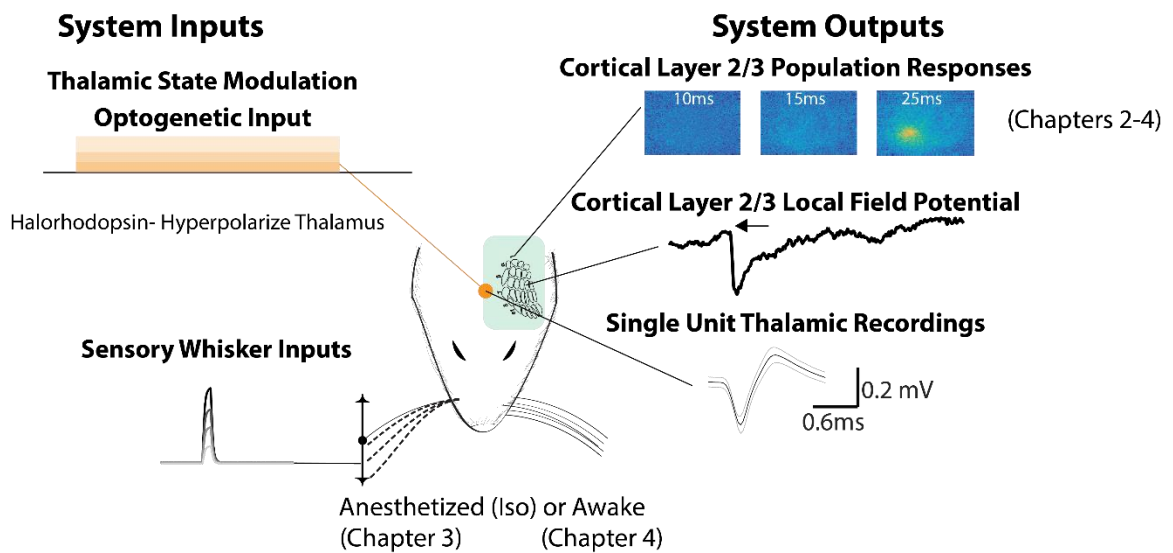


Figure 1.1. General Project Overview.

In each chapter we explore how the system inputs (thalamic state, and sensory inputs) alter the system outputs (downstream cortical response). In Chapter 2, we develop the techniques to measure cortical spatiotemporal responses. In Chapter 3, we use thalamic state modulation to determine changes in the cortical response of sensory inputs. In Chapter 4, we use the same methods from Chapter 3 to investigate the awake thalamocortical circuit.

While I focused my work on the tactile sensory pathway in rodents, the results of the work are general, and expand beyond this specific pathway. The major senses of vision, audition, and somatosensation all share similar thalamocortical circuitry. Therefore, these results will inform how state-dependent processing controls information across systems and

circuits for a generalizable model of neural function. Stated below are several sections highlighting key information for the understanding of this thesis.

1.2 The Thalamus: a Critical Component of Processing

This thesis focuses on the thalamus as a critical component of processing sensory information. The primary sensory thalamic structures (VPm, LGn, MGn, termed the lemniscal pathway) receive direct sensory information from second order nuclei, and projects almost exclusively to primary sensory cortical layers IV and V (S1,V1,A1)^{18–20}. Single thalamic neurons themselves contain relatively simple receptive fields, representing specific aspects of sensory stimuli (i.e. Cartesian space, intensity, frequency, simple edges) and typically encode two dimensions, such as position and intensity. For example, in the somatosensory system, thalamic single units correspond to somatotopically mapped regions (i.e. face, arms, legs) that correlate to the intensity or velocity of displacements of hairs or skin. However, recent work has found increasingly complex thalamic receptive fields suggesting that feature extraction and higher order processes begin very early in neural circuits²¹. The cortical input layers (primarily Layer IV/Va) pool the inputs across multiple thalamic neurons, which convert simple receptive fields to highly specific encoding of complex features of textures and objects. From thalamic inputs into cortical layers, sensory information is integrated across cortical space and sent to specialized cortical regions for additional higher order processing²⁰. Therefore, the sensory thalamus is a gate^{22–24} that controls what and how information is encoded to downstream cortical neurons.

While additional streams of sensory information do exist beyond the traditional lemniscal pathway (primary sensory thalamus projections to layer IV cortical regions) , including the

paralemniscal, extralemniscal, as well as subcortical circuits, these pathways are believed to supplement the lemniscal tract through additional sensory information^{9,25,26} and to correct for self-motion²⁵. These secondary thalamic nuclei project to different layers of the primary sensory cortices, and usually to higher order structures (S2²⁷⁻²⁹, V2/VT^{30,31}, A1 Ventral Caudal Belt³²). The Pulvinar (visual paralemniscal thalamus), for example, has shown to correlate with self-motion saccades in the visual system³³ and modulate attention effects across the cortex^{30,34}. Previous work, including lesion experiments²⁹, has shown that the lemniscal thalamus is pivotal for behavioral sensory detection tasks, whereas secondary pathways only marginally effect behavioral performance. A majority of secondary paralemniscal structures are only now being explored; and therefore, paralemniscal systems may play a more extensive role in sensory processing than currently stated. For this thesis, we will limit our investigation and manipulation to the lemniscal pathway and, unless otherwise stated, will refer to the thalamic lemniscal system exclusively as the thalamus.

1.3 Thalamocortical Responses Are Influenced by Ongoing Thalamic State

Historically, the thalamus was considered to represent a simple sensory relay station; however, this theory of thalamic function has been largely rebuked due to the complex and nonlinear transformations that occur in thalamic nuclei^{22,23,35,36}. The thalamus receives synaptic inputs (Post Synaptic Potentials or PSPs) that impact the overall membrane potential which controls the spiking output of the neuron. In general, as the excitatory PSPs (EPSPs) depolarize the neuron, the likelihood of a spiking event increases as the cell moves closer to spiking threshold in the spike initiation zone. Conversely, other inputs can hyperpolarize the cell (inhibitory PSPs or IPSPs), moving the membrane potential farther

from threshold. The combination of EPSPs and IPSPs forms the overall thalamic polarization that dictates the state of the thalamus and will determine the output to cortex.

The awake thalamus is in constant flux and receives tens of synaptic events a second³⁷. While some of these inputs are driven from sensory events, other inputs are not correlated with sensory inputs and are likely internally driven³⁷. Therefore, in a typical neuron, a more depolarized cell will have an increased response to sensory inputs, compared to a more hyperpolarized cell which will have a decreased response to sensory inputs. However, thalamic neurons have nonlinear dynamics which dramatically alter this typical input-output relationship. In particular, the membrane polarization will impact the thalamic firing mode, the state of the thalamocortical synapse, and the synchronization of thalamic inputs which will all determine how information is transmitted downstream.

In Section 1.4 we will investigate some of the origins of these modulatory inputs; however, first, in this section, we will explore how changes in thalamic activity alter thalamocortical state and the implications for the processing of sensory features. This will give context for the different modulatory inputs discussed in the next section.

1.3.1 Thalamic Polarization Controls Thalamic Burst and Tonic Firing Modes

Thalamic neurons have distinct firing modes³⁸ (i.e. tonic and burst). In tonic firing a thalamic neuron is at, or above, resting potential where a small depolarizing input causes a linear spiking output. However, after long periods of hyperpolarization (100s of ms), thalamic neurons enter a burst mode, where small depolarizing inputs cause a barrage of action potentials within a short (10 ms) time frame³⁹. In the thalamus, hyperpolarization de-inactivates low threshold T-type Ca^{2+} channels⁴⁰, which enable bursting through slow waves of calcium influx in response to a depolarizing input. These bursts of action

potentials are usually of high frequency (3-400Hz, see review ⁴¹); however, in vivo recording have shown thalamic bursts with inter-spike-interval's as low as 1.8ms⁴². Thalamic T-type channels (Cav3.1) undergo a conformation change during periods of hyperpolarization that is dependent on the period and strength of hyperpolarization⁴³. Typically, thalamocortical neurons must be hyperpolarized for a period of at least 100ms to form bursting behavior; however, the de-inactivation of T-type channels is a continuous process and can produce sizeable T-currents 70ms under extreme levels of hyperpolarization. Additionally, the strength of the T-type calcium current has temporal dynamics and reaches a peak current 500ms after the channels have been de-inactivated⁴³. While thalamic bursts (2 or more action potentials) are a hallmark feature of T-type currents, thalamic neurons do not always burst. Instead the effective threshold during hyperpolarization is reduced, and T-type channels create low-voltage spikes to depolarizing inputs⁴⁴. T-type currents have been shown to play dynamic roles in the ongoing and spontaneous firing in the awake mouse, even beyond the formation of thalamic bursts⁴⁵. While the biophysical dynamics of the thalamic bursting are becoming more understood, the exact role of thalamic bursting in sensory processing remains a mystery.

1.3.2 Thalamic Bursting– Regulating Sleep or Enhancing Stimulus Detection?

Currently, there are two main competing theories on the importance of thalamic bursting. Endogenously driven thalamic bursts have been historically associated with sleep states characterized by the emergence of slow wave signals in the cortex (1-4 Hz, Delta). These prolonged periods of bursting are highly reproducible and suggest that thalamic bursting represents a decrease in the vigilance of the animal, and a decrease in the transmission of sensory information associated with sleep-like conditions. Previous studies have found that cortical neural responses are reduced in the visual system⁴⁶ during behavioral states of

known bursting. Often, when the thalamus is in a prolonged period of bursting, the animal appears drowsy⁴⁷, or non-alert⁴⁸. However, to the best of our knowledge, there has not yet been a causal link between an increase in burst firing with a change in cortical sensory evoked responses.

Alternatively, sensory driven thalamic bursts have been theorized to act as a powerful “wake up call”⁴⁹ to the cortex, providing strong sensory input to downstream cortical targets. Awake spontaneous bursting is substantially lower than during sleep^{15,37}; however, a majority of these studies either do not provide sensory stimuli, or do not have single neuron recordings to determine firing patterns during behavior. Stimulus evoked bursting^{37,49–54} appears to be more common than spontaneous bursting. Furthermore, recent work suggests that sensory driven bursts in the visual thalamus (lateral geniculate nucleus, LGN) correlate with an increase in the detectability of visual stimuli in monkeys⁵⁴, suggesting that thalamic bursting may play a role in enhancing information flow.

Spontaneous thalamic bursting increases the probability of evoking a downstream cortical response in paired recordings^{47,55,56}; however, it is unclear how thalamic bursts influence behavioral detectability and cortical response of sensory driven activity. Thalamic neurons form strong synapses with cortical inhibitory populations⁵⁷ that control spatial integration (such as lateral inhibition), levels of overall excitability, and windows of opportunity. In particular, due to the strong facilitation of post-synaptic potentials (PSPs) onto somatostatin positive (SOM) interneurons, synchronized thalamic bursts could cause activations of the SOM network⁵⁸. Activation of the SOM interneuron network could have dramatic effects on the excitatory and inhibitory balance and the cortical activity as a whole. SOM interneurons have extremely diverse roles including providing widespread cortical hyperpolarization^{59–61}, inhibiting other subtypes of interneurons, or synchronizing

network inhibition⁶². Furthermore, work in the our lab suggests that an important variable is not just the magnitude of thalamic bursting, but the corresponding level of synchrony (i.e. coordinated firing across the neural population) of the thalamic bursting⁶³.

While many of these studies have shown dynamic effects of thalamic bursting, they are largely limited to either *in vitro* or in anesthetized preparations which are not representative of the awake behaving circuit⁶⁴. Thalamic state and thalamic bursting appear to play a critical role in both ongoing vigilance and sensory feature encoding but may represent context and brain-state dependent functions. Through this thesis, I specifically explore how different bursting states alter the transformation of sensory information in the anesthetized (Chapter 3) and awake (Chapter 4) animal in order to determine how these two theories of thalamic bursting may relate to each other.

1.3.3 Thalamic Activity and Synchrony Shape the Thalamocortical Synapse

While the most obvious effects of changes to thalamic polarization are on the neuron itself, changes in activity can have dramatic implications on downstream transmission. Inputs into the thalamus modulate the membrane polarization and dictate the overall spiking output and neurotransmitter release at the thalamocortical (TC) synapse. As stated above, a more depolarized neuron will generally increase the response and likelihood of evoking a spike to inputs. Alternatively, a more hyperpolarized neuron would (typically) decrease the likelihood of evoking a response to synaptic inputs. Therefore, the overall thalamic polarization will determine the ongoing thalamic firing rate, and the overall signal sent downstream to the cortex through the TC synapse.

The TC synapse plays an integral role in shaping sensory evoked cortical responses though numerous diffuse connections and significant synaptic depression. A single thalamic

synapse onto a cortical neuron (Layer IV) produces very weak ($<1\text{mV}$) excitatory post synaptic potentials (EPSP)^{56,65}. Therefore, evoking a downstream cortical spike requires numerous and synchronous events for propagation of sensory signals^{47,56}. The synaptic input onto a single cortical neuron is quite broad, where it is estimated that 85 thalamic neurons project onto a single cortical cell⁵⁶. These numerous but weak thalamocortical connections increase the impact of thalamic state (such as thalamic synchrony, bursting, and overall evoked rate) on the encoding of sensory stimuli. Due to the small evoked responses of a EPSP onto cortical neurons, it is theorized that highly synchronous events and thalamic bursts are required to drive downstream cortical activity⁵⁶. Thalamic synchrony has been found to be critical for neural phenomena, such as adaptation⁶⁶⁻⁶⁹.

In addition to being relatively weak, thalamocortical synapses are continuously modulated by the level of preceding activity through synaptic depression of the TC synapse. In particular, the thalamocortical synapse decreases evoked responses with even moderate pre-stimulus firing rates ($>2\text{Hz}$)⁷⁰⁻⁷². Due to the high firing rates of awake animals, *in vivo* thalamocortical synapses are theorized to be at some level of synaptic depression⁷³, with significant modulations of thalamic evoked responses lasting for seconds⁷⁰. The amount of synaptic depression can be quite profound (up to 75% of peak response) and is highly dependent on the magnitude and frequency of preceding spiking responses⁷¹. However, one important caveat is that these studies have often been conducted in the anesthetized animal, where neuromodulatory effects and overall firing rates are much different than the awake brain. Therefore, the temporal pattern of preceding activity is extremely important in shaping the magnitude of the evoked response, and presumably the level of detectability of sensory signals.

1.4 Ongoing Thalamic Polarization and State is Controlled Through Modulatory Inputs

Although the thalamus is predominantly responsible for transmitting sensory information to the cortex, the vast majority of the synaptic inputs on thalamic neurons are modulatory in nature⁷. For example, only 5-10% of the synaptic inputs into the visual thalamus (LGN) are from the retina (the primary visual sensory organ)⁷⁴. Modulator and driver synapses are part of a model of thalamic inputs proposed to distinguish the overall functional role of synapses and the organization of primary and high-order thalamic structures^{7,75}. Driver inputs form large synapses onto post-synaptic ionotropic receptors and originate from second order nuclei that contain direct sensory information and determine the overall thalamic receptive field (Figure 1.2). Modulatory synapses differ from “driver” inputs by the smaller physical size of the actual synapse, smaller post-synaptic-potential (PSPs), synaptic location on the more distal dendrite, and decreased likelihood of producing spiking output. Modulatory synapses can produce either direct effects on the ongoing thalamic membrane potential through Excitatory PSPs (EPSPs) and inhibitory PSPs (IPSPs) through ionotropic receptors or more complex nonlinear interactions through metabotropic receptors (typically G-coupled proteins). Ultimately, it is the accumulation of inputs, including EPSPs and IPSPs that determines the ongoing thalamic polarization (i.e, state).

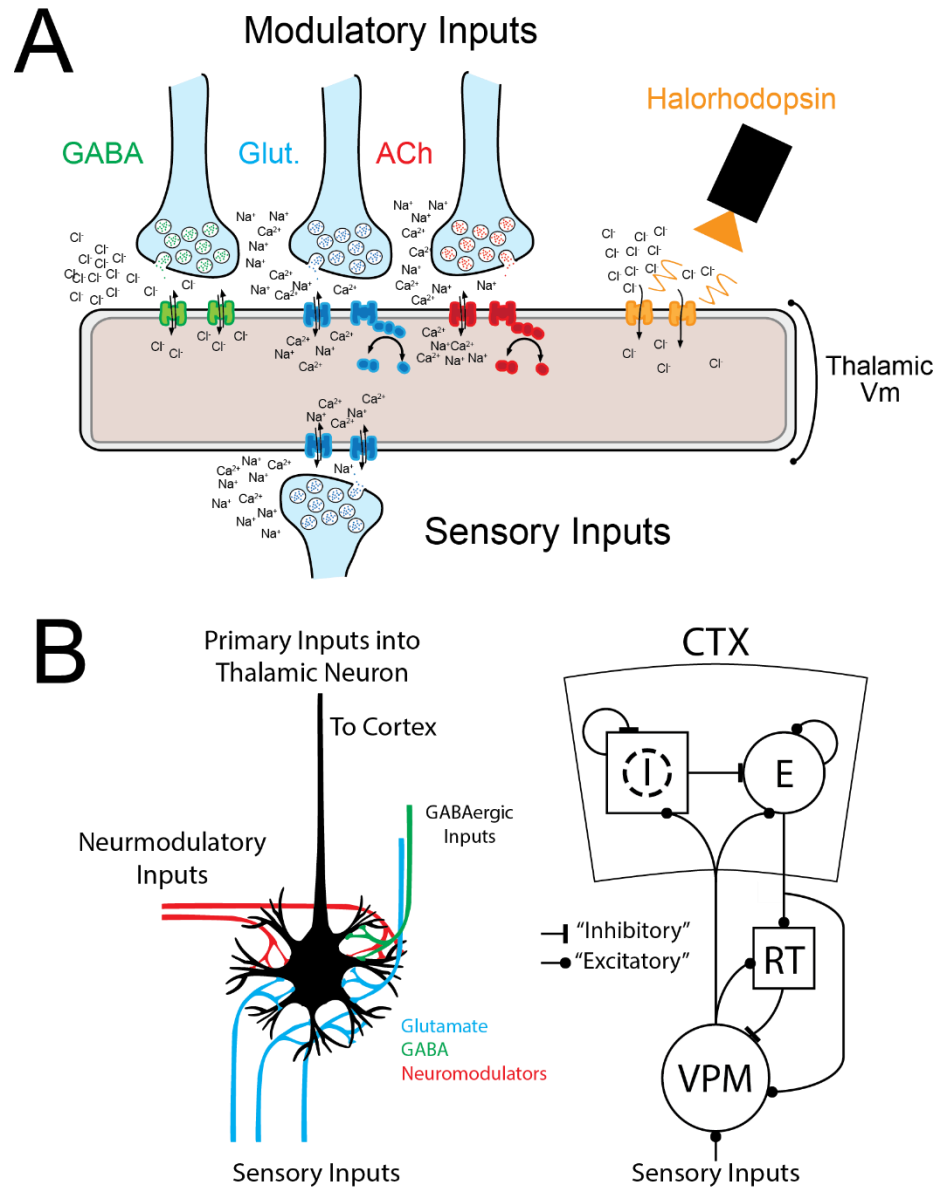


Figure 1.2. Thalamic Polarization is Controlled by Modulatory and Sensory Inputs.

A. Cartoon outline of the most common inputs into thalamic neurons that form the EPSPs and IPSPs that ultimately combine to impact the overall thalamic baseline polarization. **B. Left.** Cartoon description of thalamic inputs that control the overall activity. **B. Right.** Thalamocortical circuit diagram showing the projections from the thalamus into the inhibitory and excitatory cortex networks for the somatosensory whisker pathway. In addition to modulatory and sensory inputs, the thalamus is part of a more complex and interconnected thalamocortical circuit.

Although awake thalamic firing is highly correlated with sensory inputs, there are distinct states of activity that are independent from sensory inputs³⁷. The thalamus receives a diverse range of modulatory inputs from top-down sensory feedback from the cortex³⁶ and thalamic reticular nucleus^{76,77} to widespread neuromodulatory control from the reticular formation, many of these processes are still being fully discovered⁷⁸. In primary sensory thalamic nuclei, the vast majority of modulatory inputs come from cortical Layer VI and acetylcholine (ACh) centers, with only minor contributions from other neuromodulators. These modulatory inputs can alter thalamic polarization across many temporal scales⁷⁹ (minutes to hours) that form a highly dynamic and time-varying system. In addition to direct manipulations of thalamic state, the thalamus can be modulated through bottom-up mechanisms such as sensory adaptation⁸⁰.

Taken together, ongoing thalamic activity is in constant flux as it receives modulatory inputs that interact with the sensory inputs to shape the downstream processing of sensory information. While many studies have identified thalamic inputs that alter ongoing activity, it is fairly uncertain how different levels of thalamic polarization shape sensory transmission across thalamic and cortical structures. Here, we explore a single axis of thalamic state with the examination of how hyperpolarized states alter the transmission of sensory information. In this next subsection, we explore the major inputs to the thalamus, and the impact of ongoing thalamic states on both thalamocortical sensory representations and thalamic firing modes to develop a framework for thalamic function.

1.4.1 Manipulation of Thalamic Activity Through Thalamic Reticular Nucleus and Cortical Layer VI Inputs

The thalamus is a single part in an interconnected excitatory and inhibitory network that includes thalamic reticular nucleus (TRN) and cortical layer VI input. These two regions provide the primary neurotransmitter (GABA and Glutamate) control of thalamic polarization. With this work, we examine the relationship between ongoing thalamic firing and induced hyperpolarizing states on sensory encoding, which could represent naturally occurring modulations of thalamic activity from the TRN and through cortical feedback.

The primary GABAergic (IPSP) input into the sensory thalamus is from the TRN, a thin shell region that surrounds the thalamus (for review see ^{77,81}). GABA binds to with chloride channels to provide hyperpolarizing inputs to thalamic neurons, which have a profoundly low reversal chloride potential (-81mV)⁸². The TRN receives bottom-up input from the primary sensory thalamus, and top down control from layer VI of topographic primary sensory cortices, as well as other long range cortical projections to form multisensory receptive fields⁸³. The TRN is spontaneously highly active, and therefore, is constantly shaping the ongoing thalamic polarization^{84,85}. While TRN excitation is theorized to inhibit thalamic activity, very few studies have directly modulated TRN activity while measuring thalamic responses. The TRN itself contains a network of electrically coupled cells and inhibitory circuits that add further complication to the network. The majority of studies have optogenetically excited the TRN to attempt to silence thalamic responses⁸⁶⁻⁸⁸. In order to shut down thalamic responses, these studies have used very high levels of optogenetic input (100's of mW/mm²) resulting in varying levels of success.⁸⁶⁻⁸⁸ In fact, published work⁸⁷ and personal communication have found the thalamus to be particularly resistant to silencing due to T-type calcium channels, which enable low-voltage spiking activity and

bursting states. Often, after short time periods of TRN excitation, thalamic cells will begin to fire with increased levels of thalamic bursting⁸⁷.

These complex inputs from thalamic and cortical sources into the TRN create multisensory receptive fields that have led researchers to investigate the TRN as a central component of basic sensory attention and filtering, termed the “searchlight” hypothesis⁸⁹. Indeed, the TRN is differentially controlled through visual and auditory spatial attention tasks in mice⁹⁰ and monkeys²² which suggest that the TRN can be controlled in a task dependent manner to control ongoing thalamic activity. In addition to controlling levels of cognition and sensory salience, TRN activity has also been implicated in controlling sleep-wave cycles through increased thalamic bursting and cortical spindles^{21,91}. However, due to the limitations of traditional electrical and chemical manipulation techniques, TRN research has been limited.

In addition to TRN input, cortical layer VI inputs are sent to the thalamus via bifurcating axonal projections from the cortex that also excite TRN and sensory thalamic regions^{36,92}, usually across topographically aligned cortical areas. The bifurcating axonal projections have been found to have complex temporal dynamics that can either cause a net depolarization or hyperpolarization in thalamus based on the frequency of stimulation^{36,93}. Gross modulation and removal of cortical activity has been shown to have a net increase in thalamic responses to visual sensory stimuli^{21,94}; however, opposing effects have been seen across different sensory modalities⁹⁵. Layer VI cortical inputs have been shown to be linked to metabotropic glutamate receptors, which operate on long timescales (100’s of ms), and have an important role in changing thalamic burst and tonic modes⁹⁶ (see Chapter 1.3.2). Layer VI activity is sparse in the awake brain⁹⁷, and are only now being thoroughly investigated as a major component of thalamocortical processing due to recently developed

targeted genetic tools. In summary, the thalamus receives direct inputs from either the TRN or through cortical feedback which can control ongoing thalamic polarization.

1.4.2 Neuromodulatory Control of Ongoing Thalamic Activity

While this work does not directly utilize neuromodulators, overall levels of thalamic activity and state are influenced by neuromodulatory networks. Neuromodulatory inputs shape spontaneous thalamic activity through direct changes to the baseline thalamic polarization (ionotropic receptors) and additional effects of metabotropic receptors⁹⁸. Metabotropic neuromodulatory effects can even modulate the synapses themselves to alter the transmission of synaptic signals⁹⁹. Thalamic neurons receive a wide range of neuromodulatory inputs including acetylcholine, norepinephrine, dopamine, histamine, and others (for review see⁷).

Primary sensory thalamic neurons have been shown to be very sensitive to acetylcholine (ACh). Roughly 50% of the modulatory inputs originate from ACh centers, in particular the pedunculopontine tegmental nucleus (PPT) and the basal forebrain complex. Acetylcholine has been found to predominantly depolarize the thalamus, and with a pronounced effect on the baseline firing rate. Electrical stimulation of the reticular formation (including the PPT) has shown to increase thalamic baseline activity, and prevent effects of sensory adaptation to repetitive frequency stimulation^{100–103}. Thus, ACh may play a role in thalamic gating. Acetylcholine has recently been found to be continually regulated in the awake brain during states of attention¹⁰⁴ and pupil dilation¹⁰⁵, and therefore may represent a global neural state.

In addition to direct modulation of thalamic polarization, neuromodulators have been found to impact the thalamocortical network with differential effects. For instance, while

acetylcholine depolarizes the thalamus, ACh hyperpolarizes the reticular thalamus nucleus (TRN), which diminishes the overall GABAergic input into sensory regions. Other neuromodulators (including norepinephrine) will selectively enhance TRN activity⁹⁹, suggesting dynamic control of the thalamus through release of neuromodulators across the thalamocortical circuit. Taken together, neuromodulatory inputs are constantly shaping the thalamic state through direct and indirect mechanisms.

1.4.3 Sensory Inputs and Self-Motion Alter Ongoing Thalamic State

On top of any internally modulated thalamic states, it is important to also consider the thalamocortical circuit in relation to the sensory organ itself. In the awake animal, the sensory organ of the eyes and/or skin is actively involved in sensing either through saccades or rhythmic touch to scan the environment. In rodents, active sensation in the vibrissal pathway is driven by rhythmic movements of the whiskers, termed whisking, and occurs during periods of exploration, navigation, and general movement. Active sensing has been found to not only change the animal's external representation of the stimulus, but also the underlying internal state as the animal becomes engaged in the task. In the thalamus, these active states have been found to have a profound effect on thalamic activity, either preceding or during active sensation³⁷, or during behavioral tasks. Previous work in the Stanley laboratory has found that ongoing sensory inputs themselves can dramatically alter the encoding of sensory information through changes in evoked thalamic responses and thalamic synchrony^{67,68,106}. While external sensory induced changes to thalamic activity goes beyond the focus of the work presented here, these effects of self-driven activity become especially important when investigating the awake animal (Chapter 4).

1.4.4 Thalamic State Coupled to Cortical State

Due to the anatomical and functional connectivity of the thalamus and cortex, the thalamic and cortical states are innately coupled. Thalamic neurons drive cortical responses, where recurrent connections directly (Layer VI feedback) or indirectly (TRN) modulate thalamic state^{36,107}. However, the extent of how the thalamus can regulate, and be regulated by the cortex is still relatively unknown. Therefore, while experimentation throughout this thesis focuses on manipulation of thalamic state, we are not simply modulating the firing properties of the thalamic population (i.e., tonic or burst, synchrony, and overall firing rate) but also the ongoing cortical state¹⁰⁸. Additionally, thalamic neurons synapse onto both excitatory and inhibitory cortical neurons⁴⁷, with very strong connections to inhibitory circuits⁸⁸. Modulation of thalamic states has been shown to drive the cortex into various different cortical regimes^{37,109}. Additionally, ongoing cortical states (including UP and DOWN as well as desynchronized and synchronized) have been shown to influence the sensory representation in anesthetized¹¹⁰ and awake animals^{109,111}, although the influence on behavioral percepts is still unclear¹¹². Relatively few studies have directly manipulated and/or controlled thalamic state and observed the influence on downstream cortical responses. By dynamically controlling the thalamic state, we will be able to examine how thalamic state modulates ongoing cortical activity and ongoing cortical networks.

1.5 Dysfunction of Thalamic Activity: Insights from disease

Thalamic dysfunction has been associated with a number of clinical neurological diseases in humans including central pain^{113,114}, epilepsy^{115,116}, schizophrenia^{17,117}, and tremor¹¹⁸, which highlight the importance of proper thalamic function. For instance, thalamic dysfunction has been highlighted as an important center for regulating muscle control for tremor in Parkinson's Disease. The first Deep Brain Stimulation (DBS) treatment option

for tremor was approved by the FDA for stimulation in the ventral intermedial (VIM) thalamus¹¹⁹. Often, in neurological disorders, thalamic dysfunction is one of many neural centers affected by each disease. Parkinson's is also accompanied with widespread changes in neurologic function including loss of sensory perception¹²⁰, as well as dramatic loss of dopaminergic regions in the brain. Therefore, it can be difficult to correlate thalamic dysfunction with particular symptoms.

While rare, specific somatic sensory thalamic neural lesions do occur in people, which cause a significant loss of sensory perception (contralateral hemianesthesia) and complete loss of temperature and pain sensation. Whereas cortical lesions can result in specific loss of high level function, or particular sensations, thalamic lesions are distinct in the loss of all aspects of perception. Partial thalamic lesions, or damage from stroke, can cause strong feelings of pain, which often accompany changes in ongoing thalamic activity with a noted change in thalamic bursting^{113,114}. Central or thalamic pain is very difficult to treat using common pharmacologic agents due to the changes in the encoding of sensory information itself. Additionally, in more complicated neurologic diseases involving changes to sensory perception (such as schizophrenia, and bipolar disorder), evidence is now emerging of dysfunctions in thalamocortical control circuits, particularly in TRN¹²¹. Taken together, the sensory thalamus plays a particularly important role in perception of sensory information; therefore, by determining how thalamic systems communicate under non-pathologic conditions we gain deeper insights into neural disease that will aid in the development of novel treatments.

1.6 GEVIs for Measuring Thalamocortical Modulation across Behaviorally Relevant Cortical Regions

In the thalamocortical sensory circuit, sensory inputs diverge across multiple cortical regions¹²² representing a complex spatial network. These inputs are often subthreshold and historically have only been measured using meticulous intracellular recordings¹²³. Sensory information travels through the thalamus and activates the primary and secondary somatosensory cortices¹²⁴, and motor cortices^{125,126} through long range projections at high temporal speeds (10's of milliseconds). Taken together, small changes in thalamic state and thalamic sensory encoding can dramatically alter neurological function across large regions of the cortex at high temporal speeds. Beyond sensory processing, higher order functions including decision-making and working memory have been shown to incorporate across the cortex^{127,128}. However, due to the limitations of technology, experiments with high spatial (millimeters) and temporal resolution (10's of milliseconds) across large cortical regions have been historically difficult.

Neurons have a weak natural functional fluorescence (Flavoproteins¹²⁹), and, therefore, additional contrast agents are needed for imaging of neural activity. Traditionally, voltage sensitive indicators were organic dyes (ie di-4-ANEPPS¹³⁰, RH155¹³¹, RH1691¹³²) that required staining of the neural membranes. However, voltage sensitive dyes have many limitations which have hindered their use in the awake behaving animal including, phototoxicity, pharmacological effects¹³⁰, and invasive staining procedures¹³⁰. Within the past decade, novel voltage indicators have enabled large scale imaging of neural circuits with increased temporal dynamics and fluorescent responses. Genetically expressed voltage indicators (GEVIs) are voltage sensitive fluorescent proteins that allow for direct measurement of membrane potential changes through changes in fluorescence. These GEVIs (including ArcLight¹³³, Butterfly 1.2¹³⁴, Quasar1¹³⁵, and mNeon-Ace¹³⁶) have shown incredible promise to record neural responses (for review:^{137,138}). However, GEVIs have yet to be fully characterized, which has limited their overall use and adoption in the

field. Through this thesis work, we hope to bridge this gap by thoroughly evaluating the use of these optical recording techniques, and by applying these techniques to understand complex scientific questions of thalamocortical processing during behavior.

1.6.1 Widefield Imaging of GEVIs for Measuring Voltage over Large Cortical Regions

Single photon wide-field imaging of GEVIs allows for large scale cortical recording with moderate temporal (10s of ms) and spatial resolution (10s of μm) of the superficial cortical layers. Currently, due to limitations of GEVIs and imaging techniques, fast (>10 Hz) single cell resolution imaging over large spatial scales (millimeters) remains difficult (see Appendix A.1). As with every recording modality there is a dynamic tradeoff between spatial and temporal resolution as well as overall scale of recordings. Whole cell intracellular recordings are the current gold standard with high spatial and temporal resolution; however, these recordings are severely limited in scale. Other techniques including multichannel extracellular recordings, allow for increased scale (100s of μm); however, physically implanted traditional probes severely degrade over time (days to months). Therefore, widefield imaging of GEVI signals enables the measurement of large cortical structures with high spatial and temporal resolution that can be recorded chronically.

1.7 General Experimental Design for Controlling Thalamic State and Measuring Effects on Thalamocortical Processing

The primary goal of this thesis is to determine how different thalamic states modulate sensory spatiotemporal encoding in the thalamus and cortex. In particular, this work aims

not to simply investigate correlative relationships between thalamic states but to causally link different thalamic states to changes in sensory processing. In order to achieve these goals, we utilized a simple experimental design, and recent advances in optogenetics, to control ongoing thalamic state by applying a constant offset to the membrane polarization while providing simple sensory inputs.

1.7.1 Optogenetics as a tool for manipulating thalamocortical states

Optogenetics is a novel recombinant DNA technique where we use advances in genetics to insert a plasmid into the cellular genome for the expression of proteins for the modulation of neural activity. Optogenetic constructs are light sensitive membrane bound proteins that control the influx of ions into the cell, where each construct is activated at particular wavelengths of light for dynamic control of the neural membrane potential (see review¹³⁹). Due to the fast temporal dynamics of the optogenetic constructs, we achieve millisecond resolution whose level of polarization can be modulated across the neuron through overall light intensity (mW/mm^2). Instead of driving or silencing neural responses, we used optogenetics to provide a modulatory effect, by using various levels of light intensity to adjust the overall magnitude of polarizing states. Throughout this manuscript, we utilized a viral vector or genetic breeding to express optogenetic constructs into thalamic structures for optogenetic manipulation of thalamic activity.

Here, we alter one aspect of thalamic state through modulation by providing brief periods of hyperpolarizing input into the thalamic population using the optogenetic chloride pump halorhodopsin (eNrph3.0). Based on known thalamic research (see Chapter 1.2-1.3), the thalamus experiences various alterations in state, from complex burst-tonic relationships to dramatic changes in ongoing firing rate. While thalamic state encompasses all variations of different thalamic activity, at the crux, most general changes to thalamic state arise from

shifts in baseline polarization, through either direct circuit input (IPSCs and EPSCs) or neuromodulatory inputs. By using halorhodopsin, we are able to explore how changes in relatively hyperpolarized (halorhodopsin on) states differ from relatively depolarized (halorhodopsin off, control) states in the anesthetized and awake circuit. Additionally, with halorhodopsin, we can specifically activate bursting properties of the thalamus to determine how burst and tonic modes directly impact thalamic and cortical processing.

1.7.2 Rodent vibrissal pathway as an ideal model of thalamocortical circuits

Throughout this thesis work, we used the rodent vibrissal pathway as an ideal model system for studying the effects of different thalamic states on thalamocortical processing^{1,9}. Rodents are the most widely used model system for studying thalamocortical sensory processing and therefore there is a rich research history to compare to our observed results. Rodents are primarily nocturnal creatures that rely heavily on their whiskers to explore their surroundings. Therefore, the vibrissal system has large dedicated areas of neural processing in the thalamic nucleus and in the Primary Somatosensory (S1) Cortex (see review^{1,20,140}). These distinct areas of processing combined with the discrete nature of the whisker system are ideal for testing sensory processing. Additionally, rodents can be trained to respond to simple detection tasks with whisker stimulation^{106,141,142}, and therefore, allow the neural data to be coupled with the behavioral output. Finally, the genetic variants of rodents allow for tightly controlled genetic expression to specific neural regions¹⁴³ (such as the specific thalamic nuclei, i.e. the VPM), which makes these animals highly suited for this project.

1.7.3 ArcLight GEVI for Recording Cortical Layer II/III Activity

Here, we developed the techniques and tools for using GEVIs to measure fast timescale changes in membrane voltage across cortical systems. Although several investigators have demonstrated the capabilities of GEVIs, most of these studies have reported responses through *in vitro* models^{129,133,144,145}, *Drosophila*^{146–149}, or the mouse olfactory system^{129,133}.

In this thesis, we utilized the novel voltage indicator ArcLight as a spatial measurement of suprafacial cortical membrane potential. ArcLight, a modified GFP protein, has fast temporal resolution (~10 ms) with relatively large changes in fluorescence in response to membrane fluctuations. There are many reasons we selected ArcLight as the voltage indicator for this particular work, including the high photostability, fast temporal dynamics, and relatively large corresponding changes in fluorescence. Additionally, in order to optically stimulate and record neural activity, we need spectral separation between our sensor (ArcLight) and our actuator (Halorhodopsin, eNph3.0). Other Fluorescence Resonance Energy Transfer (FRET) based sensors, such as Butterfly 1.2, offer better signal-to-noise ratio *in vivo*, but require more spectral operating space, which makes paired optogenetic recording difficult. Currently, there is no perfect GEVI for measuring *in vivo* responses.

1.8 Organization of Thesis

This thesis has been organized in a particular manner to best present the results in a logical and clear fashion. In Chapter 1 (Introduction), we have outlined the central concepts that will be discussed throughout and we have identified major gaps in knowledge that will be investigated further throughout each chapter. This chapter is meant to give a broad overview of the thalamocortical circuit and highlight gaps in knowledge that will be filled

through this research. Chapter 1 is not a definitive review of every aspect of thalamocortical function, but its purpose is to give the lay-reader enough knowledge to understand and judge this body of work.

In Chapters 2 ,3, and 4, we have focused on a particular area of research that was pivotal for answering the central questions and progression of the thesis. Chapters 2, 3, and 4 are written to stand alone as individual contributions to the scientific community; however, they each form different components of the overall narrative of understanding the impact of thalamic states on cortical processing. In Chapter 2, we develop a central novel imaging technique that was developed to measure specific aspects of neural function that are pivotal for the remaining chapters. In Chapter 3, we utilized this novel imaging technique in combination with additional techniques to manipulate thalamocortical function in a controlled manner. Here, we further develop tools, techniques, and a framework of thalamocortical function while investigating a controlled thalamic and cortical environment. In Chapter 4, we combine all of these techniques to alter the thalamocortical processing in the awake circuit, and compare these results to the more controlled setting of Chapter 3. Chapter 4 represents the pinnacle of the experimental methodology to probe the awake and highly dynamic neural circuit. Finally, in Chapter 5, we present the ultimate findings of my graduate work with predictions for the overall implications of changes in thalamic activity along with a road map for future studies.

CHAPTER II: ARCLIGHT FOR IMAGING LARGE SCALE CORTICAL ACTIVITY IN THE ANESTHETIZED AND AWAKE MOUSE

The following chapter has been presented several conferences^{150–152}, and is currently in print as: Borden, P. Y. *et al.* Genetically expressed voltage sensor ArcLight for imaging large scale cortical activity in the anesthetized and awake mouse. *Neurophotonics* 4, 031212 (2017).

2.1 Introduction

With the recent breakthrough in genetically expressed voltage indicators (GEVIs), there has been a tremendous demand to quantify the capabilities of these sensors *in vivo*. Novel voltage sensitive fluorescent proteins allow for direct measurement of membrane potential changes through changes in fluorescence. These GEVIs, including ArcLight¹⁴⁶, VSFP 2.3¹³⁴, Butterfly 1.2¹⁵³, Quasar1¹³⁵, and mNeon-Ace¹³⁶, have shown incredible promise to record neural responses^{137,138}. However, these approaches have not yet been widely applied in scientific studies in the mammalian nervous system (for review^{138,154}). Although recent calcium probes have greatly increased the understanding of complex neural systems, they still offer only moderate temporal resolution (50-100ms)¹⁵⁵ and report only on byproducts of suprathreshold neural spiking activity through calcium responses. Additionally, many studies try to deconvolve the calcium signal to glean information about ongoing membrane potential with mixed success (for review¹⁵⁶). In contrast, voltage sensors allow for fast temporal information (i.e., milliseconds) and have the potential to report even subthreshold information.

We present an investigation into the functional capabilities of ArcLight, one of the sensors available as an in-vivo probe of wide-field cortical signals. ArcLight¹³³, a modified GFP protein, has fast temporal resolution (~10 ms) with relatively large changes in fluorescence

in response to membrane fluctuations. Although several investigators have demonstrated the capabilities of ArcLight, most of these studies have reported responses through *in vitro* models^{144,145}, *Drosophila*,^{146,148,149,157,158} or in the mouse olfactory system^{129,146}. Other sensors, including VSFP 2.3¹³⁴, and Butterfly 1.2¹⁵⁹, have been previously shown to be successful for *in vivo* cortical sensory recordings (for review¹³⁸). In this work however, we are the first, to our knowledge, to demonstrate the use of ArcLight in cortical structures in the awake and anesthetized mammalian brain.

Here, we demonstrate that ArcLight produces a robust and reliable sensory evoked fluorescent response in the S1 barrel cortex to sensory stimulation. We found that in the S1 barrel cortex the spectral overlap with the hemodynamic activity was substantial in its raw form and required long imaging experiments and trial averaging to reduce noise. In order to address this large hemodynamic signal, we subtracted a scaled Off-ROI signal to remove ongoing noise. Although this method dramatically removes the hemodynamic response, there are several assumptions and concerns which limits the widespread use of this technique. Using this *post hoc* subtraction method, we found that the evoked response matched the fast temporal dynamics of other voltage indicators including voltage sensitive dye RH1691^{111,126,160,161}, VSFP 2.3¹⁶¹ and Butterfly 1.2¹⁵³. ArcLight showed clear stimulus-evoked fluorescence for stimuli with frequency content up to 20 Hz with high fidelity. By using paired local field potential recordings, we determined a high correlation between the average LFP and ArcLight signals in response to sensory stimuli; however, on a single trial the two signals showed weak correlation. Finally, we were able to resolve sensory evoked fluorescence in awake mice. Based on these results, we conclude that ArcLight has a capacity to measure chronic *in vivo* cortical responses. ArcLight would be suited for *in vivo* experiments where a single fluorophore sensor is desired, in particular experiments that require long bouts of continuous imaging

2.2 Methods

All procedures were approved by the Georgia Institute of Technology Institutional Animal Care and Use Committee and followed guidelines established by the National Institutes of Health.

2.2.1 AAV Delivery

At least four weeks prior to experimentation, six week old female mice (C57BL/6, Jackson Laboratories) were anesthetized using Isoflurane, 3-5% in a small induction chamber, and maintained at 1-3% Isoflurane. Following anesthetization, 1-2 small craniotomies were created over the barrel field of the primary somatosensory cortex (S1) according to stereotaxic measurements taken from the bregma (3.5mm x 1.5 mm, and 2.5mm x 3 mm). The virus was loaded into a Hamilton syringe (701-N). A custom ~35µm pulled borosilicate glass pipette filled with a silicone gel and secured onto the tip of the Hamilton syringe to increase taper and to reduce damage to the cortex caused during the injection. The injection pipette was initially lowered to the target depth below the pia surface (500µm) using a 10µm resolution stereotaxic arm (Kopf, Ltd). Following a 1 minute delay to allow for tissue relaxation, each animal was injected with 1µL of AAV1-hsyn1-ArcLight-D-WPRE-SV40 (UPenn Viral Vector Core, AV-1-36857P) at a flow rate of 0.1µL/minute (0.5µL each for two injections). After injection, the pipette remained in place for an additional 5 minutes before slowly being removed from the brain. The craniotomies were then filled with bone wax, or left to close naturally. In all cases, the skull was sealed by clamping the skin using wound clips. During the injection, mice were kept warm using a water heating system to maintain body temperature. Throughout the experiment, sterile techniques were used to keep the injection area clean and free from

infection. Additionally, no antibiotics were given to prevent infection. All mice survived this minor procedure.

2.2.2 Headplate and Prep

After at least four weeks post injection, we secured a metal headplate to the skull for fixation in order to reduce vibration and allow headfixation during imaging experiments. The custom metal headplate (titanium) formed a ring (inner radius 5mm) around the entire cortex and contained flared v-shape projections (~10mm) for attachment to a custom vice to reduce vibration. Mice were initially anesthetized using isoflurane (3-5%) and then placed on a heated platform (FHC, Inc) with a stereotaxic nose cone to maintain anesthesia. A large incision was made over the skull. The connective tissue and muscles surrounding the skull were removed using a fine scalpel blade (Henry Schein #10). A headplate was attached using a three stage dental acrylic, Metabond (Parkell, Inc.). The Metabond was chilled using ice, slowly applied to the surface of the skull, and allowed to cure for 5-10 minutes. After securing the headplate, the skull was left either exposed or was lightly thinned using a dental drill and covered with a thin layer of clear adhesive (LockTight 401, ULine, Inc.). We found that the Metabond dental acrylic alone was able to firmly adhere to the animal's skull and could not be removed without destroying the adhered bone. During preparation for histological validation, the headplate could not be separated from the attached skull and the brain was extracted by removing the lower jaw. The final headplate and dental acrylic structure additionally created a well for saline which helped maintain skull transparency for imaging during the intact skull preparation. The headplate was then transferred to a flexible arm to align the camera for imaging of the cortex. The nose cone was realigned to allow for continuous delivery of isoflurane while having access to the whiskers. After surgery, the isoflurane levels were dropped to ~1% for all imaging and electrophysiological experiments. The animal's heart rate, repertory

rate, blood oxygenation, and toe-pinch responses were constantly measured for anesthesia depth. Isoflurane levels were adjusted to maintain a constant level of light anesthetization, monitored by heart rate, respiration rate, and functional cortical response.

2.2.3 Whisker Stimulator

All single whiskers were stimulated by a galvanometer system (Cambridge Technologies) to yield high fidelity sensory stimuli. The galvanometer stimulator has a 15mm extension to target single whiskers. The galvanometer system was controlled using a custom developed hardware/software system (Matlab Realtime Simulink, Mathworks). The real-time system controls the stimulus using two computers, a target and a host. The target computer ran a proprietary Linux kernel that was controlled by the host computer. The entire system was updated at a 1 kHz sampling rate, with a custom developed algorithm to output voltage commands using an analog output card (National Instruments). The galvanometer system was positioned ~10mm from the mouse whisker pad and delivered deflections on the single whisker in the rostral-caudal plane. Unless otherwise noted we used a simple exponential sawtooth (rise and fall time = 8ms) for punctate whisker deflections⁸⁰. The reported waveform stimulus velocity was determined as the peak velocity during the waveform (1200 Deg/s). All stimulus waveforms were delivered in a pseudorandom order with at least 4 seconds between trials to reduce potential confounds. Due to the fast rising edge of the sawtooth, all latencies were defined relative to stimulus onset.

2.2.4 Cortical ArcLight and Intrinsic Imaging

ArcLight transfected mice were imaged through either intact or thinned skull using a wide-field fluorescence imaging system to measure cortical spatial activity (MiCam02HR

Scimedia, Ltd). During all imaging experiments, isoflurane anesthesia levels were lowered to approximately 1%. The headplate was used as a saline well to keep the bone surface wet during imaging, which dramatically increases transparency of the mouse's skull. Some animals were chronically imaged through either intact or thinned skull covered with a glass coverslip and/or Cyanoacrylate glue. The cortex was imaged using a 184x123 pixel CCD Camera (Scimedia MiCam2 HR Camera) at 200 Hz. In all experiments, we had a field of view of 4x3mm with a total of a 1.6 Magnification (48 pixels/mm). The particular optical system used in this work has an optical resolution of 2.25 μm (Numerical Aperture = 0.141, optical resolution = $0.61\lambda/\text{NA}$). The camera in combination with the optics had a spatial resolution of $\sim 20\mu\text{m}$ per pixel; however, this resolution does not consider the scattering of the light in the tissue. During experimental imaging, the illumination excitation light was left continuously on. The entire cortical area was illuminated at 465nm with a $400\text{mW}/\text{cm}^2$ LED system (Scimedia, Ltd) to excite the ArcLight fluorophore. The excitation light was further filtered (Cutoff: 472/30nm bandpass filter, Semrock, Inc) and projected onto the cortical surface using a dichroic mirror (Cutoff: 495nm, Semrock, Inc). Collected light was filtered with a bandpass emission filter between wavelengths of 520/35 nm (Semrock, Inc). The imaging system was focused at approximately $300\mu\text{m}$ below the cortical surface to target cortical layer 2/3. The procedures for mapping and recording sensory responses in the barrel cortex with the ArcLight voltage sensor is outlined below. For intrinsic imaging of the hemodynamic response, the cortical surface was illuminated by a 625nm red LED (ThorLabs), and imaged with the same camera system as above, at a temporal resolution of 10Hz. During intrinsic imaging, no emission filters were used. In order to evoke a cortical intrinsic response, the whisker was repetitively stimulated at 10Hz for 6 seconds.

2.2.5

The mouse's whisker system was first mapped by imaging the rapid response to a high velocity (1200 Deg/s) sensory stimulus to at least three whiskers. We used three criteria to localize and isolate the barrel cortex: stereotaxic localization, relative evoked temporal response, and topographic mapping of cortical activation. All imaging experiments were centered on standard stereotaxic location of S1 (~3mm lateral, 0.5-1.5mm caudal from bregma). The resulting whisker responses were averaged over 20 trials. The response was determined to likely be from the barrel cortex if the average evoked fluorescence at the onset of the evoked response (20 to 25 ms after stimulation) was spatially limited to approximately a 250 μm x 250 μm area. Additionally, another criterion for functionally identifying S1 barrel cortex was through topographic mapping - if the center of mass of activation across whiskers moved consistently with the post-hoc histologically identified barrels, activity was attributed to the barrel cortex. In some cases, S2 activation was detected in response to whisker deflection and was rejected based on an extreme lateral response (~3.5- 4mm from midline) and lack of a clear topographic representation of the whisker barrels. Once the barrel field was appropriately mapped, we selected a single whisker to be deflected for the entire experiment.

2.2.6 Simultaneous Blood Oxygenation Measurements with Custom Monitor

During experiments where the combination of blood oxygenation and blood flow was simultaneously captured, a small LED sensor was attached to the rodent's hindpaw. The specific sensor (Easy Pulse Sensor v1.1, Embedded Lab) was modified to have frequency filtering within the typical rodent heart beat (Analog Lowpass Filter Cutoff: 15 Hz). The recorded value measures the changes in the absorption of infrared light (~940nm) to measure changes in blood oxygenation (and blood flow) over time. The reported values of the heartbeat generated from the custom oxygenation sensor were cross validated with

blood flow recordings of the commercially available physiological suite (Kent Scientific). Paired blood flow recordings and imaging was achieved using the simultaneous analog inputs in to the camera system at 4 kHz (MiCam02HR, Scimedia, Ltd.).

2.2.7 Simultaneous Local Field Potential Recordings and Analysis

In a subset of experiments, we simultaneously recorded the local field potential (LFP) along with the ArcLight imaging, using a similar prep as described above (see section, Cortical ArcLight Imaging). After mapping the mouse cortical barrels, we removed a small portion of the bone over the selected barrel (~ 1.5mm x 1.5mm area) to have access to the underlying cortical surface. We lowered a low impedance tungsten electrode (<500kOhms, FHC Inc.) using a micromanipulator (Luigs & Neumann) to 300 μ m below the cortical surface to approximately layer 2/3. We identified the principle whisker through repetitive manual stimulation of different single whiskers. Once we localized the principle whisker, we attached the whisker stimulator and applied the sensory stimulus (above). We recorded electrophysiological data using a 128- Channel Cerebus system (Blackrock Microsystem LLC.) continuously sampled at 2k Hz. All LFP signals were notch filtered at 60 Hz to remove any electrical noise. Furthermore, we normalized LFP signals on a trial-by-trial basis by subtracting the average 200ms pre-stimulus activity. In all cases, a zero-phase filter approach was utilized using custom Matlab (Mathworks) scripts.

2.2.8 Chronic Multiday Imaging Under Anesthesia

Three mice were first injected with the AAV construct and were outfitted with a custom developed headplate device to maintain stable recordings (see above). In order to increase the fluorescence recorded, the mouse's skull was thinned to approximately 25% of the original thickness (or until transparent) using a surgical drill over the injected region

(roughly 3mm x 3mm). After thinning, the mouse's skull was sealed using clear adhesive (Loctite 401 Adhesive, Uline). During skull thinning, the ArcLight fluorescent responses were briefly mapped to identify and localize the barrel cortex. After implantation, mice were left to recover for at least 1 week before imaging again. Day 1 corresponds to the first imaging experiment after 1 week of recovery post headplate implantation. The same mouse whisker (A1) was imaged over the course of 28 days, specifically on days 1, 3, 5, 7, 14, 21, 28. Isoflurane anesthesia was held to similar levels across imaging experiment by maintaining heart rate between 500-600 bpm from the animal's paw (Kent Scientific, ~1% Isoflurane). During imaging the mouse cortical responses were mapped with at least two whiskers to identify the correct region, and presented with a velocity stimulus (described above). The entire imaging experiment lasted approximately 1-2 hours each day. After imaging, the cortical surface was covered with a silicone plug (Kwik - Cast, World Precision Instruments LLC) to prevent photobleaching of the fluorophore between experiments. Mice were only imaged during the specific time points listed above.

2.2.9 Awake Imaging

At least four weeks after ArcLight viral injection, mice were anesthetized under isoflurane and were headplated using the above stated protocol. Over the course of 3 days preceding the first imaging experiment mice were routinely handled to gain familiarity with the imaging system and immobilization device. During this acclimatization period mice, were increasingly head fixed for longer periods of time, for 15, 30, and 45 minutes respectively. During stimulation of the whisker, mice were prevented from interacting with the whisker stimulator by obstructing the path from the paws to the whisker. Mice were rewarded with sweetened milk (Nestle, Ltd.) throughout imaging, which greatly helped to reduce animal frustration. After 3 days of handling and acclimating, mice appeared to be calm while the head was immobilized in the headplate restraint system. During passive stimulation of the

whiskers the mice often actively moved their whiskers. Therefore, the galvanometer was placed 5mm from the face to prevent the whisker from slipping out of the manipulator; however, the amplitude of the deflection was adjusted to maintain a consistent velocity stimulation (1200 Deg/s) as presented in the anesthetized case (see above).

2.2.10 Histology

Histological samples were prepared by perfusing the animal transcardially with PBS (Phosphate Buffered Saline) followed by 4% paraformaldehyde. Brains were post-fixed overnight in 4% paraformaldehyde then transferred to PBS before sectioning. Thick sections were cut using a vibratome (100 μ m, Leica) and either directly mounted or saved for staining. In some cases, we cryosectioned the post-fixed brains to achieve thinner sections (20 μ m) for better imaging. Before sectioning, samples were submerged in 30% sucrose in PBS post-fixation until saturated with sucrose (causing the tissue to sink). The tissue was then snap frozen and embedded in OCT (Optimal Cutting Temperature Compound, Tedpella, Inc). Thin sections were cut on a cryotome (20 μ m). ArcLight was stained against using a Rabbit anti-GFP polyclonal antibody (Abcam) and Alexa 488 secondary (Life Technologies, Inc.). After staining, the sections were then counterstained with Nissl (Neurotrace 640 Life Technologies, Inc.) to isolate neurons. ArcLight was imaged using the 405nm laser on an NLO 710 confocal microscope (Zeiss) and processed using Zen software (Zeiss).

2.2.11 Voltage Imaging Data Analysis

In this section, we have limited our description of the analytical methods used to the processing of the raw fluorescence signal. For specific description of the methods for each figure shown, see the corresponding results Section 2.3.2-3.3. All data analysis for

ArcLight imaging was accomplished using custom written image-analysis software (Matlab 2015a, Mathworks, Inc). A general outline of the image analysis is shown in Figure 2.3.

Raw images were loaded and converted from the proprietary file format of the imaging system using custom scripts. Due to the natural decay of the fluorescent signal caused by photobleaching, each trial was first normalized to a baseline and reported as a percent change in fluorescent activity ($\Delta F/F_0$). The $\Delta F/F_0$ measurement was calculated by subtracting and dividing each trials fluorescence $F(x,y,t)$ by the frame preceding the stimulus delivery:

$$\frac{\Delta F}{F_0} = \frac{F - F_0}{F_0}$$

where $F_0(x,y)$ is the frame of stimulus delivery ($F_0 = F$ at $t=0$). A single region of interest (ROI) was identified using the largest 9x9 pixel ($\sim 150 \times \sim 150 \mu\text{m}$) area response at 25ms post 1200 Deg/s stimulus onset.

After normalization to a $\Delta F/F_0$ measurement, the signal still contained a large component of hemodynamic noise (for example see Figure 2.3B). The observed noise was determined to be centered around 7-10 Hz which corresponded with the animals ongoing heartbeat (see Figure 2.3B, Appendix 1.1). This hemodynamic noise was removed using a highly correlated region of interest (Off-ROI). This Off-ROI was defined as the 9x9 average pixel region ($\sim 150 \times \sim 150 \mu\text{m}$ area) at least 48 pixels ($\sim 1\text{mm}$) away from the ROI with the highest average correlation of fluorescence during the first *non-stimulus* trial (See Appendix 1.2). The Off-ROI region was fixed during all subsequent trials. The separation of 1mm typically results in a background measurement that is highly correlated with the ROI while avoiding the evoked response. We found that this distance did not cause changes in the evoked mean

response (see Figure 2. 3F and corresponding results section), while allowing for subtraction of ongoing hemodynamic fluctuations.

On each trial, the activity in the Off-ROI 200ms preceding stimulus delivery was projected onto the ROI using a linear regression model (Figure 2. 3C), which was then removed from the activity within the ROI to produce the final time series data that was used for all calculations (see Figure 2. 3 legend for more detail). Due to the fluorophore¹⁶², positive changes in membrane potential correspond to a decrease in ArcLight fluorescent activity. Therefore, all traces here have been inverted to show a decrease in fluorescence as an increase in intensity for aesthetic purposes.

2.2.12 Statistics:

In all cases, we first determined if the specific data sets were normally distributed using the Lilliefors test for normality¹⁶³. If the data were normal we used the appropriate (paired or unpaired) t-test for statistical difference. If the population was determined to have non-normal distributions, we conducted non-parametric Wilcoxon signed-rank tests to determine statistical significance. All tests were conducted using the Matlab Statistics Toolbox (Mathworks, Inc).

2.3 Results

2.3.1 Experimental Setup and Histological Validation of Genetic Expression in Barrel Cortex

We validated the location of expression of the ArcLight injections in the S1 barrel cortex through post-experiment fixation and histological analysis of transfected animals. We

localized the GEVI ArcLight in the mouse barrel cortex by injecting 1 μ l of AAV1-hsyn1-ArcLight-D-WPRE-SV40 (UPenn Viral Vector Core, AV-1-36857P) using stereotaxic coordinates and a micro-injector system (see Section 2.2.3). Similar to other published work, we found that under the human synapsin promotor (hsyn1), ArcLight expressed predominantly in layers 2/3 and 5 of the mouse cortex ¹⁶⁴ (Figure 2. 1B-C). Based on the limitations of blue light penetration to the superficial cortical layers, our recorded fluorescence signals are a combination of layer 2/3 somatic, axonal, and dendritic information along with layer 5 apical dendrites. Under further magnification, ArcLight appeared to express across the cellular membrane (Figure 2. 1D), suggesting that the wide-field response is a combination of all membrane related neural responses from the expressed areas (i.e. soma, dendrite, axon). ArcLight has been shown in previous work to highly express in the cellular membrane ^{133,165}. We confirmed the expression of ArcLight to the neural membrane, through anti-GFP (Figure 2. 1D) and Nissl (Figure 2. 1E) staining, the combination of which is shown in Figure 2. 1F. ArcLight is derived from the GFP molecule ¹⁴⁶ and therefore was counterstained with polyclonal anti-GFP molecules to improve signal to noise over background fluorescence. These observations of ArcLight neuronal membrane expression are highly consistent with recent work in the olfactory bulb under similar conditions with the hsyn1 promoter ¹²⁹. The histology highlights the ability of ArcLight, under hsyn1 promoter, to genetically target all neural membranes, which offers higher selectivity than traditional voltage sensitive dyes (VSDs) that bind to all cellular membranes (neuronal and glial).

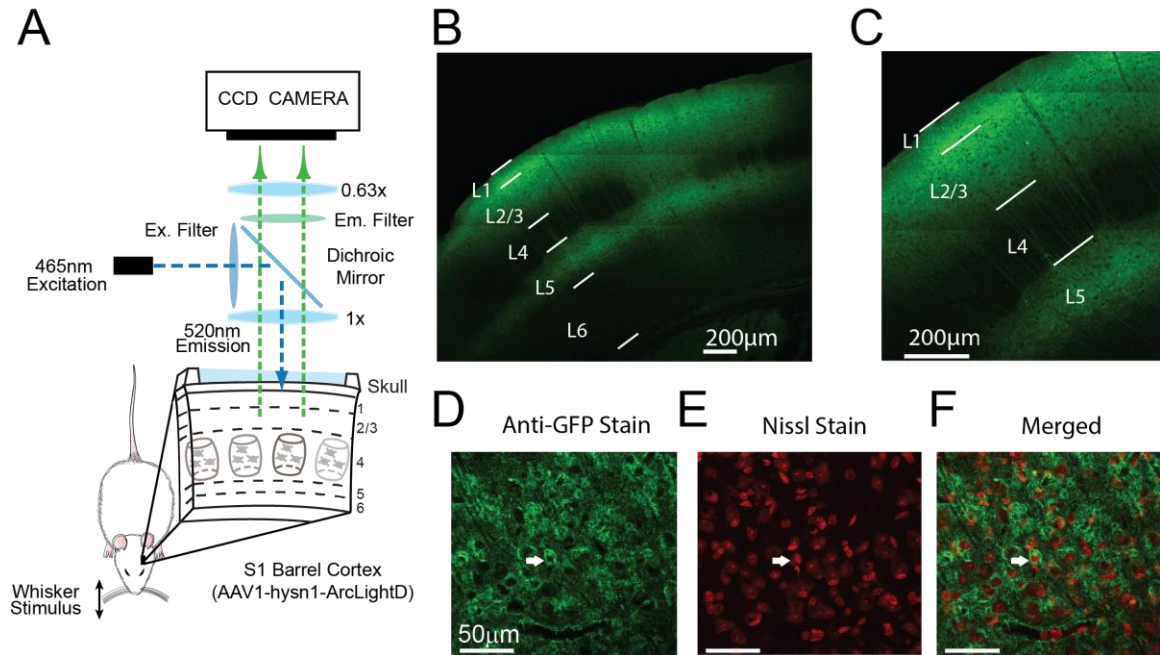


Figure 2.1. Experimental Setup and Histological Validation of ArcLight Expression.

A. The experimental setup for ArcLight imaging. **B.** Confocal image of the characteristic spread of ArcLight in the S1 barrel cortex (see Section 2.2.2 Methods). Fluorescence (green) from ArcLight excited with 465nm LED. Layers based on characteristic depths are outlined in white, cross validated with Nissl stain. **C.** Confocal image of ArcLight expression. The ArcLight expression can be clearly seen **across** layer 2/3 and layer 5. **D.** Confocal image of ArcLight expression in cortical region cryosectioned and stained using an anti-GFP polyclonal antibody. Fluorescence is clearly expressing in the neural membranes. An example cell is highlighted with the white arrow. **E.** Same section as D, stained with Nissl (red) for identification of neural cell bodies. **F.** Merged image from D and E shows fluorescent expression in membranes surrounding Nissl (red) stained neural somas. Expression appears to be targeted to both somatic, dendritic, and axonal neural membranes.

2.3.2 ArcLight Response to Single Whisker Deflections

We measured the spatio-temporal ArcLight fluorescence in cortex using a fluorescence microscope and a CCD camera system (imaged at 200 Hz, for setup see Figure 2.1A). We first applied our sensory stimuli to a single mouse whisker using a customized actuator (see Section 2.2.2) and recorded the evoked fluorescence response in the primary somatosensory cortex (S1) (Figure 2.2). Specifically, we presented a strong (1200 Deg/s) stimulus to a single whisker and recorded the evoked fluorescent cortical response (Figure

2.2A). Stimulus features such as these have been widely used across a range of laboratories including our own^{80,166}, inspired by high velocity transients of whisker motion observed in active sensing^{167–169}.

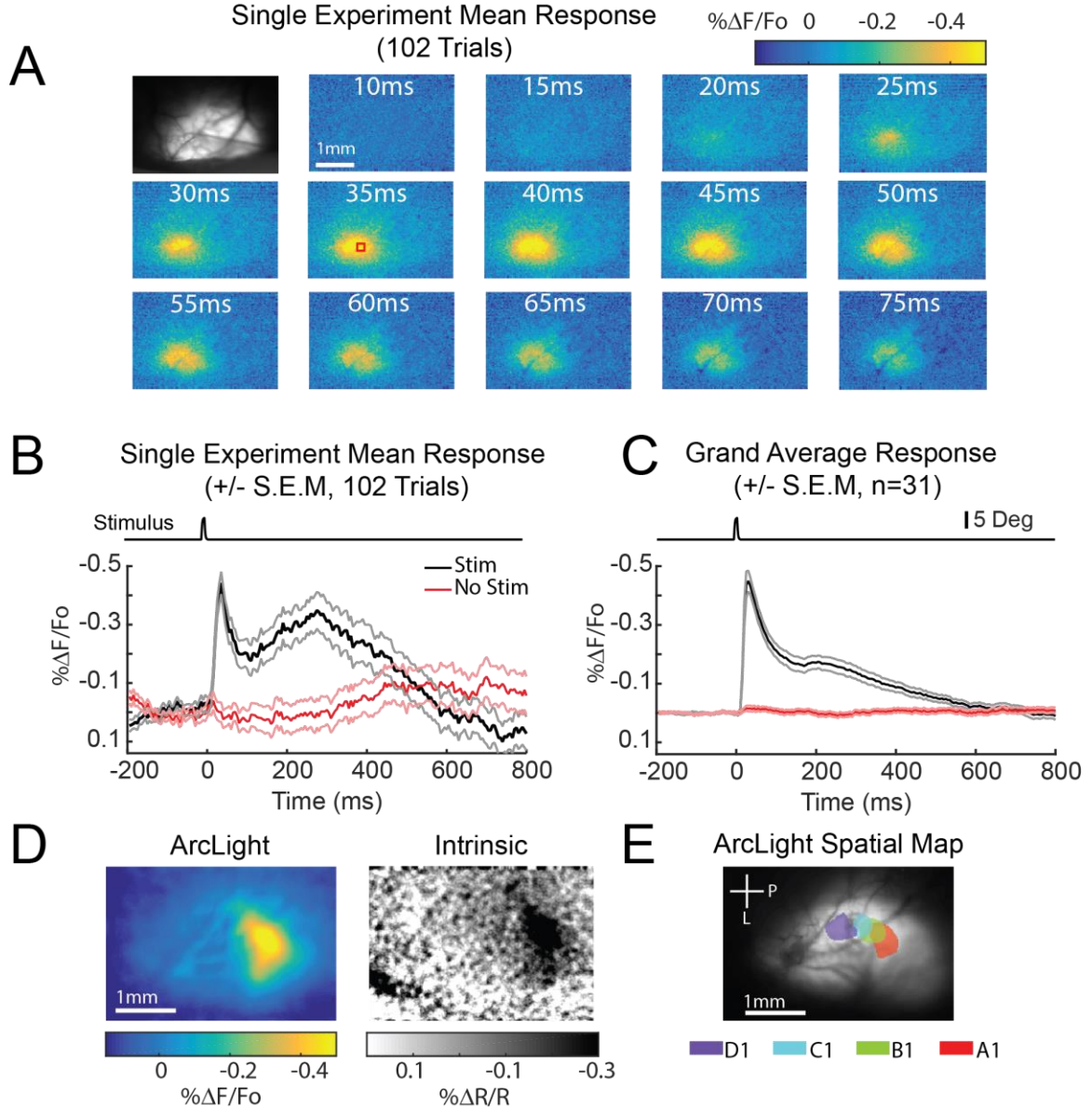


Figure 2.2. ArcLight S1 Cortical Response to Punctate Deflection

A. Single session ArcLight fluorescent response to single whisker deflection. Top numbers in each frame represents the time post stimulus, captured at 200 Hz. Each frame is normalized to the frame at stimulus delivery and averaged over 102 trials of stimulus presentation. All data shown in Figure 2.2, has also been post-processed using the Off-ROI subtraction method shown in Figure 2.3, and Figure A1.2-3 (see Methods Section 2.2.11). The signal starts at time 20ms post stimulus and grows to activate a larger region of the barrel field and slowly dissipates back to baseline fluorescence. **B.** Mean single

session temporal response from a single 150 x150 mm region (red square 35ms post in A) within the spatial activity in Figure 2.2A (102 Trials) +/- S.E.M. Top trace represents galvanometer input to the whisker system. **C.** Grand average temporal response within the peak 150 x150 mm region (n=31 experiments, across 8 animals). **D.** Spatial comparison between ArcLight response (Left, 102 Trials) and Intrinsic (Right, 10 Trials) response in the same animal reveals similar localization of activation to S1 barrel cortex. Intrinsic response captured at 10Hz with 625nm excitation. ArcLight spatial image represents the mean 40ms to 100ms response to an 11 degree ramp and hold deflection. Intrinsic spatial image represents the mean 0.8s to 2s response to during a 6s 10 Hz 1500 degree/s pulsatile stimulus. **1E.** Evoked activity map generated by stimulating four whiskers independently (D1,C1,B1,A1). Overlay represents a 50% contour of the fluorescent sensory signal.

fluorescence consistent with the reported topography of S1 barrel cortex. Each imaging experiment consisted of 50-100 trials, which were subsequently averaged, and post processed using the stated methods (Section 2.2.11). Unless otherwise noted, we utilized an Off-ROI subtraction method to remove the hemodynamic signal on a pixel by pixel basis across the entire image. For every experiment, an Off-ROI was selected, scaled, and subtracted from the ROI to reduce ongoing hemodynamic noise (see Figure 2.3 and Section 2.2.11 for more details of this procedure). Note that the Off-ROI subtraction method produced similar results to the raw averaged signal (data not shown). Similar to published wide-field voltage sensitive dye imaging^{166,170–173}, the recorded voltage response initially started in a small region approximately the size of a single mouse barrel and rapidly increased to a much larger area encompassing much of the barrel cortex (Figure 2.2A, at ~35ms post stimulus). The fluorescence then decayed over the course of ~600ms, until returning to baseline activity. We calculated the total area of activation by normalizing each dataset as a percent change over each trial's baseline activity ($\% \Delta F / F_0$, see Section 2.2.11), and spatially smoothing the images with a small 100x100 μm Gaussian filter (similar to Gollnick et al., 2015). The total area of activation was calculated as the cortical area corresponding to the 50% contour of the mean peak response between 25-35 ms post stimulus (See Section 2.2.11). We measured the initial spatial response to be on average 1.92 ± 0.879 (SD) $10^5 \mu\text{m}^2$ (N=31 experiments, 7 animals). This initial activation

corresponds to a region of approximately $425 \times 425 \mu\text{m}$, or 1-2 cortical barrels^{174,175}. These results correlate well with intracellular recordings from layer 2/3 cortical neurons that show that surrounding barrels receive subthreshold sensory input from a single whisker¹²²

In order to determine if the area of expression caused by the viral injection changed the observed evoked spatial response, we compared the evoked spatial response across different mice with different patterns of ArcLight expression. Using a non-injected mouse, we determined the overall level of baseline autofluorescence with our imaging system. We developed a threshold (two times the baseline average autofluorescence from the non-injected mouse) to approximate the area expressing the ArcLight protein. We found that our cortical injections produced expression across approximately 50 % ($\pm 19.4\%$ SD) of the recorded 4mm x 3mm Field of View. We found no correlation between the expressed area and the evoked spatial response ($R^2 = 0.075$).

To characterize the temporal dynamics of the evoked signal, we reduced the spatial information down to a single region of interest corresponding to a mouse cortical barrel. A single region of interest (ROI) $150 \times 150 \mu\text{m}$ square was selected as the area of maximal response to the whisker deflection (see box outlined at 35ms, Figure 2.2A). The following analysis was conducted on the average response in each experiment (containing 50-100 trials). For every experiment, an Off-ROI was selected, scaled, and subtracted from the ROI to reduce ongoing hemodynamic noise (see Figure 2.3 and Section 2.2.11 for more details of this procedure). A representative temporal response from the ROI during a single imaging experiment is shown in Figure 2.2B (Grand Average Figure 2.2C). In order to provide the best estimate of the temporal parameters based on our sampling frequency (200 Hz), we approximated the measurements using linear interpolation and approximated the signal corresponding to the observed frame. The average signal onset, defined as the post

stimulus time corresponding to the first frame reaching 10% of the maximal value, was determined to be 15ms \pm 5ms (SD, standard deviation). We calculated the average time from stimulus presentations to 50% and 90% of the peak response as 20ms \pm 5ms and 30ms \pm 10ms (SD), respectively (across experiments, n=31, 7 animals). The mean ArcLight cortical response signal reached peak intensity at 35ms \pm 15ms (SD) post stimulus with a mean peak response of -0.51 \pm 0.24 (SD) % Δ F/Fo. Given the intrinsic ArcLight fluorophore reported rise-time, time between onset and peak, of 10-20ms^{129,133,146}, our observations here correspond well with published *in-vivo* anesthetized cortical extracellular single unit activity in layer 2/3¹⁷⁶ and simultaneously recorded LFP signals (See Figure 2.4). Upon reaching peak, the signal decayed back to baseline over a highly variable range from 5 - 300ms. Across all animals (Figure 2.2C, n=31 experiments, 7 animals), the mean decay rate to 50% and 25% of maximal response was 95ms \pm 105ms and 245 \pm 200ms (SD) [median: 50ms and 155ms], respectively. A smaller secondary activation typically occurred approximately 100-200ms post stimulus (Figure 2.2B and Figure 2.2C). A large secondary onset was only found in approximately 25% of experiments, and was defined as a period of rising activity for a duration of \sim 100ms post-stimulus, and has been shown in widefield recording using voltage sensitive dyes¹⁷⁷.

The determined amplitude of the average evoked Δ F/Fo ArcLight response is similar to other reported voltage sensors average peak responses in the S1 barrel cortex [Mean Evoked Amplitudes, VSFP 2.3: 0.79 \pm 0.21% Δ R/R¹⁶¹, RH1691: 0.70 \pm 0.4% Δ F/Fo¹⁶¹, and RH1691: 0.26% \pm 0.11% Δ F/Fo¹²⁶] regardless of imaging setup, sampling rates, and anesthesia. Note even the same sensor (Example, RH1691^{126,160}) has produced a wide range of reported amplitudes, and varies heavily on experimental preparations. The average peak amplitude of the evoked response is similar, but reduced compared to *in vivo* ArcLight responses from the olfactory bulb (reported 1.2% \pm 0.05 Δ F/Fo¹²⁹, sampled at 125Hz). The

spatial and temporal results are also similar to published wide-field imaging responses using organic voltage sensitive dyes (RH 1691^{126,160,170}, and RH 795¹⁷⁷) as well as other GEVIs (VSFP 2.3¹⁶¹). Taken together, this evidence demonstrates that on average ArcLight is able to resolve sensory evoked cortical responses that are comparable to other voltage sensors.

One key benefit of wide-field imaging using voltage sensors is the ability to resolve functionally-relevant cortical structures. As an initial validation, in one experiment we compared the spatial component of the ArcLight activation to that obtained through conventional intrinsic imaging (see Section 2.2.11, Figure 2.2D, left panel ArcLight, right panel intrinsic imaging). This resulted in good topographical correspondence between the two approaches. We further recorded spatial activity using ArcLight when stimulating multiple individual whiskers to generate an activity map of the barrel cortex. We stimulated surrounding whiskers one-by-one using the precise galvanometer while recording the evoked sensory response using ArcLight. We found that multiple whisker representations could be isolated across the barrel cortex (Figure 2.2E). When we superimposed these cortical activation regions, the resulting ArcLight responses correlated well with the stereotaxic alignment of a typical the histological barrel map (data not shown).

2.3.3 ArcLight Shows Slow Rate of Photobleaching in vivo

To achieve the fidelity of imaging presented in Figure 2.2, we developed several analytical tools that are described in-depth here. ArcLight has been shown to be very photostable over long periods of excitation *in-vitro*^{129,144,145} and therefore is ideal for long imaging experiments. We also found this to be the case here, where ArcLight showed only a small, slow linear decay of fluorescence over time. We determined this by continuously exposing the cortical surface to constant blue (465nm) excitation during each imaging experiment

(~35 min), and applied either a whisker stimulus or no stimulus. During the no stimulus portion, we calculated the mean fluorescence in the selected ROI, and fit a linear model to predict the decay over time. The average slope of the linear decay of the ArcLight was found to be a $0.3 \pm 0.24\%$ S.E.M change in fluorescence per minute (n= 31 experiments across 7 mice; mean R^2 value=0.69, Figure 2.3A, with $400\text{mW}/\text{cm}^2$ LED system, Methods). Based on our optics, this LED excitation corresponds to an approximate $40\text{mW}/\text{cm}^2$ overall intensity. The overall result of the slow rate of photobleaching appears to be consistent with *in-vitro* findings¹⁴⁶. We subsequently accounted for the ArcLight photobleaching decay, as well as differing amounts of overall baseline fluorescence, by normalizing each frame as a percent over the baseline response [$\% \Delta F/F_0$]. This approach has been widely used in fluorescence imaging as a method to normalize and compare across animals¹⁷⁸. In this work, we define our baseline fluorescence (F_0) as the single frame when the stimulus was delivered.

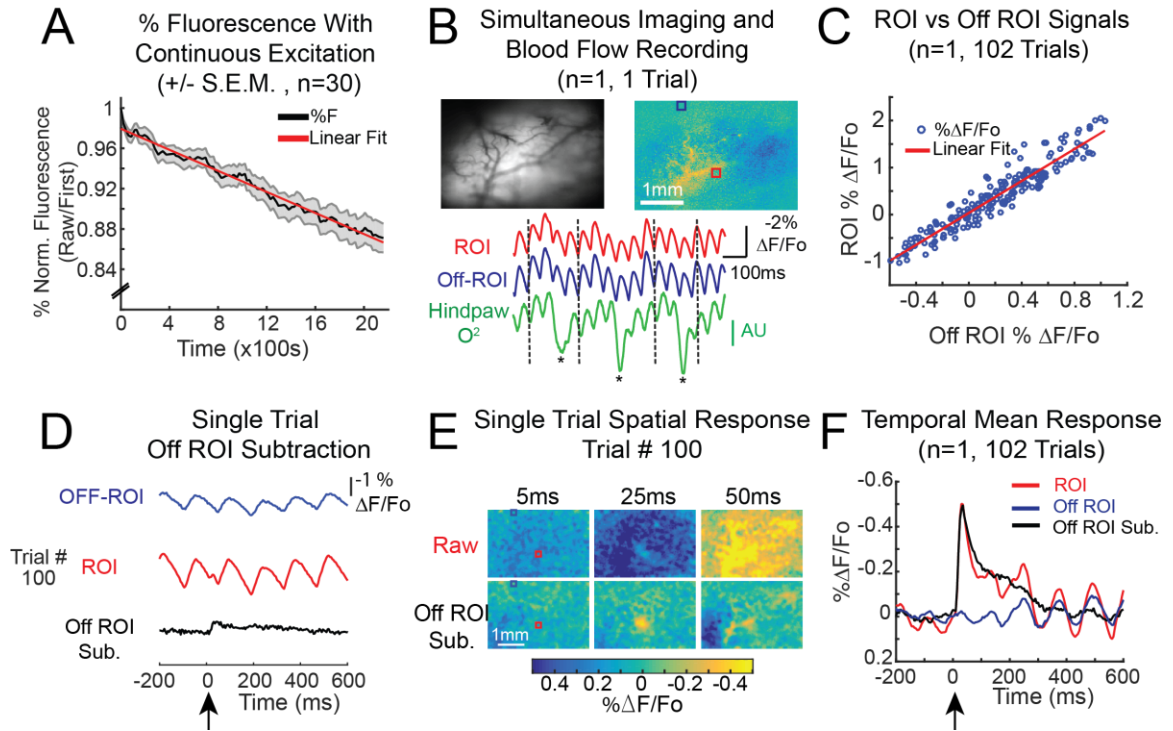


Figure 2.3. Post-Hoc Analytical Methods For ArcLight Widefield Imaging.

A. Continuous 465nm excitation of ArcLight causes slow decay of fluorescence over time. Each session was normalized to the first frame to compare responses across animals. Each imaging session was sampled every 6-8 seconds over approximately 35 minutes and fit to a simple linear model to calculate the slope of decay (mean experiment $R^2=0.70$, $n=31$).

B. Normalized $\% \Delta F/F_0$ single frame and representative temporal traces show hemodynamic signal. Blood vessels are clearly seen outlined in yellow. Regions of interest (ROIs) separated by ~1 mm show highly correlated signal during non-stimulated trials. Simultaneously recorded blood oxygenation (green) taken from the hindpaw shows a similar phase shifted signal matching the ROI (red) and Off-ROI (blue) response. Asterisks (*) highlight times of large artifacts and potential respiration. Black guidelines help visually determine alignment of the signals.

C. Pre-stimulus (200ms) normalized ($\% \Delta F/F_0$) period shows highly correlated signals with a linear relationship ($R^2=0.89$, 1Trial). Pre-stimulus fitting was used to generate model for ongoing activity for subtraction.

D. Example trials comparing raw Off-ROI $\% \Delta F/F_0$ (blue), ROI $\% \Delta F/F_0$ (red) and the Off-ROI subtraction (black) method. Stimulus given at time ($t=0$) black arrow.

E. Comparison of raw and Off-ROI subtracted single frames taken from Trial 100 (Figure 2.3D top). Off-ROI subtraction shows clear reduction in the hemodynamic response.

F. Mean response between the raw ROI (red), raw Off-ROI (blue), and Off-ROI Subtracted (black) method shows similar temporal averages ($n=1,102$ Trials). Clear oscillations are still prevalent in raw averaged condition; however, these oscillations are absent in the Off ROI Subtracted condition.

2.3.4 Reducing Hemodynamic Signal With Post Hoc Off-ROI Subtraction

Analysis

In addition to the decay caused by the photobleaching, we observed large fluctuations in the fluorescence signal at frequencies consistent with hemodynamics (Figure 2.3B, 7-10Hz). Hemodynamic signal is a common feature of blue-green light excitation fluorophores due to the overlapping absorption spectra of hemoglobin^{159,179}. We directly measured the hemodynamic signal in the fluorescence imaging using simultaneous recording of the blood oxygenation with a custom developed blood oxygenation sensor on the mouse's hindpaw (see Section 2.2.8). We determined that the hemodynamic signal was moderately correlated at fixed 30ms delay (mean Pearson correlation: 0.54 (+/- 0.16 SD), across 102 trials) with changes in blood flow and oxygenation in the hind-paw. The general single trial pattern of activity between the two signals showed good correspondence (Figure 2.3B), suggesting that the observed oscillatory signal was likely due to the overlapped excitation frequency (465nm) between the ArcLight fluorophore and hemoglobin (See Appendix 1.3). Although the blood oxygenation signal is similar to the hemodynamic signal in the voltage fluorescence imaging, we observed differences in the two signals, specifically in the introduction of larger artifacts likely due to respiration (Figure 2.3B, black asterisks[*]) that were absent in the fluorescence response. Therefore, we sought additional methods as a model to remove the ongoing hemodynamic response in the fluorescent signal. A simple notch filtering at the heartbeat frequency (7 -10Hz) dramatically distorted and reduced the evoked ArcLight response, and was thus not a viable approach (See Appendix 1.1).

To counter the hemodynamic interference, we instead developed a simple *post-hoc* linear model to take advantage of the highly correlated nature of the hemodynamic signal in the fluorescence signal across pixels. Using this method, we extracted single trial information

by subtracting a linear projection of an Off-ROI signal from the ROI time series. The Off-ROI was selected as a highly correlated region at least 1mm away from the ROI, as defined from the evoked response (Figure 2.3C, Methods, mean distance between ROI and Off-ROI: 1.35mm, range of distance: [1.15 -1.85mm]). The Off-ROI region was always placed further than the 50% contour of the maximal sensory evoked response (mean max evoked radius: 0.60 +/- 0.261 mm). To avoid subtracting stimulus information, we only used 200ms of pre-stimulus activity to determine the corresponding coefficients of the projection. Similar to other widely used subtraction methods¹⁸⁰, there is a potential of the introduction of neural responses, and the negation of common brain states. Despite these limitations, we found this Off-ROI subtraction technique was suitable for our purposes of measuring the relative evoked activity caused by the sensory stimulus.

Using both fluorescence normalization and Off-ROI subtraction, we dramatically reduced the ongoing noise and improved the single trial signal-to-noise ratios (Figure 2.3D, single trial example; Figure 2.3E, trial averaged). Qualitatively, we observed that the Off-ROI subtraction significantly reduced the hemodynamic component of the ArcLight signal, without compromising the evoked response, seen in both time series and spatial representations (Figure 2.3D, E, for details see Appendix A.1.2). To better quantify the reduction in noise, we assessed the ability to detect evoked responses from the ArcLight signal with and without Off-ROI subtraction. Here, we measured single trial signal-to-noise ratio (SNR) by comparing the mean evoked response between 25-30ms post stimulus to the variability of on-going noise across all sessions (n=31 Experiments, 3008 Single Trials). The noise (N) was defined as the mean standard deviation of the ArcLight signal over the 200ms window before stimulus onset. We found that with trial averaging the ArcLight response could be detected [mean response SNR: 11.63 (+/- 9.5 SD)]; however, single trials were too embedded in the noise to be clearly separated [Single-Trial SNR: 0.99

(± 1.64 SD)]. In contrast, the Off-ROI subtraction method dramatically increased both mean [30.0 (± 27.37 SD)] and single trial [4.02 (± 1.93 SD)] SNRs (Figure 2.3D, F). The ArcLight SNR of the average response (with and without Off-ROI subtraction) is comparable to other voltage indicators, (VSFP Butterfly 1.2¹⁵⁹). However, without Off-ROI subtraction, the raw single trial SNR is noticeably worse than the reported single trial SNR values in other GEVIs (VSFP Butterfly 1.2¹⁵⁹), and VSFP 2.3¹³⁴. However, it is important to note that these FRET based GEVIs utilize post-hoc ratiometric subtraction methods to improve SNR. By gaining access to single trial information with Off-ROI subtraction, we dramatically increase the usability for wide-field imaging of ArcLight in behaviorally relevant contexts.

2.3.5 Comparison of ArcLight Response to Simultaneously Recorded Local Field Potential

In order to validate ArcLight as a correlate of neural activity, we simultaneously measured the local field potential (LFP) while imaging the cortical response to punctate whisker deflections (Figure 2.4). Based on the histological analysis, and the limitations of blue light excitation¹⁸¹, we expect that the ArcLight response is predominantly from layer 2/3 neurons (Figure 2.1). Thus, we inserted a low impedance electrode approximately 250-300 μm below the cortical surface near the centroid of the evoked response, and simultaneously recorded the corresponding LFP during an anesthetized imaging experiment (see Section 2.2.7). The following data represents comparisons between the simultaneously recorded ArcLight and LFP responses (for details see Section 2.2.7). The LFP signal has been notched filtered at 60Hz.

We compared the resulting stimulus evoked responses in the LFP and the evoked fluorescence, and found similar characteristics between the two signals, shown in Figure

2.4B. Specifically, we found that the average LFP and ArcLight responses during whisker stimulation were correlated [mean peak Pearson correlation: 0.65 (+/- 0.0.118 SD)] shown in Figure 2.4A (n=5 experiments, across 2 mice). Furthermore, we determined the peak correlation between the LFP and the ArcLight response was 35ms (+-20ms SD, Median: 25ms), delayed relative to the LFP signal (Figure 2.4B). Note, the determined ArcLight peak response was highly variable (range 25-100ms). During the simultaneous ArcLight-LFP experiments, the average peak response was 70+/-20ms (SD) post stimulus (Median: 60ms, n=5 paired recordings, across 2 mice).

We directly compared the difference in temporal dynamics between the evoked LFP and the cortical ArcLight responses (Figure 2.4C) by measuring the onset, 10% to 90% rise time, and the 50% decay time for the simultaneously collected LFP and ArcLight signals. Note, the relationship between the LFP and the membrane potential is quite complex (for review see ¹⁸²), where the exact coupling between the LFP and the membrane potential is still being discovered¹⁸³. Other work has suggested that the LFP is an approximation of the temporal derivative of the membrane potential ¹⁸⁴. However, more recent work has noted the potential influence of filtering properties on relating the LFP to the membrane potential, and thus caution needs to be used in interpreting this relationship¹⁸⁵. Our comparison between the temporal dynamics of the LFP and the ArcLight response may not account for this complex relationship between the LFP and the membrane potential.

We found that in general, the response onset (mean onset (+/- SD) LFP: 8.6 (0.75) ms, ArcLight: 20 (5) ms) and rise time (mean rise time (+/- SD) LFP: 4.7 (1.7) ms, ArcLight: 30 (15) ms) of the evoked cortical ArcLight signal was 10-25ms later than the LFP response (Figure 2.4C). However, the mean ArcLight signal decay time was prolonged relative to the LFP decay time (mean decay (+/-SD) LFP: 35.5 (18.5) ms, ArcLight: 170 (108) ms).

This long excitatory tail has been a characteristic of other voltage sensitive imaging techniques, including voltage sensitive dyes ¹⁷⁷ which have substantially faster temporal dynamics, as well as other GEVIs including VSFP 2.3 ¹⁶¹. Therefore, this slow decay from the initial response may not entirely represent limitations of the molecule, but potentially additional physiologically relevant information. An alternative possibility is that the long tail is a hemodynamic artifact that has not been removed with the Off-ROI Subtraction technique or is part of an intrinsic hemodynamic response. However, due to the prevalence of this long tail in other published sensors, ^{160,161} it is likely that the prolonged fluorescence response represents prolonged excitation caused by a strong sensory stimulus. These data suggest that at the least the average ArcLight signal represents the average fast transients present in the LFP.

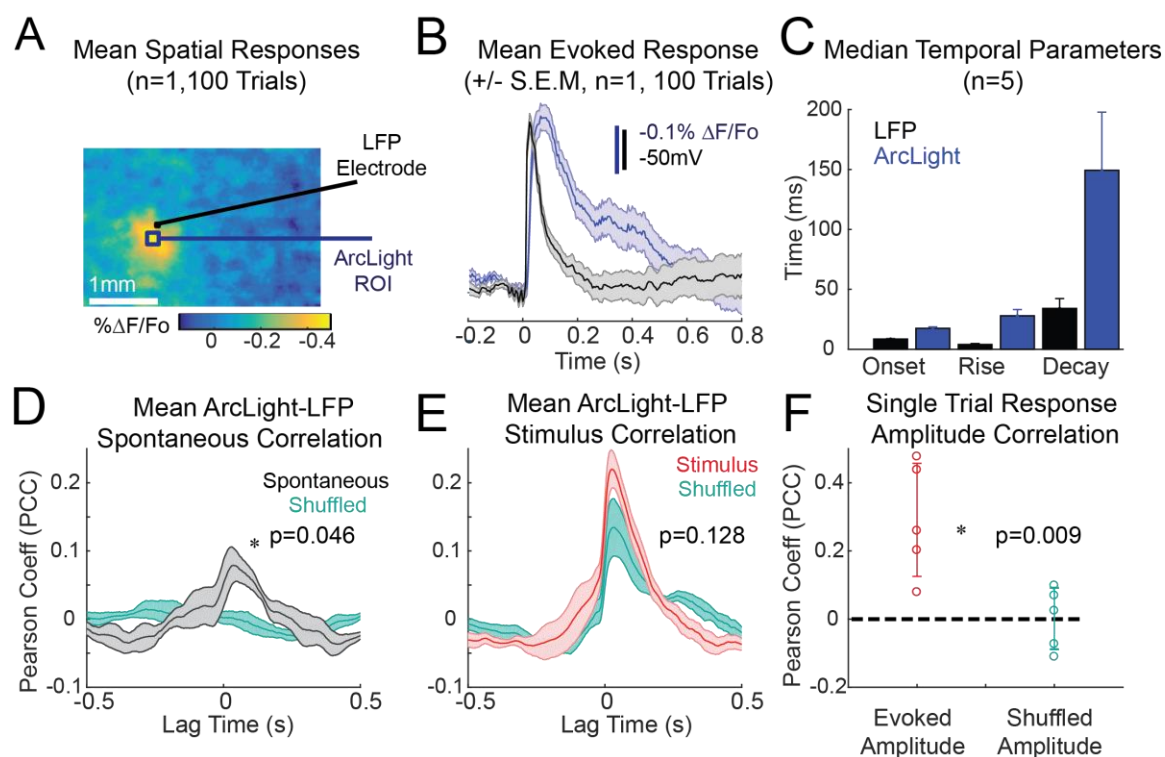


Figure 2.4. Simultaneous Paired Extracellular Local Field Potential and ArcLight Fluorescent Recordings.

A. Spatial average fluorescent response (100 Trials) to strong whisker deflection 25ms post stimulus showing the ROI for peak ArcLight signal (captured at 200Hz) and the LFP location (captured at 2kHz). All GEVI data shown in Figure 2.4 has also been post-processed using the Off-ROI subtraction method shown in Figure 2.3, and Figure 2.11 (see Methods Section 2.2.11). **B.** An example simultaneously captured mean LFP (black) and ArcLight (blue) response (+/- S.E.M.) to single punctate whisker deflection (n=1, 100 Trials). Note that LFP and ArcLight signals have been inverted. Both signals have been low-pass filtered at 100Hz using a 2nd order Butterworth filter (n=1). **C.** Comparison between the temporal characteristics of the two signals. Note the similarly delayed 20-30ms onset and rise times compared to the LFP signal, and dramatically longer decay observed in ArcLight responses (n=5, +/- S.E.M). **D** Spontaneous correlation between the simultaneously recorded LFP and the measured ArcLight response shows weak but significant correlation (n=5, 100 trials each). P-value for the max correlation ($p=0.046$, at 35ms lag). **E.** Mean correlation across single trial responses between simultaneous LFP and ArcLight (n=5, 100 trials each). Stimulus (red) and Shuffled Stimulus (turquoise) condition show similar correlation between signals suggesting common inputs. **F** Pearson correlation coefficient between peak amplitudes (across a 20ms window) of LFP and ArcLight response shows significant differences between the Stimulus and Shuffled Stimulus condition (n=5 experiments).

In addition to comparing the mean LFP and ArcLight response, we determined how well the ArcLight signal captured the single trial LFP response (Figure 2.4 D-E, $n=5$ whiskers, across 2 mice, 100 trials each). On a single trial, we measured the correlation between the ongoing LFP signal and the resulting ArcLight fluorescent response. We found that the spontaneous LFP and ArcLight responses were only weakly correlated periods of quiescence, Figure 2.4D, [maximum average Pearson coefficient Spontaneous: 0.076 ($0.067 \pm$ SD) at 35ms post stimulus], that was significantly different compared to a trial shuffled case [mean Pearson correlation Shuffled Spontaneous, 0.002 (\pm 0.02 SD), $p=0.046$, unpaired t-test]. Although the single trial correlation between LFP and ArcLight is low, these results are consistent with the weakly correlated single trial LFP and similar wide-field voltage sensitive imaging techniques ¹⁷¹. During stimulation periods, Figure 2.4E, we also found that the LFP and the ArcLight were slightly more correlated [mean Pearson correlation Stimulus: 0.22 (\pm 0.063 SD), temporal lag of 35ms], shown in Figure 2.4D (red trace). However, when we shuffled the trials to determine the correlative effects from the input, the correlation between shuffled and unshuffled signals was very similar [mean Pearson correlation Shuffled Stimulus: 0.13 (\pm 0.10 SD), $p=0.1275$, unpaired t-test], suggesting that the correlation observed during stimulation was predominantly associated with the strong evoked response.

Instead of simply correlating the entire signal, we focused our analysis on determining if the LFP signal and the ArcLight evoked stimulus response amplitudes co-varied. Here, we define the single trial response amplitude as the difference in activity between the signal preceding the stimulus and maximum response within a 20ms window during each imaging session's peak response (Figure 2.4F). By limiting the analysis to the evoked peaks, we determined that the evoked response amplitudes between the two signals were correlated [mean Pearson correlation Amplitude: 0.29 (\pm 0.17 SD)]. Moreover, when we shuffled

the trials this correlation between the response amplitudes disappeared [mean Pearson correlation Shuffled Amplitude: -0.0018 (\pm 0.09 SD), $p=0.009$, unpaired t-test]. These data suggest that the ArcLight and LFP amplitudes weakly co-vary in response to a sensory input. Taken together, these results suggest that ArcLight has the capacity to capture evoked features similar to evoked LFP, and potentially provides additional information on ongoing cortical processes.

2.3.6 ArcLight Cortical Response to Complex Stimuli

Given the relatively long decay of the signal as measured by ArcLight in response to a single, punctate sensory stimulus, this naturally begs the question as to the nature of the response to more complex inputs. To determine the temporal capabilities of ArcLight to represent complex stimuli, we presented a range of inputs to the whisker and recorded the downstream evoked cortical fluorescent response. We selected complex inputs that have been commonly used in the rodent vibrissa system^{176,186–189}, and therefore, these stimuli represent an additional comparison to published traditional electrophysiological recordings. Again, mice were anesthetized under low isoflurane (Methods), and stimulated using a high fidelity galvanometer device on a single whisker 10mm from the face. We presented a range of sensory inputs from a simple ramp-and-hold^{190,191} to pulsatile frequency deflections (2.5-40hz), and recorded the evoked ArcLight response (Figure 2.5A, $n=3$ whiskers, across 2 animals). Each trace represents the average response (100 trials per animal, 3 animals) within a single region of interest taken as the maximal response 25ms after stimulus presentation. In response to the ramp-and-hold stimulus, the cortical ArcLight response shows two clear peaks of activity corresponding to the rising (ON) and falling (OFF) stimulus events (Figure 2.5A, *panel 1*). The two ON and OFF sensory peaks are representative of a well-documented velocity sensitivity of the rodent whisker somatosensory pathway^{168,176,190}. Additionally, we found that ArcLight S1 cortical

responses clearly resolved repetitive frequency dependent inputs between the ranges of 2.5-20 Hz (Figure 2.5A, *panel 2-5*), with evoked peaks of activity corresponding to the presented sensory stimulus. However, high frequency (Figure 2.5A, *panel 6*, 40Hz) deflections produced an overall increase in fluorescence that failed to clearly follow the sensory input. These results are summarized in Figure 2.5B, showing the amplitude of the peak ArcLight response as a function of stimulus frequency. The high frequency 40Hz stimulation is at the upper limit of the innate capabilities of ArcLight based on *in-vitro* studies¹⁴⁶. These *in-vitro* ArcLight experiments demonstrate fast temporal dynamics with a 10-20ms rise time^{129,144}, and approximately 20ms decay, which limits the fluorophore's ability to represent high frequency information greater than 40Hz. Note that few studies have specifically examined the frequency encoding in mice under isoflurane anesthesia, so the limitations from a coding perspective are presently unclear. Taken together, these data demonstrate the use of ArcLight as a measurement of complex stimuli and frequency content in the S1 barrel cortex, and highlights the potential limitations to resolve high frequency information.

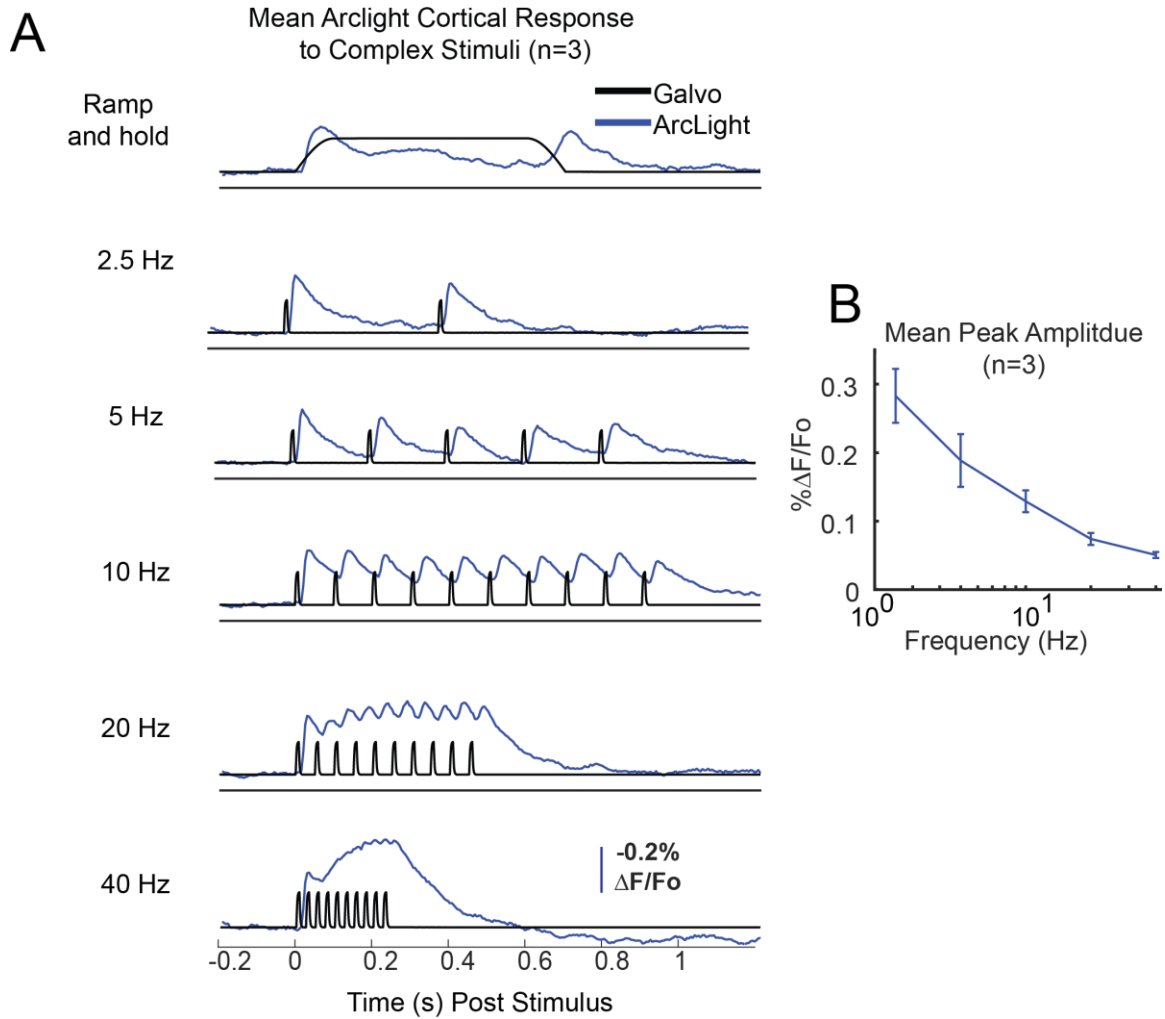


Figure 2.5. ArcLight Response to Complex Stimuli.

A. All GEVI data shown in Figure 2.5 has been post-processed using the Off-ROI subtraction method shown in Figure 2.3, and Figure A1.3 (see Methods Section 2.2.11). Each panel shows the temporal response taken from a single ROI during specific complex whisker stimulation (n=3). Each panel shows the corresponding galvanometer input (black trace), and the corresponding ArcLight (blue trace) output response. ArcLight shows clear response from 2.5 to 20 Hz; however, ArcLight is unable to clearly resolve whisker inputs of 40 Hz. **B.** Mean peak amplitude for each stimulus taken as the difference between the evoked peak fluorescence and the fluorescence preceding each pulse.

2.3.7 Stability and Variability of ArcLight as a Measure of Cortical Response

One critical component of any imaging fluorophore is the stability of the observed response over time. Our goal was to determine if the ArcLight cortical response dramatically changed during a long imaging experiment with continuous excitation. On a single trial, we would expect differences in activation of the barrel cortex due to various sources of neural variability^{192,193}; however, the average response over many trials will ideally remain relatively consistent during each experiment. Here, we analyzed the single trial evoked sensory response during an imaging session after removing the shared hemodynamic signal using the post-hoc Off-ROI subtraction method. Figure 2.6A shows the peak response frame averaged across trials for a single whisker deflection. For this analysis, we limited our investigation of stability to the temporal component of the main region of interest of a single mouse barrel (Figure 2.6A, red square, 150 x150 μm). For the outlined region of interest, Figure 2.6B *Top* shows the time series of fluorescence on a trial-by-trial basis over 102 trials. Notice, on single trial there is trial-to-trial variability (Figure 2.6B: 102 trials, Figure 2.6C *Top*: 25 sequential trials). However, when we average over blocks of 25 trials, the evoked signals appear to be quite similar, shown in Figure 2.6C *Bottom*.

We evaluated the stability within an imaging experiment by measuring the resulting distribution of responses within blocks of 25 sequential trials (~600 seconds). In this analysis, we only included one (the first) imaging experiment from each animal (n=7) to avoid skewing the results with data from a single mouse. Each experiment was normalized to the mean peak response for comparisons across animals. Specifically, we measured the peak response amplitude within a 20ms window (Figure 2.6D *Left*). We compared the resulting distributions of single trial response amplitudes between the first trial block (~600s), and last trial block (2493s) of the experiment across each animal (Figure 2.6E

Right). We found that within all experiments (7 mice) the difference between single trial response amplitudes between the first and last 25 trial blocks were statistically insignificant (Figure 2.6E *Right*, $p > 0.05$, paired Student T Test). These results suggest that across the entire imaging experiment the peak response amplitude remained highly consistent.

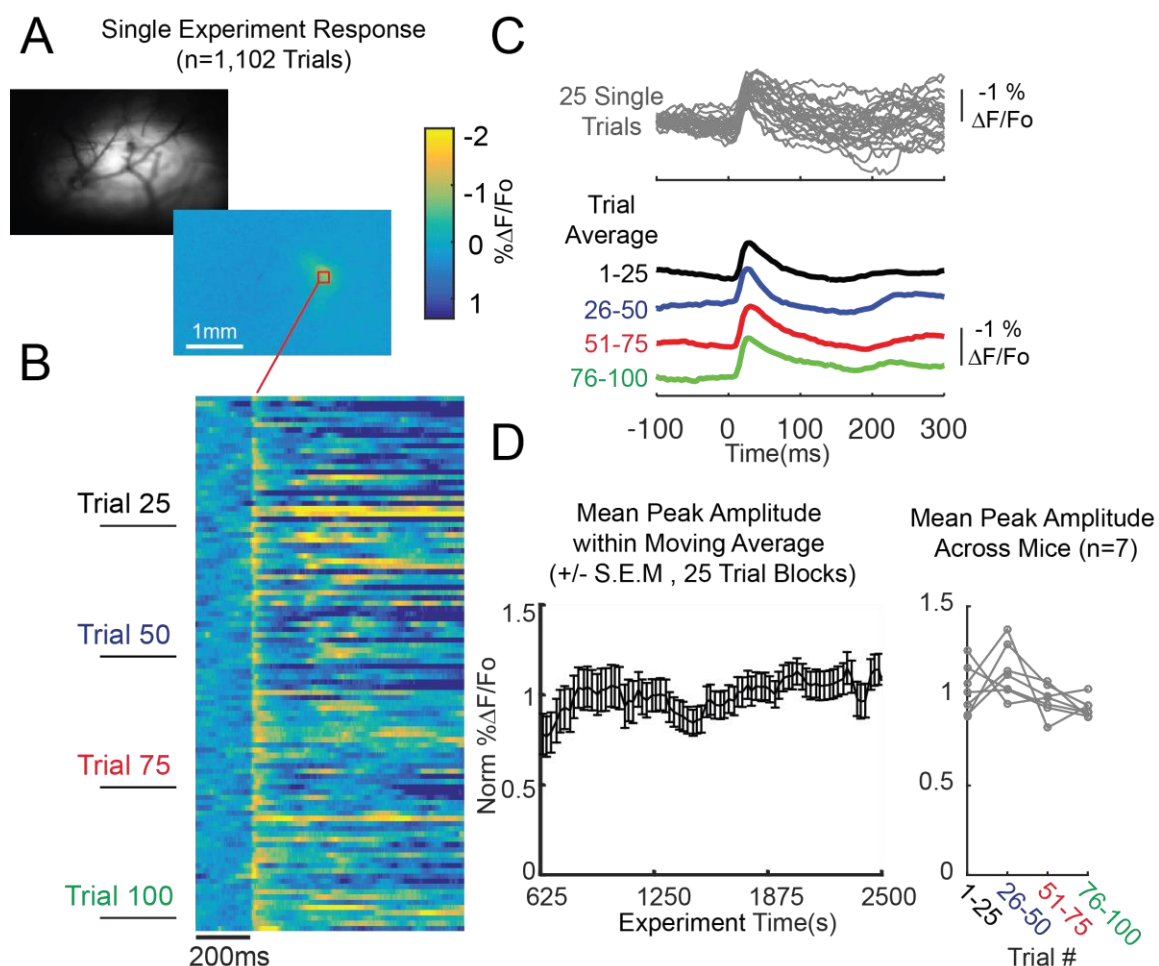


Figure 2.6. Within Experiment Variability of ArcLight Responses to Single Whisker Deflection

Note, all GEVI data shown in Figure 2.6 has been post-processed using the Off-ROI subtraction method shown in Figure 2.3, and Figure A1.3 (see Methods Section 2.2.11). **A.** Example of the average cortical response (102 Trials) of a 1200 Deg/s single whisker deflection. The spatial activity is reduced to a single response of a 9x9 pixel (~150 x150 mm) area for subsequent analyses. **B.** Single trial variability of the ArcLight response. Stimulus onset at 200ms. Each row represents a single trial in an entire session, where each column represents the region of interest at a single frame (200 Hz frame rate). **C. Top.** Single trial timeseries of the first 25 sequential trials. On a single trial, the evoked response is quite variable. **C. Bottom.** The average response is quite stable over time as determined by the similarity of the 25 trial averages. **D. Left.** Mean peak amplitude (+/- S.E.M) of the response in a 25 trial moving average over an entire imaging session **D. Right.** Mean responses across all mice (n=7) in 25 trial blocks during imaging session. Across all animals the first and last trial blocks were not significantly different (n=7, p>0.05 Paired t-Test).

In addition to the stability of the ArcLight response, we also determined the within experiment variability of the evoked response, regardless of any temporal drift. Similar to published voltage sensitive dye recordings ¹⁹⁴, ArcLight exhibited high variability in fluorescent responses to a simple stimulus, shown as a 25 trial example in Figure 2.6C (102 trials, 1 animal)]. We used the methods described above and averaged the fluorescent response across a moving 25 trial window to track parameters over time. We found that the within-experiment ArcLight response amplitude varied by 12.2 % [\pm 4.6 SD across 7 mice], measured as the standard deviation across an entire imaging experiment. These data suggest that the ArcLight cortical response is relatively stable across a long imaging experiment and exhibit variability that is consistent with other measurement modalities.

2.3.8 Repeatability of ArcLight Recording over Multiple Days

One of the great benefits of genetically expressed voltage probes is the ability to record from an animal over many days, weeks, and months. Repeatedly imaging over many days dramatically increases the data gained from a single animal, which may be of particular importance for behavioral experiments where mice need to be trained over weeks or months. To test the repeatability of the ArcLight response, we recorded the evoked fluorescence to the deflection of the same single whisker over a series of days (1,3,5,7,14,21,28). Each imaging experiment lasted approximately 1-2 hours. We controlled isoflurane levels through constant measurement of physiological parameters (mainly heart rate, see Section 2.2.8) to minimize effects of different depths of anesthesia across days. Furthermore, we always attempted to stimulate the same whisker across imaging experiments. During one imaging experiment (Mouse 2, Day 14), the animal's target whisker was not present, and therefore, we imaged the response to a different whisker in this isolated case.

We found that we were able to record the evoked responses over the course of 28 days (Figure 2.7A, n=3 mice). After 28 days, the fluorescence response was still clearly visible, suggesting additional time-points could continue. Over the course of a month the resulting spatial (Figure 2.7A,C) and temporal dynamics (Figure 2.7B), were consistent within an animal across days to weeks. Across all experiments, we found that the peak response amplitude (measured as normalized to Day 01 $\Delta F/F_0$), was relatively consistent during repeated imaging sessions [mean response amplitude: 96 ± 18.3 SD % Norm $\Delta F/F_0$, n=3 mice over 7 imaging sessions]. Furthermore, we found that the response amplitude variability across sessions in the same mouse was slightly less than the observed variability across different mice, but greater than the variability within an imaging session (Amplitude SD Same Mouse: 18.3%, n=3, Amplitude SD Across Mice: 23%, n=7, Amplitude SD Within Session, 12.2%, n=7). Although we attempted to image under the same experimental conditions, the variability across days is expected to be higher than the within session variability due to slight changes in window quality, anesthesia level, and camera alignment. In order to assess the consistency of the spatial information, we compared the area of the evoked response across each day (Figure 2.7C). We measured the area of activation as the 50% contour of the peak response of the mean 25-35ms post stimulus frames (Methods). We found that the evoked cortical area to be relatively consistent across all repeated imaging experiment on the same whisker [mean area: $1.66 (\pm 0.348 \text{ SD}) \times 10^5 \mu\text{m}^2$, Figure 2.7D]. The evoked area variability (SD) observed across repeated imaging experiments in the same mouse was less than the variability across mice and different whiskers (Area SD Across Experiments Same Mouse: 21.0%, n=3, Area SD Across Mice, 41.4% n=7). These results suggest that repeatable imaging of ArcLight is consistent over the many weeks and months.

Above, we considered variability independent of possible trends across days; however, in order to determine potential drift, we compared the resulting distribution of single trial responses between the first day, and final day of imaging (mean shown in Figure 2.7B). We determined that a majority of the animals (2/3) experienced insignificant differences between the 1st day and 28th day ($p < 0.05$, paired Wilcoxon Signed-Rank Test) of imaging. Additionally, we found no clear trend in the evoked area of the evoked response (Figure 2.7C, shown as the square root of the area). Here, the evoked area 25-35ms post stimulus in Mouse 2 slightly increased, in Mouse 3 slightly decreased, and in Mouse 1 remained constant. Even under extreme care, it is difficult to definitively determine the origin of the change in evoked fluorescence considering the many different parameters including window quality, experiment prep, and anesthesia level across imaging experiments and across mice. Therefore, it is unclear whether this change in evoked response is due to changes of the fluorophore (and expression) over time. Taken together, the above results demonstrate the capabilities of ArcLight to capture spatial and temporal information over many weeks and months. However, based on the day-to-day variability, careful analysis must be conducted when comparing and combining responses across days.

In addition to the evoked response amplitude, we determined if temporal dynamics remained consistent across many days of imaging. As shown in a subset of days (Figure 2.7B), the temporal dynamics appear to be highly consistent across imaging experiments. We measured the Pearson correlation coefficient (PCC) across each imaging experiment to determine the changes in temporal waveform of activation. Here, we found that the PCC to be highly correlated across imaging days mean 0.753 ± 0.128 . In some imaging experiments slight changes in evoked response did occur, particularly ~150ms post stimulus in the presence or absence of the secondary activation. However, the overall high correlation between evoked waveforms across weeks of imaging suggest that under highly

controlled conditions, the same whisker stimulation produces very similar temporal activation.

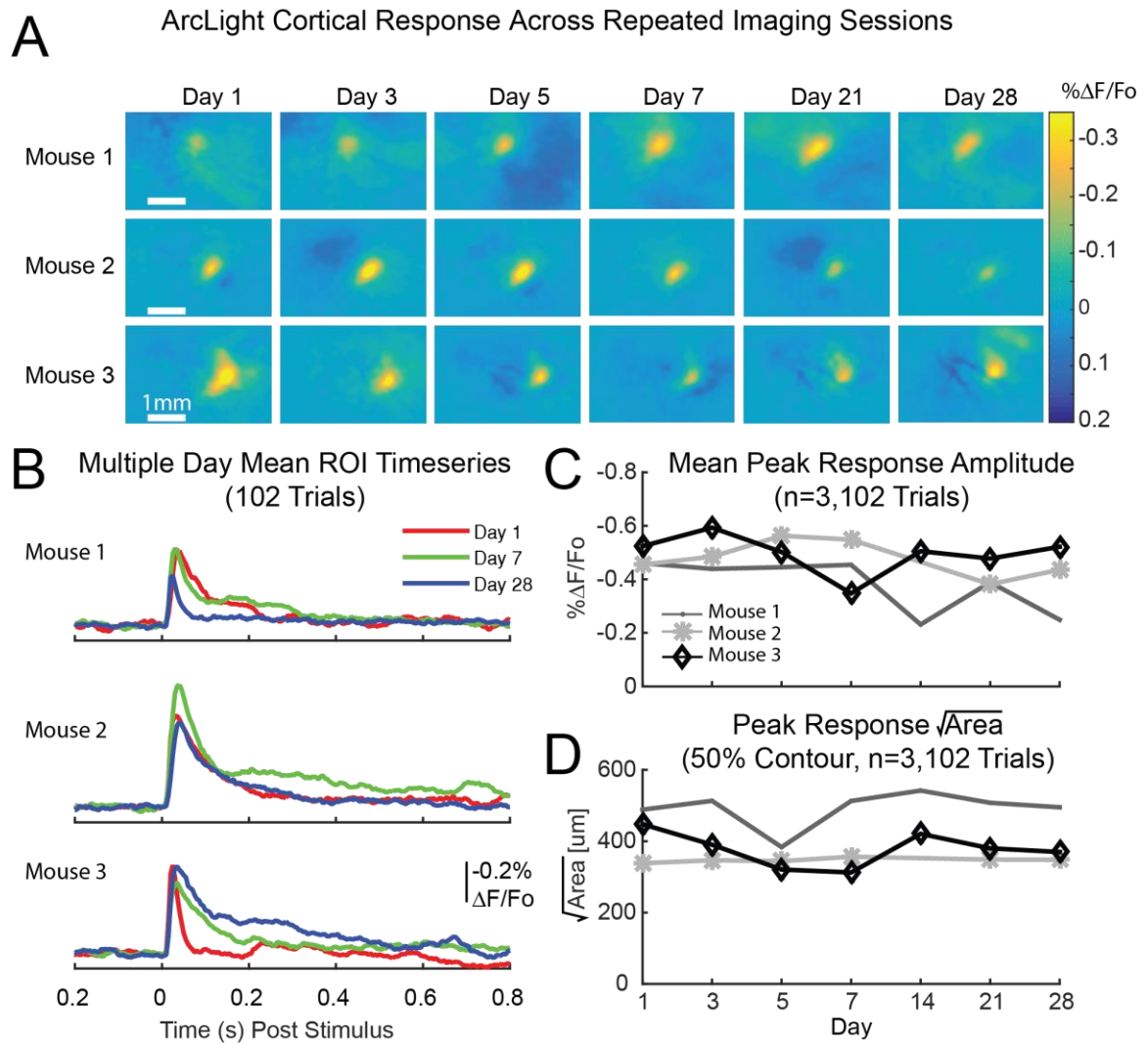


Figure 2.7. Multiday Imaging of ArcLight Cortical Response.

Note, all GEVI data shown in Figure 2.7 has been post-processed using the Off-ROI subtraction method shown in Figure 2.3, (see Methods Section 2.2.11). **A.** Each image represents the averaged Off-ROI subtracted $\% \Delta F / F_0$ cortical response between 25-35ms post whisker deflection over the course of 28 days (each day 102 Trials). **B.** Timeseries of the ROI on selected days (1 [red], 7 [green], 28 [blue]). The timeseries shows consistent waveforms across imaging sessions **C.** Evoked peak response amplitude across repeated days. Across all mice there is no apparent trend during the 28 day period. **D.** The 50% contour of the evoked response seen in A. In this panel, the square root of the area is displayed to show an intuitive measurement of overall size of the evoked response (assuming a $n \times n$ square). Again, there is no clear trend across the three mice during the 28 day period.

2.3.9 Awake Recordings of Evoked ArcLight Mean and Single Trial Responses

Finally, our goal was to determine if ArcLight had the capacity to represent cortical sensory responses in the awake rodent. Although previous studies have shown awake response of ArcLight, these examples were in either different species (*Drosophila*) or systems (mouse olfactory bulb), which would not guarantee clear fluorescent responses in cortical structures. Again, mice were left to express for four weeks before imaging (see Section 2.2.9). Mice were habituated over a period of three days to withstand long sessions of headfixation (Methods), but were not trained on any task. In order to prevent whiskers from slipping out of the whisker stimulator galvanometer, the device was placed 5mm from the face. We applied a similar stimulus as shown in Figure 2.2; however, the stimulus was adjusted for the adjusted distance to the face. We report that ArcLight reveals a robust sensory evoked response even under awake conditions in the S1 barrel cortex (Figure 2.8). In Figure 2.8, we have shown a representative sensory evoked S1 cortical response; however, we observed similar responses across imaging experiments (5 whiskers across 3 mice). In the awake animal, we observed a decrease in the evoked $\Delta F/F_0$ response with a corresponding decrease in the signal-to-noise ratio (SNR, 2.43 ± 0.92 SD, $n=5$). During periods of no stimulus presented to the whisker, the average spatial and temporal responses were negligible, as expected (Figure 2.8A *top*, B). When the whisker was deflected with a 1200 Deg/s pulse, the evoked response showed clear spatial and temporal activity similar to the anesthetized case (Figure 2.2, as compared Figure 2.8A and B). Due to the high variability of the ArcLight response, we would need substantially more data to make additional comparisons to the anesthetized case, and goes beyond the scope of this work. Taken together, this work highlights the ability of ArcLight as a robust spatial and temporal measurement tool of ongoing neural activity.

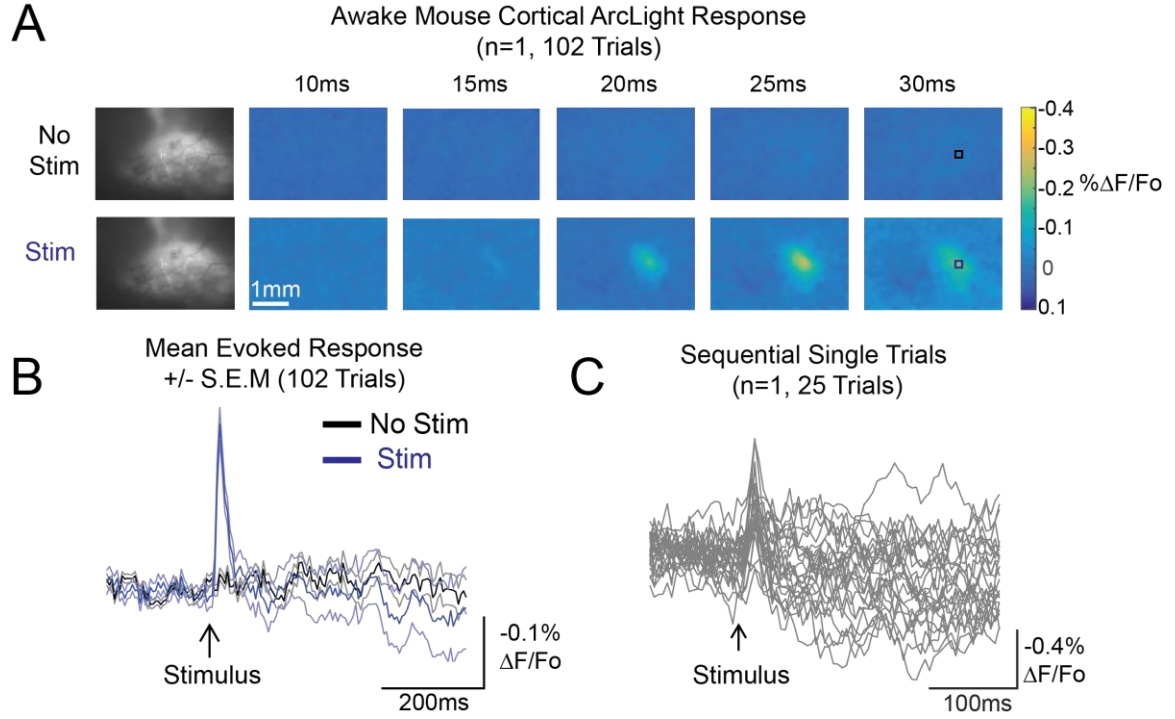


Figure 2.8. Cortical ArcLight Fluorescent Responses in the Awake Mouse

Note, all GEVI data shown in Figure 2.8 has been post-processed using the Off-ROI subtraction method shown in Figure 2.3 (see Methods Section 2.2.11). **A**. Mean fluorescent responses taken from the awake mouse (102 Trials). **A Top**. Average spatial response during no stimulus presentation. **A Bottom**. Average spatial response during stimulus presentation (1200 Deg/s punctate deflection). **B**. Mean temporal fluorescent responses from the ROI (black square, 30ms in A) with \pm S.E.M. **C**. Example of 25 sequential single trial responses taken from the same data set in the awake mouse. Clear stimulus evoked activity approximately 20 ms post stimulus. Stimulus presentation represented by black arrow.

2.4 Discussion

In this work, we examined the functional characteristics of the genetically expressed voltage indicator (GEVI) ArcLight through testing in the widely used rodent sensory whisker pathway. With recent advances in GEVIs, there is a large demand to determine the *in vivo* functional limitations and capabilities for each new voltage probe. Since the initial discovery and publication¹³³, to our knowledge ArcLight has been predominantly adopted as a tool for neuroscience research in *Drosophila* (Haynes et al., 2015; Kallman et al., 2015; Klein et al., 2015; Sitaraman et al., 2015; Raccuglia et al., 2016), and has not been widely utilized in mammals. Other FRET based GEVIs such as Butterfly 1.2, and VSFP 2.3 have been shown to measure widefield cortical responses *in vivo*; however, the monochromatic fluorophore ArcLight has yet been tested in *in vivo* cortical systems. We found that ArcLight produced a robust fluorescent response in the S1 barrel cortex in the anesthetized and awake mouse at high temporal and spatial resolution. We intend for this work not to exclusively highlight the promise of ArcLight as a technique, but also to provide a roadmap and a set of criteria for future GEVIs to be tested before widespread use.

2.4.1 ArcLight Imaging as a Method for Measuring Cortical Activation on a Mesoscopic Scale

Here, we used wide-field imaging to capture changes in population dynamics across the S1 barrel cortex on a mesoscopic scale (10's of μm). Wide-field imaging is an alternative imaging modality that enables high temporal resolution recording across large structures on the order of cortical columns^{196,197}. We found that ArcLight was able to provide clear and repeatable fluorescence responses spatially resolved at the level of a single cortical barrel on fast timescales (10's of ms, Figure 2.2,4,6), which makes it well suited for investigations into sensory precepts.

One of the biggest concerns with wide-field imaging is the uncertainty of the origin of the neurological signal responsible for the recorded evoked fluorescence. Using GEVIs, such as ArcLight, we gain additional selectivity over traditional voltage sensitive dyes (e.g. RH1691) by specifically targeting only neuron membranes and avoiding the pharmacological effects of staining with dyes¹⁹⁸. In this work, we utilized the human synapsin 1 (hsyn1) promoter to express ArcLight in predominately layer 2/3 and layer 5 neurons (Figure 2.1). Additional genetic lines could reduce the uncertainty of expression to a single layer, or neuronal subtype, thereby increasing the utilization of GEVIs to measure specific *in vivo* circuit dynamics.

Similar to local field potential (LFP), ECoG, and BOLD fMRI, the underlying neural correlate of the wide-field GEVI response represents a combination of electrophysiological sources. We directly compared simultaneous recordings of LFP and ArcLight fluorescence during sensory stimulation (Figure 2.4) to determine the relationship between these two modalities. On average the stimulus-evoked LFP and fluorescence were correlated with some differences in temporal dynamics. However, on a single trial, the ArcLight and LFP signals were weakly correlated even during large evoked sensory features. Although the single trial relationships between these signals are weak, the results are similar to weak correlations found between LFP and voltage sensitive dye imaging¹⁷¹. Furthermore, propagating waves of cortical activity traverse the cortical layers in complex patterns¹⁹⁹, and may compound as dynamic signals in the *in vivo* fluorescent response that is not represented in the evoked LFP. Additionally, wide-field recorded ArcLight fluorescence is believed to represent a spatial measurement of neural membrane potential^{129,133}, which is fundamentally different from extracellularly recorded LFP. Furthermore, the relationship between the LFP and the membrane potential is quite complex (for review¹⁸²), with some

work proposing that the LFP represents the first derivative of the ongoing membrane potential¹⁸⁴. However, this finding should be regarded with caution as the filtering properties have been shown to strongly influence the nature of the LFP and membrane potential relationship.²⁰⁰ In paired intracellular and LFP recording experiments, LFP only explains a limited amount of the signal variance in the membrane potential¹⁸³. Finally, due to the large hemodynamic noise in the raw single trial, and the limitations of the Off-ROI subtraction technique, careful consideration must be taken when examining ArcLight single trials. Taken together, our results suggest that while there are aspects of the wide-field ArcLight imaging that reflect features of the LFP, the ArcLight fluorescence contains different and potentially additional information about cortical activation.

2.4.2 ArcLight Excitation Causes Substantial Hemodynamic Noise in Recordings

Hemodynamic noise is a known issue for *in vivo* imaging of fluorophores with blue-green excitation and emission^{159,179} due to the overlap with the absorption spectrum of hemoglobin. Most of the current GEVIs including ArcLight, Butterfly 1.2, and mNeon-Ace¹³⁸ all share blue-green excitation and emission wavelengths which cause tremendous noise for *in vivo* imaging. GEVIs based on FRET (Fluorescence Resonance Energy Transfer) voltage probes, including Butterfly VSFP 2.1, have advantages *in vivo* systems due to the ratiometric approach of the two fluorescence signals, which allows direct subtraction of a scaled hemodynamic signal. However, even these ratiometric approaches still require additional post-hoc analysis to remove the properly scaled hemodynamic components from the recorded signals, which has been shown to be a non-trivial issue.^{159,201} For the non-FRET-based imaging methodology of ArcLight, we found that the ongoing hemodynamic noise required additional post hoc processing through Off-ROI subtraction to gain access to single trial responses in the S1 cortex of the anesthetized mouse.

2.4.3 Limitations of the Off-ROI Subtraction Method as a Tool for Removing Hemodynamic Noise

Throughout this work, we implemented a scaled Off-ROI subtraction method to improve our ArcLight response and reduce ongoing hemodynamic noise, similar to techniques employed traditionally in processing *in vivo* wide-field imaging responses in voltage sensitive recording^{130,171,180,202,203}. However, this technique has several assumptions and limitations. By scaling and subtracting an Off-ROI region, we are making general assumptions about the shared dynamics of the noise spatially across the image. While this Off-ROI subtraction method does have success in removing temporal hemodynamic noise, careful considerations must be taken for spatial information, especially in locations far from the region of interest. Additionally, the general assumption is that the observed signal of interest is spatially confined, and care should be taken for signals not confined to a particular brain region. We compared the mean of the raw data, and the post processed ROI subtracted obtained similar spatial signals (Figure A1.3). Additionally, similar to other reference methods^{180,204}, we are subtracting shared information, which may include spatiotemporal brain states, or evoked responses. To avoid these issues, we defined a 1mm radius, which separates our region of interest and the model template. This assumption is region specific to the S1 mouse barrel cortex, and therefore, must be adapted based on anatomy, and functional responses. Overall, the methods described here detail the basis of a general model for subtracting common noise; however, there is a demand for better techniques for removing hemodynamic noise from spectrally overlapped excitation wavelengths. Furthermore, future development of brighter and more redshifted GEVIs will greatly reduce the hemodynamic influence in the recorded fluorescence signal.

2.4.4 Comparison of ArcLight Cortical Responses to Previously Reported Voltage Sensors

In this work, we focused on the performance of ArcLight to reflect the spatial and temporal evoked response in the S1 barrel cortex. Although we did not directly compare ArcLight to other GEVIs, the whisker evoked fluorescence responses are within the range of the published temporal dynamics of voltage sensitive indicators in similar preparations^{126,160,161}. Very few studies have conducted cortical recordings using the same preparations described in this work; therefore, a direct comparison between GEVIs remains difficult. However, certain features of the mesoscopic whisker evoked S1 cortical response are consistent across imaging sensors and probes. We observed a strong sensory driven cortical response, that produced fluorescence changes similar to other GEVIs (VSFP Butterfly 1.2, and VSFP 2.3) and Voltage Sensitive Dyes (RH1691). These features include a sharp rising transient event lasting approximately 30-50ms^{126,160,161}, and a longer tail which follows the response and decays over a period a few 100's of milliseconds^{134,161}. Additionally, the average evoked response SNR for ArcLight was similar to other GEVIs; however, on a single trial the SNR was substantially worse which required the post-hoc Off-ROI subtraction method to recover these signals. We observed that ArcLight was only able to represent content up to approximately 20 Hz whisker stimulation; however, how much of this limitation is due to the imaging modality versus the dynamics of the pathway is unclear. Other FRET based sensors have also reported frequencies of up to 20 Hz to sensory stimuli in other systems using similar techniques^{159,205}. Recently developed GEVI's including ASAP1²⁰⁶, Ace-mNeon¹³⁶, Mac-mCitrine²⁰⁷, and Quasar1 report higher temporal resolution; however, most of these voltage probes have not yet been fully tested *in vivo*. We found ArcLight imaging had a slow rate of photobleaching with consistent responses recorded over a duration of approximately 35 minutes of uninterrupted imaging (Figure 2.3). Currently, there is no perfect GEVI that combines dynamic fluorescence range,

photostability, large signals, and fast temporal dynamics. The results of this work, suggest that ArcLight is capable of reporting sensory evoked responses in the cortex, and can be used chronically to measure over many days to weeks.

2.4.5 Future Applications of ArcLight and GEVI Imaging

In summary, this work has demonstrated the potential use of the GEVI ArcLight as an *in vivo* method for investigating cortical circuits on a mesoscopic scale in the awake and anesthetized animal. GEVI's in general show tremendous promise in providing voltage measurements from small networks of cells simultaneously that can be selected based on genetic markers, and has the potential to ultimately offer single cell resolution. Like the many variants of opsins used, each study should select the proper GEVI for that particular work. ArcLight is a single example that provides a clear and reliable response to sensory stimuli in the sensory cortex, and we speculate would be ideal for behavioral experiments that require long imaging sessions. However, due to the potentially largely hemodynamic noise caused by the spectral overlap with hemoglobin, the user must take special precautions to remove this noise. Here, we utilized a scaled Off-ROI method which may not be applicable for all studies. Based on our results, ArcLight would be well-suited for *in vivo* experiments where a single fluorophore is desired for example during paired optogenetics or multispectral imaging of multiple cell types. Moreover, the true advantage using a GEVI such as ArcLight is the ability to record the evoked response over the course of months and in the awake animal. Here, we found that both awake and repeated imaging experiments are feasible using the ArcLight voltage sensor. Future work is clearly needed to optimize the imaging and analytical techniques of these sensitive fluorescent probes.

2.4.6 Acknowledgements

The authors would like to thank William Stoy, Ilya Kolb, and Timothy Lee, as well as other members of the Precision Biosystems Lab at Georgia Tech, for additional support and advice on imaging. Additionally, we thank Kyle Blum for feedback on imaging analysis and illustrations. We would also like to acknowledge He Zheng for pilot work on the ArcLight imaging. Furthermore, we would like to thank Vincent A. Pieribone for supplying us with the initial ArcLight protein and for imaging advice.

CHAPTER III: THALAMIC STATE SHAPES SPATIOTEMPORAL REPRESENTATIONS IN SENSORY CORTEX

The following chapter has been presented at several conference ^{152,208,209}.

3.1 Introduction

The sensory thalamus is a critical gate that shapes how sensory information about the external world is transmitted from sensors in the periphery to cognitive centers in the cerebral cortex. In addition to direct afferent inputs that serve as the primary drive of thalamocortical activity, thalamic nuclei receive more subtle modulatory inputs from a range of sources, including cortical-thalamic feedback ^{92,210}, thalamic reticular nucleus ⁸¹, as well as diffuse inputs from the reticular formation ¹⁰¹ and other neuromodulatory centers (See Review⁷)

Modulation in thalamic membrane potential has important implications both for levels of spontaneous thalamic firing activity and for sensory-evoked responses. Even small changes in baseline membrane potential have been shown to have appreciable effects on spontaneous firing of thalamic neurons ²¹¹. The use of pharmacology to directly modulate thalamus ^{96,108,212} or opto/microstimulation and pharmacology to indirectly affect the thalamus through cortical ^{36,213,214} and subcortical ¹⁰⁰ inputs has further revealed the sensitivity of overall thalamic drive to cortex.

The ongoing pattern of spontaneous thalamic firing activity has long been postulated to play an important role in modulating the sensory-evoked responses in both thalamus and cortex ²¹⁵. Ongoing thalamic activity affects the thalamocortical synaptic strength ^{99,216}, thalamic firing mode ^{68,217}, and ongoing cortical activity ^{108,218}. The thalamocortical synapse is weak ⁵⁶, and therefore downstream cortical neurons need

multiple temporally clustered inputs (within 10's of ms) to evoke cortical responses. Additionally, the thalamocortical synapse strongly depresses ^{219,220}, and therefore is affected by the temporal distribution of preceding spiking activity, setting the stage for non-trivial gating of signals from the periphery to cortex. Moreover, thalamic neurons exhibit distinct tonic versus burst firing modes ²²¹, the switching of which is highly sensitive to baseline membrane potential, and the de-inactivation of T-type calcium channels ^{40,44}. Thalamocortical high frequency bursting events have a significant impact on downstream cortical activation ⁴⁷ and on sensory encoding ^{42,222}. The gating of thalamic signaling through the aggregate effects of all these properties (i.e. state) is hypothesized to serve a critical role in processing sensory information; however, this has not been investigated extensively in the intact brain due to the lack of methodological approaches to precisely manipulate thalamic properties. Recent advances in optogenetic approaches enable repeatable and reversible modulation of thalamic baseline membrane potential, while permitting the simultaneous measurement of local thalamic activity and the downstream cortical impact.

Here, we directly determined how thalamic gating properties control sensory-evoked thalamic and cortical responses in the vibrissa pathway of the anesthetized mouse. Instead of driving or silencing neural activity, optogenetic manipulation was used to modulate ongoing thalamic polarization while recording extracellular thalamic activity and acquiring widefield cortical voltage imaging, using the voltage indicator ArcLight ^{133,223}. We found that increasing levels of baseline thalamic hyperpolarization acted to increase the thalamic and cortical sensory evoked response. Specifically, by placing the thalamus in a hyperpolarized regime, we found an increase in spontaneous and stimulus-evoked thalamic bursting. Using an ideal observer of the downstream cortical response, we found that hyperpolarization increased the detectability without an apparent degradation in

discriminability between velocities of vibrissa deflection, or between deflections of neighboring vibrissae. Our results highlight how ongoing thalamic state and the resultant thalamic activity dynamically shape sensory encoding in the thalamus and cortex.

3.2 Methods

All procedures were approved by the Institutional Animal Care and Use Committee at the Georgia Institute of Technology and were in agreement with guidelines established by the NIH.

AAV Delivery: At least 5 weeks prior to experimentation, young (~6 weeks) female C57BL/6J (Jackson Laboratories) mice were injected with different viral constructs either in the Ventral posteromedial (VPm) thalamic region with AAV-5-CamKinaseII-eNph3.0 (UNC Viral Vector core), in the primary somatosensory (S1) cortex with AAV-1-hsyn1-ArcLight (UPenn Viral Vector Core), or both. Mice were anesthetized using Isoflurane (3-5%). After the mouse was fully anesthetized, small bore holes were placed over the regions of interest and were aligned using stereotaxic measurements (For VPm, 1.8mm Lateral from Midline by 1.8mm Caudal from Bregma). For cortical expression, either single or multiple injection sites were used surrounding the barrel cortex (center on 1.5mm caudal from Bregma and 3mm lateral from midline). The virus was loaded into a modified Hamilton syringe (701-N) with a ~35 micron borosilicate glass pipette type. The syringe was initially lowered to the corresponding depth below the surface (for VPm: 3mm and For CTx: 0.5mm) and let rest for 1 minute before injection. Both sites received injections of 0.5-1 μ l of viral construct at a flow rate of 0.1 μ l/minute. After injection, the pipette remained in place for an additional 5 minutes before slowly being removed from the brain. The bore holes were filled with either bone wax or left to close naturally. Throughout injection, mice were kept warm using a water heating system to maintain body temperature at 37 C.

3.2.1 Anesthetized Electrophysiology:

Mice were initially anesthetized using isoflurane (3-5%) and then placed on a heated platform (FHC, Inc.) in a stereotaxic nose cone to maintain anesthesia. A large incision was placed over the animal's skull, and the connective tissue and muscle surrounding the skull was removed using a fine scalpel blade. A modified headplate was attached using dental acrylic (Metabond) and secured to the skull. For cortical imaging, the skull was thinned with a dental drill, until transparent or removed entirely and covered with saline or ringers solution. After surgery, the isoflurane levels were dropped to $\sim <1\%$ for all imaging and electrophysiology experiments. The animals vitals (heart rate and respiratory rate) were constantly measured for anesthesia depth.

3.2.2 Thalamic Electrophysiology:

A small craniotomy was made over the primary whisker sensitive thalamic ventral-posterior medial (VPM) region of the mouse, around the injection site (see above). First, the VPM was mapped with a 2M Ω tungsten electrode (FHC) which was slowly lowered until 2.5mm below the cortical surface. The mouse VPM was identified using both stereotaxic measurements and depth as well as electrophysiological features (such as latency, peak response, whisker selectivity). A neural unit was determined to be located in the VPM if the Post-Stimulus Time Histogram (PSTH) contained a peak response 3ms - 10ms after a 1200 degree/s (Deg/s) single whisker stimulation and did not have a latency shift by more than 20ms after 1s of 10hz adapting stimulus²²⁴. The principle whisker was first determined using a manual probe to isolate the whisker with the largest evoked response. If further isolation was needed, the principle whisker was determined by the largest 30ms PSTH response of the surrounding three whiskers. After the conclusion of

the study either a small 7uA 10s lesion, or a fluorescent dye was placed near the recording location and confirmed using histological validation. Neuronal signals were band-pass filtered (500 Hz –5 kHz), digitized at 30 kHz/ channel and collected using a 96-channel data-acquisition system (Blackrock Microsystems, Salt Lake City, UT, USA). Offline spike sorting was accomplished using Plexon Offline Spike Sorter v4 (Plexon, Inc). Additional data analysis utilized custom scripts using Matlab (Mathworks, Inc).

The rodent whiskers were deflected by a high fidelity (1k Hz) galvanometer system (Cambridge Technologies). A typical velocity sweep stimulus was applied by positioning the custom designed galvanometer 5-10mm from the face and delivering an exponential sawtooth (rise and fall time = 5ms). The waveform stimulus velocity was taken by averaging the time to peak velocity of the stimulus. The velocity was adjusted based on distance from the face.

3.2.3 Cortical Fluorescent ArcLight Imaging:

ArcLight transfected mice were imaged through the thinned or removed skull using a Scimedia Imaging system to measure cortical spatial activity. The cortex was imaged using a 184 x123 pixel CCD Camera, MiCam2 HR Camera (Scimedia, Ltd) at 200 Hz, and a tandem lens microscope (Figure 3.1A). The entire cortical area was illuminated at 465 nm with a 400 mW/cm² LED system (Scimedia, Ltd.) to excite the ArcLight fluorophore. The excitation light was further filtered (cutoff: 472/30-nm bandpass filter, Semrock, Inc.) and projected onto the cortical surface using a dichroic mirror (cutoff: 495 nm, Semrock, Inc.). Collected light was filtered with a bandpass emission filter between wavelengths of 520/35 nm (Semrock, Inc.). The imaging system was focused approximately 300µm below the surface of the brain or cortical layer 2/3.

3.2.4 Functional Fluorescent Mapping of Barrel Cortex:

The mouse's whisker system was first mapped by imaging the rapid ArcLight response (800ms) to a high velocity (1200 Deg/s) sensory stimuli to three mouse whiskers. The resulting whisker response averaged over 20 trials was determined to be associated with a principle whisker, and barrel, if the evoked response was spatially limited to roughly a 0.2 mm x 0.2 mm area 25-30ms after stimulation. Additionally, the response was determined to be originating from the barrel field if the center of mass of activation moved consistently with previously published barrel field histology and was within the standard stereotaxic location of S1 (~3mm lateral, 0.5-1.5mm from bregma). After mapping, a single whisker was deflected with an ethologically relevant velocity sweep (0-1200 Deg/s) designed to simulate high velocity slip-stick events, either with or without thalamic optogenetic hyperpolarization to determine the cortical responses to various velocities.

3.2.5 Simultaneous Imaging and Thalamic Optogenetic Stimulation:

After mapping both the thalamic and cortical regions, an optrode (2M Ohm tungsten electrode mounted to an 200um optic fiber) was positioned to the stereotaxic locations of the pre-mapped thalamic region and lowered to the corresponding depth. Once a single thalamic unit was identified, the unit was determined to be sensitive to optical stimulation by briefly (1-2s) hyperpolarizing the cells using ~16mW/mm² 590nm from an LED light source (Thorlabs, M590-F1). Due to the low baseline firing rate (<1Hz), each cell was determined to be a thalamic optically sensitive unit if the cessation of the 590nm light caused a rebound burst³⁸. After identifying an optically sensitive thalamic unit, the same velocity stimulus was delivered in a pseudorandom order to the whiskers under various light conditions. Light stimulation for all cases was presented 500ms preceding and following whisker deflection (1s total light illumination). The light was delivered in a

pseudorandom order with a long variable gap (3-19s) between stimulus deliveries to allow for recovery of halorhodopsin (eNphR3.0). Each session imaged 200ms-1s of preceding frames to measure spontaneous activity. Light power was measured from the tip of the ground optical fiber before each experiment to maintain approximate light intensities delivered to each cell (0-16mW/mm²). During stimulation, the downstream cortical response was recorded using the same imaging system and voltage indicator as listed above. All recording was done under low isoflurane conditions ~0.5-1%. The optogenetic and viral expression of each experiment was verified through confocal and brightfield imaging of fixed slices.

3.2.6 Histology:

Histology samples were prepared by perfusing the animal transcardially with phosphate buffered saline (PBS) followed by 4% paraformaldehyde. Brains were post-fixed overnight in 4% paraformaldehyde then transferred to PBS before sectioning. Thick sections were cut using a vibratome (100 μ m, Leica, VTS 1000) and either directly mounted or saved for staining.

3.2.7 Thalamic Electrophysiology Data Analysis- Mean Response, Burst Ratio, and First Spike Latency:

We report several different basic measurements of spiking activity from our thalamic units including evoked response, evoked bursting response, latency and jitter. We determined thalamic evoked response as the initial response (0-30ms) to sensory stimuli. Each single unit recording was averaged over many trials (15-50) to produce a single response curve for that unit. The evoked response was determined as the average spikes per trial in the 0-30ms period post stimulus. The corresponding evoked bursting response was determined as number of bursting spikes per trial in that same post stimulus period. Bursting spikes

were defined as 2 or more spikes that fire at most 4ms apart preceded by 100ms of silence. The 100ms pre-stimulus activity is based on reported values for T-type calcium bursts^{47,68}. The First Spike Latency (FSL) was determined as the average first spike after stimulus delivery ($t=0$). Trials in which no spikes occurred within the response window were determined to be nonresponsive trials and were excluded from the analysis. To compare to other thalamic studies, it is important to note that the sawtooth stimulus used for whisker deflection reached peak velocity 2ms after stimulus onset. The spiking jitter was determined as the standard deviation of the first spike latencies for each recording. We measured the effect of ongoing spiking activity by comparing the distribution of firing rates of each recorded neuron during 1s during control (no LED) and optogenetic stimulation using the Mann Whitney rank sum test, significant modulations were determined if $p < 0.05$. All data analysis of the recorded extracellular thalamic units was accomplished using custom Matlab scripts.

3.2.8 Thalamic Electrophysiology Data Analysis: Detectability and

Discriminability:

To measure the theoretical detectability of the evoked signals under different light intensities, we used a signal detection theory framework. Specifically, we tested two distributions, a signal and a noise, and asked an ideal observer to perform a Receiver Operator Characteristic (ROC) analysis. Briefly, a ROC analysis uses a sliding threshold to determine the false positive rate and the true positive rate for discriminating the distributions of two signals, creating an ROC curve (see Figure 3.4). The area under this curve (AUROC) is then used as a measure of overall detectability of one signal versus the other (i.e. the noise), where an AUROC of 1 is perfectly detectability, and 0.5 is indistinguishable from noise. For each neuron recorded, we compared the distribution of number of spikes for each trial during the response window (above) for each velocity to

the noise distribution (no stimulus – 0-Deg/s), and performed a ROC analysis. The resulting area under the AUROC for each session is shown as the final measure of detectability for each velocity under either control or eNphR3.0 activation conditions.

To determine velocity discriminability, we performed a pairwise ROC analysis between each velocity distribution of evoked spikes within the post stimulus window. The resulting analysis produces an AUROC matrix, where the column corresponds to the “noise” velocity, and the row to the “signal” velocity. To measure the discrimination performance, we took the average AUROC between neighboring stimuli (i.e. 50 Deg/s and 125 Deg/s, 125 Deg/s and 300 Deg/s, etc.) for each neuron.

3.2.9 Voltage Sensitive Imaging Data Analysis:

Raw images were loaded and converted from the “. gsd” format using custom scripts and down-sampled by a factor of two. Each dataset was first normalized to a $\% \Delta F / F_0$ measurement by subtracting and dividing each trial by the temporal average frame between 0 and 200ms preceding the stimulus or light delivery (F_0 = mean response frame from 200ms to 0ms preceding stimulus or light delivery). Hemodynamic noise was removed using a PCA Background subtraction method discussed below.

As described in detail ²²³, *in vivo* ArcLight imaging overlaps with the hemoglobin absorption spectrum, and therefore contains hemodynamic noise that must be removed for analysis. Similar to the methods described in Borden et al, 2017²²³, this hemodynamic noise was removed using a background subtraction method. Imaging the wildtype mouse cortical surface using the same blue excitation and the ArcLight filter set revealed similar patterns of oscillatory activity, likely through autofluorescence and effect of hemodynamic absorption and blood flow ²²⁵. The Background PCA subtraction utilizes autofluorescence

signal from non-ArcLight transfected regions to predict the hemodynamic signal across the recorded space.

Specifically, the Background PCA subtraction method uses principle component analysis of non-expressing low background autofluorescence regions (determined from the maximum fluorescence from a non-inject animal) to find the ongoing hemodynamic components on a single trial basis. Additionally, the background fluorescence regions were selected at least 1mm away from the recorded whisker evoked response (Borden et al, 2017). Ideally, these criteria would create a spatial defined region with little or no ArcLight fluorescence to isolate the hemodynamic signal from the neurometric signal. Each frame is first spatially averaged by a 200 μm x 200 μm averaging filter. On a single trial, the corresponding top five principle components of the low background regions (which contains approximately 85% of the variance explained) are projected on a pixel by pixel basis across the entire recording using lasso regression method with regularization. The lasso regression utilizes a cross validated approach to determine the minimum number of components to develop the model of hemodynamic noise. In order to prevent the removal of any stimulus evoked activity, each pixel was fit on pre-stimulus activity (either before light onset for experiments involving optogenetics, or immediately preceding stimulus delivery). The final predicted hemodynamic signal for each pixel was subtracted across the entire recording on a pixel by pixel basis. Due to the complex waveform of the hemodynamic response, a simple notch filter is not effective at separating the signal from the noise²²³.

We found that the updated Background PCA subtraction method greatly reduced hemodynamic signal across the entire frame, compared to the off-ROI method (Borden et al, 2017). In some instances, brief onset and offset light artifacts of the 590nm light was

visible in the recorded ArcLight Cortical signal. We removed this DC signal from the final fluorescence to remove optogenetic transient light artifacts. Both raw and processed images showed qualitatively similar results. Unless otherwise noted, each dataset was processed with the Background PCA subtraction method as stated above.

3.2.10 Imaging Data Analysis – Peak amplitude, Normalized Peak, and Temporal Properties:

We measured the effect of the optogenetic stimulation on the peak amplitude of the evoked mean ArcLight fluorescence in the determined cortical barrel. The cortical barrel region of interest (ROI) for each stimulated barrel and each data set, was selected as the 200 μm x 200 μm region with the largest response 30ms after stimulus delivery. This determined ROI was used for all subsequent analysis of the temporal response. To better isolate the evoked amplitude, the frame of stimulus delivery ($t=0$) was subtracted from the resulting recorded signal. For each recording, the peak amplitude was defined as the $\Delta F/F_0$ at the time of the maximum average response between 0 and 110ms for the strongest stimuli (1200 Deg/s) presented under control and various optogenetic conditions. In order to measure the temporal properties of the evoked response, we concentrated on the timeseries data from the determined cortical barrel ROI. For normalized fluorescence (Norm $\Delta F/F_0$), each session's peak response was divided by the average peak response to the strongest stimulus (1200 Deg/s) under the control condition. The normalization allows for a better comparison across animals which may have different levels of ArcLight expression. We measured the time to peak as the time from sensory onset (10% of the peak signal) to the peak evoked response between 0 and 110 ms post stimulus. As a further measure of the temporal properties, we measured the overall duration of the response as the time between sensory onset (10% of the peak signal) and sensory offset (defined as the return to 10% of the peak signal, Borden et al, 2017).

3.2.11 Imaging Data Analysis – Area Measurements:

In addition to measuring the peak response, we also measured the effect of different thalamic polarizations on the evoked area of sensory cortical activity. We measured the activated area by the number of pixels over a threshold using the average response 25-35 ms post stimulus frame. Similar to other studies^{226,227}, we measured the spatial activation using the 70% threshold of the maximum delivered stimulus (1200 Deg/s) under the non-optogenetic (Control) condition to compare datasets with different levels of ArcLight expression. The threshold was calculated based on each recording session's peak response 25-35ms post stimulus for the largest velocity. In order to isolate the evoked activity from ongoing activity, we subtracted the frame at stimulus delivery ($t=0$). Different thresholds had no effect on the observed trends.

3.2.12 Imaging Data Analysis– Detectability:

Similar to the thalamic data, we used an ROC analysis between two distributions, signal and noise, to determine the detectability of the evoked response. For each imaging session, we compared the signal trial stimulus response distribution at the determined maximum amplitude response time to a 0 degree/s “noise” distribution at the same time. The peak response time for each recording session was determined as the time of maximum response for the strongest delivered stimuli (1200 Deg/s). To determine velocity discriminability for the cortical response, we performed a pairwise ROC analysis between each velocity distribution of evoked fluorescence within the peak post stimulus frame. We took the average AUROC value between each neighboring pair of stimuli for each cortical recording.

3.2.13 Imaging Data Analysis– Spatial Discriminability:

To determine the spatial discriminability of the evoked responses, we compared the single trial fluorescence in a barrel to the single trial fluorescence in a neighboring barrel (similar to the technique described in Zheng et al., 2015). The primary somatosensory barrel cortex has discrete cortical columns that correspond to somatotopically mapped whiskers. During each recording session, the cortical space was mapped using a strong sensory stimulus applied to at least three mouse whiskers to determine the orientation of the S1 cortical barrels (see above). The averaged response (at least 20 trials), was then used to determine the centroid for a particular barrel. Using the position of both barrels (determined by experimental mapping or projecting based on anatomy), we compared the single trial fluorescence for the positions in both barrels. We then applied a winner-take-all comparison where the barrel with the strongest fluorescence was determined to be the whisker detected. Therefore, the level of discriminability was determined as the probability of detecting whisker 1 given whisker 1 was stimulated ($Wk1 | Wk1$). We determined the location of the neighboring barrel mapping the location of various whiskers during each recording session.

3.2.14 Model of Light Intensity and Optogenetic Activated Area:

To capture the effects of the light intensity on the optogenetic stimulation, we used a previously published model ²²⁸ of light that simulates the transmission of light in neural tissue. For our experiments, we used a 200 μ m diameter optic fiber that was ground down to a point to prevent dimpling of neural tissue and ease of insertion. Additionally, the pointed optic fiber increases the numerical aperture (unground N.A. 0.22, to ground N.A. 0.375, Stark et al., 2012) and spread of light along the pointed tip. In order to estimate the area activated by the light from the optic fiber tip, we based a threshold of 25% peak photocurrent of the eNphR3.0 pump (at 590 nm stimulation) from published metrics ¹³⁹, or

approximately 2.5 mW/mm². We considered the activated optogenetic region to be the simulated area exceeding this 25% threshold for each light intensity (used 5-16mW/mm²)

3.2.15 Experimental Design and Statistical Analysis:

For all measurements, we determined if the specific data sets were normally distributed using the Lilliefors test for normality. If the data were normal, we used the appropriate (paired or unpaired) t-test for statistical difference, and an one way ANOVA for across different groups. If the population was determined to have non-normal distributions, we conducted nonparametric Wilcoxon signed-rank tests to determine statistical significance and the Friedman test to for across groups comparisons. Multiple comparison tests were corrected using the Holm-Bonferroni method. All tests were conducted using the MATLAB Statistics Toolbox (Mathworks, Inc.) or SPSS (IBM). All sample sizes are reported in the figure captions and text. Data is available upon request.

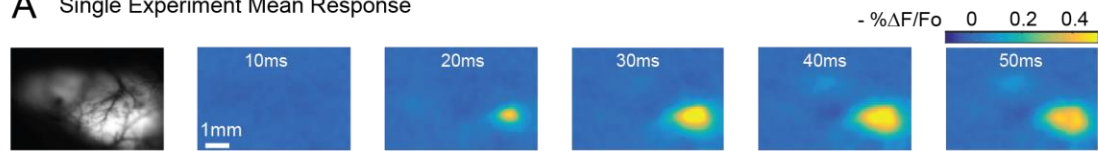
3.3 Results

Here, we simultaneously modulated and recorded thalamic activity while also using widefield imaging to characterize cortical sensory processing. Specifically, we imaged the GEVI ArcLight (example, Figure 3.1A, setup Figure 3.1B), for which we have previously presented a detailed methodological approach²²³ as a robust spatiotemporal measurement of ongoing cortical voltage activity across primary somatosensory cortex at a high temporal (200 Hz) and spatial resolution (10's of μm).

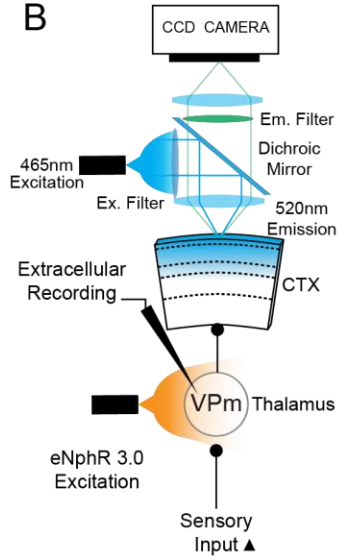
To modulate ongoing thalamic activity, we injected mice with viral vectors to express a light activated chloride pump halorhodopsin (eNphR3.0) in the thalamus, and the GEVI ArcLight in the cortex. After at least 5 weeks post injection, mice were lightly anesthetized with isoflurane, and an optrode (optic fiber with a tungsten electrode) was positioned into the mouse lemniscal thalamic region (VPm) to deliver light, and to record

the resulting single unit thalamic responses at different levels of thalamic hyperpolarization. Note that the optogenetic stimulation is presented as 1s of continuous delivery, to act as a modulator of baseline membrane potential as opposed to a driver of thalamic spiking.

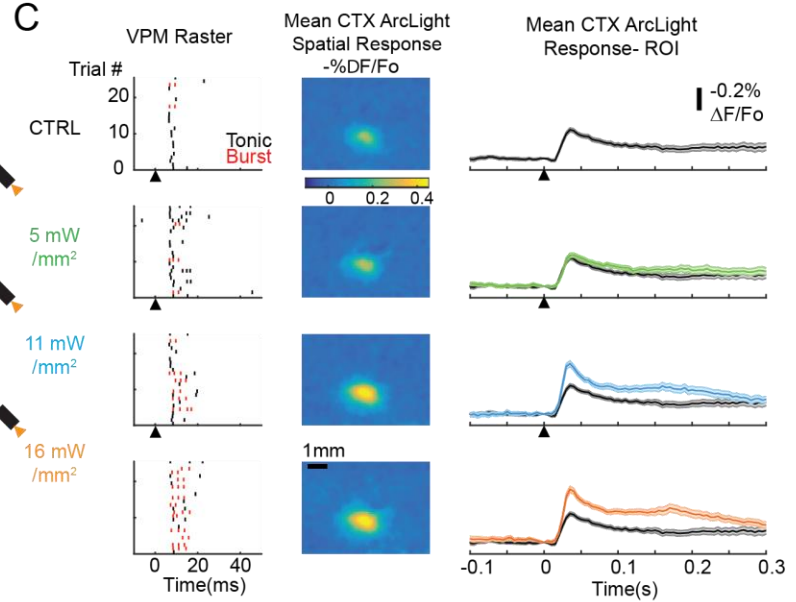
A Single Experiment Mean Response



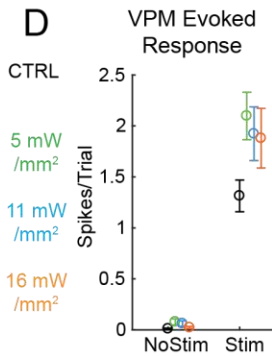
B



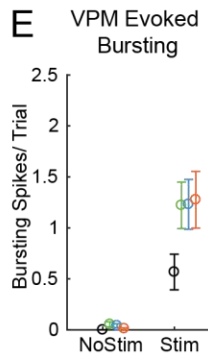
C



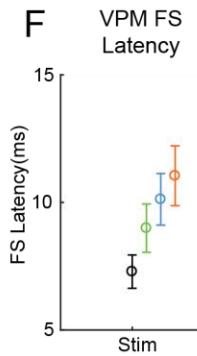
D



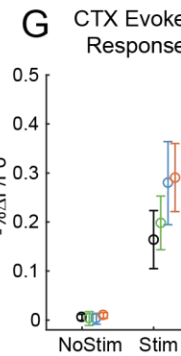
E



F



G



H

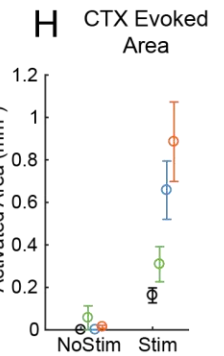


Figure 3.1. Thalamic Optogenetic Hyperpolarization Increases Thalamic and Cortical Stimulus Response.

A. Example average (102 trial) widefield ArcLight cortical response to sensory stimulus (Methods, 200Hz), and background fluorescence. **B.** Experimental setup. Mice are injected with two viral vectors, ArcLight in cortex (AAV1-hsyn1- ArcLightD- SV40), and eNphR3.0 (AAV5-CamIIKianse-eNphR3.0-mCherry). Thalamic units stimulated with light from a 200 μ m optic fiber and recorded simultaneously with a single tungsten electrode. For all light intensities, the LED illumination starts at 0.5s preceding stimulus ($t = -0.5$ s) and ends 0.5s after stimulus ($t = 0.5$ s). **C. Left** Simultaneous thalamic single unit extracellular raster to various levels of LED power during a sensory stimulus ($t = 0$) in mice expressing eNphR3.0. Black dashes – tonic spikes, Red dashes- burst spikes, Methods. **C. Middle.** Average evoked cortical ArcLight spatial response (25-35 ms post stimulus, 51 trials). **C. Right.** Average cortical timeseries (51 trials) of a 200 x 200 μ m stimulus activated region of the interest (ROI) for each condition. The black trace is the control (LED OFF) stimulus evoked response. Mean \pm S.E.M (51 Trials). **D.** Thalamic evoked response (spikes per trial, 0-30ms) post stimulus during various LED conditions (right to left with increasing LED power during ongoing (no stim) and stimulus delivered (stim) trials. Friedman Test $p = 0.0038$, Control vs 5mW/mm², 11mW/mm², 16mW/mm² Wilcoxon Signed rank, $p = 7.3 \times 10^{-4}$, $p = 0.017$, $p = 0.031$, respectively, $n = 13$ single units. **E.** Thalamic evoked bursting (burst spikes per trial) during the same period as D. Friedman Test $p = 0.0023$, Control vs 5mW/mm², 11mW/mm², 16mW/mm² Wilcoxon Signed rank test, $p = 0.026$, $p = 0.022$, $p = 0.021$, respectively **F.** First spike latency during the same period as D, E. Friedman Test $p = 2.8 \times 10^{-6}$, Control vs 5mW/mm², 11mW/mm², 16mW/mm², Wilcoxon Signed rank test $p = 0.0017$, $p = 5.0 \times 10^{-4}$, $p = 7.3 \times 10^{-4}$, respectively. **G.** Peak amplitude of the cortical evoked response during increasing LED power conditions ($n = 5$ GEVI recordings). Repeated measures ANOVA, $p = 0.001$, post *hoc* paired t-test, Control vs 5mW/mm², 11mW/mm², 16mW/mm², $p = 0.0057$, $p = 0.019$, $p = 0.009$, respectively. **H.** Average cortical activated area during 25-35 ms post stimulus (Methods, $n = 5$ recordings). Repeated measures ANOVA, $p = 0.002$, post *hoc* paired t-test, Control vs 5mW/mm², 11mW/mm², 16mW/mm², $p = 0.11$, $p = 0.031$, $p = 0.034$. All post-hoc analysis adjusted with the Holm-Bonferroni correction for multiple comparisons. All errorbars represent mean \pm S.E.M.

3.3.1 Thalamic Hyperpolarization Increases both Thalamic and Cortical Sensory Evoked Responses

We found that thalamic hyperpolarization, through light activation of halorhodopsin, increased stimulus evoked thalamic and cortical response in the anesthetized mouse. A single example of the paired recordings is shown in Figure 3.1C of the simultaneous thalamic and cortical recordings during various levels of thalamic hyperpolarization (Example: Figure 3.1C *Left*, VPm Raster, 3.1C *Middle* mean cortical spatial response, and 3.1C *Right*, mean cortical ArcLight response). For the entire range of light powers used, thalamic single unit stimulus evoked responses were enhanced during periods of hyperpolarization (Control: 1.31 ± 0.16 , 5mW/mm^2 : 2.09 ± 0.23 , 11mW/mm^2 : 1.92 ± 0.26 , 16mW/mm^2 : 1.88 ± 0.29 , Spikes per stimulus, Mean \pm S.E.M, $n=13$ units, Figure 3.1D).

Pre-stimulus thalamic hyperpolarization had a range of effects on the temporal properties of the evoked responses. Across the population, thalamic hyperpolarization increased the number of evoked bursting spikes in response to a stimulus. (Control: 0.56 ± 0.17 , 5mW/mm^2 : 1.22 ± 0.23 , 11mW/mm^2 : 1.23 ± 0.24 , 16mW/mm^2 : 1.27 ± 0.28 Evoked Bursting Spikes per trial, Mean \pm S.E.M, $n=13$ units, Figure 3.1E). We defined a putative burst as two or more spikes within a 4ms inter-spike interval, with a 100ms of preceding silence (see Methods). The identification of putative T-type calcium channel burst spiking from extracellular data is based on characteristics of the spiking patterns, which obviously depends on the set of criteria used. To determine how robust the findings presented were with respect to this definition, we adjusted our bursting criteria to be less stringent and found no effects on the observed results (data not shown).

In the example shown in Figure 3.1C *Left*, we illustrate an increase in the evoked thalamic bursting rate with increasing levels of hyperpolarization; however, on average across all recording, increasing the light intensity beyond the lowest intensity (5mW/mm²) did not further enhance the evoked single unit thalamic response. We did find however, that given a bursting event, regardless of any stimuli presented, increasing levels of light significantly increased the number of spikes elicited per burst (Control: 2.14 ± 0.08 , 5mW/mm²: 2.82 ± 0.16 , 11mW/mm²: 3.08 ± 0.24 , 16mW/mm²: 3.09 ± 0.18 Spikes per Bursting Event, Mean \pm S.E.M, n=8 units). For the spikes per burst analysis, we only considered recordings that contained one or more bursts in each light condition (n= 8/13). More pronounced levels of hyperpolarization are correlated with the number of evoked bursting spikes, presumably thorough the recruitment of additional T-type channels ²³⁰.

In addition to modulating the evoked bursting of the thalamic response, thalamic hyperpolarization increased the thalamic first spike latency (FSL) (Figure 3.1F, Control: 7.3 ± 0.68 ms, 5mW/mm²: 9.0 ± 0.95 ms, 11mW/mm²: 10 ± 1.0 ms, 16mW/mm²: 11.0 ± 1.2 ms Mean \pm S.E.M, n=13 units, Figure 3.1F). Along with an increase in spike latency, we also observed an increase the first spike jitter or the standard deviation of the latency across trials (Example shown in Figure 3.1C). The increase in response latency is likely due to the slow dynamics of calcium influx during T-type channel activation, and by increasing the voltage distance between resting membrane potential and spike threshold. The increase in burst firing and the increase in the FSL are consistent with findings from thalamic *In vitro* whole cell recordings ²³¹.

Using simultaneously recorded cortical responses with the GEVI ArcLight, we found that thalamic hyperpolarization also had a profound effect on the downstream spatiotemporal cortical responses (Example shown: Figure 3.1C, *Middle/Right*). Our

results show that increasing thalamic hyperpolarization increased the cortical peak evoked response (Control: 0.16 ± 0.06 , 5mW/mm^2 : 0.20 ± 0.05 , 11mW/mm^2 : 0.28 ± 0.08 , 16mW/mm^2 : 0.29 ± 0.07 $\Delta F/F_0$ Mean \pm S.E.M, $n=5$ recordings, Figure 3.1G). At the highest level of hyperpolarization used (16mW/mm^2), this corresponded to a 50% increase in cortical evoked response. However, even more clearly, we observed that increasing levels of thalamic hyperpolarization had a dramatic effect on the evoked cortical activated area (Control: 0.16 ± 0.035 , 5mW/mm^2 : 0.31 ± 0.08 , 11mW/mm^2 : 0.65 ± 0.13 , 16mW/mm^2 : 0.88 ± 0.19 mm^2 , Mean \pm S.E.M, $n=5$ recordings, Figure 3.1H). We defined activated area as the fluorescence over a threshold of the control stimulus (70%, Methods, Lustig et al., 2013; Millard et al., 2015).

We hypothesize that the increase in light intensity would have greater impact on the cortical excitation which pools responses across many thalamic inputs. To determine the spatial extent of the optogenetic modulation, we used established models of light in neural tissue (Methods, Stujenske et al., 2015) along with known biophysical information about the eNphR3.0 pump¹³⁹. Based on a light threshold for an approximate 25% activation of eNphR3.0, we found that that our range in light intensity ($5\text{-}16\text{mW/mm}^2$) activated a peak cross-sectional area between $0.05\text{-}0.1$ mm^2 of neural tissue surrounding the optic fiber tip (data not shown). Due to the oblong nature of the barreloid, we predict that the optogenetic light source partially activated multiple thalamic barreloids. However, in terms of a single barreloid^{232,233}, we estimate that increasing LED power from 5 to 16mW/mm^2 increased the total single barreloid activation from approximately 30 to 50%.

It is important to note that our viral expression extended beyond the location of the primary whisker nuclei, VPm (Figure A.2.1), and extended into neighboring thalamic regions (i.e. POm, VPL, etc.). Due to the location of the optic fiber (a few 100 microns

from the electrode tip), the intensity of light used ($0\text{-}16\text{mW/mm}^2$) and our simulations of light intensity, we expect the VPM region to be the locus of optogenetic manipulation; however, we cannot rule out the impact of other thalamic nuclei on the cortical results.

Throughout the rest of this manuscript, we examined the impact on sensory coding in higher detail under the highest optogenetic intensity. Taken together these results show that modulation of thalamic polarization can influence the evoked cortical responses, both in evoked amplitude of the response, and the spatial area activated.

3.3.2 Thalamic Hyperpolarization Modulates Ongoing Thalamic and Cortical Activity

Along with the effects on the evoked sensory responses, we observed that brief periods of hyperpolarization modulated the ongoing activity in the thalamic and cortical networks. Here, we limited our analysis to continuous light at the highest light intensity (16mW/mm^2). In extracellular thalamic recordings, significant changes were determined by comparing each neuron's distribution of firing rate during baseline firing and thalamic hyperpolarization (see Methods, non-parametric rank sum unpaired test, $p < 0.05$). Across individual cells, we found that ongoing thalamic hyperpolarization did not significantly impact the spontaneous firing activity in the majority of neurons (64%, $n=18/28$), and only a subset of units either increased (Figure 3.2A *Top*, 29% $n=8/28$) or decreased (Figure 3.2A *Bottom*, 7% $n=2/28$) their spontaneous activity (summary Figure 3.2C *Top*). Therefore, over the entire 1s of hyperpolarizing light, the recorded thalamic population did not significantly alter the ongoing population spontaneous average firing rate. However, in all cells halorhodopsin activation caused a period of reduced firing during the initial 200-250ms of light onset (Figure 3.2B), after which there was an increase burst rate of the recorded neurons (Example Figure 3.2B, Bursts -red spikes). Periods of silence of at least a hundred milliseconds de-inactivate thalamic T-type calcium channels, which are responsible for generating thalamic bursts⁴⁰. Specifically, thalamic hyperpolarization increased the thalamic burst event rate in approximately a third of the recorded units (Figure 3.2C *Bottom*), and across the population caused significant increase in the spontaneous average burst rate (Control: 0.008 ± 0.0006 , TH-Halo (16mW/mm^2): $0.136 \pm$

0.0091, mean burst events per second, $p=7.3e-4$, Wilcoxon Signed rank test). Upon limiting our analysis until after the initial silence, we found that hyperpolarization caused an approximate threefold increase in spontaneous spiking activity (Control: 0.18 ± 0.01 Hz, TH-Halo(16mW/mm^2): 0.57 ± 0.04 Hz, mean firing rate \pm S.E.M $p=0.044$, Wilcoxon Signed rank test). It is important to note, that the spontaneous firing rate in the isoflurane anesthetized mouse thalamus is quite low, with a majority of neurons (64%, $n=18/28$) firing less than 0.1 Hz. Therefore, it is difficult to accurately measure significant decreases in neural firing.

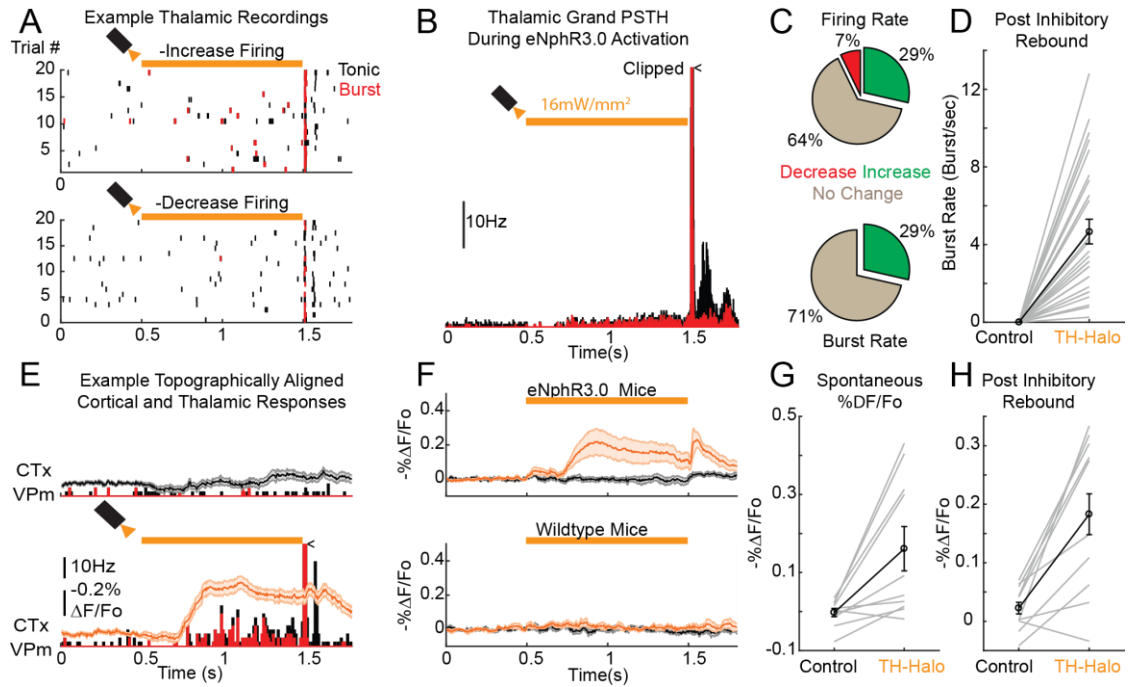


Figure 3.2. Thalamic Optogenetic Hyperpolarization Modulates Ongoing Thalamic and Cortical Activity.

A. Example extracellular single trial rasters depicting two different effects of thalamic hyperpolarization, **top**, increasing firing rate, **bottom**, decreasing firing rate ($p < 0.05$, Mann–Whitney U test, Methods). Black dashes indicated tonic spikes, Red dashes indicate burst spikes. Light onset at 0.5 and offset at 1.5s. **B.** Grand PSTH ($n = 28$ units) shows a dip in activity 0.5–0.7s and a steady increase in firing and bursting between 0.7–1.5s. After light offset the post-inhibitory event is clipped to show the low baseline firing rates. **C.** Breakdown of significantly modulated firing rates (top) and burst rates (bottom) across all recordings ($p < 0.05$, non-parametric Mann–Whitney U test, $n = 28$ units) by eNphR3.0 activation during LED onset (0.5–1.5s). **D.** Post inhibitory burst event rate (0–75ms after light offset) across all recordings with eNphR3.0 injections for Control (LED OFF) and TH-Halo (LED ON) conditions. **E.** Average topographically aligned thalamic extracellular recordings (below) and cortical ArcLight (top) recordings (Mean \pm S.E.M., 51 trials). ArcLight timeseries is determined from the primarily sensory cortex barrel (region of interest [ROI], Methods). **F.** Average cortical ArcLight ROI fluorescence response in eNphR3.0 injected mice (Top, $n = 10$ recordings) and non-injected mice (Bottom, $n = 4$ recordings). Mean \pm S.E.M. We did not capture a complete 1s of pre-stimulus fluorescence for two datasets in the eNphR3.0 mice, and thus they were excluded from spontaneous analysis. **G.** Comparison of spontaneous fluorescence during control (LED OFF) and thalamus hyperpolarized (TH-Halo) periods between 0.75–1.5s in eNphR3.0 injected mice ($p = 0.01$, paired t test, $n = 10$ recordings). **H.** Same as G, except during post inhibitory rebound 0–0.075s post LED offset ($p = 0.0018$, paired t test, $n = 12$ recordings). All errorbars (black) represent mean \pm S.E.M. across each population, and grey lines denote single recordings.

While the exact relationship between the activation of halorhodopsin and the properties of the neurons in the recorded population is unknown without simultaneous intracellular recordings, the reported characteristics of halorhodopsin¹³⁹ and the observations here suggest a net hyperpolarization of thalamus. During periods of light activation, neurons increased their burst firing, which is associated with a more hyperpolarized condition (Sherman, 2001). Furthermore under increasing levels of hyperpolarization we observed a graded increase in the number of spikes evoked in a burst²³⁰. Finally, upon offset of light, there was a large increase in activity in all recorded units, with an increase in firing rate (Figure 3.2B) and burst rate (Figure 3.2D) 0-75ms post light offset and is likely due to the post-inhibitory rebound associated with thalamic units⁴⁰. One alternative hypothesis, is that halorhodopsin can modulate the chloride reversal which could have dynamic effects on the ongoing thalamic activity. However, due to the timescale (~150ms) and intensity of the reported changes in reversal potential caused by halorhodopsin, this theory is unlikely to be a primary driver of the observed effect. We have specifically addressed this issue with a detailed examination of our data, in vitro recordings, and a computation model, which suggest that the deinactivation of the T-type channels is the main driver of increased thalamic activity. Taken together, all of this suggests that the most likely effect of the activation of halorhodopsin is a net hyperpolarization of the thalamic units, which increases overall thalamic firing and bursting.

In a subset of mice, we performed paired thalamic and cortical recordings to determine the effect of thalamic modulation on downstream cortical networks. We observed similar increases in cortical responses in the GEVI ArcLight signal during periods of hyperpolarization (simultaneously recorded example Figure 3.2E, Population Figure

3.2F *Top*). The increase in cortical activity occurred with an approximate 250 ms delay which corresponded to the delay observed in thalamic firing (Figure 3.2B). The post-inhibitory rebound response was also reflected in the downstream cortical signal following light offset (Example Figure 3.2E, and Population Response, Figure 3.2F, Figure 2H). These results suggest that thalamic hyperpolarization, which causes approximately 30% of the thalamic neurons to increase spontaneous firing and bursting, initiates changes in ongoing cortical activity. We tested if the observed effects could be caused by LED activation alone by performing the same experiment in wild type mice only injected with the ArcLight AAV vector (i.e. not injected with eNphR3.0). We found no effect on the ongoing activity caused by the LED activation alone (Figure 3.2F, bottom). In summary, we found that thalamic hyperpolarization modulated the ongoing thalamic burst rate, which corresponded with an overall increase in evoked cortical activity.

3.3.3 Thalamic Hyperpolarization Modulates the Thalamic Output and Downstream Cortical Response to Sensory Stimuli

To measure the effect of thalamic hyperpolarization on thalamocortical stimulus encoding, we provided 500ms of pre-stimulus hyperpolarization, at a single light intensity (16mW/mm^2), while presenting a range of sensory stimuli to the whisker system. Similar to previous work^{176,224}, the thalamus responded in a graded fashion to different punctate whisker deflection velocities. We found that hyperpolarizing the thalamus increased the single unit thalamic response to a majority of the velocities (Figure 3.3A, B). Similar to Figure 3.1, thalamic hyperpolarization not only altered the stimulus evoked response size, but also the temporal structure of the response with an increase in evoked bursting (Figure 3.3C), and response latency for all stimuli (seen as a temporal shift in histogram Figure

3.3A). Interestingly, thalamic hyperpolarization did not impact the probability of eliciting any response (spike or a burst) to the sensory stimuli (Figure 3.3D). However, given any response, thalamic hyperpolarization produced an approximate 40% increase in spiking output across each velocity (Figure 3.3E).

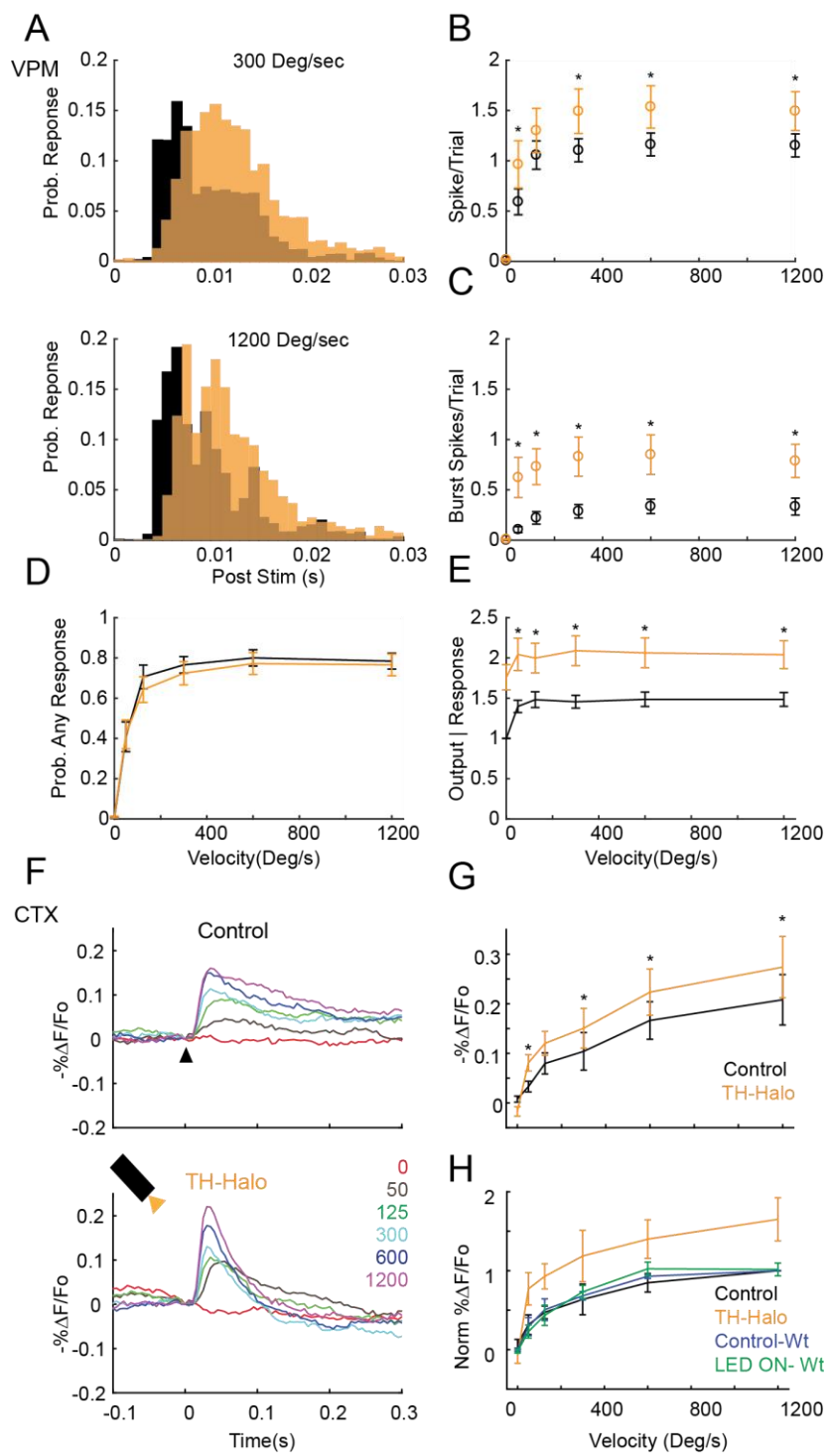


Figure 3.3. Thalamic Hyperpolarization Increases Thalamic and Cortical Velocity Response Curve.

A. Grand PSTH response to sensory stimulus($t=0$) of 300 Deg/s (top) and 1200 Deg/s (bottom) ($n=28$ single units) during control (LED OFF) and ongoing hyperpolarization (500ms preceding and post stimulus). Black – control, Orange– ongoing eNphR3.0 activation (TH Hyper). **B.** Evoked thalamic response (spike count per trial), 0-30ms post-stimulus under various velocities for control and thalamus hyperpolarized conditions. Wilcoxon Signed Rank Test, Control vs TH-Halo for 0 Deg/s, 50 Deg/s, 125 Deg/s, 300 Deg/s, 600 Deg/s, 1200 Deg/s, $p = 0.38, 0.0022, 0.056, 0.043, 0.026, 0.016$, $n=28$ respectively. **C.** The evoked bursting spikes per trial during the same period as in B. Wilcoxon Signed Rank Test, Control vs TH-Halo for 0 Deg/s, 50 Deg/s, 125 Deg/s, 300 Deg/s, 600 Deg/s, 1200 Deg/s, $p = 0.25, 3.8e-4, 1.1e-4, 0.001, 0.002, 0.001$, $n=28$ units respectively. **D.** The probability of evoking any response under control and hyperpolarized conditions. **E.** The average evoked output given any response across various velocities ($n=28$ units). Wilcoxon Signed Rank Test, Control vs TH-Halo for 0 Deg/s, 50 Deg/s, 125 Deg/s, 300 Deg/s, 600 Deg/s, 1200 Deg/s, $p = 1.00, 7.1e-4, 0.0022, 9.1e-4, 0.0028, 0.0043$, $n=28$ units respectively. **F.** Average cortical sensory evoked response to various velocity stimuli (0 -1200 Degree/s, $n=12$ recordings) under control (top- Control), and thalamus hyperpolarized (bottom-TH-Halo) conditions. **G.** Peak evoked amplitude for various velocities across the recorded population in injected eNphR3.0 mice. Wilcoxon Signed Rank Test, Control vs TH-Halo for 0 Deg/s, 50 Deg/s, 125 Deg/s, 300 Deg/s, 600 Deg/s, 1200 Deg/s, $p = 0.203, 0.001, 0.110, 0.002, 0.003, 0.027$, $n=12$ recordings respectively. **H.** Normalized ArcLight peak evoked amplitude during control and hyperpolarized conditions in injected eNphR3.0 ($n=12$ recordings) and non-injected wildtype (-Wt) mice ($n=4$ recordings). Responses are normalized to the 1200 Deg/s response under the control condition (LED OFF) for each recording. All errorbars represent Mean \pm S.E.M. * $p<0.05$.

In a subset of experiments, we simultaneously recorded the cortical temporal and spatial response using the GEVI ArcLight as a measure of spatiotemporal evoked activity while modulating ongoing thalamic polarization. Under control (no hyperpolarization) conditions the central barrel response responded with an overall monotonic increase in peak evoked amplitude (see Methods) with increasing deflection velocity (average across all sessions, Figure 3.3F, n=12 recordings). The timing of the peak ArcLight response was variable across recordings (range: 35-110ms). Therefore, to compare across recordings, we defined the peak evoked amplitude as the evoked fluorescence during the peak evoked frame (0-110ms post stimulus) of the strongest stimulus delivered for each recording under each condition. During periods of pre-stimulus hyperpolarization, we found that across most velocities, the evoked mean peak cortical amplitude increased (Figure 3.3 G, H). Importantly, this increase in response magnitude was not due to effects of LED activation, as shown in the ArcLight only (Wt-) control animals (i.e. no eNphR3.0, Figure 3.3H). To determine whether the results here were sensitive to the specific choice of integration time-bin, we tested a range of time-bins for integration of the evoked fluorescence and found that the qualitative conclusions were unchanged (data not shown).

In the cortex, upon examining a larger dataset than presented in Figure 3.1, we also observed that thalamic hyperpolarization altered the temporal properties of the evoked response (Figure 3.3F) by decreasing the overall evoked response duration (1200 Deg/s Duration: 305 ± 5 ms, TH-Halo: 124 ± 19 ms, $p=0.0069$, paired t test, n=12 recordings, Methods) and the time to peak (1200 Deg/s: 60 ± 9 ms, TH-Halo: 40 ± 3 ms, Mean \pm (S.E.M), $p=0.020$, paired t test, n=12 recordings, Methods). This observed larger and faster rising cortical response with a corresponding shorter duration, suggests that under hyperpolarized conditions, there was an increase in drive to both the excitatory and inhibitory cortical networks leading to strong inhibitory feedback⁸⁸. Our combined results

imply that pre-stimulus thalamic polarization can alter the evoked magnitude and temporal structure of the thalamic and cortical sensory evoked responses, which may have important implications for neural coding and perception.

3.3.4 Ideal Observer Detection from Single Trial Thalamic and Cortical Signals

We applied a signal detection framework to determine the single trial performance of an ideal observer to detect evoked thalamic and cortical signals. The ideal observer analysis demonstrates that the information necessary for detection or discrimination between two signals is present. Here, we first establish the framework in the context of velocity sensitivity (Figure 3.4) before turning to the optogenetic manipulation of thalamus. We asked how detectable the velocity evoked responses were from a noise distribution using a Receiver Operating Characteristic (ROC) analysis (Figure 3.4), and the area under the ROC curve (AUROC), as a metric of overall detectability of the sensory information (see Methods).

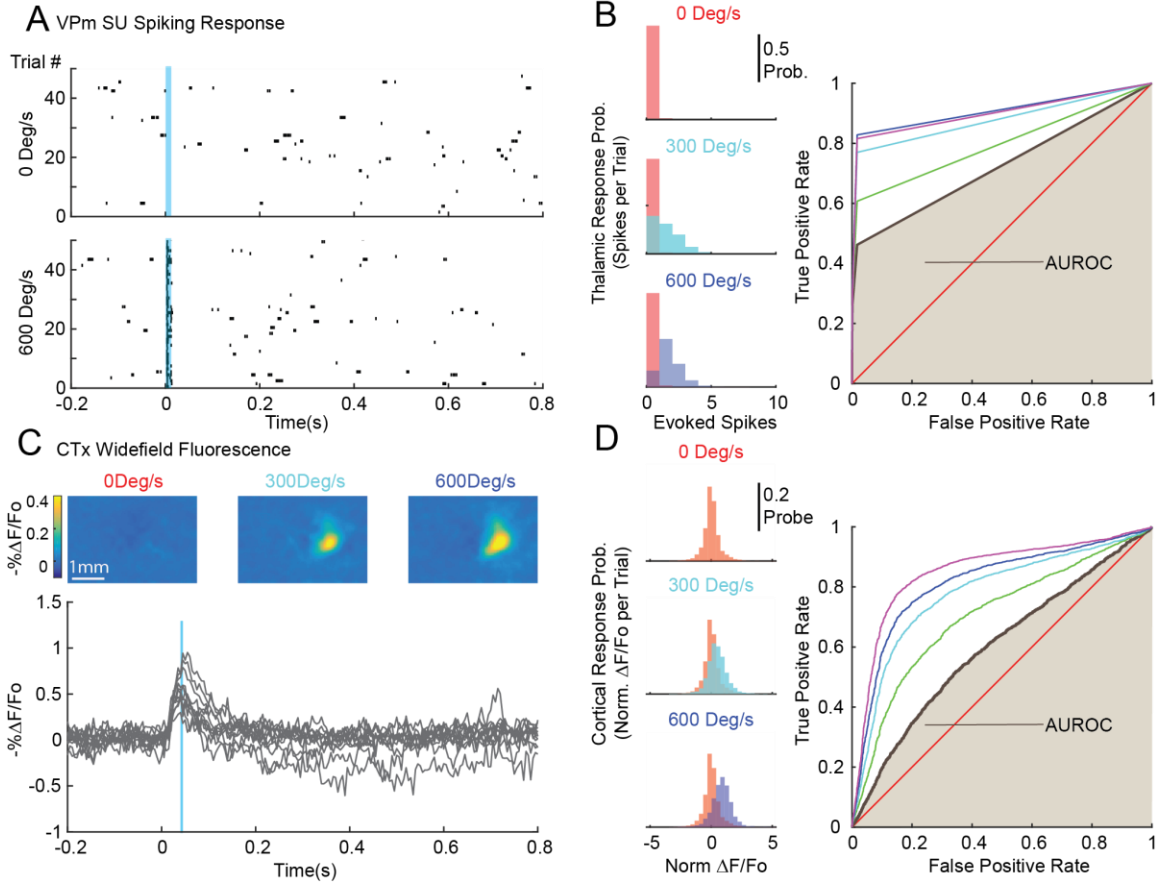


Figure 3.4. Thalamic and Cortical Activity Examined With an Ideal Observer.

A. Single trial raster of a thalamic recording with a spontaneous (0 Deg/s-top) and stimulus (600 Deg/s- bottom). Response period of 30ms shown in blue. **B. Left.** Combined thalamic evoked spike count during the 30ms window post stimulus for each stimulus across all single trials recorded. The thalamic noise distribution (red) is developed from the 0 Deg/s stimulus. **B. Right.** Receiver Operator Characteristic (ROC) analysis of the evoked thalamic spikes to determine the true positive and false negative rate from the evoked spike count (B left). The AUROC is highlighted as the area under the ROC curve. **C. Top.** Cortical spatial averages of 25-35ms post-stimulus of increasing velocities. **C. Bottom,** Single trial cortical ArcLight timeseries responses to a sensory stimulus (600 Deg/s, 5 Trials). The blue bar indicates that recordings peak response window. **D. Left.** Combined normalized evoked cortical response (Methods) during the peak window for each stimulus across all single trials recorded. The cortical noise distribution (red) is developed from the 0 Deg/s stimulus at the same time as the peak response. **D. Right.** ROC analysis for each velocity depicts the true positive and false negative rate from the evoked cortical responses (normalized $\Delta F/F_0$) based on the sliding threshold. The AUROC is highlighted as the area under the ROC curve (AUROC).

In the thalamus, we found that the thalamic single unit recordings had an initial velocity dependent response that lasted approximately 30 milliseconds post stimulation (Figure 3.4A, blue bar), and an increase in the number of evoked spikes per trial with increasing velocity (rightward shift in spike count histograms across all recordings, $n=1530$ trials from 15 single unit recordings across 9 mice, Figure 3.4B *Left*). As we increased the velocity delivered to the whisker system, the separation between the thalamic stimulus and noise distributions increased which resulted in an increase in the AUROC (Figure 3.4B *Right*, AUROC 50 Deg/s 0.72, to 1200 Deg/s 0.90), and thus detectability of evoked features.

The cortex fluorescence recordings had a velocity dependent response that was longer than the thalamic response (Figure 3.4C) and lasted for 100's of milliseconds. Here, we used the peak amplitude as a measure of cortical response. The timing of the peak cortical response was variable across recording sessions²²³; therefore, for each session we limited our analysis to the normalized evoked fluorescence peak response based on the strongest stimuli presented (Methods, blue bar). Similar to the thalamic data, we found that increasing the stimulus velocity increased the separation between the evoked peak cortical fluorescence from the noise ($n=3034$ trials, across 8 mice, Figure 3.4D *Left* histogram across all recordings). Therefore, velocity was positively correlated with the increased performance of the ideal observer in detecting the presence of the sensory feature (Figure 3.4D *Right*, AUROC 50 Deg/s 0.60, to 1200 Deg/s 0.85). These results correspond well with previously published analysis conducted on similar thalamic^{68,222} and cortical data^{166,234}, along with behavioral performance of a rodent during a single whisker detection task¹⁴¹.

3.3.5 Thalamic Hyperpolarization Modulates Cortical Detectability of Sensory Stimuli

Using this signal detection framework, we examined the impact of thalamic hyperpolarization on the thalamic and cortical single trial detectability of sensory features. We specifically sought to determine the effects of the relative changes to ongoing and evoked activity in thalamus and cortex under manipulation of thalamic polarization. Again, we considered the distribution of thalamic evoked responses (0-30 ms post stimulus) under control (Figure 3.5A, B - black) and hyperpolarized (Figure 3.5A, B - orange) conditions and compared them to the ongoing noise (Figure 3.5A-B, blue).

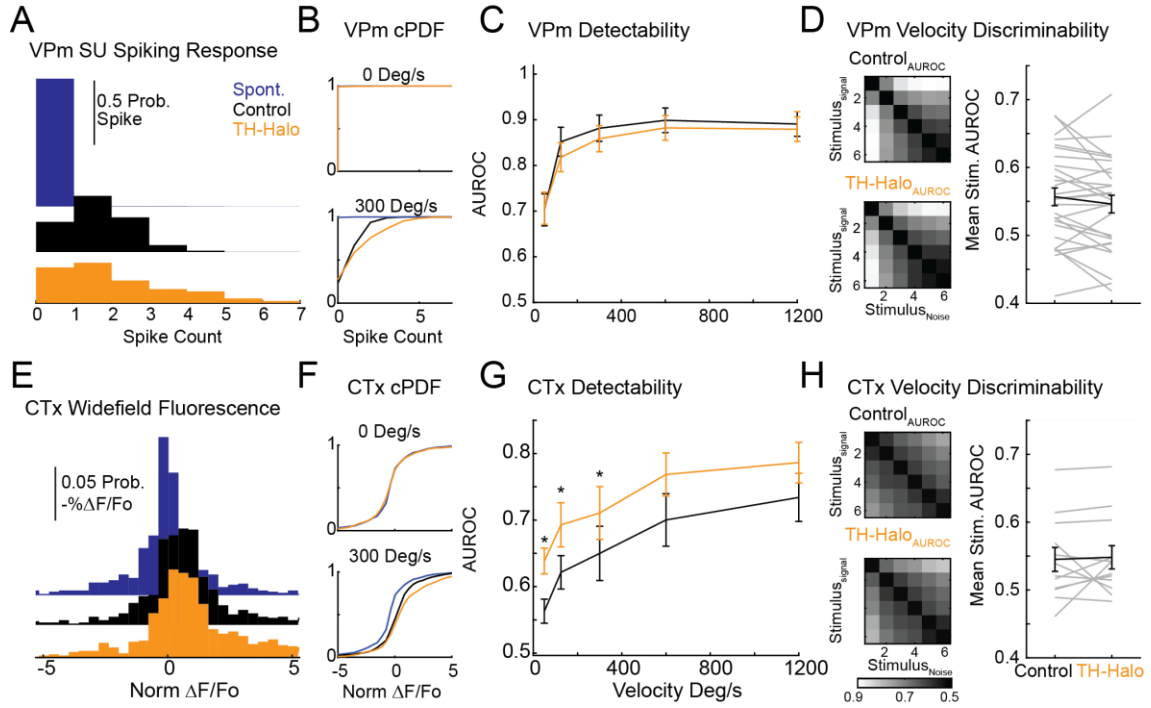


Figure 3.5. Thalamic Hyperpolarization Increases Cortical Theoretical Detectability of Sensory Responses.

A. Comparison of thalamic spiking in the noise (blue), and evoked thalamic spikes (0-30ms post stimulus) in the control (LED OFF- black), and thalamus hyperpolarized (TH-Halo- Orange) conditions across all recording sessions (28 units, 1347 trials) at a single velocity (300 Deg/s). Noise distribution (blue) determined using the same post-stimulus time during 0 Deg/s trials. **B.** Cumulative probability distributions of the same data shown in A for 0 Deg/s (top) and 300 Deg/s (bottom) stimuli. **C.** AUROC analysis of the thalamic spiking response each velocity stimuli under control (LED OFF- black) and thalamic hyperpolarization (TH-Halo - Orange) conditions (Mean, \pm S.E.M, across $n=28$ units). **D. Left.** AUROC matrix comparing the pairwise ROC analysis for each stimulus. Stimuli labeled in ascending order of intensity (i.e. 1=0 Deg/s, 6=1200 Deg/s). **D. Right.** Average thalamic AUROC across each recording for neighboring stimulus strengths. Thalamic velocity discrimination between neighboring strengths remains unchanged during thalamic hyperpolarization ($n=28$ units). **E.** Same as A, except for the evoked cortical response (across 12 recordings, 601 trials). Comparison of cortical fluorescence in the noise (blue), and a 300 Deg/s stimulus condition during control (LED OFF- black), and thalamus hyperpolarized (TH-Halo - Orange). Each bin represents the normalized fluorescence (Methods) across all recording sessions at a single velocity (300 Deg/s). Noise response was determined at the same window during 0 Deg/s trials. **F.** Cumulative probability distributions of the cortical fluorescence response for noise (blue), control (black) and thalamus hyperpolarized (orange) conditions for 0 Deg/s (top) and 300 Deg/s (bottom) stimuli. **G.** AUROC analysis of the evoked cortical fluorescence for each velocity stimuli under control (LED OFF- black) and thalamus hyperpolarized (TH-Halo

-Orange) conditions for each recording (n=12). Significant changes in detectability between control vs thalamic hyperpolarization found in the weaker velocities, paired t-test, $p=0.004, 0.043, 0.028, 0.060, 0.082$ for each velocity (50-1200 Deg/s, n=12 recordings). **H. Left.** Same as D, except with cortical response distributions. **H Right.** Average cortical AUROC across each recording for neighboring stimulus strengths. Cortical Velocity discrimination remains unchanged between control and thalamic hyperpolarized conditions. All errorbars represent Mean \pm S.E.M. * $p<0.05$

We found that thalamic hyperpolarization had little to no effect on the thalamic detectability for each single unit across sensory stimuli (Figure 3.5C, n= 28 units). Due to the low background thalamic firing rate in the anesthetized mouse, the evoked responses were very salient compared to spontaneous at all velocities, and thus were close to a “ceiling”. Although thalamic hyperpolarization increased the evoked responses (Figure 3.5A), the relationship between the single unit evoked and spontaneous activity remained unchanged (Figure 3.5B), and therefore did not impact the detectability of sensory responses. However, this relationship is likely to be different in conditions with elevated background thalamic firing rates, as has been demonstrated in the awake animal (see Discussion). We considered downstream targets could have different integration windows for thalamic information; therefore, we tested a range of temporal post stimulus bins, and found no changes to the observed trends when accounting for changes in thalamic response latency (data not shown).

In addition to the thalamic detectability, we also measured the effect of thalamic hyperpolarization on the detectability of cortical responses utilizing the evoked fluorescence from the GEVI ArcLight signal (Figure 3.5, *Bottom Row*). Again, we used the peak evoked amplitude to construct distributions of the evoked response and background spontaneous activity (Figure 3.5E-F, shown across all trials 601 trials, 12 recordings). Across each experimental session, we found that thalamic hyperpolarization

increased in the detectability of the evoked response. This increase in cortical detectability produced significant effects in the low velocity stimuli (Figure 3.5F).

We determined the observer's corresponding ability to discriminate between sensory stimuli, and the corresponding effects of thalamic hyperpolarization. This framework is very similar to that of the detection problem described above, but instead of discriminating signal from noise, we are discriminating one stimulus velocity from another. Again, this involves evaluation of the separability of two distributions, resulting in an AUROC measure to capture the overall discriminability performance. Specifically, to measure the discrimination, we compared the average AUROC across neighboring velocities (shown in Figure 3.5D, H) for each recording. We determined the discrimination performance by comparing the evoked distributions of each velocity to each other (i.e. 50 vs 125, 125 vs 300), and averaging the AUROC for the neighboring velocities. We found in both the thalamus and in the cortex, thalamic hyperpolarization surprisingly had no effect on sensory discrimination (Figure 3.5D, H), despite the effects on the overall activity in both parts of the circuit. In addition to the AUROC analysis, we also used a maximum likelihood approach with the same distributions (Wang et al, 2012, Whitmire et al 2016) with similar results. In summary, our results suggest that thalamic hyperpolarization enhances detectability of sensory inputs from cortical responses despite little or no effect on thalamic detectability, and the enhanced cortical detectability does not come at the expense of diminished discriminability of sensory features.

3.3.6 Thalamic Hyperpolarization Increases the Sensory Evoked Active Spatial Area

Given that thalamic hyperpolarization increased the evoked area of sensory inputs from cortical activity, it is natural to question the impact of the thalamic hyperpolarization on spatial information and spatial discrimination. We examined the spatial activity using two metrics: the overall activated area of the evoked response (Figure 3.6A-B), and the relative fluorescence across multiple barrels (Figure 3.6D-F). In both of these analyses we only examined the average cortical response in a 25-35ms post-stimulus window (see Methods). Across imaging sessions, we had high expression of ArcLight across the cortical surface (Mean 5.24 ± 0.55 (S.E.M.) mm^2 , $n = 12$ imaging sessions), enabling a characterization of the spatial activation of cortex in addition to the temporal components presented previously. To determine the activated cortical area, we used a threshold, 70% of the maximum response at the maximum velocity, under the control condition. The area exceeding this threshold was considered activated (see Methods). Similar to previous findings¹⁶⁶, we found that the S1 Barrel cortical activated area increased spatially with increasing velocity stimuli applied to the whisker (Figure 3.6A-B). During periods of hyperpolarization, the activated spatial area was greatly enhanced across a majority of stimuli, with the evoked area of the largest stimuli increasing approximately fivefold (Figure 3.6B, 1200 degree/s Control: $0.10 \pm 0.016 \text{ mm}^2$ TH-Halo: $0.47 \pm 0.08 \text{ mm}^2$, $p=0.002$, paired t-test, $n= 12$ recordings). Using activated area as a correlate of increased spiking, these results suggest that thalamic hyperpolarization increases the total evoked active cortical space.

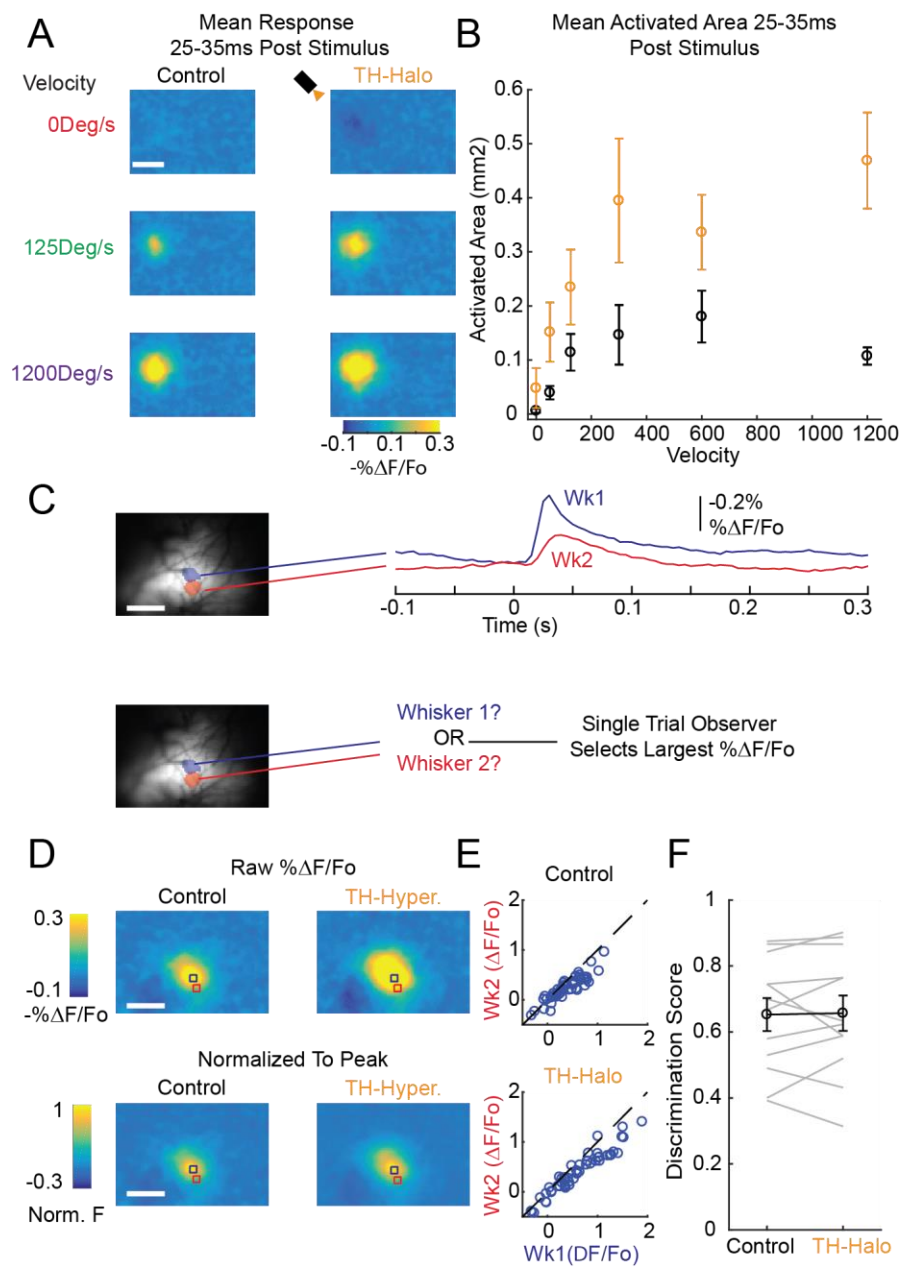


Figure 3.6. Thalamic Hyperpolarization Increases Activated Cortical Area with no Loss in Spatial Discrimination.

A. Single example of cortical spatial responses (mean 25-35ms post-stimulus response, $n=50$ trials) of increasing sensory stimuli under control (left), and thalamic hyperpolarized (TH-Halo right) conditions. **B.** Mean activated area during 25-35ms post-stimulus frame is increased during thalamic hyperpolarization across all stimuli. Activated area determined by the 70% threshold of the peak control response to the strongest (1200 Deg/s) stimulus for each session (Methods). **C. Top.** Example Cortical Mapping of two neighboring whiskers, Wk1, and Wk2. Right shows the expressing region of ArcLight probe, and the corresponding 70% threshold of the spatial activation. **C. Right.** Shows the timeseries of the spatial regions identified Wk1, and Wk2. **C. Bottom.** Ideal observer determines which whisker was deflected on a single trial by the largest fluorescence during 25-35ms post-stimulus. **D.** Comparison of the same data with different color scales, either raw $\% \Delta F/F_0$ (Top) or Normalized to the peak (Bottom). Relative relationship between neighboring barrels is conserved under thalamic hyperpolarization, although magnitude of fluorescence increases. **E.** Single trial evoked fluorescence in each identified barrel region (Wk1 vs Wk2) under Control(top) and Thalamus hyperpolarized (Bottom) conditions. Blue circles are single trial example of fluorescence responses between whisker region 1 and whisker region 2 (see C). **F.** Discrimination score between whisker 1 and whisker 2 in control and hyperpolarized conditions across each recording ($n=12$ recordings). Thalamic hyperpolarization had no effect across the population on the single trial discriminability across spatial barrels. All scale bars are 1mm, and all errorbars represent $\text{Mean} \pm \text{S.E.M.}$

Given the increase of activated area, we examined the resulting discriminability of the evoked responses. Specifically, we measured the evoked fluorescence of a neighboring cortical column (see Methods) during the initial evoked response (25-35 ms post stimulus, Figure 3.6C) or estimated by known anatomical distances between columns (~0.2 mm, Woolsey and Wann, 1976). During each imaging session, neighboring columns (Barrels) were identified by stimulating the surrounding whiskers. Interestingly, when we normalized the fluorescence response to the maximum response, the normalized evoked area remained largely unchanged during thalamic hyperpolarization (Figure 3.6D). These results suggest that thalamic hyperpolarization is increasing the spatial signal (i.e. gain) without altering the shape of the activation.

To formally examine this relationship, we compared the single trial responses in each identified barrel region during a single whisker deflection in either the control condition (Figure 3.6E *Top*) or thalamic hyperpolarized conditions (Figure 3.6E *Bottom*) and used a single trial classifier to predict the stimulated whisker. The classifier selected which whisker was stimulated based on the relative difference in evoked fluorescence in each identified region and assigned the largest response to that whisker. Across all recordings, we found that under both control and hyperpolarized conditions, the classifier performed equally well at determining the correct whisker stimulated (Classifier Performance Control: $65.2 \pm 5.0\%$, TH-Halo $65.7 \pm 5.3\%$, Mean Percent Correct \pm SEM, $n=12$ recordings). Therefore, the spatial discrimination of the evoked response was unchanged during periods of thalamic hyperpolarization (Figure 3.6F). Taken together, our findings suggest that thalamic hyperpolarization increases the spatial activation in response to a sensory stimulus, while maintaining the relative relationship of each cortical barrel, which would potentially maintain the spatial fidelity of the representation of complex stimuli, and thus the spatial discriminability.

3.4 Discussion:

Here, we used thalamic extracellular recordings and widefield imaging of ArcLight^{133,223} to capture the effects of reversible optogenetic thalamic modulation across the primary sensory cortex. To our knowledge, this work is the first to directly control thalamic activity through hyperpolarization and link large-scale spatial and temporal downstream consequences for sensory encoding.

Our primary result is that brief periods of thalamic hyperpolarization modulated the magnitude, temporal structure, and spatial extent of thalamocortical sensory response to punctate stimuli. Specifically, we observed that thalamic hyperpolarization increased both the stimulus evoked (Figure 3.1) and spontaneous (Figure 3.2) bursting in the thalamus which corresponded with a larger and but temporally shorter cortical population responses (Figure 3.1,3.3). Additionally, we found that thalamic hyperpolarization increased thalamic latency, and jitter in response to sensory inputs. Therefore, brief periods of thalamic hyperpolarization may have dynamic implications on sensory encoding beyond the observed enhancement of sensory features²³⁵.

One consideration is that these data was collected under isoflurane anesthesia where presumably the thalamus is relatively hyperpolarized. While quiet and inattentive states may resemble anesthetized recordings, it is certain that thalamic hyperpolarization will have more complex and nuanced results in the awake animal. We predict that the principles of thalamic hyperpolarization shown here represent circuit properties that should still apply in the awake thalamocortical network. Additionally, it is important to note that our widefield cortical fluorescence measurement is a combination of voltage signals predominantly from dendritic inputs in the upper cortical layers^{132,203}. Although the cortical output is correlated to the voltage potential, this relationship is nonlinear and future work is needed to determine the impact of hyperpolarization on awake cortical processing.

3.4.1 Thalamic Hyperpolarization Alters Both Thalamic and Cortical Sensory Encoding Through Modulation of Thalamic Bursts

We found that through brief (500ms) periods of pre-stimulus hyperpolarization, we observed an increase in the thalamic gain (Figure 3.3) across sensory inputs, which corresponded to an approximate 50% increase in cortical response. Notably, thalamic pre-stimulus hyperpolarization increased evoked thalamic bursting by approximately 150%. The thalamocortical (TC) synapse is weak ⁵⁶ and rapidly adapts to ongoing input ²²⁰; therefore, the TC synapse is dependent on temporal distribution of incoming signals ^{101,216}. Furthermore, due to excitatory and inhibitory cortical circuitry, there is a short (~10-20ms) window of opportunity ²²⁴ for evoking cortical responses. Our results show that thalamic polarization controls the level of sensory evoked bursting which dictates how signals are transmitted to the cortex.

Thalamic bursts, and bursting modes, have a controversial history in sensory processing from preventing transmission ²³⁶ to increasing sensory detection ^{49,54} to containing additional sensory information ⁴². Ongoing thalamic spontaneous bursting events were traditionally only associated with slow wave sleep or anesthesia; however, this has been largely disproven, with low rates of bursts occurring both spontaneously and during naturalistic stimuli in awake somatosensory ^{47,68,216}, visual ²³⁷, and auditory systems ²³⁸. Additionally, the disruption of transmission of sensory information in bursting modes is under additional scrutiny in the auditory pathways, where thalamic burst modes during slow-wave-sleep consistently transmits sensory evoked features to the primary auditory cortex ^{239,240}. Therefore, altering the thalamic firing mode, through slight changes in net polarization, may be critical for controlling thalamic gating of sensory information in the awake thalamocortical circuit.

3.4.2 Thalamic Modulation Changes Ongoing Cortical Activity

During optogenetic thalamic hyperpolarization we observed an increase in both the thalamic and cortical background (Figure 3.2), with increased thalamic bursting. Therefore, the reported changes in the cortical response could be elicited by changes in ongoing cortical activity alone. While the cortex is capable of generating ongoing cortical activity²⁴¹, thalamic and cortical states have been found to be dynamically interconnected. Additionally, ongoing cortical activity has a long history of impacting the evoked sensory response^{242,243}. Previous studies that have hyperpolarized thalamic nuclei using Thalamic Reticular Nucleus activation (Lewis et al 2015) or muscimol injections (Poulet et al 2012) have observed a large increase in cortical low frequency activity. Additionally, thalamic neurons project onto both excitatory (E) and inhibitory (I) cortical populations, with markedly strong feedforward projections to inhibitory neurons^{59,88}. *In vitro* work has also revealed that thalamic bursts themselves can interact with selective excitatory and inhibitory SOM populations²⁴⁴. Therefore, ongoing thalamic firing and bursting could cause dynamic network changes in cortical E/I balance. Whether the ultimate cause of the increase in cortical evoked activity is solely due to thalamic activity or the entire thalamocortical network, thalamic hyperpolarization has a profound effect on stimulus representation across the network.

3.4.3 Direct Thalamic Hyperpolarization Increases Ideal Observer Detection with No Change in Discrimination of Sensory Events

We found that thalamic hyperpolarization did not simply increase cortical activity, but preferentially increased the evoked signal compared to the ongoing noise, thereby

increasing the detectability of cortical sensory information from the perspective of an ideal observer (Figures 3.4,3.5). Interestingly, thalamic hyperpolarization did not impact the detectability of thalamic sensory information (Figure 3.5C). A current conceptual model of thalamocortical gating is to control coding properties to trade-off between detection and discrimination^{36,49}. These regimes are thought to be continuous; in the more hyperpolarized burst mode the thalamus would favor detection of sensory stimuli, whereas, conversely, in a depolarized tonic mode, the thalamus would transmit more information of the stimulus content (Whitmire et al, 2016). Our results aligned with aspects of this framework, where thalamic hyperpolarization increased cortical detectability; however, we observed no change in the discriminability of sensory information either across stimulus strengths (Figure 3.5) or across space (Figure 3.6). Historically there is a dynamic tradeoff between detection and discrimination^{66,106}; however, these tradeoffs are largely associated with sensory adaptation, which activates the thalamocortical network in a different manner as compared to direct thalamic modulation. Furthermore, a loss in sensory discrimination may only impact a wider range of hyperpolarized conditions and sensory stimuli beyond what was examined in this work.

While thalamic hyperpolarization may not impact sensory discrimination, there are other potential perceptual tradeoffs. Sensory perception dysfunctions such as auditory tinnitus²⁴⁵, and chronic pain (Saab and Barrett, 2017 For Review: Perez-Reyes, 2003), that represent sensitivity to sensory information are associated with an increase in thalamic bursting. These neurological disorders represent a failure in thalamic gating of sensory information and show that modulation of thalamic polarization, and specifically thalamic bursting, is essential for healthy sensory processing.

3.4.4 Thalamic Hyperpolarization Modulates the Spatial Activation of Cortex in Response to Sensory Stimuli

Using widefield GEVI imaging, we determined that thalamic hyperpolarization not only increased the evoked amplitude, but additionally caused a fivefold increase in the evoked spatial response (Figures 3.1,3.6). The rodent whisker system ⁹ has a discrete somatotopic map of functional cortical columns related to each whisker, or barrels. Each cortical barrel predominantly responds to a single whisker deflection; however, *in vivo* intracellular recordings reveal subthreshold receptive fields for many whiskers for simple stimuli ¹²². Our widefield voltage recordings showed two results: 1. an increase in sensory evoked spatial activation across the cortex, 2. no cost in spatial discrimination. These data suggest that thalamic hyperpolarization may increase the spatial thalamocortical gain, which ultimately may broaden the spatial activation. In the visual pathway in awake quiescent animals, a decrease in spontaneous activity with an increase in thalamic bursting is correlated with an increase in the non-preferred response in the thalamus ⁴⁸ and cortex ⁴⁶. Therefore, thalamic hyperpolarization may tilt the network toward a hyper-detectible state where the occurrence of any sensory stimuli would activate many sensory cortical columns to send a powerful signal downstream.

3.4.5 Conclusion

Our results suggest a pronounced effect of thalamic state on the downstream cortical response across temporal and spatial scales. Therefore, we predict that short periods of thalamic hyperpolarization could increase the salience of incoming sensory information. In the awake animal, the spontaneous thalamic firing rate is in constant transition between internal ³⁷ and external ²⁴⁶ sensory driven states. The thalamus receives a diverse set of excitatory and inhibitory inputs from the corticothalamic pathway, the thalamic reticular nucleus, and neuromodulatory centers. In particular, brief periods of hyperpolarization could be controlled through inhibitory inputs from the thalamic reticular

nucleus ⁸¹, which has been shown to modulate thalamic activity in a task dependent manner ⁹⁰. Taken together, our results highlight the important role of ongoing thalamic polarization on evoked cortical activity and predicts how thalamic firing modes can impact how we perceive and detect sensory information.

CHAPTER IV: THE MODULATION OF THALAMOCORTICAL STATE IN THE AWAKE AND ANESTHETIZED BRAIN.

4.1 Introduction:

The major senses of audition, somatosensation, and vision send information through thalamic relay nuclei before further processing in the cortex. In the awake animal ongoing spontaneous thalamic spiking activity is constantly in flux as the animal shifts through various behaviors^{247–249}, engages in active sensation^{37,246}, or receives sensory inputs (for review see^{1,140}). Synapses onto thalamic nuclei have been suggested to be overwhelmingly modulatory in nature^{7,250,251}, changing the current thalamic state across a variety of timescales (milliseconds to minutes)²⁵². While the exact origin of these particular states are still being uncovered, it is clear that ongoing thalamic activity is modulated through various mechanisms including direct cortical innervation^{36,253}, neuromodulatory input, and reticular thalamic inhibitory circuits^{86,254–256}. In particular, the thalamus receives direct GABAergic hyperpolarizing inputs through the thalamic reticular nucleus (TRN), which can be indirectly controlled through cortical feedback⁹². TRN modulation has been shown to be incredibly dynamic in the awake brain^{78,81}, and has even been shown to be modulated during attention and behavior tasks⁹⁰. In addition to ongoing inputs, thalamic nuclei are embedded in interconnected circuits that alter downstream cortical targets¹⁰⁸ and impact thalamic firing through feedback systems²⁵⁷.

Beyond changes in absolute firing rate, thalamic neurons can enter different temporal regimes of spiking, from tonic to burst firing modes²²¹. Thalamic neurons contain specific T-type calcium channels that become de-inactivated during brief periods of hyperpolarization lasting at least 100 ms⁴⁰. Once these channels are active, depolarizing

inputs cause a slow-wave of calcium influx into the cell which results in multiple action potentials with short interspike intervals (2-4 ms). Thalamic bursts have been found to perform two seemingly contradictory roles: of regulating sleep processes²⁵⁸, while also transmitting sensory information for detecting sensory events in the awake brain. Thalamic bursts are most commonly found spontaneously during Slow-Wave-Sleep (SWS); however, bursts are not limited to sleep states²⁵⁹. Although more selectively generated, bursts have been identified during awake processes¹⁰³ and during behavioral detection tasks^{68,258}. In particular, bursts and stimulus evoked bursting has been theorized to play an important role for the encoding of sensory information^{42,49}. Bursting has been shown to increase evoked downstream responses, and are theorized to send powerful signals to the cortex⁴⁷. While many studies have investigated the impacts of different thalamic states and firing modes across *in vitro*^{93,244,260} and anesthetized *in vivo* preparations^{224,261–264}, few studies have explored thalamic states in the awake brain^{47,70,265}. Furthermore, even fewer²⁶⁶ have causally determined how different thalamic states alter sensory signals across the thalamocortical pathway.

Here, we investigated how modulations in ongoing thalamic activity shape the encoding of a simple sensory stimulus in the thalamus and cortex in the mouse somatosensory pathway. Specifically, we explored how different levels of hyperpolarization alter the encoding in the thalamus and investigated the role of thalamic bursting in the awake and anesthetized brain. Under anesthesia, neural activity is suppressed and allows for a detailed examination of the thalamocortical circuit without the influence of external factors. Whereas in the awake animal, we were able to examine how thalamocortical interactions are altered by ongoing activity and behavioral states. In order to manipulate the thalamocortical circuit, we used optogenetic stimulation of virally expressed halorhodopsin in the mouse thalamus while simultaneously measuring the thalamic extracellular activity and downstream

cortical responses using a genetically expressed voltage indicator (GEVI). With the GEVI ArcLight, we were able to measure how different optogenetically imposed states alter the transformation of temporal and spatial information across the primary somatosensory cortex. We found that through increasing levels of activation of halorhodopsin in the thalamus (with increasing LED intensity) we were able to transition thalamic firing modes from tonic to increasingly burst firing, in both the anesthetized and awake circuit. Under both conditions (anesthetized and awake), we found that a more hyperpolarized condition increased the sensory evoked thalamic response to sensory inputs. In the cortex we found a dichotomy of effects with thalamic hyperpolarization across anesthetized and awake states. In anesthetized animals, we found that thalamic hyperpolarization monotonically increased the evoked cortical spatial and temporal response to sensory inputs. However, in awake animals, we found that that increasing levels of thalamic hyperpolarization and corresponding burst mode caused a monotonic decrease in the evoked cortical response. To further explore this paradox, we examined the ongoing, spontaneous firing and burst rates. We found that prolonged halorhodopsin activation further increased an already elevated thalamic firing rate in the awake animal, likely changing the context for the subsequent sensory evoked response. These results suggest that the complex nature of thalamic state is highly dependent on ongoing cortical and neural states for transmitting sensory information downstream.

4.2 Methods

All procedures were approved by the Institutional Animal Care and Use Committee at the Georgia Institute of Technology and were in agreement with guidelines established by the NIH.

4.2.1 AAV Delivery:

At least 5 weeks prior to experimentation, young (~6 weeks) female C57BL/6J (Jackson Laboratories) mice were injected with different viral constructs either in the Ventral posteromedial (VPm) thalamic region with AAV-5-CamKinaseII-eNph3.0 (UNC Viral Vector core), in the primary somatosensory (S1) cortex with AAV-1-hsyn1-ArcLight (UPenn Viral Vector Core), or both. Mice were anesthetized using Isoflurane (3-5%). After the mouse was fully anesthetized, small bore holes were placed over the regions of interest and were aligned using stereotaxic measurements (For VPm, 1.8mm Lateral from Midline by 1.8mm Caudal from Bregma). For cortical expression, either single or multiple injection sites were used surrounding the barrel cortex (center on 1.5mm caudal from Bregma and 3mm lateral from midline). The virus was loaded into a modified Hamilton syringe (701-N) with a ~35 micron borosilicate glass pipette type. The syringe was initially lowered to the corresponding depth below the surface (for VPm: 3mm and For CTx: 0.5mm) and let rest for 1 minute before injection. Both sites received injections of 0.5-1 μ l²⁶⁶ of viral construct at a flow rate of 0.1 μ l/minute. After injection, the pipette remained in place for an additional 5 minutes before slowly being removed from the brain. The bore holes were filled with either bone wax or left to close naturally. Throughout injection, mice were kept warm using a water heating system to maintain body heat.

4.2.2 Anesthetized Electrophysiology:

Mice were initially anesthetized using isoflurane (3-5%) and then placed on a heated platform (FHC, Inc.) in a stereotaxic nose cone to maintain anesthesia. A large incision was placed over the animal's skull, and the connective tissue and muscle surrounding the skull was removed using a scalpel blade. A modified headplate was attached using dental acrylic (Metabond) and secured to the skull. For cortical imaging, the skull was thinned with a dental drill, until transparent or removed entirely and covered with saline or ringers solution. After surgery, the isoflurane levels were dropped to $\sim <1\%$ for all imaging and electrophysiology experiments. The animals vitals (heart rate and respiratory rate) were constantly measured for anesthesia depth.

4.2.3 Awake Behavioral Training:

At least four weeks after ArcLight and eNphR3.0 viral injection, mice were anesthetized under isoflurane and were headplated using the above stated protocol. Over the course of 5-14 days preceding the first imaging experiment mice were routinely handled to gain familiarity with the imaging system and immobilization device. During this acclimatization period, mice were increasingly head fixed for longer periods of time, from 15 minutes to 1.5 hours. During stimulation of the whisker, mice were prevented from interacting with the whisker stimulator by obstructing the path from the paws to the whisker. Mice were rewarded with sweetened milk (Nestle, Ltd.) throughout imaging, which greatly helped to reduce animal frustration. After 5 days of handling and acclimating, mice appeared to be calm while the head was immobilized in the headplate restraint system. During passive stimulation of the whiskers the mice often actively moved their whiskers. Therefore, the galvanometer was placed 5mm from the face to prevent the whisker from slipping out of the manipulator; however, the amplitude of the deflection was adjusted to maintain a

consistent velocity stimulation (1200 Deg/s) as presented in the anesthetized case (see above).

4.2.4 Thalamic Electrophysiology:

A small craniotomy was placed over the primary whisker sensitive thalamic ventral-posterior medial (VPm) region of the mouse, around the injection site (see above). First, the VPm was mapped with a 2M Ω tungsten electrode (FHC) which was slowly lowered until 2.5mm below the cortical surface. The mouse VPm was identified using both stereotaxic measurements and depth as well as electrophysiological features (such as latency, peak response, whisker selectivity). A neural unit was determined to be located in the VPm if the Post-Stimulus Time Histogram (PSTH) contained a peak response 3ms - 10ms after a 1200 degree/s (Deg/s) single whisker stimulation and did not have a latency shift by more than 20ms after 1s of 10hz adapting stimulus²²⁴. The principle whisker was first determined using a manual probe to isolate the whisker with the largest evoked response. If further isolation was needed, the principle whisker was determined by the largest 30ms PSTH response of the surrounding three whiskers. After the conclusion of the study either a small 7 μ A 10s lesion, or a fluorescent dye was placed near the recording location and confirmed using histological validation. Awake recordings lasted up to 4 hours in duration. If the animal became agitated during recording, the session was ended early.

Neuronal signals were band-pass filtered (500 Hz –5 kHz), digitized at 30 kHz/ channel and collected using a 96-channel data-acquisition system (Blackrock Microsystems, Salt Lake City, UT, USA). Offline spike sorting was accomplished using Plexon Offline Spike Sorter v4 (Plexon, Inc). Additional data analysis utilized custom scripts using Matlab (Mathworks, Inc).

The rodent whiskers were deflected by a high fidelity (1k Hz) galvanometer system (Cambridge Technologies). A typical velocity sweep stimulus was applied by positioning the custom designed galvanometer 5-10mm from the face and delivering an exponential sawtooth (rise and fall time = 5ms). The waveform stimulus velocity was taken by averaging the time to peak velocity of the stimulus. The velocity was adjusted based on distance from the face.

4.2.5 Intrinsic Imaging:

Mice were imaged through either intact or thinned skull using a wide-field imaging system to measure cortical spatial activity (MiCam02HR Scimedia, Ltd). During all imaging experiments, isoflurane anesthesia levels were lowered to approximately 1%. The cortex was imaged using a 184x123 pixel CCD Camera (Sciendia MiCam2 HR Camera) at 10 Hz with a field of view of 4x3mm with a total of a 1.6 Magnification (48 pixels/mm). We used a green (535nm) or red (625nm) excitation light projected onto the cortical surface that has a high overlap with the hemodynamic absorption spectrum. Collected light was filtered with a set of dichroic mirrors (Bandpass 475/625nm and Longpass 495nm, Semrock, Inc) and a bandpass emission filter between wavelengths of 520/555 nm (Semrock, Inc). The imaging system was focused at approximately 300µm below the cortical surface to target cortical layer 2/3. In order to evoke a cortical intrinsic response, the whisker was repetitively stimulated at 10Hz for 6 seconds.

4.2.6 Awake Cortical Fluorescent ArcLight Imaging:

ArcLight transfected mice were imaged through the thinned or removed skull using a two camera system: a Scimedia Imaging system to measure cortical ArcLight spatial activity,

and a custom camera to measure hemodynamic activity for subtraction. The cortex was imaged using a 184 x 123 pixel CCD Camera, MiCam2 HR Camera (Scimedia, Ltd) at 200 Hz, and a Basler Ace (acA1920-155um) 480 x 180 pixel (4x4 binned) CMOS Camera at 200Hz, with a tandem lens microscope (Figure 3.1A). The entire cortical area was illuminated at 465 nm with a 400 mW/cm² LED system (Scimedia, Ltd.) to excite the ArcLight fluorophore and background autofluorescence. The excitation light was projected onto the cortical surface using the first dichroic mirror (bandpass: 475/625nm, Semrock, Inc.). Collected light was passed through a second dichroic mirror (Longpass cutoff: 495 nm, Semrock, Inc.) for collection of the ArcLight and autofluorescence signal. The autofluorescence signal was filtered with a bandpass filter between the wavelengths of 465/75 nm (Semrock, Inc.). The ArcLight signal was filtered with a bandpass emission filter between wavelengths of 520/35 nm (Semrock, Inc.). The imaging system was focused approximately 300µm below the surface of the brain or cortical layer 2/3. Anesthetized imaging only utilized the single camera system as described in Chapter 3.

4.2.7 Functional Fluorescent Mapping of Barrel Cortex:

The mouse's whisker system was first mapped by imaging the rapid ArcLight response (800ms) to a high velocity (1200 Deg/s) sensory stimuli to three mouse whiskers. The resulting whisker response averaged over 20 trials was determined to be associated with a principle whisker, and barrel, if the evoked response was spatially limited to roughly a 0.2 mm x 0.2 mm area 25-30ms after stimulation. Additionally, the response was determined to be originating from the barrel field if the center of mass of activation moved consistently with the histologically defined barrel field and was within the standard stereotaxic location of S1 (~3mm lateral, 0.5-1.5mm from bregma). After mapping, a single whisker was deflected with an ethologically relevant velocity sweep (0-1200 Deg/s)

designed to simulate high velocity slip-stick events, either with or without thalamic optogenetic hyperpolarization to determine the cortical responses to various velocities.

4.2.8 Simultaneous Imaging and Thalamic Optogenetic Stimulation:

After mapping both the thalamic and cortical regions, an optrode (2M Ohm tungsten electrode mounted to an 200um optic fiber) was positioned to the stereotaxic locations of the pre-mapped thalamic region and lowered to the corresponding depth. Once a single thalamic unit was identified using the above constraints, the unit was determined to be sensitive to optical stimulation by briefly (1-2s) hyperpolarizing the cells using at least 16mW/mm^2 590nm LED light source (Thorlabs, M590-F1). Due to the low baseline firing rate ($<1\text{Hz}$), each cell was determined to be a thalamic optically sensitive unit if the cessation of the 590nm light caused a rebound burst³⁸. After identifying an optically sensitive thalamic unit, the same velocity stimulus was delivered in a pseudorandom order to the whiskers under various light conditions. Light stimulation for all cases was presented 750ms preceding and following whisker deflection (1.5s total light illumination, with a 250ms ramp up and down). There was a variable three to nineteen second gap between stimulus deliveries to allow for recovery of halorhodopsin (eNphR3.0). Each session imaged 200ms-1s of preceding frames to measure spontaneous activity. Light power was measured from the tip of the ground optical fiber before each experiment to maintain approximate light intensities delivered to each cell ($0\text{-}38\text{mW/mm}^2$). All LED light measurements are estimated to be within %20 of the reported value. During stimulation, the downstream cortical response was recorded using the same imaging system and voltage indicator as listed above. Optogenetic and viral expression of each experiment was verified through confocal and brightfield imaging of fixed slices.

4.2.9 Histology:

Histology samples were prepared by perfusing the animal transcardially with phosphate buffered saline (PBS) followed by 4% paraformaldehyde. Brains were post-fixed overnight in 4% paraformaldehyde then transferred to PBS before sectioning. Thick sections were cut using a vibratome (100 μm , Leica, VTS 1000) and either directly mounted or saved for staining.

4.2.10 Thalamic Electrophysiology Data Analysis- Mean Response, Burst Ratio, and First Spike Latency:

We report several different basic measurements of spiking activity from our thalamic units including evoked response, evoked bursting response, latency and jitter. We determined thalamic evoked response as the initial response (0-30ms) to sensory stimuli. Each single unit recording was averaged over many trials (15-50) to produce a single response curve for that unit. The evoked response was determined as the average spikes per trial in the 0-30ms period post stimulus. The corresponding evoked bursting response was determined as number of bursting spikes per trial in that same post stimulus period. Bursting spikes were defined as 2 or more spikes that fire at most 4ms apart preceded by 100ms of silence. The 100ms pre-stimulus activity is based on reported values for T-type calcium bursts^{47,68}. The First Spike (FS) Latency was determined as the average first spike after stimulus delivery ($t=0$). Trials in which no spikes occurred within the response window were determined to be nonresponsive trials and were excluded from the analysis. To compare to other thalamic studies, it is important to note that the sawtooth stimulus used for whisker deflection reached peak velocity 2ms after stimulus onset. The spiking jitter was determined as the standard deviation of the first spike latencies for each recording. We measured the effect of ongoing spiking activity by comparing the distribution of firing rates of each recorded neuron during 1s during control (no LED) and optogenetic stimulation

using the Mann Whitney rank sum test. Significant modulations were determined if $p < 0.05$. All data analysis of the recorded extracellular thalamic units was accomplished using custom Matlab scripts.

4.2.11 Voltage Sensitive Imaging Data Analysis:

Raw images were loaded and converted from the “.gsd” format using custom scripts and down-sampled by a factor of two. Each dataset was first normalized to a $\% \Delta F / F_0$ measurement by subtracting and dividing each trial by the temporal average frame between 0 and 200ms preceding the stimulus or light delivery (F_0 = mean response frame from 200ms to 0ms preceding stimulus or light delivery). Hemodynamic noise was removed using a Principle Component Analysis Background subtraction method discussed below.

As described in detail ²²³, *in vivo* ArcLight imaging overlaps with the hemoglobin absorption spectrum, and therefore contains hemodynamic noise that must be removed for analysis. Similar to the methods described in Borden et al, this hemodynamic noise was removed using a background subtraction method. Imaging the wildtype mouse cortical surface using the same blue excitation and the ArcLight filter set revealed similar patterns of oscillatory activity, likely through autofluorescence and effect of hemodynamic absorption and blood flow ²²⁵. The Background PCA subtraction utilizes autofluorescence signal from non-ArcLight transfected regions to predict the hemodynamic signal across the recorded space.

Specifically, the Background PCA subtraction method uses the background fluorescence of non-expressing autofluorescence regions to find the ongoing hemodynamic components on a single trial basis. We created a threshold to separate the background autofluorescence from the ArcLight signal using the maximum fluorescence from a non-inject animal.

Therefore, the extracted principle components would be less likely to contain ongoing neural activity. Additionally, the background fluorescence regions were selected at least 1mm away from the recorded whisker evoked response (Borden et al, 2017). Ideally, these criteria would create a spatial defined region with little or no ArcLight fluorescence to isolate the hemodynamic signal from the neurometric signal. Each frame is first spatially averaged by a $200\ \mu\text{m} \times 200\ \mu\text{m}$ averaging median filter. On a single trial, the corresponding top five principle components of the low background regions (which contains approximately 85% of the variance explained) are projected on a pixel by pixel basis across the entire recording using lasso regression method with regularization²⁶⁷. The lasso regression utilizes a cross validated approach to determine the minimum number of components to develop the model of hemodynamic noise. In order to prevent the removal of any stimulus evoked activity, each pixel was fit on pre-stimulus activity (either before light onset for experiments involving optogenetics, or immediately preceding stimulus delivery). The final predicted hemodynamic signal for each pixel was subtracted across the entire recording on a pixel by pixel basis. Due to the complex waveform of the hemodynamic response, a simple notch filter is not effective at separating the signal from the noise²²³.

We found that the updated Background PCA subtraction method greatly reduced hemodynamic signal across the entire frame, compared to the off-ROI method (Borden et al, 2017) which was more limited to the selected barrel ROI. In some instances, brief onset and offset light artifacts of the 590nm light was visible in the recorded ArcLight Cortical signal. We removed this onset and offset transient signal from the final fluorescence to remove optogenetic transient light artifacts.

4.2.12 Dual Camera Imaging – Imaging analysis:

In the awake animal, we utilized a dual camera imaging system to capture a background fluorescence signal for hemodynamic subtraction. Two different cameras were used to capture ArcLight and autofluorescence signal, and therefore, pixels could not be directly registered for subtraction for pixel by pixel correction. Instead, we utilized the same Background PCA subtraction method to find and develop models of the hemodynamic response based on the global PCA signal derived from the background image. For the dual camera files, each component was fit over the entire recording for subtraction of the hemodynamic noise. Both raw and processed images showed qualitatively similar results.

Unless otherwise noted, each dataset was processed with the Background PCA or Dual Camera subtraction method as stated above. Background PCA and Dual Camera processed files showed the same trends.

4.2.13 Imaging Data Analysis – Peak amplitude, Normalized Peak, and Temporal Properties:

We measured the effect of the optogenetic stimulation on the peak amplitude of the evoked mean ArcLight fluorescence in the determined cortical barrel. The cortical barrel region of interest (ROI) for each stimulated barrel and each data set, was selected as the 200 μm x 200 μm region with the largest response 30ms after stimulus delivery. This determined ROI was used for all subsequent analysis of the temporal response. To better isolate the evoked amplitude, the frame of stimulus delivery ($t=0$) was subtracted from the resulting recorded signal. For each recording, the peak amplitude was defined as the $\Delta F/F_0$ at the time of the maximum average response between 0 and 110ms for the strongest stimuli (1200 Deg/s) presented under control and various optogenetic conditions. In order to measure the temporal properties of the evoked response, we concentrated on the timeseries

data from the determined cortical barrel ROI. For normalized fluorescence (Norm $\Delta F/F_0$), each session's peak response was divided by the average peak response to the strongest stimulus (1200 Deg/s) under the control condition. The normalization allows for a better comparison across animals which may have different levels of ArcLight expression. We measured the time to peak as the time from sensory onset (10% of the peak signal) to the peak evoked response between 0 and 110 ms post stimulus. As a further measure of the temporal properties, we measured the overall duration of the response as the time between sensory onset (10% of the peak signal) and sensory offset (defined as the return to 10% of the peak signal, Borden et al, 2017).

4.2.14 Imaging Data Analysis – Area Measurements:

In addition to measuring the peak response, we also measured the effect of different thalamic polarizations on the evoked area of sensory cortical activity. We measured the activated area by the number of pixels over a threshold using the average response 25-35 ms post stimulus frame. Similar to other studies^{226,227}, we measured the spatial activation by the pixels over a 70% threshold of the maximum delivered stimulus (1200 Deg/s) under the non-optogenetic (Control) condition. The activation threshold was measured for each session to account for across experimental variability, ArcLight expression, and changes in ongoing fluorescence. The threshold was calculated based on each recording session's peak response 25-35ms post stimulus for the largest velocity. In order to isolate the evoked activity from ongoing activity, we subtracted the frame at stimulus delivery ($t=0$). Different thresholds had no effect on the observed trends.

4.2.15 Awake Whisking – Data Analysis:

We measured the awake whisking behavior using a Basler Ace (acA1920-155um) camera sampled with 480 x 300 pixel (4x4 binned) at 20-50 Hz. The whiskers were illuminated using either an external LED light (860nm) or by the imaging 465nm light source. Images were continually recorded through the entire recorded session and then aligned using the movement of the galvo stimulus. A select region of interest (ROI) was placed in the whisker pad close to the face to determine changes in average intensity during the recording session. A custom algorithm measured the squared change in intensity to determine periods of whisker movement. Whisker movement was assigned using a threshold of pixel intensity that was used for each imaging session. A movements had to last longer than 100ms to considered as whisking periods.

4.2.16 Experimental Design and Statistical Analysis:

For all measurements, we determined if the specific data sets were normally distributed using the Lilliefors test for normality. If the data were normal, we used the appropriate (paired or unpaired) t-test for statistical difference, and a one way ANOVA for across different groups. If the population was determined to have non-normal distributions, we conducted nonparametric Wilcoxon signed-rank tests to determine statistical significance and the Friedman test to for across groups comparisons. Multiple comparison tests were corrected using the Holm-Bonferroni method. All tests were conducted using the MATLAB Statistics Toolbox (Mathworks, Inc.) or SPSS (IBM). All sample sizes are reported in the figure captions and text. Data is available upon request.

4.3 Results:

4.3.1 Simultaneous Thalamic Manipulation and Cortical Recordings in the Awake and Anesthetized mouse.

We performed simultaneous traditional thalamic electrophysiology and widefield cortical voltage imaging to determine the effect of various thalamic states on thalamocortical sensory processing. We measured cortical spatiotemporal activity with widefield imaging of the genetically expressed voltage indicator (GEVI), ArcLight, at a high temporal resolution of 200Hz (see Methods, Chapter 2&3). Based on our previously published methods (see Methods, Chapter 2; Borden et al, 2017), ArcLight provides a measurement of cortical voltage activity across time (sampled at 200 Hz) across millimeters of cortical space.

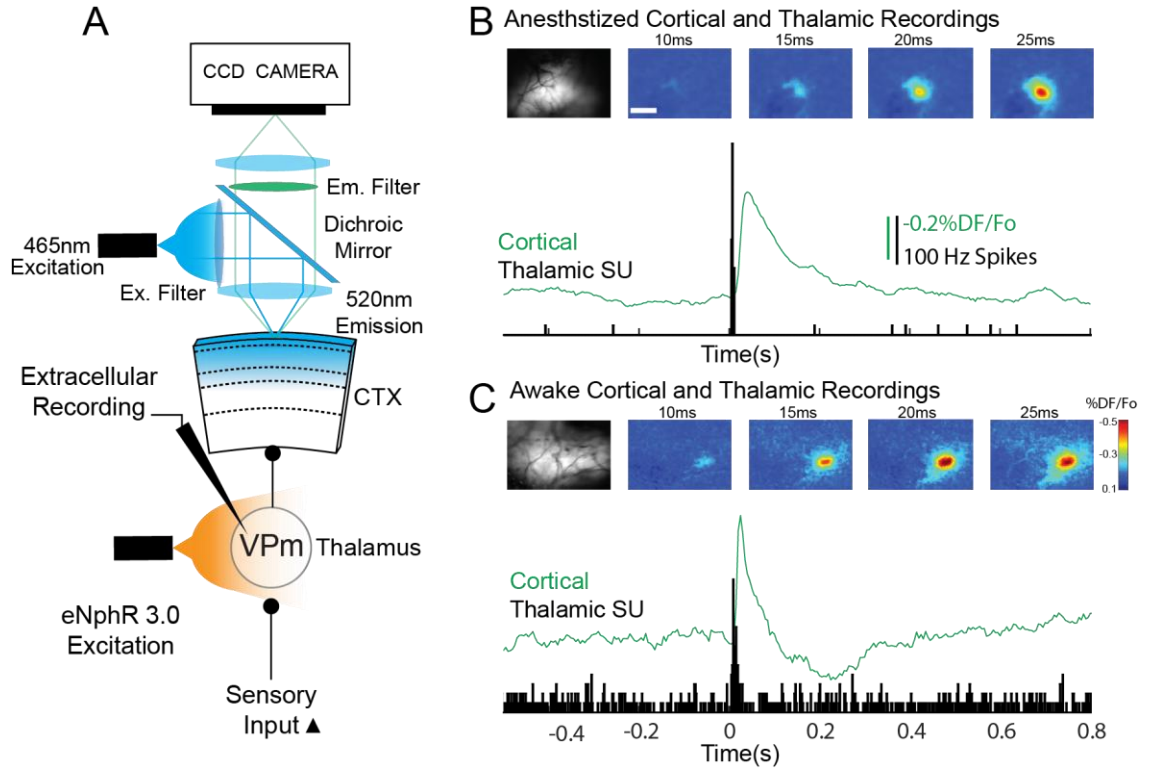


Figure 4.1. Experimental Setup for Simultaneous Thalamic and Cortical recordings in the Anesthetized and Awake Brain.

A. Experimental Setup for Cortical Widefield Imaging of the voltage indicator ArcLight. Paired thalamic recordings were conducted using extracellular electrodes in the thalamus, attached to an optic fiber (200 μ m). The thalamus was manipulated using light through the optic fiber (590nm) in order to activate Halorhodopsin (a light sensitive chloride pump) in the thalamus (see Methods for details). **B. Top.** Anesthetized Cortical ArcLight spatial response to a whisker stimulus (at Time=0). **B. Bottom.** Timeseries of thalamic and cortical responses to a whisker stimulus. Mean cortical fluorescence response (51 trials, green) selected from a 200 μ m x 200 μ m region of interest at the center of the spatial response (B. Top). Mean Thalamic PSTH (51 trials, black) for a thalamic single unit captured simultaneously with the cortical response. **C.** Same as B, except the animal is awake and headfixed during recording and whisker stimulation.

We investigated the impact of thalamic manipulation on sensory processing in the mouse whisker system in both the anesthetized (isoflurane) and awake conditions (see Methods for details). Under both awake (Figure 4.1B) and anesthetized conditions (Figure 4.1C), we observed robust sensory evoked response in the primary thalamic and somatosensory cortical regions. In the awake condition, the mouse was headfixed with no behavioral task, and given periodic rewards while measuring whisker movements (see Methods 4.2.3). In particular, the awake and anesthetized thalamus responded to a punctate whisker deflection with a short latency of similar magnitude under both conditions (Anesthetized Evoked Rate 1.25 ± 0.61 Spikes per trial, $n=41$ single units, Awake Evoked Rate 1.23 ± 0.64 Spikes per trial, $n=5$ single units, Mean \pm SD, and overall duration (between 4-30 ms). However, we observed a striking difference between the anesthetized and awake thalamic spontaneous firing rate (Mean Anesthetized Firing Rate 0.15 ± 0.36 Hz, $n=41$ and Mean Awake Firing Rate 5.6 ± 2.7 Hz, $n=5$ single units).

Similarly, in the cortex, we found that both conditions (awake and anesthetized) produced a strong stimulus evoked response, with a similar reported change in fluorescence (Awake Peak Response -0.28 ± 0.15 % $\Delta F/F_0$, $n=9$, Anesthetized Peak Response -0.19 ± 0.16 % $\Delta F/F_0$, $n=12$, $p=0.28$, unpaired t-test). Additionally, the widefield ArcLight signal began locally at approximately 10 ms post stimulus and rapidly spread across the cortex. Due to the typical fluorescence measurement utilizing a percent difference (% $\Delta F/F_0$), changes in ongoing activity are difficult to measure; however, published studies have found a dramatic increase in spontaneous activity across the cortex in awake compared to anesthetized conditions^{237,249}.

4.3.2 Halorhodopsin Activation Transitions Awake Thalamus into a Bursting State in Awake Brain

We combined thalamic and cortical recording techniques with optogenetics to manipulate ongoing thalamic firing and to shift the thalamus into different spiking regimes in the awake (Figure 4.2-6) and anesthetized brain (Figure 4.4,4.5). While in Chapter 3 we conducted similar experiments in the anesthetized mouse, we will focus initially on the observed effects of thalamic manipulations in the awake animal but follow with the anesthetized results for comparison (as shown in Chapter 3).

Specifically, we expressed halorhodopsin, a light sensitive chloride pump, through a viral vector (AAV5-CamIIRKinase-eNrph3.0, see methods, Chapter3, Figure 3.1A), into the mouse sensory thalamus to apply a modulatory input on the underlying thalamic polarization. After at least 4 weeks of expression, we trained animals to tolerate head fixation for prolonged periods. After training, a small craniotomy was placed over the thalamic region of interest. Instead of using halorhodopsin to silence neural activity, we sought to provide changes to ongoing thalamic polarization while providing a simple sensory input to the mouse whisker. We delivered varying levels of LED light power into the thalamus using a (1-200 μ m) fiber optic cable attached to a tungsten electrode to modulate and record the ongoing thalamic activity. We recorded the effects of the different levels of the halorhodopsin activation on single (Figure 4.2A-C,) and multiunit (Figures 4.2D-E) populations in the sensory thalamus.

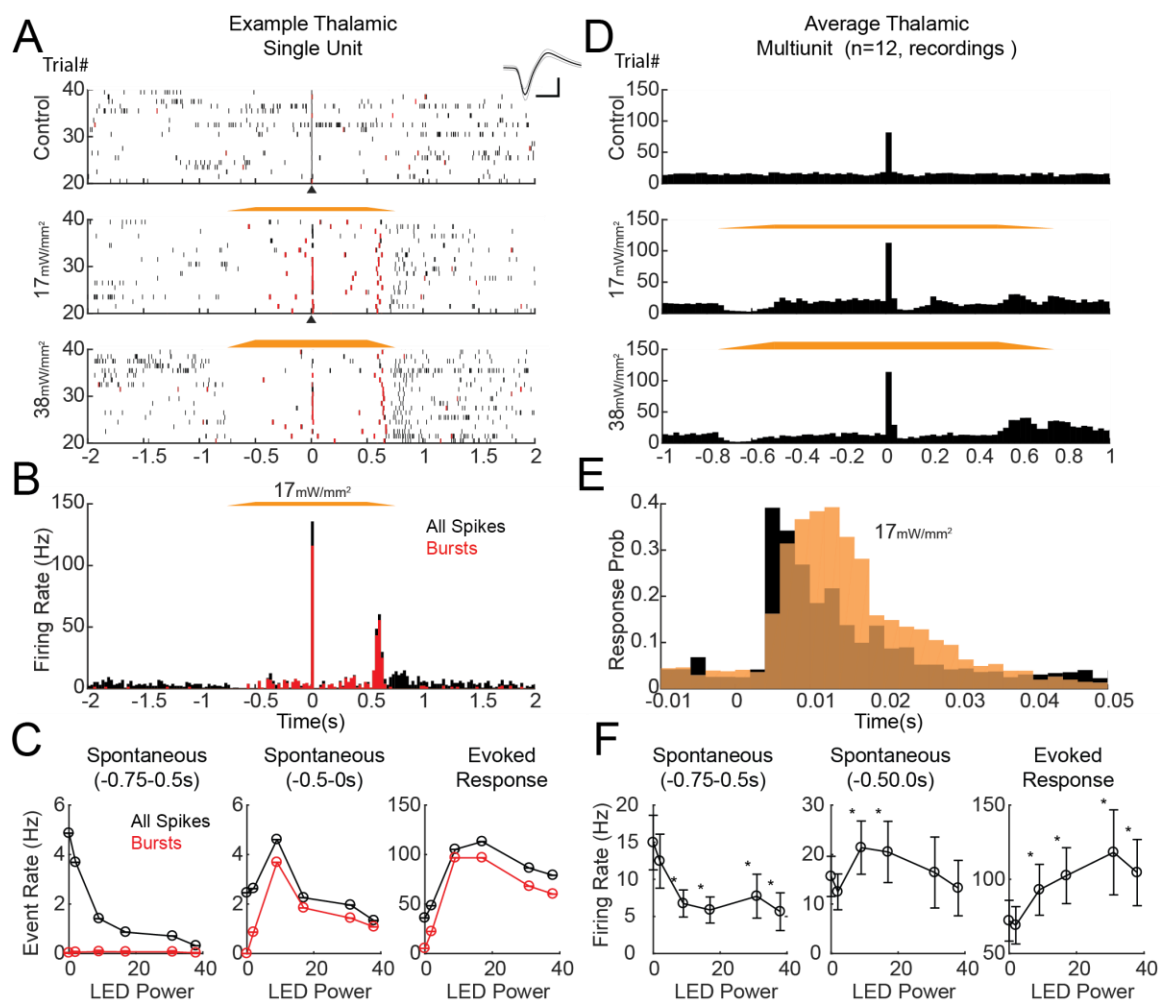


Figure 4.2. Halorhodopsin Excitation Transitions Awake Thalamus into a Burst State.

A-C. Example thalamic single unit stimulus response under various levels of optogenetic light intensity. **A.** Single trial raster of thalamic neuron under three different light conditions (Control, 17mW/mm², and 38mW/mm²). Halorhodopsin excitation induces a period of silence during optogenetics onset that reduces ongoing firing rate. After 100-250ms, thalamic neuron increases baseline firing rate (black ticks) with elevated levels of thalamic bursting (red ticks). **A. inset.** Average thalamic unit waveform and standard deviation. **B.** Poststimulus time histogram (PSTH) across same unit in A. **C.** Average response for all spikes (black), and bursting spikes (red) during the onset (-0.75 to -0.5s), pre-stimulus (-0.5 to 0s), and response (0 to 0.03s), periods for the example neuron. During halorhodopsin excitation there is a marked increase in ongoing thalamic bursting and an increased thalamic response to sensory stimuli. **D-F.** Multiunit response properties in awake thalamus under the optogenetic conditions (A). **A.** Average PSTH across all recordings (n=12, 3 mice). **E.** Thalamic response PSTH under control (black) and optogenetic (Amber) conditions. Halorhodopsin excitation (17mW/mm²) increases the thalamic MU response, with a marked increase in thalamic latency. **F.** Average response for all multiunit recordings (n=12 recordings) spikes (black), and bursting spikes (red) during the onset (-0.75 to -0.5s), pre-stimulus(-0.5 to 0s), and response (0 to 0.03s), periods for the example neuron. Halorhodopsin excitation causes a significant decrease in spontaneous activity within 250ms of light onset, and a significant increase in evoked response across most light intensities. Paired t-test.*p<0.05, n=12 recordings. All errorbars represent mean and standard error.

In the awake thalamus, we found that short periods (1 s continuous LED excitation with 0.25 s ramp on and off) of halorhodopsin activation resulted in dynamic changes in ongoing thalamic activity with a marked transition from tonic to burst firing (Figure 4.2A top-bottom, example thalamic single unit). In all cases we delivered a strong whisker stimulus (1200 Deg/s Sawtooth, at 0.750 ms post LED onset). The observed increase in thalamic bursting (red ticks) appeared throughout the halorhodopsin activation period, with a large increase of stimulus evoked bursts ($t=0$, shown in Figure 4.2A,B). With increasing levels of halorhodopsin activation (with increasing levels of LED power 1-38 mW/mm²), the thalamic response increased both thalamic spiking and bursting thalamic response compared to the control stimulus (no LED). At moderate levels of halorhodopsin activation we observed an almost 2-fold increase in thalamic response. We found similar trends across a larger dataset of collected multiunit data (Figure 4.2D-F). While we are unable to clearly separate tonic and burst firing in the multi-unit data, we did observe similar effects of the light on overall firing rates. Specifically, thalamic halorhodopsin activation increased the evoked thalamic response to simple stimuli, as well as modulated ongoing thalamic firing rate (Figure 4.2D,E), consistent with the engagement with T-type calcium channel dynamics.

Beyond changes in the stimulus evoked activity, we observed three distinct periods over the course of the halorhodopsin activation: 1. an initial period of silence lasting between 100-250 ms immediately following LED onset (Figure 4.2A & 4.2D at -0.75 to -0.5 s), 2. a period of increased spontaneous firing with an increase in thalamic bursts (Figure 2A & 2D at -0.5 to 0 s), 3. A post inhibitory rebound period lasting approximately 250-400 ms post halorhodopsin offset. Each of these phases are evident in both the single and average multiunit data (Figure 4.2A,B,D). The initial period of silence (Figure 4.2C) displayed a decreasing relationship with increasing levels of LED Power. During this phase,

halorhodopsin reduces the ongoing firing rates without altering firing patterns (i.e. bursting). Additionally, this period of silence lasted approximately 100-250 ms, which is the estimated time constant for the de-inactivation of T-type channels⁴⁴. After the period of silence (Figure 4.2A,B,D), there was an increase in bursting, and overall thalamic firing, which is counter-intuitive to the effects seen in other studies using halorhodopsin in other brain regions²⁶⁸. Thalamic neurons contain T-type calcium channels which are only de-inactivated during periods of hyperpolarization⁴¹. During the ramp down of the stimulus (at 0.5 s post stimulus), most cells displayed a robust increase in firing typical of a post inhibitory rebound of thalamic neurons. Taken together, these results demonstrate that thalamic halorhodopsin activation increased the stimulus evoked response, and had dynamic interactions with the ongoing thalamic spontaneous firing.

It is important to note that halorhodopsin is a chloride pump and therefore will hyperpolarize neurons during periods of activation²⁶⁹. While some studies have found prolonged periods of halorhodopsin activation can alter the reversal potential of chloride²⁷⁰ (ie. Chloride loading), the overall timescales used in this paper would suggest that this is not the primary driver for this observed effect (See Appendix A.3 Chloride Reversal Potential and Halorhodopsin). Instead, halorhodopsin is likely interacting with the T-type calcium currents which are only activated during periods of hyperpolarization. Additionally, work by Reinhold et. al. 2015 used an alternative mechanism to hyperpolarize thalamic activity through thalamic reticular nucleus (TRN) stimulation and observed an increase in thalamic firing and bursting after 100-250 ms of silence. Activation of the GABAergic TRN would have less impact on the chloride reversal potential, and therefore is secondary evidence of this observed phenomena (i.e. increase in thalamic bursts) under different stimulation techniques. However, without intracellular recording of

thalamic neurons during periods of hyperpolarization we can only assume the effects on thalamic membrane potential, reversal potentials, and resulting activity.

4.3.3 Thalamic Halorhodopsin Activation Decreases Cortical Evoked Response in Awake Mice

In a subset of experiments, we measured the effect of thalamic halorhodopsin activation on downstream cortical processing using widefield cortical imaging of the GEVI ArcLight in awake mice. Again, mice were injected with an additional viral construct for the GEVI ArcLight (AAV1-hsyn1-ArcLightD-WPRE-SV40, Methods) along with a halorhodopsin (see above section, Methods) and training for paired thalamic and cortical awake recordings.

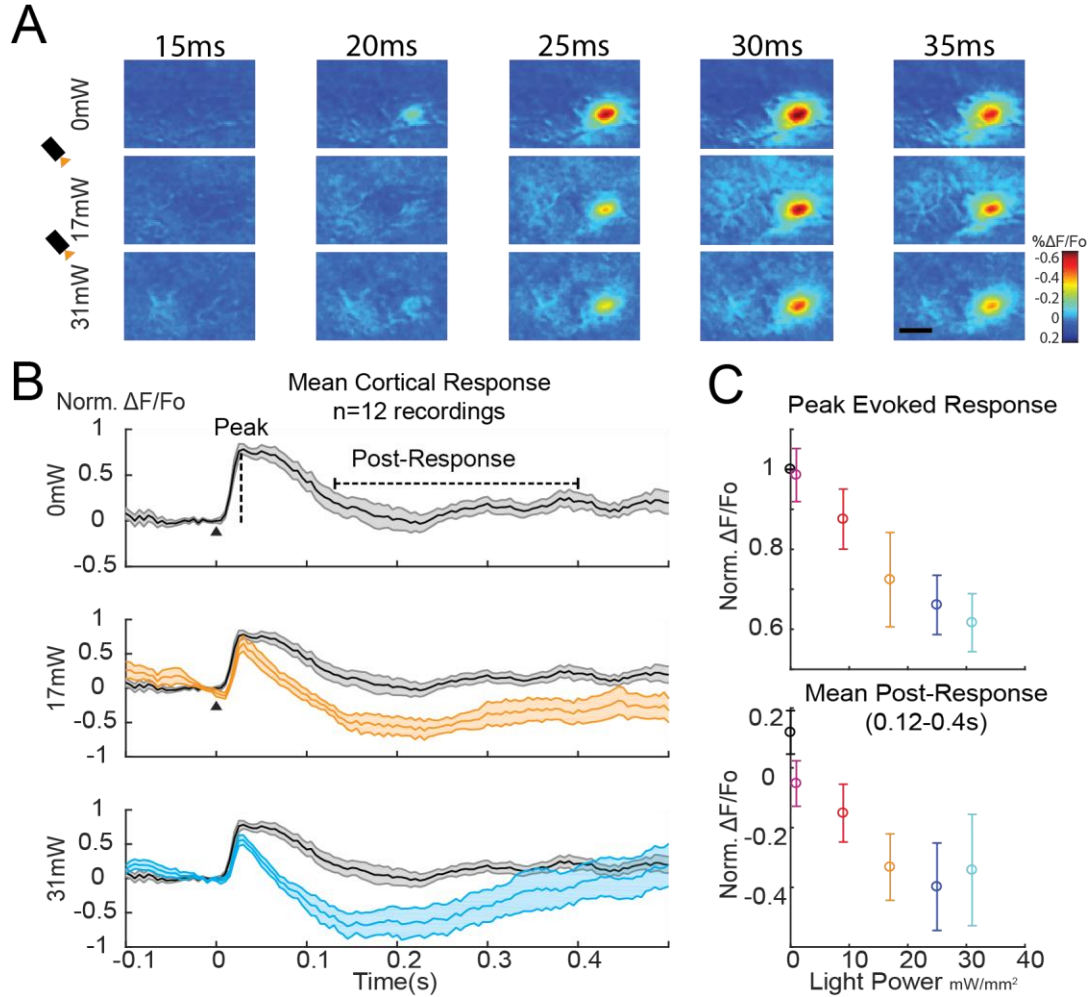


Figure 4.3 Awake S1 Barrel Cortical Evoked Response Decreases During Periods of Thalamic Halorhodopsin Activation

A. Cortical ArcLight fluorescence under various levels of thalamic halorhodopsin activation control, 17mW/mm², and 38mW/mm². Increasing levels of thalamic halorhodopsin activation decrease the evoked cortical response. **B.** Temporal fluorescence responses taken from the barrel region of interest (ROI) under the same optogenetic stimulation as A. Whisker stimulus (black triangle). B Top to Bottom. Increasing levels of thalamic hyperpolarization reduces the evoked cortical response. **C. Top.** Average peak response for each recording (between 0 and 110ms post stimulus) across increasing levels of thalamic halorhodopsin activation. Increasing levels of thalamic halorhodopsin activation decreases cortical peak evoked response (n=9-12 recordings). **C. Bottom.** Average Post-Response (0.12-0.4s) fluorescence under increasing levels of halorhodopsin activation after a whisker stimulus. All errorbars represent mean and standard error.

Using simultaneous recording with thalamic neurons, we found that thalamic halorhodopsin activation had dramatically different results in the primary somatosensory cortex in response to a stimulus. We found that while halorhodopsin increased the thalamic evoked response (Figure 4.2), the relative peak evoked cortical activity decreased with increasing levels of thalamic modulation compared to control conditions (Figure 4.3A-B). We measured the relative peak amplitude by measuring the peak evoked fluorescence between 0 and 110 ms post stimulus relative to the average fluorescence 25 ms preceding the stimulus onset ($t=0$). We used a relative peak measurement to account for changes in baseline fluorescence activity before onset of the stimulus. In order to account for slight differences of expression across animals and across cortical space, we normalized each response to the average control stimulus. At the maximum LED intensity tested (38 mW/mm^2), this resulted in an approximate 35% reduction in evoked peak response (Control Peak $-0.28 \pm 0.15 \text{ Norm } \% \Delta F/F_0$, 38 mW/mm^2 Peak $-0.18 \pm 0.13 \text{ Norm } \% \Delta F/F_0$, $p=4.08\text{e-}4$, paired t-test, $n=9$).

Additionally, we observed that along with a decrease in the evoked peak, there was an accompanying decrease in the post-response fluorescence between 120 ms to 400 ms after stimulus onset (Figure 4.3C). This decrease in fluorescence ($\Delta F/F_0$) likely represents a relative decrease in cortical activity following stimulus delivery and suggests a strong inhibitory response to the sensory feature. Given the feedforward nature of the thalamocortical pathway, and in the observed results in Chapter 3, it is not immediately obvious why an increase in thalamic evoked activity would cause a subsequent decrease in evoked cortical response. In order to investigate this effect further, we performed a subset of experiments under isoflurane anesthesia to determine if the observed phenomena were related to external, behavioral, or other high level processes.

4.3.4 Thalamic Halorhodopsin Activation Creates Opposite Cortical Effects in Awake and Anesthetized Mice

In order to control for external and internal sources of variability, we performed complementary experiments in the anesthetized mouse under isoflurane (see Methods, Chapter 3). The experimental preparation and protocol for both conditions was similar (see Methods); however, animals used for the anesthetized work were not trained for prolonged headfixation, and were simply anesthetized on the day of the procedure. Under both conditions thalamic halorhodopsin activation generally increased the sensory evoked thalamic response over the control (summary Figure 4.4D), with similar increases in thalamic evoked bursting (Figure 4.4A,B*Left* 4.4D). While thalamic halorhodopsin activation had similar effects on the evoked thalamic response in the anesthetized and awake mice, the net cortical outcome was quite different (Figure 4.4A,B*Right*, 4.4C). In the anesthetized mouse, the optogenetic manipulation monotonically increased the cortical response; whereas, in the awake brain the optogenetic manipulation monotonically decreased the cortical response. One prominent difference between these two conditions was the effect of the halorhodopsin activation on the pre-stimulus activity (Figures 4.4E,F). Under isoflurane anesthesia, we found that spontaneous thalamic activity was very suppressed relative to the awake animal (Figure 4E). While under both conditions the thalamic halorhodopsin activation transitioned the thalamus into bursting modes, the magnitude of increased burst firing was much greater in the awake condition. Compared to the anesthetized condition, awake halorhodopsin activation induced an approximate 2.5-fold difference in absolute spontaneous burst firing (Figure 4.4F). The difference between the magnitude of the awake and anesthetized ongoing burst firing may cause more nuanced activations of the cortical inhibitory and excitatory networks which could explain the

observed cortical trends (see Discussion). In particular, one theory for the observed differential effects is due to high levels of spontaneous bursting induced in the awake mouse. Specifically, prolonged increased thalamic bursting may dictate the activation of specific inhibitory cortical subtypes, i.e. Somatostatin positive interneurons, and circuits which could increase in network inhibition.

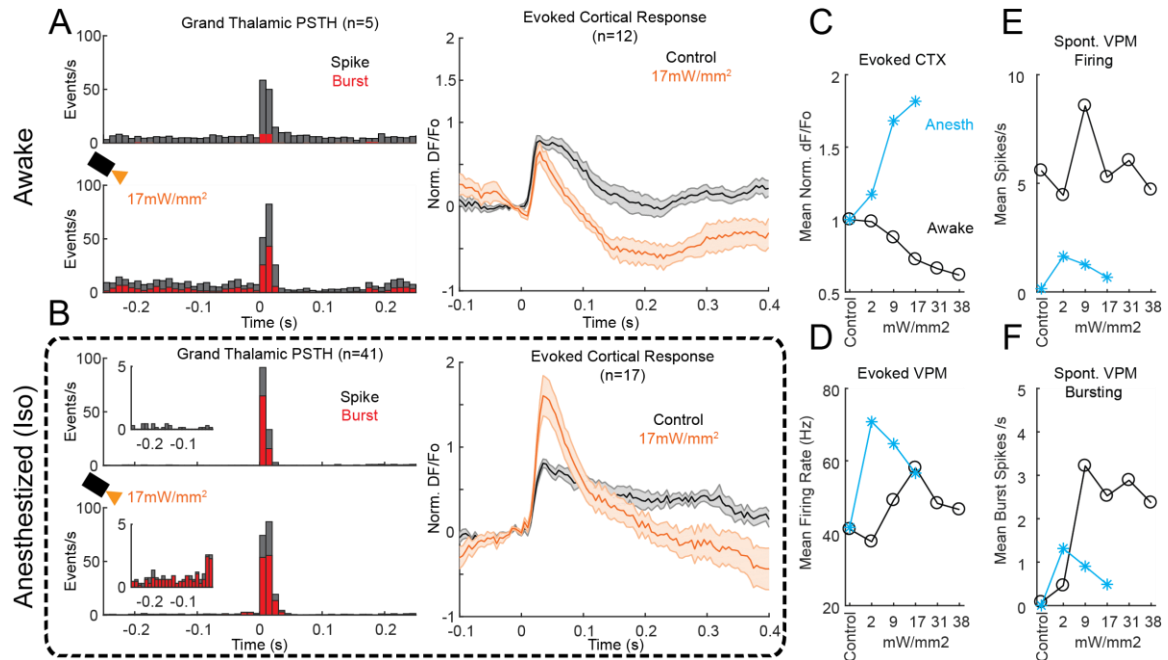


Figure 4.4. Thalamic and Cortical Sensory Processing with Halorhodopsin Activation in Awake and Anesthetized Brain.

A. Awake Thalamic and Cortical Response to halorhodopsin excitation. A. Left. Average thalamic single unit PSTH (n=5) response. All spikes (Black). Burst Spikes (Red). Under halorhodopsin excitation there is an increase in baseline and stimulus evoked bursting (red).

A. Right. Average Cortical Response (n=12) under control (black) and optogenetic conditions (amber). Awake stimulus was embedded in 1.5s of LED activation with 250ms of ramping on and off.

B. Anesthetized (isoflurane) Thalamic and Cortical Response to halorhodopsin excitation. B. Left. Average thalamic single unit PSTH (n=41 units) under control (top) and optogenetic stimulation (bottom) in response to whisker deflection (t=0).

B. Left. Inset. Baseline firing under both conditions. Note, under anesthesia stimulus was embedded in 1s of LED activation with no ramping on or off.

B. Right. Average anesthetized cortical response (n=12) under control (black) and optogenetic conditions (amber).

C. Mean evoked cortical responses for various LED intensities under both conditions awake (O-Black, n=9-12) and anesthetized (*- Blue, n=12). Optogenetic stimulation has opposite effects in awake and anesthetized conditions.

D. Mean evoked thalamic response to sensory stimulus for anesthetized (n=13-41 single units) and awake (n=5 single units) conditions. In both conditions optogenetic stimulation elevated thalamic evoked responses relative to control responses.

E. Spontaneous thalamic firing preceding stimulus (250ms).

F. Pre-stimulus spontaneous bursting in same period as E.

4.3.5 Thalamic Halorhodopsin Activation Reduces Evoked Area in Awake Animal

We utilized the ArcLight GEVI to not only measure voltage changes over time, but also across cortical space. Given the dichotomous relationship of the stimulus evoked peak response between anesthetized and awake mice, we considered the effect of the spatial activation under both conditions (Figure 4.5A). We measured spatial activation using two different metrics, spatial area over a raw threshold and the normalized area greater set percentage (see Methods). For the raw data, we used a previously established (Borden et al, 2017; Gollnick et al, 2016) threshold of 70% activation of the control stimulus condition. While these metrics seem similar, they highlight two different aspects of the spatial signal. The raw evoked threshold gives an estimate of area activated above a particular strength (i.e., the area and amplitude are correlated). Whereas the normalized area gives an estimate of the area activated regardless of amplitude and is an estimate of the sharpening and broadening of spatial activation.

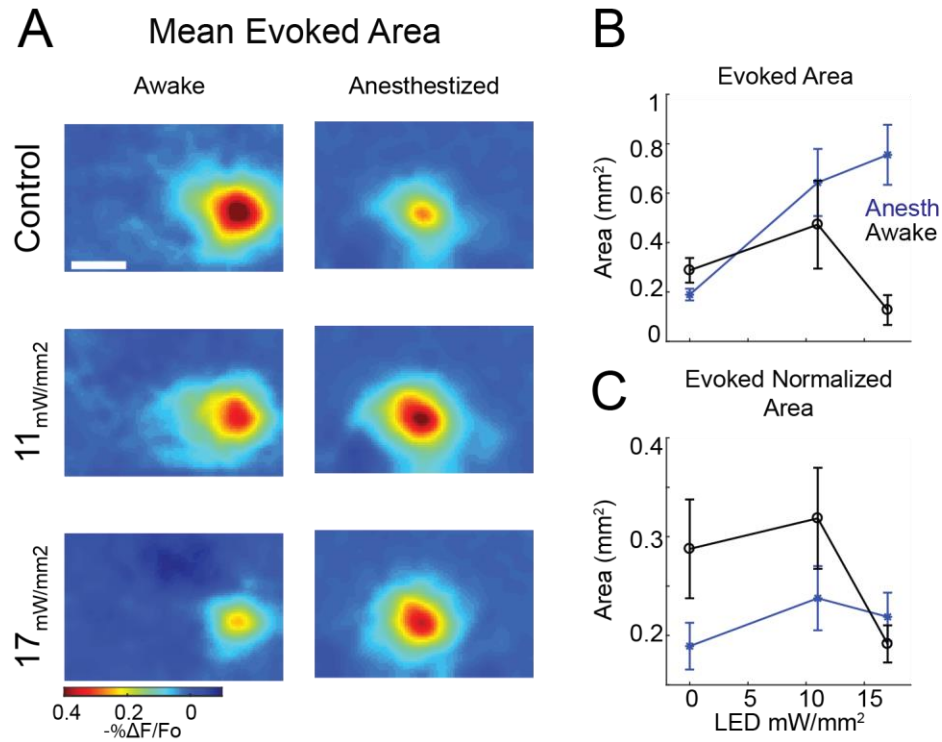


Figure 4.5. Cortical Spatial Response Across Awake and Anesthetized States.

A Mean cortical spatial response 25-35ms post stimulus to increasing levels of optogenetic stimulation (51 trials). Bar 1mm. **B.** Raw evoked area over 70% of the control stimulus threshold for the same period as **A**, across awake (o-black, n=9-12) and anesthetized (*-blue, n=5) recordings **C.** Normalized evoked area response for the same period as **A** across all recordings for anesthetized (n=5). Normalized area adjusts the peak amplitude for each stimulus. All errorbars represent mean and standard error.

We found that the raw spatial activation shared similar trends with the peak evoked response, with opposing effects in the anesthetized and awake conditions. Under awake conditions the evoked area generally decreased with increasing levels of thalamic halorhodopsin activation; whereas in the anesthetized case, the evoked area had a monotonically increasing relationship. For example, at moderate intensity (17 mW/mm²) and under anesthesia, thalamic halorhodopsin increased the activated cortical area by a factor of 5, where the same intensity halved the spatial activation relative to control in the awake animal (Figure 4.5B). When accounting for the changes in evoked amplitude, we found that under anesthesia the normalized area remained the same and decreased in the awake mouse (Figure 4.5C). Previous work has estimated that the normalized area is a metric of the width of the spatial response curve^{166,271}, where a decrease in normalized area represents a sharpening of sensory activation. Taken together, with increasing levels of thalamic halorhodopsin, the awake evoked response is more spatially contained than the anesthetized animal suggesting an increase in network inhibition.

4.3.6 Internally Driven Whisking and Non-Whisking States Determine Extent of Optogenetic Manipulation

In the awake mouse there are a variety of internal states and external factors which may shape the perception, cortical activity, and evoked stimulus response. One such internal state is the movement of the sensory organ during active sensation processes which has shown to have dramatic effects on both thalamic and cortical networks across sensory modalities. In this work, we measured the thalamocortical transformation in the whisker system as a model system of sensory processing. Mice and other rodents are known to utilize their whiskers for a variety of tasks, including exploration of the surrounding world⁹. As such, mice will often whisk or provide rhythmic protrusion and extrusion of the

whiskers during states of active attention²⁷², and exploration²⁷³. Whisking has been found to produce dynamic changes to ongoing thalamic and cortical networks¹⁰⁸, and therefore represents an additional variable to be considered during optogenetic manipulation.

We measured whisking activity using simultaneous video capture (20-50 Hz) of the whiskers during recording sessions. We captured the movement of whiskers by measuring the change in luminance intensity in a small region of interest in the mouse whisker pad. When the mouse moved their whiskers, a large change in luminance was detected (Figure 4.6A). Using a custom algorithm (see Methods) we classified trials into whisking and non-whisking based on a threshold of change in intensity and duration.

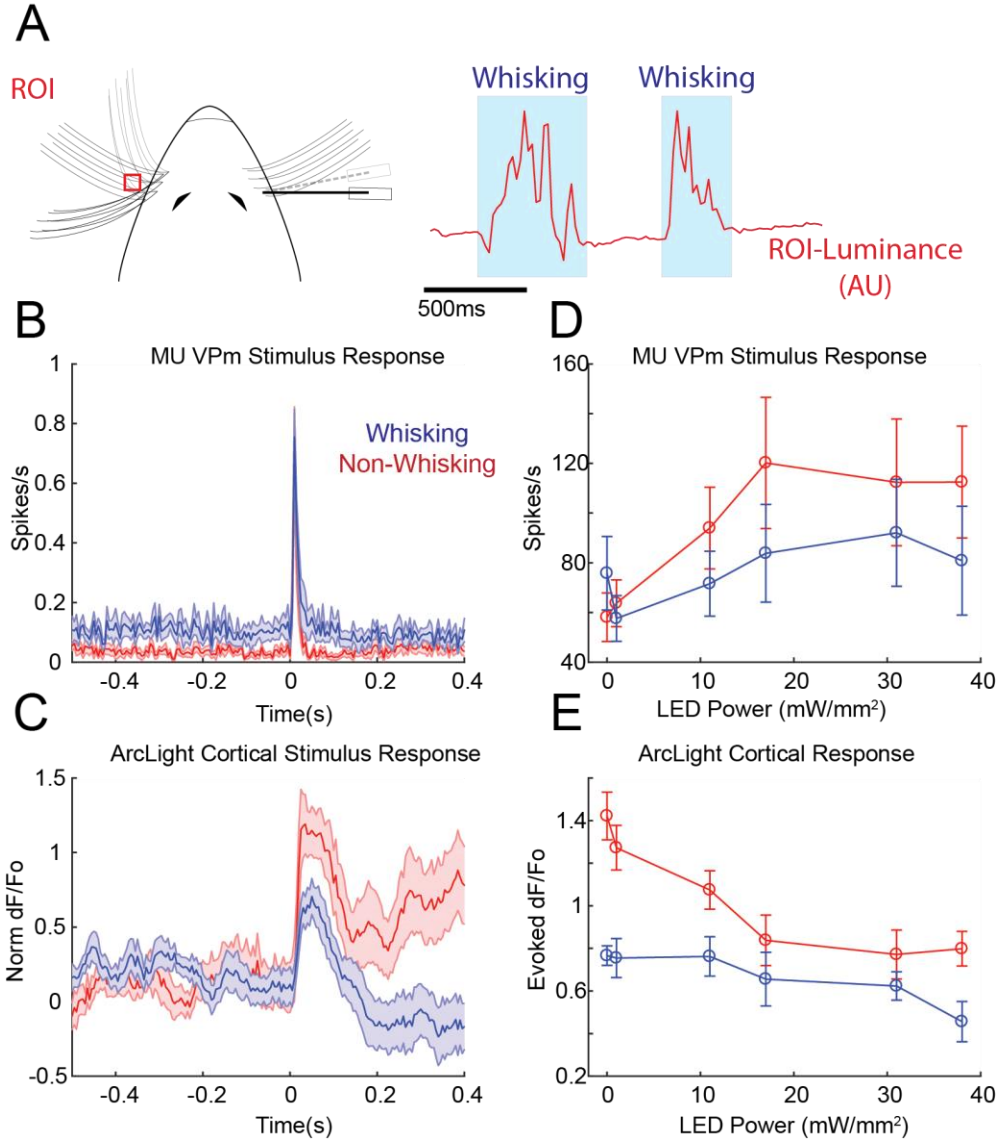


Figure 4.6. Whisking States Alter the Magnitude of Thalamic Optogenetic Stimulation.

A. Diagram depicting algorithm for detecting whisking and non whisking states using a region of interest (ROI) in the whisker pad as a measure of movement (see Methods). **B.** Mean thalamic multiunit stimulus evoked response sorted based on whisking (blue) and non-whisking (red) trials (n=11 recordings) for control (non-optogenetic) condition. **C.** Mean cortical evoked responses (n=12 mice) for the same trials whisking and non-whisking trials in B. **D.** Mean Evoked multiunit response across various levels of optogenetic stimulation for whisking and non-whisking trials (n=11, recordings). **E.** Evoked cortical response across same trials as D (n=9-12). Errorbars represent mean \pm standard error.

We found that in thalamus and cortex, whisking states had a dramatic effect on the thalamic (Figure 4.6B) pre-stimulus firing and the corresponding evoked cortical response (Figure 4.6C). We observed that the mouse whisked on average 25 % of the time throughout the recording session. In the thalamus, we found that during trials with pre-stimulus whisking there was a general increase in spontaneous firing rate (Mean Pre-stimulus (250-0 ms) Whisking 37.0 \pm 9.1 Hz, Non-whisking 14.22 \pm 3.5 Hz (SEM), Multiunit firing rate $p=0.011$, paired t-test), with trending on a significant change in evoked response (Mean Pre-stimulus (250-0 ms) Whisking 75.8 \pm 14.8 Hz, Non-whisking 58.22 \pm 9.7 Hz (SEM), Multiunit firing rate $p=0.0533$, paired t-test). In the cortex, we found that increased levels of thalamic firing did not alter spontaneous $\Delta F/F_0$ measurements but produced a weaker sensory evoked cortical response. These results correspond well with previous studies using voltage sensitive dye imaging in the awake mouse (Ferezou et al 2006) and thalamic extracellular recordings²⁴⁶.

During optogenetic manipulation, we found differences in the evoked thalamic and cortical responses in the whisking and non-whisking states. In non-whisking trials, halorhodopsin significantly increased the thalamic evoked response almost 3-fold (Figure 4.6D), whereas in the whisking case thalamic evoked responses only trended on increasing. In the cortex, we also observed differences between whisking and non-whisking trials under optogenetic activation. While at the highest intensity (38 mW/mm²) optogenetic thalamic stimulation decreased both whisking and non-whisking trial peak cortical responses, non-whisking cortical trials appeared to be more sensitive to optogenetic stimulation (Figure 4.6E). Whisking trials would determine the resting polarization and amount of baseline activity during optogenetic trials, and therefore may determine the impact of slight changes in thalamic polarization. Additionally, whisking has been shown to involve the entire thalamocortical network and extend beyond primary sensory cortices and therefore

represents large scale changes across the brain. These changes may go beyond simple differences in thalamic polarization and may represent changes in the entire circuits function. It is important to note that mice appeared to whisk equally during control and LED intensities (Control 24.8 +/- 7.1% vs 38 mW/mm² 26.2 +/- 8.8% whisking), and therefore this analysis is not due to changes in overall trial counts. Taken together, these results suggest that the internal driven states play an integral role in how changes in polarization (i.e. halorhodopsin optogenetic stimulation) shape cortical evoked signals.

4.4 Discussion:

In this work, we investigated the impact of different thalamic states on the transformation of sensory information in the thalamocortical circuit in the awake and anesthetized mouse. We utilized a combination of extracellular recordings with GEVI imaging to measure the effects of optogenetic induced thalamic states on thalamic and cortical processing of sensory information. In the cortex, we measured the spatiotemporal activity with widefield imaging of the genetically expressed voltage sensor ArcLight. To our knowledge, this work is the first to directly compare the impact of induced thalamic states on sensory spatiotemporal representations across thalamocortical structures in the awake brain.

Here, we used the chloride pump halorhodopsin to determine how different polarized states alter thalamocortical sensory processing. We found that thalamic neurons produced dynamic effects to an imposed hyperpolarized state that altered both spontaneous and sensory evoked responses. In particular, we found that hyperpolarization transitioned the awake and anesthetized mouse thalamus from a tonic to more bursting firing modes (Figure 4.2,4.4). Thalamic neurons have particular T-type calcium channels that become de-inactivated during periods of hyperpolarization, and produce large volleys of action potentials with short inter-spike-intervals (2-4ms)²⁵⁰. Interestingly, we found that our

induced thalamic hyperpolarization contained two distinct phases: a period of silence, and a period of increased thalamic firing and bursting. In particular, we found that immediately following optogenetic onset (0-250ms) there was a monotonically decreasing relationship between the level of LED intensity (Figure 4.2C,4.2E) and the ongoing firing rate of thalamic neurons. Thalamic T-type calcium channels require prolonged periods (around 100ms) of silence before becoming fully de-inactivated which aligns with this initial period of silence⁴⁴. While not directly investigated in this work, these results suggest that the timescale and duration of hyperpolarizing inputs may have dynamic implications for sensory processing.

Thalamic bursting and thalamic burst modes have often been reported as playing conflicting roles in stimulus processing and in overall alertness⁴⁹. Prolonged thalamic bursts modes are most often associated with Slow-Wave-Sleep (SWS)²⁴⁶ and drowsiness²⁵⁹, and are more selectively prevalent than in the anesthetized or awake brain^{237,238,259}. Furthermore, during known periods of awake bursting in the visual pathway, cortical neurons have shown a decrease in sensory responses^{46,237}. However, bursting has also been identified in awake thalamocortical processing^{48,258,274}, and has even been measured in behavioral tasks. Stimulus evoked thalamic bursting has been observed to increase the transformation of sensory information from thalamus to cortex, and has been argued to be critical to drive downstream cortical neurons^{47,56}. A single thalamocortical synapse is quite weak, and requires a synchronous volley of synaptic events to drive cortical responses⁵⁶. Often termed a “wake-up” call to the cortex⁴⁹, bursts have been proposed to send powerful signals downstream and even carry additional information through the multiplexing⁴² of sensory information.

One of the primary results of this work was observing opposing effects of induced thalamic hyperpolarized states in the anesthetized and awake brain on cortical sensory processing, while producing similar effects on the thalamic evoked response. Under periods of thalamic hyperpolarization, we observed an increase of approximately 50% in the stimulus evoked thalamic response, under both the awake and anesthetized conditions. In particular, under both conditions, there was an increase in the thalamic evoked bursting. While in the cortex, we found that induced thalamic hyperpolarization produced a monotonically decrease in awake cortical response (Figure 4.3) and a monotonically increasing cortical response in the anesthetized brain (Figure 4.4). We found that the spatial activation followed a similar trend. Under thalamic hyperpolarization evoked area increased 5-fold in the anesthetized animal and decreased by 50% in the awake animal (Figure 4.5). Given the presumed feedforward nature of the thalamocortical system, it is intriguing that enhancement of thalamic signals would not produce a similar enhancement in downstream cortical responses in the awake animal.

Due to the conflicting nature of the cortical results, we investigated the differences observed in the circuit under awake and anesthetized conditions. Given the observed similarity in the magnitude of the evoked thalamic response under both anesthetized and awake conditions, we assume the differences are not due to the evoked response magnitude. While there has been some evidence that thalamic hyperpolarization increases the jitter in the evoked response²³⁵, it is not immediately clear if this effect would drive differences in the anesthetized and awake brain. Furthermore, we considered whether the observed results could be related to known changes in thalamocortical processing during bouts of whisking (or active sensation)²⁷¹. While we found differences in the effect of the optogenetic induced states during whisking and non-whisking periods (Figure 4.6), these results related to the

overall magnitude of the decrease in cortical response, but the qualitative trend was the same.

During periods of induced thalamic hyperpolarization, we found that the ongoing thalamic firing rate and bursting rate increased differently under both anesthetized and awake conditions. While the relative thalamic bursting and activity increased in both anesthetized and awake conditions, the absolute levels of firing and bursting were different (Figure 4.4). In particular, the absolute spontaneous thalamic bursting rate was 2.5-fold higher in the awake animal. Therefore, increases in absolute pre-stimulus firing could alter the level of thalamocortical synaptic depression²⁷⁵ or alter the cortical excitatory and inhibitory network which would decrease the evoked cortical activity²⁴⁴.

Thalamic and cortical states are dynamically connected¹⁰⁸ and therefore slight modulations of thalamic firing may have profound effects on downstream cortical activity. Thalamic bursts have been shown to preferentially activate somatostatin (SOM) interneuron populations²⁴⁴ *in vitro*. Somatostatin interneurons have been found to have a wide range of inhibitory functions^{276–278}, including synchronizing larger inhibitory networks which may shift the network into a more inhibitory mode^{279–281}. We observed two additional results that are indicative of increased network inhibition. We found that as we increased the thalamic hyperpolarization we decreased the normalized spatial spread of the evoked response, which may be related to an increase in inhibitory activity²⁸². Additionally, during induced hyperpolarized states in the awake brain we found a large negative dip in the fluorescence immediately following evoked response, which would suggest a stronger inhibitory response post-stimulus. Furthermore, previous work has shown that inhibitory networks are more activated in the awake condition compared to the anesthetized condition^{64,283} which suggests that changes in cortical inhibitory networks may be masked

under anesthesia. Therefore, bursting states may alter the excitatory/inhibitory balance in the thalamocortical pathway, decreasing the evoked response in the awake compared to anesthetized brain. Future work is needed to determine the role the pre-stimulus bursting plays and the impact of different timescales of hyperpolarization on sensory representations across the thalamocortical network.

With this work there are several important considerations that may play a vital role in the interpretation of the data. One important consideration is the recorded widefield ArcLight fluorescence, which captures predominantly the dendritic information in the upper supragranular layers of the cortex^{170,223}, as well as somatic and axonal information. Therefore, the summed information is a combination of voltage activity across all neuronal subtypes (not just excitatory inputs). Additionally, due to the enhanced neural activity in the awake mouse, fluorescence normalization, and the nonlinear transformation between voltage and fluorescence output, the fluorescent activity may be saturated in the awake animal. Beyond the limitations of the ArcLight imaging, the optogenetic manipulations here were only localized using stereotaxic viral injections and limited light spread from the optic fiber (see Chapter 3). While we attempted to only record and manipulate from the ventral posterior medial thalamic region, our manipulations may have extended throughout thalamic nuclei. Future work is needed to determine how specific thalamic nuclei contribute to the thalamocortical transformations shown here.

Taken together, we found that induced hyperpolarized thalamic states differentially shape the evoked cortical response across anesthetized and awake brain states, and highlights the complexity of thalamic modulations of ongoing polarization. Thalamic evoked bursts, and hyperpolarized induced states, may have dynamic interactions with cortical networks that dramatically alter sensory evoked responses. We speculate that ongoing thalamic activity

may have specific implications for cortical inhibitory networks; however, future work should investigate other potential explanations such as synaptic depression. While this work highlights a single instance where awake burst modes decrease the evoked cortical response, this may not always be the case. During our recordings we presented a relatively long period of hyperpolarizing input (1.5s), which revealed different temporal dynamics in the thalamic spontaneous activity. Shorter or longer periods of thalamic hyperpolarization may have more dynamic effects on cortical sensory encoding that go beyond this work. While the interactions of ongoing thalamic states on the thalamic encoding of sensory information are now just being investigated, future work should consider how thalamocortical networks interact as a whole in various states to alter sensory representations.

CHAPTER V: CONCLUSIONS AND FUTURE DIRECTIONS

5.1 Overview of Thesis Results

In this thesis, we developed and utilized advanced techniques to measure how different thalamic states alter the transmission of sensory information in the thalamocortical pathway. In particular, the objective of this thesis was to determine how fluctuations in membrane potential, that continuously change the operating point of thalamic neurons, alter the encoding of sensory information across spatial and temporal scales in the cortex. Until recently, due to the limitations of traditional methods, measuring large scale voltage cortical activity would have been confined to anesthetized experiments (voltage sensitive dyes), or restricted in spatial resolution (intracellular recording). Furthermore, manipulations to thalamic activity would have been limited to gross activation of largescale neural networks with electrical stimulation. However, with the advent of genetically expressed voltage indicators (GEVIs) and optogenetics, as well as the methodologies developed in this thesis (Chapter 2), we were able to conduct novel experiments to uncover the impact of thalamic states in the anesthetized (Chapter 3) and awake thalamocortical circuit (Chapter 4). Below we investigate these results in more detail and speculate on the impact of this research while presenting a roadmap for the future.

5.2 GEVIs as a Tool for Measuring Spatiotemporal Cortical Information

In Chapter 2 we found that the GEVIs have wide applications for the measurement of spatiotemporal cortical activity, with stable and long-term recordings of voltage responses in the primary somatosensory mouse cortex. Specifically, we found that the GEVI ArcLight produced a robust sensory evoked fluorescence response to punctate whisker stimuli, and demonstrated low amounts of photobleaching within an imaging session or across 28 days of recording. While we found that ArcLight as a whole was able to capture the spatiotemporal responses across the cortex, we found that the overlap with the

hemodynamic signal and the low overall signal-to-noise ratio to be a serious limitation in its use as an indicator. While our investigation only included a detailed examination of the GEVI ArcLight, these observations seem to span across the current state of GEVIs as a whole. Through this next section, we will investigate the overall functionality of ArcLight, and speculate on the future for GEVI imaging.

5.2.1 Widefield GEVI Imaging: Long-term Potential for Measuring Cortical Dynamics

Here, we were the one of the first to use GEVIs for imaging mouse cortical activity *in vivo*. Across Chapters 2-4 we utilized the GEVI ArcLight to measure spatiotemporal responses across the cortex in the anesthetized (Chapter 1,3) and awake (Chapter 1,4) mouse. ArcLight was originally developed as a modified green fluorescent protein (GFP) by Vincent Peribone in 2012¹⁶². At the start of this project, ArcLight represented a novel breakthrough with GEVIs, with relatively high signal-to-noise ratios and moderate temporal dynamics (~10-40Hz temporal resolution). Quickly after, ArcLight was adapted for imaging of neural activity throughout the drosophila^{146,149}; however, ArcLight had not been used for measuring *in vivo* cortical responses in the rodent model. For this work, we sought a GEVI that would rival the signal-to-noise and temporal resolution of traditional voltage sensitive dyes. Furthermore, we needed a voltage probe that could be combined for optogenetics with manipulation of the thalamocortical pathway. The confined excitation-emission spectrum of ArcLight, enabled us to combine the imaging with a hyperpolarizing opsin, most of which are red-shifted. Taken together, ArcLight represented an ideal voltage sensor for the measurement of cortical voltage signals, while also allowing our future work with optogenetic manipulation of the thalamocortical network.

In this work (Chapters 2-4) the GEVI ArcLight was determined to be a powerful tool for the investigation of spatiotemporal responses and enabled novel insights into the

encoding of sensory information. On average, we found that the ArcLight probe had a similar fluorescence response to sensory inputs compared to other published GEVIs (in particular FRET based Butterfly 1.2) and traditional voltage sensitive dyes (i.e. RH1691), thus making ArcLight on par with comparable technologies for the time. Furthermore, ArcLight produced a highly stable response that enabled repeated imaging over many days and weeks, which is beyond the capabilities of voltage sensitive dyes. ArcLight demonstrated evoked averaged responses which were highly correlated with simultaneous average Local Field Potential (LFP) recordings. However, on a single trial ArcLight was not well correlated with the ongoing local field potential, and had only moderate correlation with the peak response evoked responses. This suggests that while the ArcLight captures some of the basic elements of sensory evoked responses that other approaches measure (i.e. electrical recordings), ArcLight may also provide some other aspects of the electrophysiological response that go beyond these techniques.

Additionally, we found that on a single trial, the evoked responses contained high spectral overlap with the hemodynamics in the brain. This is likely due to the blue-green excitation-emission wavelengths which are shared with hemoglobin. Using paired pulse-oximeter recordings, we found that the ongoing blood flow showed high correlations with the ongoing fluorescence activity, suggesting large artifacts due to blood flow. On a single trial, the hemodynamic response produced a signal 5-fold greater than the evoked neural activity. While we generated several methods to reduce the influence of the hemodynamic signal, these methods were unable to completely remove the hemodynamic artifacts from every trial.

Throughout this work, we used several different methods to try to remove the hemodynamics response, including off-ROI subtraction (Chapter 2), Background PCA subtraction (Chapter 3), and dual camera fluorescence imaging (Chapter 4). The off-ROI and Background PCA methods (Chapter 2-3) all hinged on the shared global nature of the

hemodynamic signal to create models of the blood flow for subtraction of the ongoing signal. However, both the off-ROI and Background PCA methods are less ideal, with the added risk of adding noise to the recording.

In Chapter 4, we introduced the final method to reduce the hemodynamic artifact attempted in this thesis, simultaneous dual camera imaging of a similar wavelength to capture hemodynamic trends without neural components. Specifically, we excited the cortex with a broad blue excitation LED light source and captured a narrow band of blue light that was reflected or fluoresced from the cortical surface. This narrow band of blue light (475-495nm) is before the emission of ArcLight spectrum and therefore, could be used as a measure of hemodynamic activity without containing the neural activity. While this method was successful, we were forced to use a different camera which decreased the overall efficacy of the system to capture the same hemodynamic responses. As with all subtractive techniques, the correction methods can dramatically influence the final processed result. In particular, it is the responsibility of the researcher to ensure proper fitting of the models and setting criteria to prevent the subtraction of the underlying neural signal. Additionally, these models for predicting the hemodynamic response were not perfect, and often still required averaging over several trials to remove the hemodynamic influence. We found that overall, all three methods yielded the same general efficacy at removing hemodynamic artifacts from the captured ArcLight signal with only modest gains with each iteration.

In summary, this thesis highlights the promise of genetically expressed voltage indicators as a tool for measuring spatiotemporal responses across the cortex. While ArcLight represented the perfect GEVI for our intended task, there are major areas to improve the voltage sensor as a whole. Overall the limitation to clearly resolve single trial responses is ArcLight's greatest weakness as a voltage indicator. Future work should be conducted on optimizing better voltage probes that are far-red shifted or near infrared to

avoid the complications caused by hemodynamic interferences. While FRET based probes provide a method to reduce the hemodynamic noise, they often utilize the majority of the visual spectrum and limit the use of combined optogenetics techniques. With the advent of novel voltage indicators such as FlicR1²⁸⁴, we have observed the field is moving in this direction. Throughout this thesis, we have highlighted the importance of spatiotemporal voltage techniques for studying cortical structures.

5.3 Thalamic State Modulates Thalamocortical Function

In Chapters 3 and 4, we investigated how different thalamic states alter the transformation of sensory signals in the thalamus and cortex, using the methods developed in Chapter 1 to record spatiotemporal cortical information. Here, we utilized the same optogenetic tools to alter the thalamic baseline polarization in the thalamocortical system. The thalamus receives a tremendous amount of modulatory input that shapes the ongoing level of polarization, through continuous input of EPSPs and IPSPs (See Chapter 1.1.3). In both conditions (anesthetized in Chapter 3 and awake in Chapter 4) we found similar modulations in ongoing and evoked thalamic activity, with an increase in thalamic bursting. Thalamic neurons have distinct T-type calcium channels that de-inactivate during periods of hyperpolarization and cause bursts, or a barrage of two or more high frequency (300-400 Hz) action potentials. Due to the dramatic tonic and burst firing modes, and the ubiquitous presentation throughout the thalamus, thalamic bursts have interested neuroscientists for decades; however, their exact role remains uncertain. Currently, there are two competing roles of thalamic bursting and bursting states: 1) thalamic bursts increase the salience of sensory inputs with implications for sensory encoding, and 2) thalamic bursts are involved with dissociated thalamocortical networks sensory in sleep and drowsiness. Our results from the anesthetized recordings (Chapter 3) suggest that thalamic bursts are involved with increasing the detectability of sensory signals; however,

our results from the awake animals (Chapter 4) would suggest the opposite effect, with a net decrease in cortical responses. Therefore, we found evidence for both the theories of thalamic bursting and thalamic hyperpolarized states. In this section, we will explore the combined results from the anesthetized and awake brain (Chapter 3 and 4) in more detail and create a new generalized model for how thalamic bursts may be involved in both processes.

5.3.1 The Dichotomy of Thalamic Hyperpolarized States

In the anesthetized brain (Chapter 3) our main result was that periods of hyperpolarization enhanced the stimulus evoked thalamic and cortical spatiotemporal responses. In particular, evoked thalamic responses were increased by approximately 30%, with a 50% increase in evoked cortical response. This increase in evoked cortical activity led to an increased separation between the evoked amplitude and the background fluorescence thereby enhancing the detectability of the sensory information. Interestingly, our results showed that thalamic hyperpolarization enhanced the detectability, without a loss in discriminating stimulus features or a loss in discriminating across space. This stimulus evoked enhancement (with a hyperpolarized thalamic state) was correlated with an overall 150% increase in thalamic bursting (see Chapter 1.1.3). As we increased the overall level of thalamic hyperpolarization with increasing light intensities (mW/mm^2) and activated area (mm^2), we observed a monotonic increase in evoked cortical response in the anesthetized animal. These results corroborate several predictions of enhanced cortical activity during hyperpolarized states based on previous observations of thalamocortical activity^{47,49,258,285} and models of thalamic responses^{68,217}.

In the awake animal (Chapter 4) our main result determined that across recording sessions thalamic hyperpolarization caused a monotonic decrease in the cortical evoked response.

However, the evoked thalamic response increased both across thalamic single-unit and multi-unit recordings with increasing levels of thalamic hyperpolarization. While we only recorded from a small sample of thalamic single units ($n=5$), we found that thalamic evoked bursting was also increased during thalamic hyperpolarization. We found that along with an increase in thalamic evoked spiking and bursting, we induced a change in spontaneous activity with a dramatic increase in spontaneous bursting behavior. In the awake thalamus, under control conditions we found that burst rates were very low (0.08 Bursts/s), which is comparable to previous extracellular recordings of bursting in the thalamic sensory region²⁵⁹. During hyperpolarization, even modest light intensities induced a 15-fold increase in spontaneous bursting behavior compared to baseline. While we did not formally examine the relationship between the theoretical detectability of stimulus evoked responses in the awake hyperpolarized case, we expect that the detectability would either stay the same or decrease due to the reduced magnitude of the response. In the awake animal, there is a known increase in ongoing synaptic activity, which may decrease the effectiveness of the optogenetics. Therefore, to control for potential different net effects of halorhodopsin activation in the awake animal, we applied a wider range of light intensities, and still observed a monotonic decrease in evoked responses. The results from Chapter 4 contradict the enhanced cortical results seen in Chapter 3, and suggest that the awake thalamocortical system may be much more complicated than the anesthetized case.

Given these general results from Chapter 3 and 4, we are left with two central questions:

- 1) How could thalamic hyperpolarization increase thalamic evoked response and increase thalamic bursting and yet, cause a decrease in the evoked cortical response in the awake brain?*
- 2) How do thalamic hyperpolarized states produce fundamentally different results in the awake and anesthetized cortical responses?*

With these guiding questions we will explore possible explanations for these observed phenomena.

5.3.2 Speculation on the Interactions of Ongoing Activity on Evoked Signals

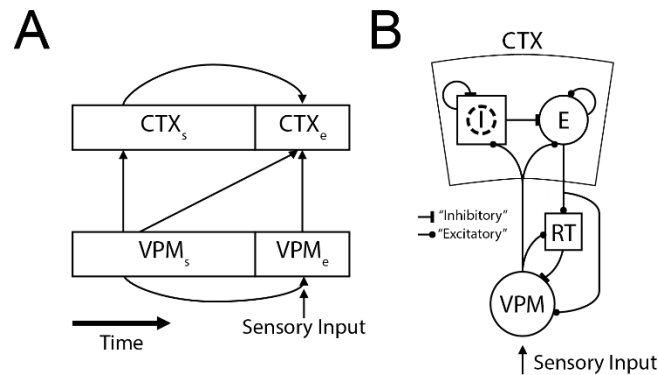


Figure 5.1. Theory on the Interaction of Thalamic State on Cortical Networks.

A. Here, we use a cartoon block model to speculate on the interactions of thalamic and cortical networks on the sensory evoked feature response in time. We predict that the spontaneous thalamic (VPMs) activity interacts with the spontaneous cortical activity (CTXs) to modulate both the evoked thalamic (VPM_e) and cortical (CTX_e) responses. **B.** Simplified diagram of the thalamocortical network. This model will be used as a basis for comparing theories of the interaction between thalamic and cortical activity.

If we assume that the thalamocortical circuit is a simple feedforward circuit (see Figure 5.1), then the evoked thalamic response should completely dictate the evoked cortical activity. And yet, in the awake brain, increased thalamic drive decreased the cortical response (Chapter 5). When examining the circuit dynamics under a controlled anesthetized setting (Chapter 4), we found that the thalamocortical response followed a feedforward relationship where increased thalamic input increased the downstream response. When comparing across both conditions, the awake and anesthetized brain showed similar levels of increased thalamic responses, and showed both a general increase

in thalamic bursting. Under both awake and anesthetized conditions, the observed thalamic evoked responses even increased to similar magnitudes (~60Hz). These results suggest that the awake thalamocortical circuit is highly dependent on the context of the ongoing thalamocortical dynamics that ultimately shape cortical responses. The thalamus is known to be part of a highly interconnected network (see Section 1.3, Figure 5.1 A,B) that is constantly modulating, and being modulated by, ongoing thalamic and cortical activity. Based on these observations, we expect that the differences between the anesthetized and awake brain are due to changes in the thalamocortical network. We have examined two possible theories to explain the differences in thalamocortical responses.

5.3.2.1 Awake Cortical Inhibition Controls Evoked Response (Theory #1)

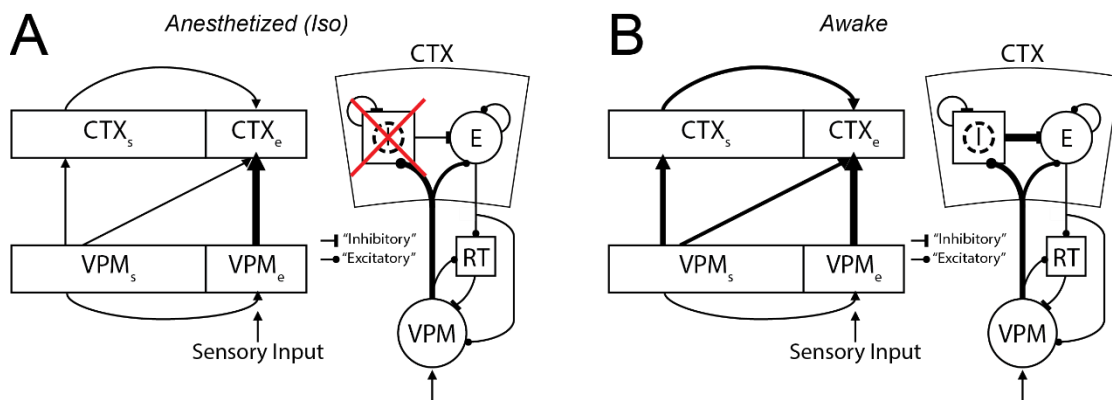


Figure 5.2.Theory#1 Thalamocortical Networks.

A . Under anesthesia, the thalamic response is enhanced during periods of hyperpolarization, and the inhibitory cortical circuit is not influenced by thalamic state due to overall levels of suppression and low spontaneous activity in the thalamus.

Increased thalamic drive (thick line from VPM_e) therefore results in an increase in the cortical response. Thick lines represent increased activity during states of halorhodopsin.

B. In the awake animal, the inhibitory cortical circuit interacts with thalamic state due to increased spontaneous activity (thick line from VPM_s) in the thalamus during periods of hyperpolarization. Increased stimulus thalamic evoked response does not correspond with an increase in cortex evoked activity due an increase in network inhibition (B. *Right*. thick line from I to E).

One possible explanation for the decrease in cortical evoked response with an increase in thalamic drive is an overall change in network inhibition in the awake animal (Figure 5.2). During hyperpolarization, we observed an increase in both spontaneous and evoked bursting. While under the anesthetized condition (Chapter 3) we observed an increase in spontaneous bursting, in the awake animal (Chapter 4) the amount of bursting was 2.5-fold higher in absolute magnitude. Given that the level of stimulus evoked activity was the same across both anesthetized and awake conditions, the discrepancy between conditions is more likely due to spontaneous firing rate and bursts. These results correspond to previous findings of reduced evoked cortical responses in the awake animals during periods of known thalamic bursting⁴⁶, suggesting that in the awake animal, bursting states may diminish evoked stimulus activity.

We observed two additional trends in the evoked cortical response which suggest changes in the cortical excitatory and inhibitory network including a decrease in fluorescence during the post response period, and a decrease in overall evoked spatial area. During periods of hyperpolarization of the thalamus, we found that after the stimulus was presented there was a consistent dip in the evoked cortical fluorescence compared to pre-stimulus activity that suggests an increase in the stimulus evoked inhibitory response. This post response decrease in fluorescence showed a monotonic relationship with the increased light levels and suggesting relationship between the level of thalamic hyperpolarization and the cortical inhibitory response to sensory features. Thalamic pre-stimulus activity could be priming the cortical inhibitory networks which cause an enhanced stimulus evoked inhibitory response. Additionally, we found that the average area activated by the stimulus was reduced compared to control conditions. The reduction in cortical area was even beyond the expected reduction in spatial spread due to a decreased evoked amplitude. Spatial area is likely a measure of the cortical inhibitory response to sensory information

and suggests an increase in the network inhibition. Together, these results suggest that during periods of hyperpolarization and increased thalamic bursting the cortical inhibitory network is increased.

Bursts themselves have been found to be very efficient at driving both excitatory and inhibitory^{47,56} downstream cortical responses. Furthermore, bursts compared to tonic spikes have been found to differentially activate somatostatin (SOM) positive interneurons, which require multiple action potentials to drive spiking activity²⁴⁴. SOM interneurons have a complex role in the cortex from general inhibition to synchronizing other major interneuron networks, and are only now beginning to be explored^{276,278,281}.

One potential reason the cortical response was representative of the feedforward thalamic inputs in the anesthetized condition was due to overall suppression of the inhibitory network under isoflurane. Previous work has found that, in general, inhibitory networks are much more active in the awake brain⁶⁴, and are suppressed under anesthesia (including the anesthetic used in this study, isoflurane). While the exact mechanism of isoflurane is unclear, isoflurane is a known GABA_A receptor agonist, that also disrupts synaptic transmission²⁸⁶. Importantly, isoflurane has been found to preferentially reduce cortical-cortical responses compared to thalamocortical responses *in vitro* and *in vivo*²⁸⁷. Based on these findings, we theorize that the ongoing thalamic interactions with the cortical inhibitory network (and potentially SOM interneurons²⁸⁸) may be a critical factor in controlling the evoked cortical response, and may play a pivotal role in the control of sensory information.

5.3.2.2 Thalamocortical Synaptic Depression Controls Evoked Response (Theory #2)

evoked responses because the synapses are very depressed in hyperpolarized bursting states. The theories of cortical inhibition and synaptic depression are not mutually exclusive, and could even work in combination to explain how hyperpolarized states change the transmission of sensory signals in the thalamocortical network.

5.3.3 Relating Bursting States to Thalamic Function in Sensory Processing and Sleep

Given our observed result of a decrease in evoked sensory response with an increase in thalamic evoked spiking, we proposed a theory of increased cortical inhibition due to an increase in network bursting (see Section 5.3.2). In particular, an increase in SOM interneurons may have dynamic effects on the cortical network and may explain our observed results. While this framework may explain our data presented here, we also considered how our model compared with additional theories of thalamic bursting, specifically with bursting in sleep states, and stimulus evoked bursting for enhanced sensory feature detection.

The intersection of the SOM network activity and bursting behavior has some merit, and both phenomena are widely found in models of sleep. As previously stated, thalamic bursts are extremely prevalent during Slow-Wave-Sleep (SWS), with both an increase in thalamic and reticular thalamic bursting. SOM interneurons are also widely active during Slow-Wave-Sleep, and have been found to be responsible for generating the characteristic delta waves that name this period. Slow-Wave-Sleep is associated with a dissociation with the outside world, where perception of sensory stimuli is absent. Therefore, SOM and prolonged periods of bursting, correlate very well with a decrease in perception of sensory information during periods of sleep. Additionally, a thalamic hyperpolarized state has shown to cause a dramatic increase in cortical slow-wave activity^{266,292}, suggesting that thalamic states and activity may also be involved with the maintenance of low frequency

activity. In terms of ongoing bursting and consciousness, previous work in the visual system and somatosensory system found prolonged thalamic burst states in the awake animal often result in the “drowsy” and “inattentive” animal^{237,293}. Awake thalamic burst states also appear during periods of quiescence²³⁷, when the animal is awake but not moving. SOM interneurons have also been found to be selectively increased during periods of quiescence²⁸⁸, and have been shown to be generally suppressive of excitatory neurons. Therefore, prolonged periods of bursting may be used to dissociate cortical networks during quiescent periods for synaptic hemostasis, memory consolidation, and other purposes of sleep. Taken together, we predict that prolonged coordinated burst states are responsible for controlling cortical SOM neurons, and initiating large scale gating of cortical circuits for inattentive and sleep states.

SOM neurons are found across most of the cortical layers, however, the thalamic targets of Layer IV and V would be the candidates for activation during bursting states (for review see²⁹⁴). While SOM interneurons represent only 20-30% of the inhibitory population, they have large effects on cortical processes. Layer IV SOM interneurons are suggested to inhibit Layer 2/3 pyramidal cells and to inhibit Layer IV FS interneurons (see review²⁷⁶). This result of inhibiting one layer and dis-inhibiting another layer would suggest dynamic control of cortical sensory encoding. However, recent research has found that Layer IV SOM interneurons may actually increase the synchrony of the inhibitory population^{279,281,295}. In Cortical Layer V, SOM interneurons have been found to be generally inhibitory but also form complex nonlinear transformations²⁷⁸. Therefore, the SOM neurons across both layers would provide a dynamic control of suppressing evoked cortical signals. Based on our results and published work, we speculate that thalamic bursts may be activating SOM networks which both increase the net inhibition on cortical networks and facilitate the synchronization of fast spiking responses for net decrease in

sensory evoked activity. In summary, our data corresponds to previous work that demonstrate that thalamic bursts may be a critical mechanism for controlling sensory gating in cortical sensory systems and suggest that prolonged burst states operate to decrease the sensory perception.

5.3.4 Relating Observations of Bursting and Enhanced Sensory Detection

With our prediction and theory relating prolonged burst states with an activation of inhibitory networks, the question remains: can thalamic bursts increase cortical detection of sensory events?

We suggest that thalamic bursts still can enhance sensory responses, depending on the overall state of the thalamocortical network as a whole. While we suggest that thalamic hyperpolarized states may be involved in sensory dissociation, we theorize that these changes are contingent on the interaction with cortical networks. In the awake animal (Chapter 4) we imposed a large scale thalamic hyperpolarization which had the net effect of initiating burst state across the entire thalamus, which resulted in a decrease in cortical response. However, when we investigated the thalamic response in the anesthetized case (Chapter 3) we found that thalamic hyperpolarization increased the cortical response. Under anesthesia, the cortical inhibitory circuits either were not activated due to the low spontaneous activity or were generally suppressed and therefore did not alter the evoked cortical responses. Based on these data, the level of either enhancement or depression of cortical responses may be a function of the interaction of pre-stimulus activity on the cortical network.

Under our hypothesis, any stimulus evoked bursting that would occur without large-scale changes to thalamic firing would still increase cortical activity. For example, stimulus evoked thalamic bursts that are evoked through excitatory and inhibitory kernels in the visual pathway would therefore still increase the cortical detectability and cortical evoked response. Previous research in the visual thalamus (LGN)²¹⁷ has found that stimulus evoked bursts are associated with naturalistic scenes and therefore may represent encoding of particular features. Additionally, stimulus evoked thalamic bursts correlated with an increase in behavioral detection in monkeys²⁵⁸ and therefore may still represent an enhancement of sensory information.

Additionally, due to our observations, we predict that enhancement or depression of sensory information may also be attributed to the timescale of thalamic hyperpolarization. The hyperpolarized states that we imposed in this work encompassed the entire thalamic region and lasted for 100's of milliseconds, which likely represented a complete network transition to a burst state. Under shorter periods of hyperpolarization thalamocortical sensory representations may be increased. Taken together, thalamic bursting may still enhance feature detection; however, this may depend on the timescale of thalamic changes and the overall thalamocortical state.

5.3.5 Future Directions: Investigation of Thalamocortical Networks

Upon completing Chapter 3 and 4, there are several unanswered questions that should be explored with additional research. While not conclusive, we hope these areas help guide future research into novel areas of insight.

In the Chapter 3 and 4 discussions, we have highlighted two potential explanations relating thalamocortical states to the interaction of cortical networks and cortical synaptic depression. Future work should specifically examine if and how these mechanisms

combine with thalamic states to enter new regimes of sensory processing. In particular, future experiments should determine how cortical inhibitory networks (including interneuron subtypes) in general interact with different thalamic states. We propose that the SOM interneuron network may become particularly active during states of thalamic bursting. Novel GEVI and calcium imaging would allow a targeted view of SOM interneurons during various states of processing in the awake animal and during periods of imposed thalamic activity (i.e. optogenetics). Cell type specific imaging could be generalized to examine how different neural subtypes are modulated by changes in thalamic polarization.

Additional work should focus on understanding the impact of pre-stimulus activity on the evoked responses in the awake animal. We propose that the depression of the thalamocortical synapse is highly dynamic and dependent on pre-stimulus thalamic firing rate, and dependent on thalamic firing modes (tonic and bursts). While insightful, previous studies have lacked the specificity to target specific thalamocortical synapses directly, and control for other changes in ongoing thalamocortical activity. Using novel methods of optogenetics, terminal excitation can be used to determine the impact of the thalamocortical synaptic changes on the processing of sensory information.

While it went beyond the scope of this work, additional research should examine other dimensions of thalamic state on thalamocortical processing. The research presented here only explored a limited axis of thalamic polarization by applying different levels of hyperpolarization, which excluded levels of depolarization or temporal modulations. We found two distinct states during periods of hyperpolarization which suggest temporal aspects may impact sensory thalamocortical processing. Our preliminary findings suggest that shorter periods of thalamic hyperpolarization, without 100's of ms of thalamic

bursting, may change the input-output relationship of thalamocortical states. Additionally, recent research in the Stanley Lab has demonstrated novel tools for closed loop optogenetic control^{296,297} of thalamic and cortical neural activity, which further expands the possibilities of future studies to explore the impact of more complex frequency modulated thalamic states on sensory processing.

Our results suggested a profound effect on the cortical responses; however, we only investigated a single sensory modality, the mouse whisker system. While the mouse whisker system is an ideal model system of thalamocortical sensory processing, other sensory systems have been shown to have distinct dynamics^{4,243}. Therefore, future research should consider exploring visual and auditory sensory modalities to determine if the observed effects are a general thalamic phenomenon.

Finally, the results shown in Chapters 3 and 4 are only thoroughly investigated using large scale GEVI cortical widefield imaging with gross modulation of thalamic structures. These observed trends may represent problems with the fluorescence imaging technique. Although unlikely, the normalization techniques (i.e. $\Delta F/F_0$), and overall range of the ArcLight indicator may prevent a true measurement of evoked voltage in the recorded cortical regions. Additionally, we only assumed the effect of thalamic halorhodopsin activation on the overall level of thalamic polarization. With the advent of robotic assisted techniques²⁹⁸, intracellular thalamic recordings are becoming more feasible which would enable a direct measurement of thalamic membrane potential. Therefore, future research should investigate how specific thalamic polarized states shape the evoked cortical response using more targeted electrophysiology techniques, such as intracellular recordings, or high density extracellular probes.

5.3.6 Concerns and Caveats

Throughout this document, we have highlighted several caveats for the presented research which should be noted during the interpretation of this data. While we have discussed many of these concerns in each individual chapter, it is important to take into consideration several of these points while examining the document as a whole. Below, we will address the serious caveats of this work, and the implications for the interpreting these data.

One of the largest areas of concern is the analysis of the ArcLight GEVI fluorescence signal. In particular, the fluorescence is measured as a relative change ($\Delta F/F_0$), where an ongoing fluorescence signal (F) is subtracted and divided by a baseline signal (F_0); a very common analysis for this type of technique. The objective of this analysis is to normalize slight variations in fluorescence expression to allow for a uniform measurement in changes in activity. What is pivotal for this type of analysis is the selection of an F_0 baseline that is distinct from any manipulation that is undergone. Here, we provide a modulation of ongoing thalamic activity using optogenetics. We found that the observed trends presented here were robust to variations in the selection of the F_0 (data not shown). In a majority of cases, we selected an F_0 that was before any optogenetic manipulations. While this $\Delta F/F_0$ technique allows for a normalization of fluorescence, it also can distort the absolute levels of the observed change. For example, since the ongoing background activity is known to change in the anesthetized and awake brains, the underlying F_0 will be different. Therefore, the same evoked signal magnitude, could have two very different $\Delta F/F_0$ signals, which could skew the observed effect when comparing across different states with different levels of activity. For this work, it is important to examine the relative changes in the fluorescence signals (i.e. increasing and decreasing) during different manipulations to ongoing states.

Another concern with the fluorescence technique is the overall limitations of the fluorescence probe in relating changes in voltage to changes in fluorescence. These limitations are mainly due to the dynamics of each probe, and the limitations of the ΔV versus ΔF curve. Most voltage probes do not have a linear association of ΔV and corresponding ΔF . ArcLight is no exception¹³⁷. ArcLight has an almost linear regime between -70mV and +25mV; however, the mapping of voltage to fluorescence is not 1:1. Additionally, these probes have resolution limits, and therefore, it is unclear if the probes are either hitting a floor or ceiling on the voltage spectrum. While currently unavoidable in the GEVI landscape, the voltage to fluorescence curve underlies all of the reported GEVI signals, including the work shown here. Therefore, in the final chapter, the observed trends could be due to the limitations of the probe to resolve on the upper end of membrane potentials. Future work should investigate the observations we presented here in more detail, specifically using techniques that have fewer limitations with normalization, and overall resolution limits, such as traditional electrophysiology.

One final concern is the possible confounds associated with the optogenetic manipulation used in this study. Here, we use a optogenetic construct (halorhodopsin) to control the level of polarization by actively pumping chloride into the neuron. Previous work has shown that under prolonged stimulation halorhodopsin can overwhelm the cell's internal hemostatic mechanisms for regulating chloride (See Appendix 3 for details), causing a dramatic increase in intracellular chloride. These large changes in chloride can have dramatic implications for the neuron and alter the communication of synaptic inputs. While we do not believe this is the case (see Appendix 3 for a detailed description), this is a possible concern and a limitation of our techniques used here. Throughout this work, we do not have a definitive measurement of intracellular chloride during optogenetics; however, based on our observations, we do not believe this is a concern with this work.

Future studies could use different opsins (Arch) that are proton pumps or stimulation of the GABAergic inputs to determine if our results are contingent on halorhodopsin.

5.4 Thalamus as a Dynamic Gate to Cortex

In conclusion, this thesis has utilized novel tools and technologies to investigate how thalamic states shape and transform thalamocortical spatiotemporal sensory representations. The thalamus is a central component of signal processing that is often overlooked as an important center for controlling how and what information is transmitted downstream. The work presented here is, to our knowledge, the first of its kind to explore how direct modulation of thalamic membrane potential alters thalamocortical processing of sensory inputs. Our data illustrated that induced thalamic states produced a range of effects on the cortical sensory responses that differed depending on the overall neural state and, perhaps, interaction with cortical networks. In particular, we found that hyperpolarized states increased the evoked thalamic responses through increased thalamic bursting, while the evoked cortical response was highly dependent on the neural circuit (anesthetized vs awake). Using this information, we predict that stimulus evoked thalamic bursting and ongoing thalamic bursting form multiple thalamocortical regimes, and it is the interaction of thalamic information with cortical networks, and vice-versa, that is pivotal in how that information is transmitted.

In this thesis, we performed only a limited investigation of thalamic states through application of a simple hyperpolarized input with a single optogenetics tool, and found highly dynamic results. It requires very little imagination to extrapolate how other subtle effects, such as slight changes in depolarization or even more complicated metabotropic systems, could shape thalamocortical processes. Taken even further, this suggests that state-dependent processing may play a paramount role in neural circuitry that extends beyond even thalamocortical circuits. While we are still only beginning to investigate neural circuitry, future work should explore how these state-dependent processes modulate the same neural circuits for multiple tasks. The thalamus, or any neural component, is not

just a simple relay, but a complex part in the emergent system that forms the conscious brain.

It is through question, experimentation, and philosophy that we begin to unravel the secrets and inner-workings of the nervous system. Through my work, I have continually marveled at the robust nature of the brain and its ability to filter vast amounts of information through webs of complex recurrent circuits. In this work, I have proposed that the thalamocortical network form even more dynamic states than previously thought, through the interactions of thalamic state, thalamic bursts, and cortical networks. While I have only scratched the surface of thalamocortical interactions in the most basic neural circuits, I hope my work will lay a foundation of knowledge that will be built upon for generations of scholars to come.

APPENDIX

A.1. ArcLight Overlap with Hemodynamic Signals

A.1.1. Removal of Hemodynamic Frequency using Notch Filtering

Due to the hemodynamic noise found in the captured fluorescence signal (Figure 2.3), our first approach for removing the noise was a simple common notch filter at the hemodynamic frequencies (main and corresponding first harmonic). We found that the hemodynamic signal we observed was correlated with the ongoing heart rate of the animal (Figure 2.3) between approximately 5-10 Hz which corresponds to a heart rate between 300-600 bpm. This estimated heart rate range matches the typical physiological heart rate of an anesthetized mouse. Below (Figure A1.1) are two examples of ArcLight evoked sensory responses and the corresponding power spectral density of the evoked fluorescence with and without notch filtering (2nd Order Butterworth, Bandstop between 5-20Hz). We found that due to the total event time of the ArcLight response (~100-300ms), simple notch filtering at 5-20 Hz would greatly disrupt the ArcLight waveform.

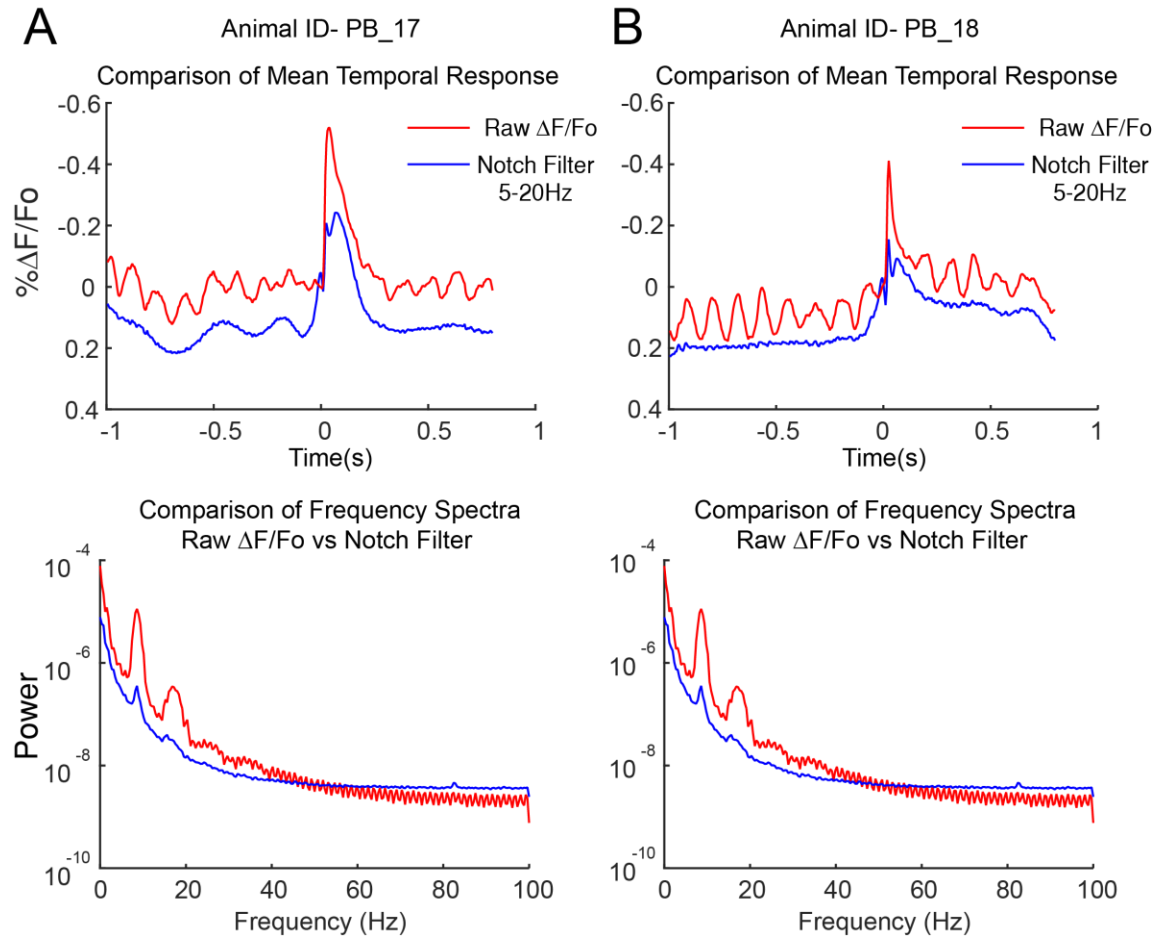


Figure A 1.1. Notch Filtering of Fluorescence Response.

A. Top- Average (102 trials) region of interest (ROI) time series ArcLight fluorescence response during a whisker deflection (stimulus delivered at time = 0). The red trace response shows a strong fluorescence response to the sensory stimulus. The blue trace illustrates the change in waveform caused by notch filtering. **A. Bottom-** Corresponding average power spectral density of the fluorescence signal. Notice the large peaks at ~10 and 20 Hz corresponding to the hemodynamic response. **B.** Same as A, but for a different experiment.

A.1.2. Removal of Hemodynamic Frequency using Off-ROI Subtraction Methods: Throughout this work, we utilized an off-ROI (region of interest) to subtract ongoing hemodynamic noise observed in the fluorescence signal. This Off-ROI technique utilized the highly correlated structure of the hemodynamic signal through the cortical tissue to subtract common noise. Below are two figures that detail the removal of the hemodynamic noise through the Off-ROI subtraction (Figure A1.2), and the effect of the off-ROI placement on the spatiotemporal response (Figure A1.3).

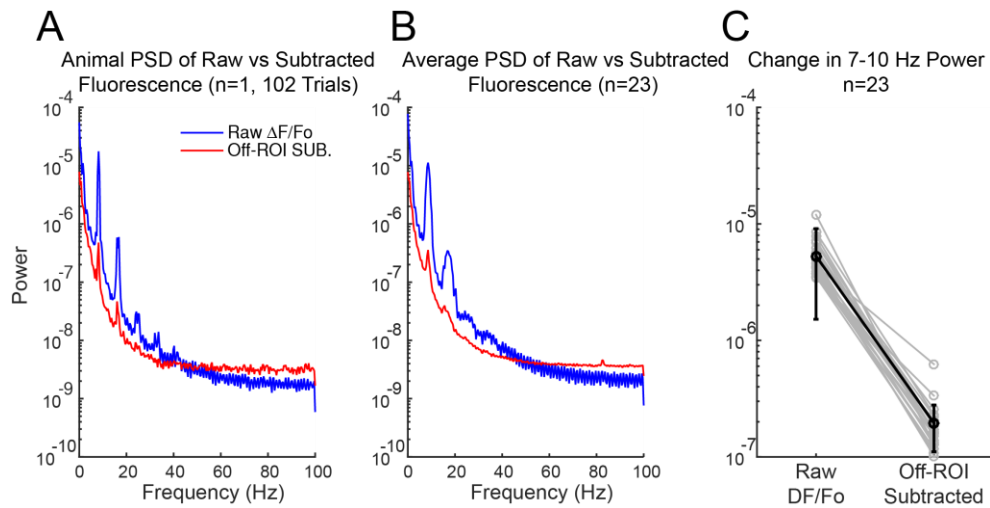


Figure A 1.2. Reduction of Hemodynamic Noise.

A. - Average power spectra of the ROI of the fluorescence before (blue -F) and after (red F-ROI Sub.) off-ROI subtraction. The off-ROI subtraction reduces the peak of 7-10 Hz frequency power. **B** Similar to A, the average power spectra of the ROI across experiments ($n=23$) before (blue) and after (red) off-ROI subtraction. **C.** Off-ROI subtraction causes a mean reduction of 95.8% ($\pm 2.8\%$ SD, $n=23$, $p=0.0033$, paired t-test) frequency power in the 7-10 band.

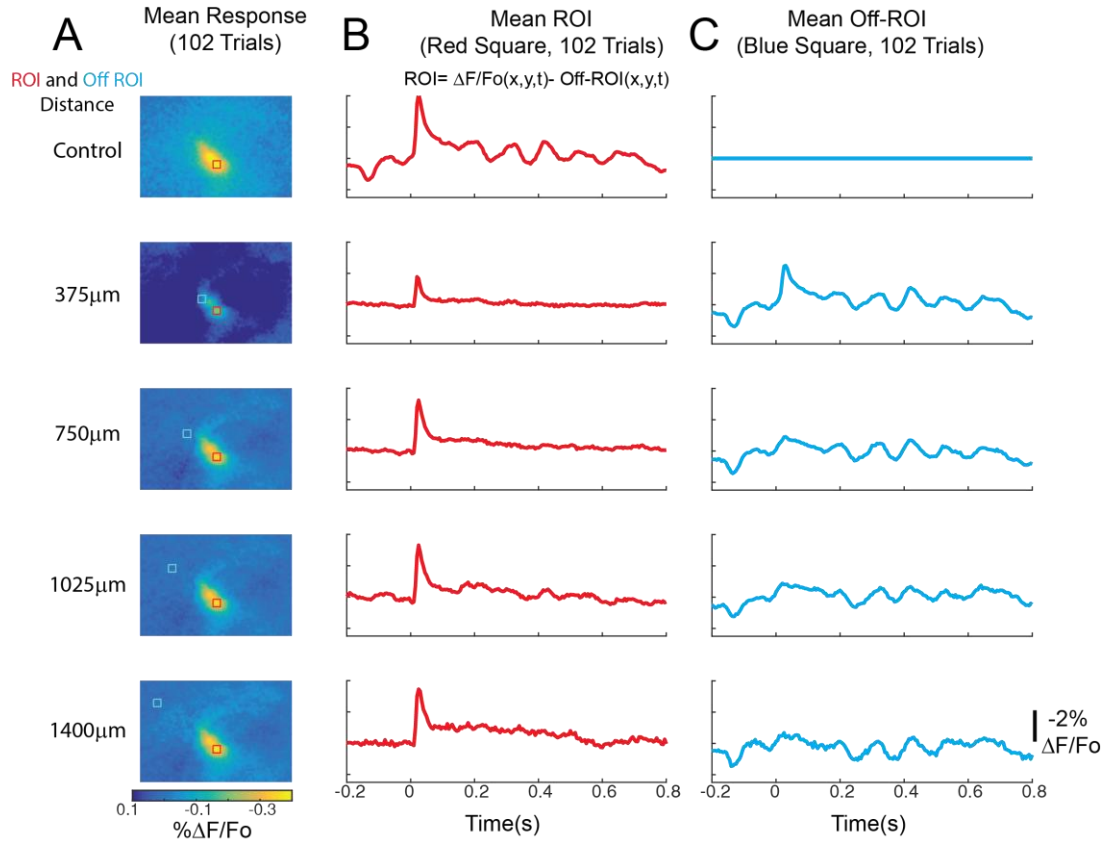


Figure A 1.3. Effect of the Position of the Off-ROI on the Evoked Spatial and Temporal Response.

A Top. Off-ROI subtracted mean spatial response 25ms after stimulus (102 Trials). Red square highlights the location of the region of interest. Blue Square highlights the Off-ROI to be scaled and subtracted. **B Top.** The average temporal trace taken from the spatial image ROI (red square) after Off-ROI subtraction. **C Top.** The average temporal trace taken from the spatial image Off-ROI (Blue square) to be subtracted from the ROI. Each row shows the same plots for increasing distance between the off ROI and the ROI (375um per row). As the Off ROI becomes more spatially separated from the ROI, there is a reduction in the influence on the spatial and temporal trace. After approximately 600um, the Off-ROI does not interfere with the evoked response.

A.1.3. Non- Injected ArcLight Control

To confirm that any effects of autofluorescence do not significantly affect our results, we conducted additional experiments examining a non-injected animal to determine the potential influence of the intrinsic auto-fluorescence on the spatial extent of the response. First, we mapped the S1 barrel cortex using intrinsic imaging (see methods on Intrinsic Imaging) to determine the proper location of the corresponding whisker sensitive cortical region. Due to the slow temporal dynamics and overall small change in signal, we measured the intrinsic response to a repetitive stimulus over several seconds. Figure 12A shows a temporal average (across 20 Trials) of the intrinsic response in a time window of 1-2 seconds after the onset of the strong repetitive whisker stimulation (1500 Degrees/second at 10Hz for 5s).

After we mapped the region using the intrinsic signal, we setup the system for ArcLight imaging described in detail in the manuscript, and applied the same single whisker punctate stimuli used in a majority of the study (single 1200 degrees/second sawtooth ($\tau = 8\text{ms}$) stimulus). Below in Figure A.1.4, we compared the intrinsically identified whisker region (Figure A.1.4A) to responses using the ArcLight setup and experimental parameters used throughout this work. Specifically, we sampled the same area at 200 Hz with blue excitation (465nm) along with the excitation and emission filters as described in the Methods. Figure A.1.4 *Left* shows the averaged spatial response over the 700ms window post stimulus (100 Trials), with no apparent qualitative difference between the identified ROI (red) and other off-ROIs (blue and aqua,). The 700-millisecond window corresponds to the approximate length of the average S1 cortical response used throughout this manuscript (Figure 2.2C). Figure A.1.4 *Right* shows the time series of integrated activity within these ROIs. We found no quantitative difference between the evoked response in

the identified (red) ROI and the background, pre-stimulus activity, indicating that there was no appreciable evoked response. [E1: Mean pre-stimulus fluorescence (-700-0 ms) $\% \Delta F/F_0$ -0.0073 \pm 0.0057 SD, Mean post-stimulus fluorescence (0-700ms) $\% \Delta F/F_0$, 0.0063 \pm 0.059 SD, $p=0.102$, Paired t Test]

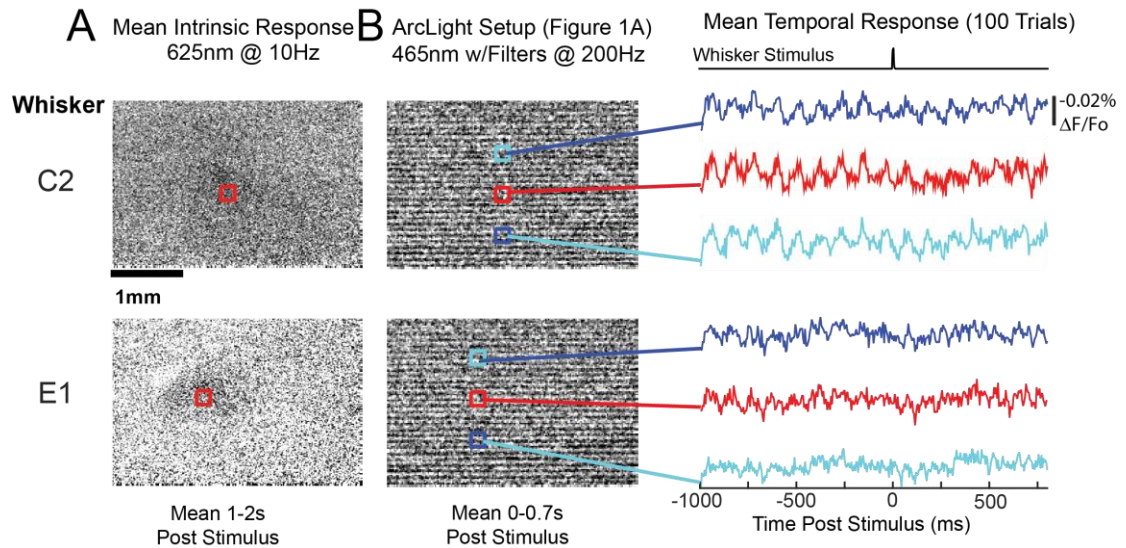


Figure A.1.4. Non-Injected Control of Intrinsic Response during Whisker Stimulus. A. Mean Intrinsic Mapped Response (20 Trials). The primary cortical barrel was first identified using the intrinsic response. The cortical surface was thinned and prepared as described in detail in the methods section. A Thorlabs red (625nm) LED illuminated the skull during repetitive stimulation of a single whisker (Top whisker C2, Bottom E1). The thumbnails show the temporal average between 1-2s after the onset of the repetitive stimulus. The spatial response was normalized and subtracted by the average background response, to increase the contrast of the evoked signal, and smoothed with a 200 μ m Gaussian filter. **B. Single Whisker Deflection with the ArcLight Setup.** Each thumbnail (*Left*) represents the mean response (100 Trials) 0 to 0.7s post stimulus to the same whisker shown in A. The imaging setup was switched from the intrinsic imaging configuration (A) to the ArcLight configuration (Figure 2.1A), sampling at 200Hz. The signals have been analyzed using the same methods (however, here no Off- ROI subtraction was used). Temporal traces of the integrated fluorescence in each of the illustrated ROIs is shown (*Right*). Each ROI (Blue, red, aqua boxes) corresponds to the temporal traces shown in the right. The timing of the whisker deflection is shown at the top.

In the non-injected mouse, in the ArcLight setup (Figure A.1.4B), we also observe oscillatory responses (8-10Hz) across both whiskers similar to the observed hemodynamic signal in the single trial responses, shown in Figure 2.3. These hemodynamic oscillations can still be seen in the C2 and E1 trial average in Figure A.1.4B. These results further suggest that this oscillatory signal is not representative of ongoing membrane potential fluctuations but is due to the blood flow across the cortical surface. Based on these controls, we expect that the observed stimulus evoked fluorescence response shown throughout our study is most likely due to the changes in neural activity associated with ArcLight, and not due to auto-fluorescence.

A.2. ArcLight and Halorhodopsin Expression

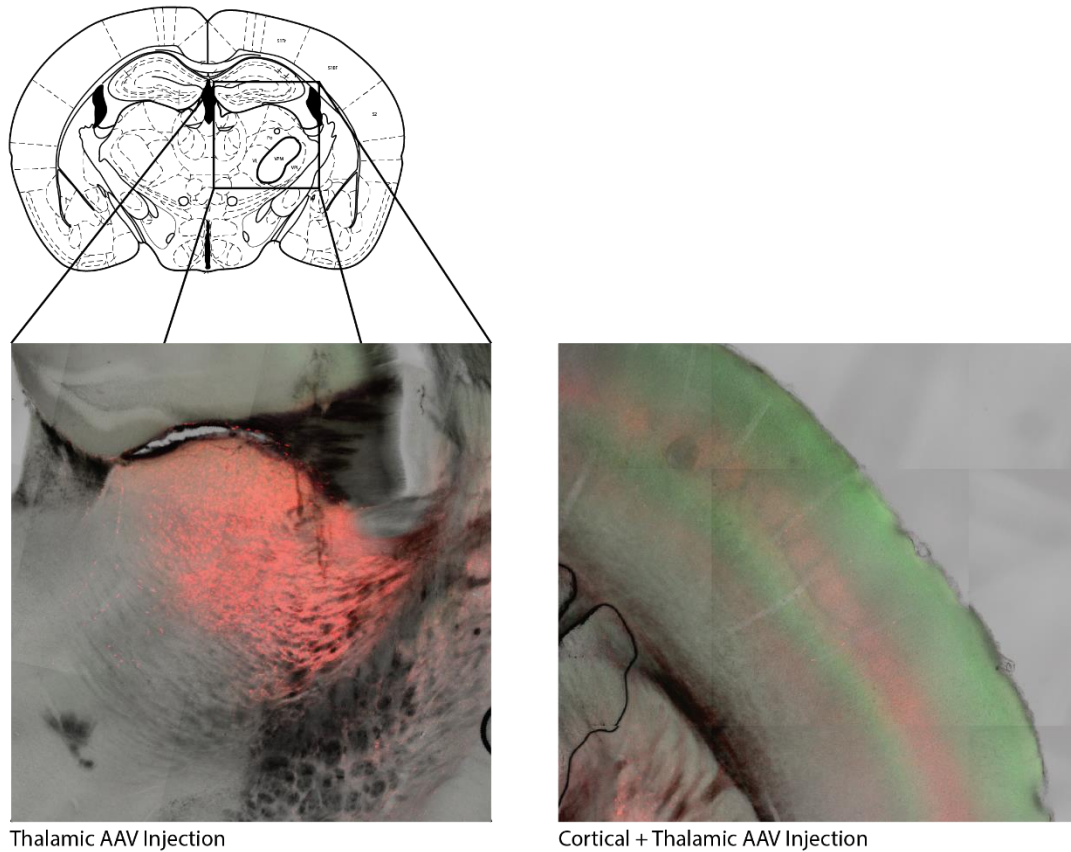


Figure A.2.1 Example of combined Halorhodopsin and ArcLight expression in Mouse Sections.

Left. Expression of Halorhodopsin in the mouse thalamus. Mice are injected with two viral vectors, ArcLight in cortex (AAV1-hsyn1- ArcLightD- SV40), and eNphR3.0 (AAV5-CamIIKianse-eNphR3.0-mCherry). Thalamic expression of Halorhodopsin (mcherry-red- Emission 608-715nm) is localized throughout the thalamic region of the mouse. Electrode tracks of the optrode (optic fiber and electrode) are seen terminating in the VPM region. **Right.** Cortical injection of ArcLight probe reveals expression throughout layer 2/3 and layer 5 across the mouse cortex (ArcLight-green-Emission 474-562nm). Thalamic expression of Halorhodopsin (mcherry-red) is also found in the axons of the thalamic neurons projecting to layer 4 and 5 of the S1 barrel cortex.

A.3. Chloride Reversal Potential and Halorhodopsin Activation

During our recordings of the thalamus (both awake and anesthetized) we found that during short periods (1-2s) of halorhodopsin activation, there was an increase in ongoing thalamic activity approximately 100-250ms after the onset of the optogenetics. Considering the typical use of halorhodopsin is to silence neural circuits, these results may be surprising. While we consider these results to correspond to the dynamics and deinactivation of the T-type calcium channels in the thalamic circuit, there could be an alternative interaction with halorhodopsin and the reversal potential of chloride. Additionally, published work⁸⁷ using another method of thalamic hyperpolarization (through TRN GABAergic optogenetics) has reported similar results as shown here. This method would not be susceptible to changes in reversal potential and corroborate our findings. In this next section, we will further explore the relationship between chloride and halorhodopsin and argue that the intrinsic properties of thalamic neurons are likely candidates for this observed effect, with additional examination of our data, in-vitro whole cell recordings, and a simple model of thalamic activity.

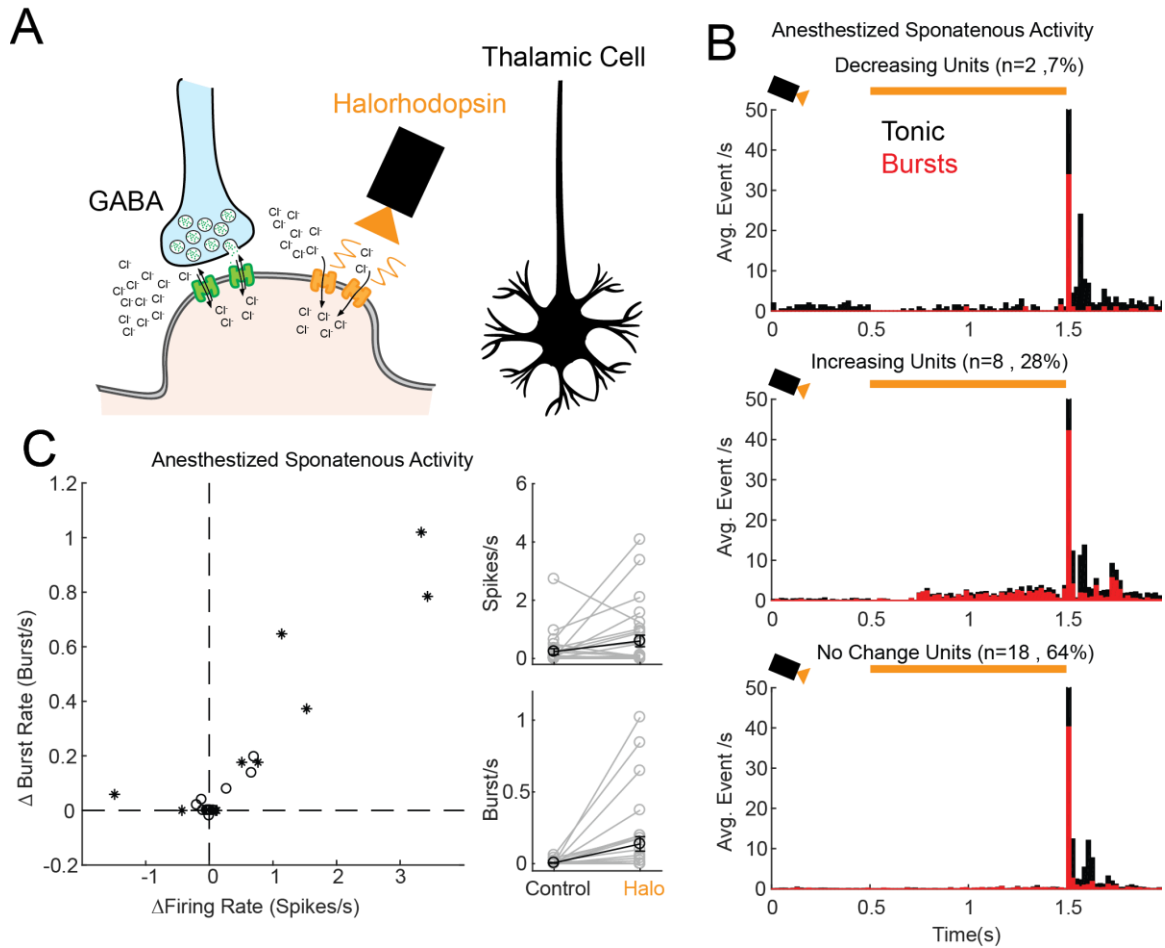


Figure A3.1. Halorhodopsin Activation Increases Ongoing Thalamic Spontaneous Firing and Bursting. **A.** Cartoon depicting chloride inputs into a thalamic cell. Halorhodopsin is a chloride channel that is activated via light (amber), compared to the traditional GABAergic receptors which open chloride channels that follow an electrochemical gradient (Green). **B.** Anesthetized Thalamic Spontaneous Responses Caused Halorhodopsin activation. We observed three general trends in our recording thalamic units in the anesthetized animal (see Chapter 3 for Methods), thalamic neurons decreased, increased, or remained silent. All recordings had a post-inhibitory rebound following the offset of the amber LED. Red- burst spikes, Black Tonic Spikes. **C Left.** Change in Bursting and Firing rate under periods of halorhodopsin activation across all cells (n=28). Cells that responded with a significant ($p < 0.05$, paired Signrank test) change in thalamic firing are marked with an asterisks (*). **C Right.** Population responses under control and halorhodopsin conditions for periods of increased activity (250ms after LED onset) for each cell for spiking (top) and burst (bottom) rates. Under halorhodopsin activation, spontaneous spiking and burst rates increased across the population.

Halorhodopsin (eNphR 3.0) is a genetically engineered chloride pump that is sensitive to amber light (590nm), and has been used throughout the nervous system to hyperpolarize neurons. Halorhodopsin will hyperpolarize the neuron by pumping extracellular chloride into the neuron at the expense of Chloride (Cl^-) reversal potential of the cell (Figure A3.1A). Naturally, chloride concentrations are higher in the extracellular space, and therefore the chloride reversal potential is typically below the resting membrane potential (usually close -70mV). Chloride is believed to play an inhibitory role in the cortex, and is controlled through the release of GABA and the interneuron population. GABAergic receptors will open chloride channels within the cellular membrane to transport chloride. Unlike Halorhodopsin, GABAergic channels allow for the passage of ions down the electrochemical concentration gradient, which is measured by the chloride reversal potential (E_{Cl^-}).

Previous work has shown that halorhodopsin²⁷⁰ can be so efficient at pumping chloride into the cell that the influx of chloride will overwhelm natural homeostatic mechanisms, causing a change in the chloride reversal potential (termed chloride loading). Changes in the chloride potential were found as quickly as 500ms after the onset of the optogenetics (at a reasonable light intensity), and increased linearly with increasing durations of stimulation. After 0.5s the reported changes were relatively small (2.4mV), but for periods of 15s of stimulation the reversal potential was substantially altered by over 40mV. Therefore, inputs that would typically hyperpolarize the neuron would become depolarizing (up to the new reversal potential). These changes in chloride potential require active transport, and therefore can last over 15 s (time constant) after stimulation. Therefore, the changes shown in Figure A3.1.1B could be caused through GABAergic IPSPs depolarizing the neuron and causing an increased spiking during hyperpolarization.

While this is a concern for the general use of halorhodopsin, we predict that chloride loading is not the primary candidate for the increased thalamic activity during periods of halorhodopsin activation (both in the awake and anesthetized recordings). In particular, we believe that the increase in thalamic activity after periods of hyperpolarization is due to the intrinsic T-type calcium channels that only become activated during periods of hyperpolarization. During periods of hyperpolarization, along with an increase in activity, we also see an increase in thalamic bursts. Bursts (2 or more spikes) are the hallmark sign of the de-inactivation of thalamic T-type channels, which cause a large calcium influx to depolarizing inputs. T-type calcium bursts require a period of hyperpolarization of at least 100ms (depending on the level of hyperpolarization) before de-inactivating. This period aligns with the first onset of thalamic activity and bursting observed during periods of 100ms after halorhodopsin activation (Figure A3.1B). Across thalamic neurons, halorhodopsin activation causes at least 100ms of silence followed by a period of increased or decreased thalamic activity relative to baseline. Due to the reported intensity and timescale of the chloride loading of halorhodopsin, 100ms is too soon for any substantial changes to the chloride reversal potential to take effect. Furthermore, chloride reversal potentials are much more hyperpolarized in the rodent thalamus (typically near -81mV^{82}) and therefore would be more resilient to subtle changes in chloride concentrations.

In addition to causing bursts, T-type channels reduce the overall spiking threshold and thus cause low voltage spiking along with bursting behavior. Across all anesthetized recordings, we found that ~35% of the neurons altered their overall spiking activity. All neurons that changed their ongoing firing were correlated with an increase in thalamic bursting (Figure A3.1C), with a strong post-inhibitory rebound response. Previous work has shown that providing any depolarizing inputs (through channelrhodopsin activation) reduces the

spontaneous bursting⁶⁸. This suggests that the halorhodopsin activation is causing a net hyperpolarizing result, which is at least de-inactivating the T-type channels.

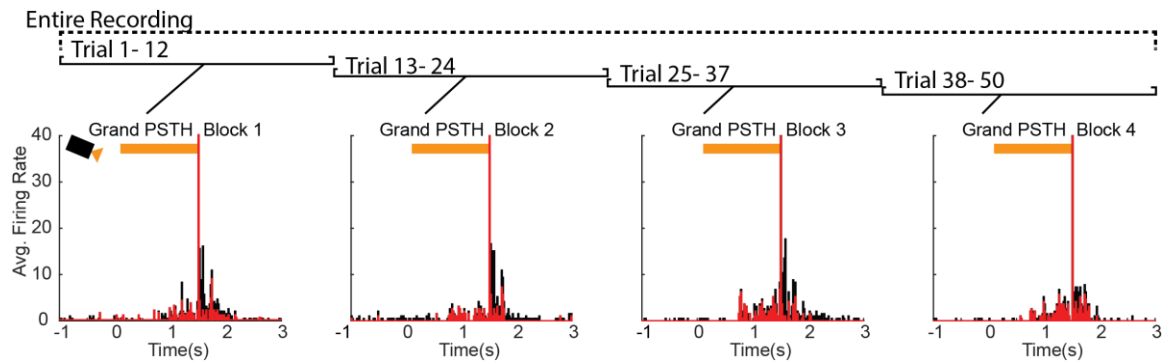


Figure A3.2. Increase in Thalamic Activity During Halorhodopsin Activation Is Consistent Across the Recording. Grand PSTH across all significant increased neurons (n=8) across the entire recording session. Each trial block represents 12 consecutive trials in the recording.

Due to the long lasting effects reported of chloride reversal (10's of seconds), we would also expect to observe a gradual increase in the effects of the halorhodopsin stimulation. We delivered the halorhodopsin LED activation in a pseudorandom order between 3 and 19s apart, and therefore if chloride loading was occurring we should see changes over time. We compared the first and last trial blocks of the recordings that demonstrated a significant change in firing rate during periods of halorhodopsin activation (Figure A.3.2). We found no changes in the spontaneous activity (First Block compared to Last Block, $p = 0.23$, Wilcoxon Sign Rank, $n=8$)

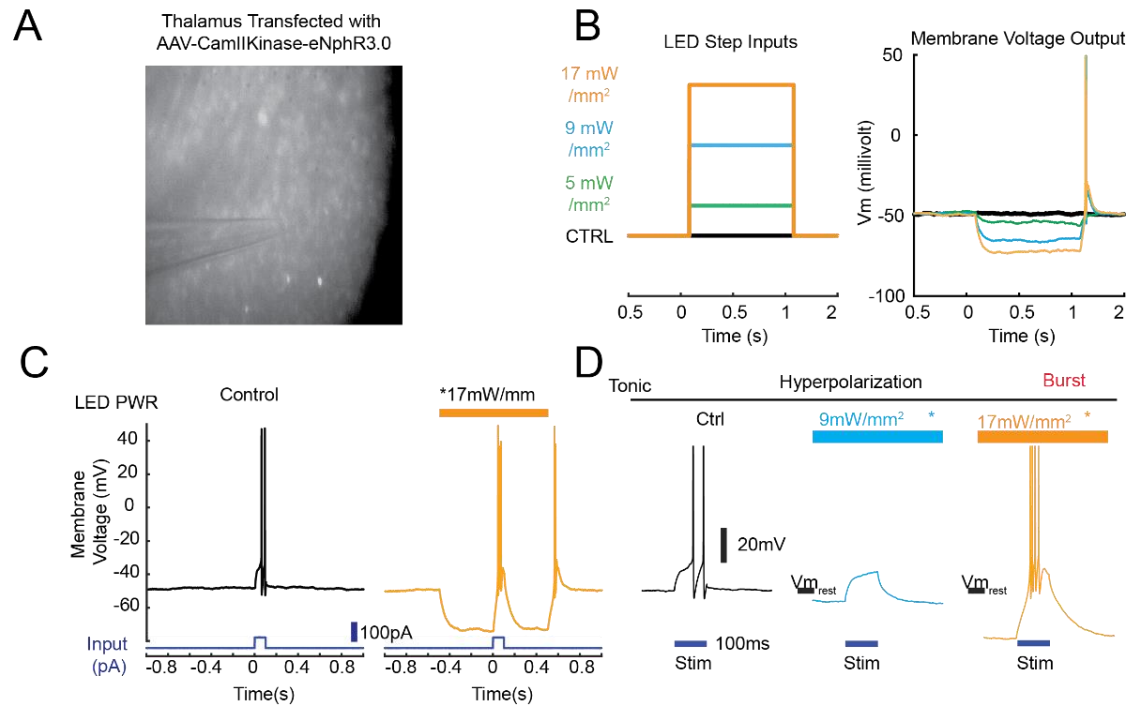


Figure A3.3. Whole Cell *in vitro* Recordings Confirm Halorhodopsin Hyperpolarization and Thalamic Bursting. **A.** Thalamic neurons transfected with halorhodopsin construct and co-expressed with mCherry fluorophore. Recording pipette show in the middle of the thalamic nucleus. **B.Left.** LED step inputs applied during whole cell recording of thalamic neuron. **B.Right.** Resulting recording during optogenetic activation at various LED intensities (shown in B). During increasing levels of LED input, halorhodopsin activation induces a hyperpolarizing current into the thalamic neuron. After the cessation of optogenetic input, the thalamic neuron responds with a characteristic post-inhibitory rebound due to T-type calcium channel de-inactivation ($t=1$). **C.** Ongoing polarization alters the encoding of the same step current input into thalamic neuron. Under control conditions (C.Right), the thalamic cell responded to a depolarizing current step with a tonic firing of two action potentials. After 500ms of hyperpolarizing input, the thalamic cell causes a burst response to the same current step. **D.** Thalamic polarization can modulate the evoked response to current inputs. Same input as shown in C, however across three different stimulation levels (Control, Black, 9mW/mm², Blue, and 17mW/mm², Orange).

In order to further validate that halorhodopsin was indeed hyperpolarizing the thalamic neurons, we performed *in-vitro* recordings of thalamic neurons. Mice were injected with halorhodopsin as described in Chapter 3 and 4 (Methods). After at least 4 weeks of expression, mice were perfused and sectioned for *in vitro* whole cell recordings (See A.3.1

Methods In Vitro). We found robust expression of the halorhodopsin (Figure A3.3A) during our recordings. In response to LED inputs, thalamic neurons demonstrated a hyperpolarizing current (Figure A3.3B), that resulted in a post-inhibitory rebound that is characteristic of thalamic neurons³⁸. Additionally, we found that during periods of hyperpolarization, thalamic neurons showed a range of responses to the same current step. Under normal conditions, thalamic neurons responded with tonic spikes (Figure A3.4C *Right*, Figure A3.4D *Right*); however, under halorhodopsin activation thalamic neurons burst in response to stimuli (Figure A3.3C-D *Left*). We observed an intermediate transitional phase where moderate levels of halorhodopsin activation (9mW/mm^2) with no evoked response (Figure A3.4D *Middle*). Taken together, our intracellular recordings further validated that halorhodopsin is indeed hyperpolarizing the neurons.

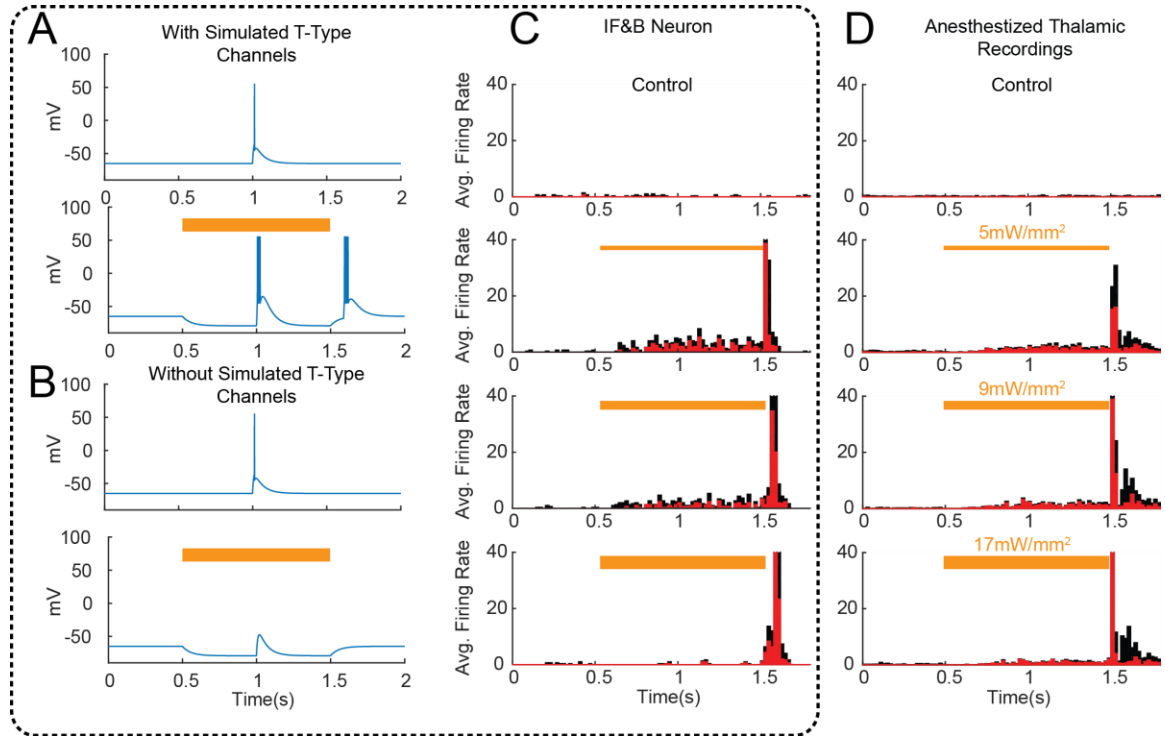


Figure A3.4. Integrate and Fire & Burst (IF&B) model neuron replicates Anesthetized *in vivo* responses to Halorhodopsin Input. A. IF&B model neuron replicates thalamic bursting and post-inhibitory rebound (as shown in Figure A3.3). A. Top

Control current injection evoked a single tonic spike. **A. Bottom.** Thalamic hyperpolarization (through simulated halorhodopsin current) causes thalamic burst to same current input as top. **B.** Same inputs as in A, however IF&B model does not contain fictive T-type calcium channels. No bursting event occurs during hyperpolarization. **C.** IF&B model PSTH responses (100 trials) to various levels of hyperpolarizing input. **D.** Anesthetized thalamic PSTH responses (n=13 units) to various level of halorhodopsin activation. Model and Real data show very similar trends.

Finally, we compared our thalamic recordings to a similar previously published Integrate and Fire & Burst (IF&B) computation model (Figure A3.4A-C, Dashed Lines). In this model, we added a simulated T-type channel to the standard integrate and fire model to enable thalamic bursts (as shown in our intracellular recordings Figure A3.4C-D), and a channel to simulate the hyperpolarizing inputs from halorhodopsin (amber periods). We were able to simulate the thalamic response to hyperpolarizing inputs with a burst response to a synaptic current input and post inhibitory rebound (Figure A3.4A). In non-thalamic cells, that do not contain T-type channels, hyperpolarizing inputs simply inhibit ongoing activity (as demonstrated in Figure A3.4B). We compared a simulated PSTH from 100 neurons with random IPSCs and EPSCs (1Hz) under various hyperpolarizing currents to similar anesthetized thalamic recordings (Simulated Thalamic Data Figure A3.4C vs Real Thalamic Data Figure A3.4C). We found that a simple IF&B neuron was able to replicate the results of an increased thalamic spiking and burst rate during periods of hyperpolarization as shown in the real thalamic dataset (n=13, Thalamic units). Therefore, a simple model with T-type calcium channels was able to capture the observed effect without the addition of other alternatives such as calcium loading.

Taken together, these results suggest that under thalamic hyperpolarization, thalamic neurons will increase ongoing activity with an elevated level of thalamic bursting. While chloride loading likely occurs during long periods of halorhodopin activation, it is unlikely to be the primary driver of this observed result in this thesis. Instead, based on additional analysis, the temporal dynamics, *in-vitro* data, and a simple model examined in this appendix, the increase in thalamic activity is most likely driven by T-type calcium currents that are de-inactivated during periods of hyperpolarization.

A.3.1. In vitro Methods

Methods taken from²⁹⁹: Mice were anesthetized and perfused with 25–30 mL of carbogenated protective artificial cerebrospinal fluid (aCSF) of the following composition: 92 mM N-methyl-D-glucamine (NMDG), 2.5 mM KCl, 1.25 mM NaH₂PO₄, 30 mM NaHCO₃, 20 mM HEPES, 25 mM glucose, 2 mM thiourea, 5 mM Na-ascorbate, 3 mM Na-pyruvate, 0.5 mM CaCl₂·4H₂O, and 10 mM MgSO₄·7H₂O. The pH of the solution was titrated to 7.3–7.4 with concentrated HCl. Brains were embedded in 2% agarose and mounted for coronal sections 300 µm thickness.

Slices were recovered for \leq 20–30 minutes at room temperature (23–25 °C) in carbogenated protective cutting aCSF. After this initial recovery period the slices were transferred into a chamber containing room temperature carbogenated aCSF of the following composition: 119 mM NaCl, 2.5 mM KCl, 1.25 mM NaH₂PO₄, 26 mM NaHCO₃, 12.5 mM glucose, 2 mM CaCl₂·4H₂O, 2 mM MgSO₄·7H₂O.

The aCSF was supplemented with 2 mM thiourea, 5 mM Na-ascorbate, and 3 mM Na-pyruvate, and slices were stored for 1–5 hours prior to transfer to the recording chamber

for use. The osmolarity of all solutions was measured at 300–310 mOsm and the pH was maintained at ~7.3 after equilibration under constant carbogenation.

The slices were perfused with room temperature (22–25 °C) carbogenated recording aCSF at a rate of 4 mL per min. Whole-cell patch-clamp recordings were obtained from visually identified neurons using borosilicate glass pipettes pulled on a horizontal pipette puller (Sutter Instruments) to a resistance of 3–8 M Ω when filled with the internal solution containing 145 mM K-Gluconate, 10 mM HEPES, 1 mM EGTA, 2 mM Mg-ATP, 0.3 mM Na²-GTP, and 2 mM MgCl

Neurons expressing Halorhodopsin were identified by visualization of membrane-targeted mCherry or YFP fluorescence. Amber laser light (590 nm) was delivered through a 200 μ m diameter optic fiber (ThorLabs) positioned near the recorded neuron. The other end of the optic fiber was coupled to an LED light source (ThorLabs). Current pulses were delivered in current clamp using Clampex software.

A.3.2. IF&B Model Methods

The Integrate and Fire & Burst neuron was derived from previously published models of thalamic function from the LGN³⁰⁰ and VPM⁶⁸. In order to simulate the experimental parameters and account for changes in thalamic activity, some additional terms and parameters were added and adjusted. Below we have outlined the model used in this Appendix, as well as the parameters for all conditions. Additionally, we generated ongoing activity using two methods, either injected current noise or synaptic events, both showed the same results. The results shown here use the synaptic event model where IPSCs and EPSCs are modulated as fixed inputs. The model itself was written and analyzed using custom scripts in Matlab 2016a.

$$C \frac{dV}{dt} = I_{EPSC} - I_{IPSC} - I_L - I_T - I_{Halo}$$

$$I_L = g_L(V - V_L)$$

$$I_L = g_L(V - V_L)$$

$$I_T = g_T m_\infty h (V - V_T)$$

$$\frac{dh}{dt} = \begin{cases} \frac{-h}{\tau_h^-}, & (V > V_h) \\ \frac{(1-h)}{\tau_h^+}, & (V < V_h) \end{cases}$$

$$I_{EPSC} = Q$$

$$I_{IPSC} = g_{gaba}(V - V_{gaba})$$

$$\frac{dI_{EPSC}}{dt} = \frac{I_{EPSC}}{\tau_s}$$

$$\frac{dI_{IPSC}}{dt} = \frac{I_{IPSC}}{\tau_s}$$

The following parameters were used to simulate thalamic activity:

$$\begin{aligned} C &= 2e - 3\mu F/cm^2, \\ g_L &= 0.035 \text{ mS}/cm^2, \\ g_T &= 0.07 \text{ mS}/cm^2, \\ g_{gaba} &= 0.1 \text{ mS}/cm^2, \\ V_L &= -65\text{mV}, \\ V_{reset} &= -45\text{mV}, \\ V_h &= -68\text{mV}, \\ V_{gaba} &= -81\text{mV}, \\ V_T &= 120\text{mV}, \\ \tau_h^+ &= 0.1\text{s}, \\ \tau_h^- &= 0.02\text{s}, \\ \tau_s &= 1e - 2\mu F/cm^2, \\ Threshold &= -35\text{mV}, \\ EPSP_{rate} &= 1.5\text{Hz}, \\ IPSP_{rate} &= 1.5\text{Hz}, \\ Q &= 2\text{mV} \end{aligned}$$

Model was updated at a 1ms steps. Absolute Refractory period set at 1ms.

REFERENCES

1. Feldmeyer, D. *et al.* Barrel cortex function. *Prog. Neurobiol.* **103**, 3–27 (2013).
2. Mitchell, A. S. The mediodorsal thalamus as a higher order thalamic relay nucleus important for learning and decision-making. *Neurosci. Biobehav. Rev.* **54**, 76–88 (2015).
3. Cohen, J. D. & Castro-Alamancos, M. A. Behavioral/Systems/Cognitive Early Sensory Pathways for Detection of Fearful Conditioned Stimuli: Tectal and Thalamic Relays. doi:10.1523/JNEUROSCI.1124-07.2007
4. Sachidhanandam, S., Sreenivasan, V., Kyriakatos, A., Kremer, Y. & Petersen, C. C. H. Membrane potential correlates of sensory perception in mouse barrel cortex. *Nat. Neurosci.* **16**, 1671–7 (2013).
5. O'Connor, D. H. *et al.* Neural coding during active somatosensation revealed using illusory touch. *Nat. Neurosci.* **16**, 958–65 (2013).
6. Miyashita, T. & Feldman, D. E. Behavioral Detection of Passive Whisker Stimuli Requires Somatosensory Cortex. *Cereb. Cortex* **23**, 1655–1662 (2013).
7. Varela, C. Thalamic neuromodulation and its implications for executive networks. *Front. Neural Circuits* **8**, 1–22 (2014).
8. McCormick, D. A. & Bal, T. Sensory gating mechanisms of the thalamus. *Curr. Opin. Neurobiol.* 550–556 (1994).
9. Diamond, M. E., von Heimendahl, M., Knutsen, P. M., Kleinfeld, D. & Ahissar, E. ‘Where’ and ‘what’ in the whisker sensorimotor system. *Nat. Rev. Neurosci.* **9**, 601–12 (2008).
10. Pifl, C., Kish, S. J. & Hornykiewicz, O. Thalamic noradrenaline in Parkinson’s disease: Deficits suggest role in motor and non-motor symptoms. *Mov. Disord.* **27**, 1618–1624 (2012).
11. Halliday, G. M. Thalamic changes in Parkinson’s disease. *Parkinsonism Relat. Disord.* **15 Suppl 3**, S152-5 (2009).
12. Portas, C. M. *et al.* A specific role for the thalamus in mediating the interaction of attention and arousal in humans. *J. Neurosci.* **18**, 8979–89 (1998).
13. Somers, D. C., Nelson, S. B. & Sur, M. An emergent model of orientation selectivity in cat visual cortical simple cells. *J. Neurosci.* **15**, 5448–65 (1995).
14. Gola, M., Kamiński, J., Brzezicka, A. & Wróbel, A. B Band Oscillations As a Correlate of Alertness--Changes in Aging. *Int. J. Psychophysiol.* **85**, 62–7 (2012).
15. Llinás, R. R. & Steriade, M. Bursting of thalamic neurons and states of vigilance. *J. Neurophysiol.* **95**, 3297–308 (2006).
16. Ruocco, H. H., Lopes-Cendes, I., Li, L. M. & Cendes, F. Evidence of thalamic dysfunction in Huntington disease by proton magnetic resonance spectroscopy. *Mov. Disord.* **22**, 2052–2056 (2007).
17. Ferrarelli, F. & Tononi, G. The thalamic reticular nucleus and schizophrenia. *Schizophr. Bull.* **37**, 306–15 (2011).
18. Constantinople, C. M. & Bruno, R. M. Deep Cortical Layers Are Activated Directly by Thalamus. *Science* (80-.). **340**, 1591–1594 (2013).
19. Bruno, R. M. & Sakmann, B. Cortex is driven by weak but synchronously active thalamocortical synapses. *Science* **312**, 1622–7 (2006).
20. Diamond, M. E. & Arabzadeh, E. Whisker sensory system - From receptor to

- decision. *Prog. Neurobiol.* (2012). doi:10.1016/j.pneurobio.2012.05.013
21. Li, Y., Ibrahim, L. A., Liu, B., Zhang, L. I. & Tao, H. W. Linear transformation of thalamocortical input by intracortical excitation. *Nat. Neurosci.* **16**, 1324–1330 (2013).
 22. McAlonan, K., Cavanaugh, J. & Wurtz, R. H. Guarding the gateway to cortex with attention in visual thalamus. *Nature* **456**, 391–4 (2008).
 23. Marlinski, V., Sirota, M. G. & Beloozerova, I. N. Differential gating of thalamocortical signals by reticular nucleus of thalamus during locomotion. *J. Neurosci.* **32**, 15823–36 (2012).
 24. Wang, H. Synchrony of Thalamocortical Inputs. *Science* **106**, 106–9 (2010).
 25. Masri, R., Bezdudnaya, T., Trageser, J. C. & Keller, A. Encoding of stimulus frequency and sensor motion in the posterior medial thalamic nucleus. *J. Neurophysiol.* **100**, 681–689 (2008).
 26. Haidarliu, S. Lemniscal and extralemniscal compartments in the VPM of the rat. *Front. Neuroanat.* **2**, (2008).
 27. Groh, A. *et al.* Convergence of Cortical and Sensory Driver Inputs on Single Thalamocortical Cells. *Cereb. Cortex* 1–13 (2013). doi:10.1093/cercor/bht173
 28. Chiaia, N. L., Rhoades, R. W., Fish, S. E. & Killackey, H. P. Thalamic processing of vibrissal information in the rat: II. Morphological and functional properties of medial ventral posterior nucleus and posterior nucleus neurons. *J. Comp. Neurol.* **314**, 217–36 (1991).
 29. Nakamura, S., Narumi, T., Tsutsui, K.-I. & Iijima, T. Difference in the functional significance between the lemniscal and paralemniscal pathways in the perception of direction of single-whisker stimulation examined by muscimol microinjection. *Neurosci. Res.* **64**, 323–9 (2009).
 30. Zhou, H., Schafer, R. J. & Desimone, R. Pulvinar-Cortex Interactions in Vision and Attention Huihui. *Neuron* **89**, 209–220 (2016).
 31. Kaas, J. H. & Lyon, D. C. Pulvinar contributions to the dorsal and ventral streams of visual processing in primates. *Brain Res. Rev.* **55**, 285–296 (2007).
 32. Abrams, D. A., Nicol, T., Zecker, S. & Kraus, N. A possible role for a paralemniscal auditory pathway in the coding of slow temporal information. *Hear. Res.* **272**, 125–34 (2011).
 33. Wurtz, R. H., McAlonan, K., Cavanaugh, J. & Berman, R. a. Thalamic pathways for active vision. *Trends Cogn. Sci.* **15**, 177–84 (2011).
 34. Shipp, S. The brain circuitry of attention. *Trends Cogn. Sci.* **8**, 223–30 (2004).
 35. Castro-alamancos, M. A. & Calcagnotto, M. E. High-pass filtering of corticothalamic activity by neuromodulators released in the thalamus during arousal: in vitro and in vivo. *J. ...* 1489–1497 (2001).
 36. Mease, R. a, Krieger, P. & Groh, A. Cortical control of adaptation and sensory relay mode in the thalamus. *Proc. Natl. Acad. Sci. U. S. A.* **111**, 6798–803 (2014).
 37. Urbain, N. *et al.* Whisking-Related Changes in Neuronal Firing and Membrane Potential Dynamics in the Somatosensory Thalamus of Awake Mice. *Cell Rep.* **13**, 647–656 (2015).
 38. Brecht, M. & Sakmann, B. Whisker maps of neuronal subclasses of the rat ventral posterior medial thalamus, identified by whole-cell voltage recording and morphological reconstruction. *J. Physiol.* 495–515 (2002).

doi:10.1013/jphysiol.2001.012334

39. Perez-Reyes, E. Molecular Physiology of Low-Voltage-Activated T-type Calcium Channels. *Physiol. Rev.* **83**, 117–161 (2003).
40. Suzuki, S. & Rogawski, M. a. T-type calcium channels mediate the transition between tonic and phasic firing in thalamic neurons. *Proc. Natl. Acad. Sci. U. S. A.* **86**, 7228–7232 (1989).
41. Perez-Reyes, E. Molecular Physiology of Low-Voltage-Activated T-type Calcium Channels. *Physiol. Rev.* **83**, (2003).
42. Mease, R. A., Kuner, T., Fairhall, A. L. & Groh, A. Multiplexed Spike Coding and Adaptation in the Thalamus. *Cell Rep.* **19**, 1130–1140 (2017).
43. Leresche, N. Paradoxical Potentiation of Neuronal T-Type Ca^{2+} Current by ATP at Resting Membrane Potential. *J. Neurosci.* **24**, 5592–5602 (2004).
44. Kim, H. R., Hong, S. Z. & Fiorillo, C. D. T-type calcium channels cause bursts of spikes in motor but not sensory thalamic neurons during mimicry of natural patterns of synaptic input. *Front. Cell. Neurosci.* **9**, 428 (2015).
45. Dreyfus, F. M. *et al.* Selective T-type calcium channel block in thalamic neurons reveals channel redundancy and physiological impact of I(T)window. *J. Neurosci.* **30**, 99–109 (2010).
46. Zhuang, J. *et al.* Brain State Effects on Layer 4 of the Awake Visual Cortex. *J. Neurosci.* **34**, 3888–3900 (2014).
47. Swadlow, H. a & Gusev, a G. The impact of ‘bursting’ thalamic impulses at a neocortical synapse. *Nat. Neurosci.* **4**, 402–8 (2001).
48. Hei, X. *et al.* Directional selective neurons in the awake LGN: response properties and modulation by brain state. *J. Neurophysiol.* **112**, 362–373 (2014).
49. Sherman, S. M. A wake-up call from the thalamus. *Nat. Neurosci.* **4**, 344–6 (2001).
50. Guido, W. & Weyand, T. Burst responses in thalamic relay cells of the awake behaving cat. *J. Neurophysiol.* **74**, (1995).
51. Reinagel, P., Godwin, D., Sherman, S. M. & Koch, C. Encoding of Visual Information by LGN Bursts. *J. Neurophysiol.* **81**, (1999).
52. Sherman, S. M. & Guillery, R. W. Functional Organization of Thalamocortical Relays. *J. Neurophysiol.* **76**, (1996).
53. Fanselow, E. E., Sameshima, K., Baccala, L. A. & Nicolelis, M. A. L. Thalamic bursting in rats during different awake behavioral states. *Proc. Natl. Acad. Sci.* **98**, 15330–15335 (2001).
54. Ortuno, T., Grieve, K. L., Cao, R., Cudeiro, J. & Rivadulla, C. Bursting thalamic responses in awake monkey contribute to visual detection and are modulated by corticofugal feedback. *Front. Behav. Neurosci.* **8**, 198 (2014).
55. Swadlow, H. a, Gusev, A. G. & Bezdudnaya, T. Activation of a cortical column by a thalamocortical impulse. *J. Neurosci.* **22**, 7766–73 (2002).
56. Bruno, R. M. & Sakmann, B. Cortex is driven by weak but synchronously active thalamocortical synapses. *Science* **312**, 1622–7 (2006).
57. Yu, J., Gutnisky, D. A., Hires, S. A. & Svoboda, K. Layer 4 fast-spiking interneurons filter thalamocortical signals during active somatosensation. *Nat. Neurosci.* **19**, 1647–1657 (2016).
58. Hu, H. & Agmon, A. Differential Excitation of Distally versus Proximally Targeting Cortical Interneurons by Unitary Thalamocortical Bursts. *J. Neurosci.* **36**, 6906–

- 6916 (2016).
59. Cruikshank, S. J., Urabe, H., Nurmikko, A. V. & Connors, B. W. Pathway-Specific Feedforward Circuits between Thalamus and Neocortex Revealed by Selective Optical Stimulation of Axons. *Neuron* **65**, 230–245 (2010).
 60. Kerlin, A. M., Andermann, M. L., Berezovskii, V. K. & Reid, R. C. Broadly tuned response properties of diverse inhibitory neuron subtypes in mouse visual cortex. *Neuron* **67**, 858–71 (2010).
 61. Gentet, L. J. *et al.* Unique functional properties of somatostatin-expressing GABAergic neurons in mouse barrel cortex. *Nat. Neurosci.* **15**, 607–12 (2012).
 62. Funk, C. M. *et al.* Role of Somatostatin-Positive Cortical Interneurons in the Generation of Sleep Slow Waves. *J. Neurosci.* **37**, 9132–9148 (2017).
 63. Whitmire, C. J., Waiblinger, C., Schwarz, C., Stanley Correspondence, G. B. & Stanley, G. B. Information Coding through Adaptive Gating of Synchronized Thalamic Bursting. *Cell Rep.* **14**, 1–13 (2015).
 64. Haider, B., Häusser, M. & Carandini, M. Inhibition dominates sensory responses in the awake cortex. *Nature* **493**, 97–102 (2013).
 65. Gil, Z., Connors, B. W. & Amitai, Y. Efficacy of Thalamocortical and Intracortical Synaptic Connections: Quanta, Innervation, and Reliability. *Neuron* **23**, 385–397 (1999).
 66. Zheng, H. J. V., Wang, Q. & Stanley, G. B. Adaptive shaping of cortical response selectivity in the vibrissa pathway. *J. Neurophysiol.* **113**, 3850–3865 (2015).
 67. Wang, Q., Webber, R. M. & Stanley, G. B. Thalamic synchrony and the adaptive gating of information flow to cortex. *Nat. Neurosci.* **13**, 1534–41 (2010).
 68. Whitmire, C. J., Waiblinger, C., Schwarz, C. & Stanley, G. B. Information Coding through Adaptive Gating of Synchronized Thalamic Bursting. *Cell Rep.* **14**, 795–807 (2016).
 69. Whitmire, C. J. & Stanley, G. B. Rapid Sensory Adaptation Redux: A Circuit Perspective. *Neuron* **92**, 298–315 (2016).
 70. Stoelzel, C. R., Bereshpolova, Y. & Swadlow, H. A. Stability of thalamocortical synaptic transmission across awake brain states. *J. Neurosci.* **29**, 6851–9 (2009).
 71. Stoelzel, C. R., Bereshpolova, Y., Gusev, A. G. & Swadlow, H. A. The Impact of an LGNd Impulse on the Awake Visual Cortex: Synaptic Dynamics and the Sustained/Transient Distinction. (2008). doi:10.1523/JNEUROSCI.4726-07.2008
 72. Chung, S., Li, X., Nelson, S. B. & Street, S. Short-term depression at thalamocortical synapses contributes to rapid adaptation of cortical sensory responses in vivo. *Neuron* **34**, 437–46 (2002).
 73. Castro-alamancos, M. A. Properties of primary sensory (lemniscal) synapses in the ventrobasal thalamus and the relay of high-frequency sensory inputs. *J. Neurophysiol.* 946–953 (2002).
 74. Hamos, J. E., Van Horn, S. C., Raczkowski, D. & Sherman, S. M. Synaptic circuits involving an individual retinogeniculate axon in the cat. *J. Comp. Neurol.* **259**, 165–192 (1987).
 75. Sherman, S. M. & Guillery, R. W. On the actions that one nerve cell can have on another: distinguishing “drivers” from “modulators”. *Proc. Natl. Acad. Sci. U. S. A.* **95**, 7121–6 (1998).
 76. Hartings, J. a, Temereanca, S. & Simons, D. J. Processing of periodic whisker

- deflections by neurons in the ventroposterior medial and thalamic reticular nuclei. *J. Neurophysiol.* **90**, 3087–94 (2003).
77. Pinault, D. *The thalamic reticular nucleus: structure, function and concept. Brain research. Brain research reviews* **46**, (2004).
 78. Halassa, M. M. *et al.* State-Dependent Architecture of Thalamic Reticular Subnetworks. *Cell* **158**, 808–821 (2014).
 79. Halassa, M. M. & Acsády, L. Thalamic Inhibition: Diverse Sources, Diverse Scales. *Trends in Neurosciences* **39**, 680–693 (2016).
 80. Wang, Q., Webber, R. M. & Stanley, G. B. Thalamic synchrony and the adaptive gating of information flow to cortex. *Nat. Neurosci.* **13**, 1534–1541 (2010).
 81. Halassa, M. M. & Acsády, L. Thalamic Inhibition: Diverse Sources, Diverse Scales. *Trends in Neurosciences* **39**, 680–693 (2016).
 82. Ulrich, D. & Huguenard, J. R. Nucleus-specific chloride homeostasis in rat thalamus. *J. Neurosci.* **17**, 2348–2354 (1997).
 83. Kimura, A. Diverse subthreshold cross-modal sensory interactions in the thalamic reticular nucleus: implications for new pathways of cross-modal attentional gating function. *Eur. J. Neurosci.* **39**, 1405–1418 (2014).
 84. Crabtree, J. W. Intrathalamic sensory connections mediated by the thalamic reticular nucleus. *Cell. Mol. Life Sci.* **56**, 683–700 (1999).
 85. Mistry, R. B., Isaac, J. T. R. & Crabtree, J. W. Two differential frequency-dependent mechanisms regulating tonic firing of thalamic reticular neurons. *Eur. J. Neurosci.* **27**, 2643–56 (2008).
 86. Lewis, L. D. *et al.* Thalamic reticular nucleus induces fast and local modulation of arousal state. *Elife* **4**, 1–23 (2015).
 87. Reinhold, K., Lien, A. D. & Scanziani, M. Distinct recurrent versus afferent dynamics in cortical visual processing. *Nat. Neurosci.* **18**, 1789–1797 (2015).
 88. Yu, J., Gutnisky, D. A., Hires, S. A. & Svoboda, K. Layer 4 fast-spiking interneurons filter thalamocortical signals during active somatosensation. *Nat. Neurosci.* **19**, 1–14 (2016).
 89. Crick, F. Function of the thalamic reticular complex: The searchlight hypothesis. *Proc. Natl. Acad. Sci. U. S. A.* **81**, 4586–4590 (1984).
 90. Wimmer, R. D. *et al.* Thalamic control of sensory selection in divided attention. *Nature* **526**, 705–709 (2015).
 91. Halassa, M. M. *et al.* Selective optical drive of thalamic reticular nucleus generates thalamic bursts and cortical spindles. *Nat. Neurosci.* **14**, 1118–20 (2011).
 92. Crandall, S. R. *et al.* A Corticothalamic Switch: Controlling the Thalamus with Dynamic Synapses. *Neuron* **86**, 1–15 (2015).
 93. Crandall, S. R., Cruikshank, S. J. & Connors, B. W. A Corticothalamic Switch: Controlling the Thalamus with Dynamic Synapses. *Neuron* **86**, 768–782 (2015).
 94. Ego-Stengel, V., Le Cam, J. & Shulz, D. E. Coding of apparent motion in the thalamic nucleus of the rat vibrissal somatosensory system. *J. Neurosci.* **32**, 3339–51 (2012).
 95. Alitto, H. J. & Usrey, W. M. Corticothalamic feedback and sensory processing. *Curr. Opin. Neurobiol.* **13**, 440–445 (2003).
 96. Godwin, D. W., Vaughan, J. W. & Sherman, S. M. Metabotropic glutamate receptors switch visual response mode of lateral geniculate nucleus cells from burst

- to tonic. *J. Neurophysiol.* **76**, 1800–16 (1996).
97. Barth, A. L. & Poulet, J. F. A. Experimental evidence for sparse firing in the neocortex. *Trends Neurosci.* **35**, 345–355 (2012).
 98. Picciotto, M. R., Higley, M. J. & Mineur, Y. S. Acetylcholine as a Neuromodulator: Cholinergic Signaling Shapes Nervous System Function and Behavior. *Neuron* **76**, 116–129 (2012).
 99. Castro-Alamancos, M. a. Dynamics of sensory thalamocortical synaptic networks during information processing states. *Prog. Neurobiol.* **74**, 213–47 (2004).
 100. Aguilar, J. R. & Castro-Alamancos, M. a. Spatiotemporal gating of sensory inputs in thalamus during quiescent and activated states. *J. Neurosci.* **25**, 10990–1002 (2005).
 101. Castro-alamancos, M. A. Different temporal processing of sensory inputs in the rat thalamus during quiescent and information processing states in vivo. 567–578 (2002). doi:10.1013/jphysiol.2001.013283
 102. Hirata, A., Aguilar, J. & Castro-Alamancos, M. a. Noradrenergic activation amplifies bottom-up and top-down signal-to-noise ratios in sensory thalamus. *J. Neurosci.* **26**, 4426–36 (2006).
 103. Lu, S. M., Guido, W. & Sherman, S. M. The brain-stem parabrachial region controls mode of response to visual stimulation of neurons in the cat's lateral geniculate nucleus. *Vis. Neurosci.* **10**, 631–42
 104. Naicker, P., Anoopkumar-Dukie, S., Grant, G. D., Neumann, D. L. & Kavanagh, J. J. Central cholinergic pathway involvement in the regulation of pupil diameter, blink rate and cognitive function. *Neuroscience* **334**, 180–190 (2016).
 105. Reimer, J. *et al.* Pupil fluctuations track rapid changes in adrenergic and cholinergic activity in cortex. *Nat. Commun.* **7**, 13289 (2016).
 106. Ollerenshaw, D. R., Zheng, H. J. V, Millard, D. C., Wang, Q. & Stanley, G. B. The adaptive trade-off between detection and discrimination in cortical representations and behavior. *Neuron* **81**, 1152–1164 (2014).
 107. Andolina, I. M., Jones, H. E., Wang, W. & Sillito, A. M. Corticothalamic feedback enhances stimulus response precision in the visual system. *Proc. Natl. Acad. Sci. U. S. A.* **104**, 1685–90 (2007).
 108. Poulet, J. F. a, Fernandez, L. M. J., Crochet, S. & Petersen, C. C. H. Thalamic control of cortical states. *Nat. Neurosci.* **15**, 370–2 (2012).
 109. Poulet, J. F. a, Fernandez, L. M. J., Crochet, S. & Petersen, C. C. H. Thalamic control of cortical states. *Nat. Neurosci.* **15**, 370–2 (2012).
 110. Petersen, C. C. H., Hahn, T. T. G., Mehta, M., Grinvald, A. & Sakmann, B. Interaction of sensory responses with spontaneous depolarization in layer 2/3 barrel cortex. **100**, (2003).
 111. Ferezou, I. *et al.* Spatiotemporal dynamics of cortical sensorimotor integration in behaving mice. *Neuron* **56**, 907–23 (2007).
 112. Sachidhanandam, S., Sreenivasan, V., Kyriakatos, A., Kremer, Y. & Petersen, C. C. H. Membrane potential correlates of sensory perception in mouse barrel cortex. *Nat. Neurosci.* **16**, 1671–1677 (2013).
 113. Saab, C. Y. & Barrett, L. F. Thalamic Bursts and the Epic Pain Model. *Front. Comput. Neurosci.* **10**, 1–6 (2017).
 114. Ralston, H. J. Pain and the primate thalamus. *Prog. Brain Res.* **149**, 1–10 (2005).

115. Piantoni, G., Halgren, E. & Cash, S. S. The contribution of thalamocortical core and matrix pathways to sleep spindles. *Neural Plast.* **2016**, (2016).
116. Langlois, M. *et al.* Involvement of the thalamic parafascicular nucleus in mesial temporal lobe epilepsy. *J. Neurosci.* **30**, 16523–16535 (2010).
117. Saalman, Y. B. Intralaminar and medial thalamic influence on cortical synchrony, information transmission and cognition. *Front. Syst. Neurosci.* **8**, 83 (2014).
118. Koller, W. *et al.* High-frequency unilateral thalamic stimulation in the treatment of essential and Parkinsonian tremor. *Ann. Neurol.* **42**, 292–299 (1997).
119. Gardner, J. A history of deep brain stimulation: Technological innovation and the role of clinical assessment tools. *Soc. Stud. Sci.* **43**, 707–728 (2013).
120. Jobst, E. E., Melnick, M. E., Byl, N. N., Dowling, G. A. & Aminoff, M. J. Sensory perception in Parkinson disease. *Arch. Neurol.* **54**, 450–4 (1997).
121. Steullet, P. *et al.* The thalamic reticular nucleus in schizophrenia and bipolar disorder: role of parvalbumin-expressing neuron networks and oxidative stress. *Mol. Psychiatry* **23**, 2057–2065 (2018).
122. Ramirez, A. *et al.* Spatiotemporal receptive fields of barrel cortex revealed by reverse correlation of synaptic input. *Nat Neurosci* **17**, 866–875 (2014).
123. Ramirez, A. *et al.* Spatiotemporal receptive fields of barrel cortex revealed by reverse correlation of synaptic input. *Nat. Publ. Gr.* **17**, 866–875 (2014).
124. Yang, H., Kwon, S. E., Severson, K. S. & O'Connor, D. H. Origins of choice-related activity in mouse somatosensory cortex. *Nat. Neurosci.* **19**, 127–134 (2015).
125. Matyas, F. *et al.* Motor control by sensory cortex. *Science* **330**, 1240–3 (2010).
126. Ferezou, I., Bolea, S. & Petersen, C. C. H. Visualizing the Cortical Representation of Whisker Touch: Voltage-Sensitive Dye Imaging in Freely Moving Mice. *Neuron* **50**, 617–629 (2006).
127. Postle, B. R. WORKING MEMORY AS AN EMERGENT PROPERTY OF THE MIND AND BRAIN The evolution of a standard model of working memory. doi:10.1016/j.neuroscience.2005.06.005
128. Harrison, S. A. & Tong, F. Decoding reveals the contents of visual working memory in early visual areas. *Nature* **458**, 632–635 (2009).
129. Storace, D. A., Braubach, O. R., Jin, L., Cohen, L. B. & Sung, U. Monitoring brain activity with protein voltage and calcium sensors. *Sci. Rep.* **5**, 10212 (2015).
130. Grandy, T. H., Greenfield, S. A. & Devonshire, I. M. An evaluation of in vivo voltage-sensitive dyes: pharmacological side effects and signal-to-noise ratios after effective removal of brain-pulsation artifacts. *J. Neurophysiol.* 2931–2945 (2012). doi:10.1152/jn.00512.2011
131. Petersen, C. C. & Sakmann, B. Functionally independent columns of rat somatosensory barrel cortex revealed with voltage-sensitive dye imaging. *J. Neurosci.* **21**, 8435–8446 (2001).
132. Petersen, C. C. H., Hahn, T. T. G., Mehta, M., Grinvald, A. & Sakmann, B. Interaction of sensory responses with spontaneous depolarization in layer 2/3 barrel cortex. *Proc. Natl. Acad. Sci. U. S. A.* **100**, 13638–43 (2003).
133. Jin, L. *et al.* Single Action Potentials and Subthreshold Electrical Events Imaged in Neurons with a Fluorescent Protein Voltage Probe. *Neuron* **75**, 779–785 (2012).
134. Akemann, W., Mutoh, H., Perron, A., Rossier, J. & Knöpfel, T. Imaging brain electric signals with genetically targeted voltage-sensitive fluorescent proteins. *Nat.*

- Methods* **7**, 643–649 (2010).
135. Hochbaum, D. R. *et al.* All-optical electrophysiology in mammalian neurons using engineered microbial rhodopsins. *Nat. Methods* **11**, 825–33 (2014).
 136. Gong, Y. *et al.* High-speed recording of neural spikes in awake mice and flies with a fluorescent voltage sensor. *Science* (80-.). **350**, 1361–1366 (2015).
 137. Nakajima, R., Jung, A., Yoon, B. J. & Baker, B. J. Optogenetic monitoring of synaptic activity with genetically encoded voltage indicators. *Front. Synaptic Neurosci.* **8**, 1–9 (2016).
 138. Storace, D. *et al.* Toward Better Genetically Encoded Sensors of Membrane Potential. *Trends Neurosci.* **39**, 277–289 (2016).
 139. Mattis, J. *et al.* Principles for applying optogenetic tools derived from direct comparative analysis of microbial opsins. *Nat. Methods* **2012**, (2012).
 140. Diamond, M. E. Texture sensation through the fingertips and the whiskers. *Curr. Opin. Neurobiol.* **20**, 319–27 (2010).
 141. Ollerenshaw, D. R. *et al.* Detection of tactile inputs in the rat vibrissa pathway. *J. Neurophysiol.* **108**, 479–90 (2012).
 142. Guo, Z. V. *et al.* Procedures for Behavioral Experiments in Head-Fixed Mice. *PLoS One* **9**, e88678 (2014).
 143. Gerfen, C. R., Paletzki, R. & Heintz, N. GENSAT BAC cre-recombinase driver lines to study the functional organization of cerebral cortical and basal ganglia circuits. *Neuron* **80**, 1368–1383 (2013).
 144. Han, Z. *et al.* Mechanistic studies of the genetically encoded fluorescent protein voltage probe ArcLight. *PLoS One* **9**, e113873 (2014).
 145. Brinks, D., Klein, A. J. & Cohen, A. E. Two-Photon Lifetime Imaging of Voltage Indicating Proteins as a Probe of Absolute Membrane Voltage. *Biophys. J.* **109**, 914–921 (2015).
 146. Cao, G. *et al.* Genetically targeted optical electrophysiology in intact neural circuits. *Cell* **154**, 904–913 (2013).
 147. Kallman, B. R., Kim, H. & Scott, K. Excitation and inhibition onto central courtship neurons biases drosophila mate choice. *Elife* **4**, 1–18 (2015).
 148. Raccuglia, D. *et al.* Presynaptic GABA Receptors Mediate Temporal Contrast Enhancement in Drosophila Olfactory Sensory Neurons and Modulate Odor-Driven Behavioral Kinetics. *eNeuro* **3**, 0080-16 (2016).
 149. Klapoetke, N. C. *et al.* Independent optical excitation of distinct neural populations. *Nat. Methods* **11**, 338–46 (2014).
 150. Morrisette, A. *et al.* BRAIN Initiative ® Investigators Meeting. in *BRAIN Initiative Investigators Meeting* (National Institute of Neurological Disorders, 2016).
 151. Borden, P. Y., Morrisette, A., Waiblinger, C., Stanley, G. B. & Jaeger, D. Multiscale Analysis of Sensory-Motor Cortical Gating in Behaving Mice. in *BRIAN Initiative Investigators Meeting* (2015).
 152. P. BORDEN, A. D. ORTIZ, H. J. V. ZHENG, G. B. S. G. Controlling transmission of sensory information by optical manipulation of the thalamocortical pathway in the anesthetized mouse. in *2015 Neuroscience Meeting Planner*. (Society for Neuroscience, 2015). doi:10.1017/CBO9781107415324.004
 153. Akemann, W. *et al.* Imaging neural circuit dynamics with a voltage-sensitive fluorescent protein. *J Neurophysiol* **108**, 2323–2337 (2012).

154. Knöpfel, T., Gallero-Salas, Y. & Song, C. Genetically encoded voltage indicators for large scale cortical imaging come of age. *Curr. Opin. Chem. Biol.* **27**, 75–83 (2015).
155. Lin, M. Z. & Schnitzer, M. J. Genetically encoded indicators of neuronal activity. *Nat. Neurosci.* **19**, 1142–53 (2016).
156. Antic, S. D., Empson, R. M. & Knöpfel, T. Voltage imaging to understand connections and functions of neuronal circuits. *J. Neurophysiol.* jn.00226.2016 (2016). doi:10.1152/jn.00226.2016
157. Sitaraman, D. *et al.* Propagation of Homeostatic Sleep Signals by Segregated Synaptic Microcircuits of the *Drosophila* Mushroom Body. *Curr. Biol.* **25**, 2915–2927 (2015).
158. Klein, M. *et al.* Sensory determinants of behavioral dynamics in *Drosophila* thermotaxis. *Proc. Natl. Acad. Sci.* **112**, E220–E229 (2015).
159. Carandini, M. *et al.* Imaging the Awake Visual Cortex with a Genetically Encoded Voltage Indicator. *J. Neurosci.* **35**, 53–63 (2015).
160. Civillico, E. F. & Contreras, D. Integration of evoked responses in supragranular cortex studied with optical recordings in vivo. *J. Neurophysiol.* **96**, 336–51 (2006).
161. Mutoh, H., Mishina, Y., Gallero-Salas, Y. & Knöpfel, T. Comparative performance of a genetically-encoded voltage indicator and a blue voltage sensitive dye for large scale cortical voltage imaging. *Front. Cell. Neurosci.* **9**, 147 (2015).
162. Jin, L. *et al.* Single action potentials and subthreshold electrical events imaged in neurons with a fluorescent protein voltage probe. *Neuron* **75**, 779–85 (2012).
163. Razali, N. M. & Wah, Y. B. Power comparisons of Shapiro-Wilk , Kolmogorov-Smirnov, Lilliefors and Anderson-Darling tests. *J. Stat. Model. Anal.* **2**, 21–33 (2011).
164. Lütcke, H. *et al.* Optical recording of neuronal activity with a genetically-encoded calcium indicator in anesthetized and freely moving mice. *Front. Neural Circuits* **4**, 9 (2010).
165. Han, Z. *et al.* Fluorescent Protein Voltage Probes Derived from ArcLight that Respond to Membrane Voltage Changes with Fast Kinetics. *PLoS One* **8**, (2013).
166. Gollnick, C. A., Millard, D. C., Ortiz, A. D., Bellamkonda, R. V. & Stanley, G. B. Response reliability observed with voltage-sensitive dye imaging of cortical layer 2/3: the probability of activation hypothesis. *J. Neurophysiol.* **115**, 2456–2469 (2016).
167. Stüttgen, M. C. & Schwarz, C. Psychophysical and neurometric detection performance under stimulus uncertainty. *Nat. Neurosci.* **11**, 1091–9 (2008).
168. Shoykhet, M., Doherty, D. & Simons, D. J. Coding of deflection velocity and amplitude by whisker primary afferent neurons: implications for higher level processing. *Somatosens. Mot. Res.* **17**, 171–80 (2000).
169. Wolfe, J. *et al.* Texture coding in the rat whisker system: Slip-stick versus differential resonance. *PLoS Biol.* **6**, 1661–1677 (2008).
170. Petersen, C. C. H., Grinvald, A. & Sakmann, B. Spatiotemporal dynamics of sensory responses in layer 2/3 of rat barrel cortex measured in vivo by voltage-sensitive dye imaging combined with whole-cell voltage recordings and neuron reconstructions. *J. Neurosci.* **23**, 1298–309 (2003).
171. Lippert, M. T., Takagaki, K., Xu, W., Huang, X. & Wu, J.-Y. Methods for Voltage-

- Sensitive Dye Imaging of Rat Cortical Activity With High Signal-to-Noise Ratio. *J Neurophysiol* **98**, 502–512 (2007).
172. Wang, Q., Millard, D. C., Zheng, H. J. V & Stanley, G. B. Erratum: Voltage-sensitive dye imaging reveals improved topographic activation of cortex in response to manipulation of thalamic microstimulation parameters. *J. Neural Eng.* **9**, 059601 (2012).
 173. Millard, D. C., Wang, Q. & Stanley, G. B. Nonlinear system identification of the thalamocortical circuit in response to thalamic microstimulation. *2011 5th Int. IEEE/EMBS Conf. Neural Eng. NER 2011* **10**, 1–4 (2011).
 174. Welker, E. & Van der Loos, H. Quantitative correlation between barrel-field size and the sensory innervation of the whiskerpad: a comparative study in six strains of mice bred for different patterns of mystacial vibrissae. *J. Neurosci.* **6**, 3355–73 (1986).
 175. Woolsey, T. A. & Wann, J. R. Areal changes in mouse cortical barrels following vibrissal damage at different postnatal ages. *J. Comp. Neurol.* **170**, 53–66 (1976).
 176. Kwegyir-Afful, E. E., Kyriazi, H. T. & Simons, D. J. Weaker feedforward inhibition accounts for less pronounced thalamocortical response transformation in mouse vs. rat barrels. *J. Neurophysiol.* **110**, 2378–92 (2013).
 177. Kleinfeld, D. & Delaney, K. R. Distributed representation of vibrissa movement in the upper layers of somatosensory cortex revealed with voltage-sensitive dyes. *J. Comp. Neurol.* **375**, 89–108 (1996).
 178. Jia, H., Rochefort, N. L., Chen, X. & Konnerth, A. In vivo two-photon imaging of sensory-evoked dendritic calcium signals in cortical neurons. *Nat. Protoc.* **6**, 28–35 (2011).
 179. Hillman, E. M. C. Optical brain imaging in vivo: techniques and applications from animal to man. *J. Biomed. Opt.* **12**, 051402 (2007).
 180. Raguet, H. *et al.* Spatially Structured Sparse Morphological Component Separation for voltage-sensitive dye optical imaging. *J. Neurosci. Methods* **257**, 76–96 (2016).
 181. Al-Juboori, S. I. *et al.* Light Scattering Properties Vary across Different Regions of the Adult Mouse Brain. *PLoS One* **8**, 1–9 (2013).
 182. Buzsáki, G., Anastassiou, C. A. & Koch, C. The origin of extracellular fields and currents — EEG, ECoG, LFP and spikes. *Nat. Rev. Neurosci.* **13**, 407–420 (2012).
 183. Haider, B., Schulz, D. P. P. A., Häusser, M. & Carandini, M. Millisecond Coupling of Local Field Potentials to Synaptic Currents in the Awake Visual Cortex. *Neuron* **90**, 35–42 (2016).
 184. Okun, M., Naim, A. & Lampl, I. The subthreshold relation between cortical local field potential and neuronal firing unveiled by intracellular recordings in awake rats. *J. Neurosci.* **30**, 4440–8 (2010).
 185. Okun, M. Artefactual origin of biphasic cortical spike-LFP correlation. *J. Comput. Neurosci.* **42**, 31–35 (2017).
 186. Khatri, V., Bruno, R. M. & Simons, D. J. Stimulus-specific and stimulus-nonspecific firing synchrony and its modulation by sensory adaptation in the whisker-to-barrel pathway. *J. Neurophysiol.* **101**, 2328–38 (2009).
 187. Khatri, V. Adaptation in Thalamic Barreloid and Cortical Barrel Neurons to Periodic Whisker Deflections Varying in Frequency and Velocity. *J. Neurophysiol.* **92**, 3244–3254 (2004).

188. Webber, R. M. & Stanley, G. B. Nonlinear encoding of tactile patterns in the barrel cortex. *J. Neurophysiol.* **91**, 2010–22 (2004).
189. Bolori, A., Jenks, R. A. & Stanley, G. B. Encoding and Decoding Cortical Representations of Tactile Features in the Vibrissa System From the quantification of these joint tuning properties , a detailed nonlinear encoding model was formulated that was highly predictive of firing. **30**, 9990–10005 (2010).
190. Kyriazi, H. T., Carvell, G. E. & Simons, D. J. OFF response transformations in the whisker/barrel system. *J. Neurophysiol.* **72**, 392–401 (1994).
191. Kwegyir-Afful, E. E., Bruno, R. M., Simons, D. J. & Keller, A. The role of thalamic inputs in surround receptive fields of barrel neurons. *J. Neurosci* **25**, 5926–5934 (2005).
192. Anderson, J., Lampl, I., Reichova, I., Carandini, M. & Ferster, D. Stimulus dependence of two-state fluctuations of membrane potential in cat visual cortex. *Nat. Neurosci.* **3**, 617–21 (2000).
193. Reich, D. S., Victor, J. D., Knight, B. W., Ozaki, T. & Kaplan, E. Response variability and timing precision of neuronal spike trains in vivo. *J. Neurophysiol.* **77**, 2836–41 (1997).
194. Singla, R. D., Wang, J. & Singla, D. K. Regulation of Notch 1 signaling in THP-1 cells enhances M2 macrophage differentiation. *Am. J. Physiol. Heart Circ. Physiol.* **307**, H1634–42 (2014).
195. Haynes, P. R., Christmann, B. L. & Griffith, L. C. A single pair of neurons links sleep to memory consolidation in *Drosophila melanogaster*. *Elife* **4**, 1–24 (2015).
196. Shtoyerman, E., Arieli, A., Slovin, H., Vanzetta, I. & Grinvald, A. Long-term optical imaging and spectroscopy reveal mechanisms underlying the intrinsic signal and stability of cortical maps in V1 of behaving monkeys. *J. Neurosci.* **20**, 8111–8121 (2000).
197. Seidemann, E. *et al.* Calcium imaging with genetically encoded indicators in behaving primates. *Elife* **5**, 1–19 (2016).
198. Grandy, T. H., Greenfield, S. A. & Devonshire, I. M. An evaluation of in vivo voltage-sensitive dyes: pharmacological side effects and signal-to-noise ratios after effective removal of brain-pulsation artifacts. *J. Neurophysiol.* 2931–2945 (2012). doi:10.1152/jn.00512.2011
199. Reyes-Puerta, V. *et al.* Propagation of spontaneous slow-wave activity across columns and layers of the adult rat barrel cortex in vivo. *Brain Struct. Funct.* **221**, 4429–4449 (2016).
200. Okun, M. Artefactual origin of biphasic cortical spike-LFP correlation. *J. Comput. Neurosci.* **42**, 31–35 (2017).
201. Wilt, B. A., Fitzgerald, J. E., Schnitzer, M. J. & Center, J. H. C. Photon Shot Noise Limits on Optical Detection of Neuronal Spikes and Estimation of Spike Timing. *Biophysj* **104**, 51–62 (2013).
202. Arieli, A., Sterkin, A., Grinvald, A. & Aertsen, A. Dynamics of ongoing activity: explanation of the large variability in evoked cortical responses. *Science* **273**, 1868–1871 (1996).
203. Grinvald, A., Lieke, E. E., Frostig, R. D. & Hildesheim, R. Cortical Point-Spread Function and Long-Range Lateral Interactions Revealed by Real-Time Optical Imaging of Macaque Monkey Primary Visual Cortex. *J. Neurosci.* **14**, 2545–2568

- (1994).
204. Ludwig, K. A., Uram, J. D., Yang, J. Y., Martin, D. C. & Kipke, D. R. Chronic neural recordings using silicon microelectrode arrays electrochemically deposited with a poly(3,4-ethylenedioxythiophene) (PEDOT) film. *J. Neural Eng.* **3**, 59–70 (2006).
 205. Madisen, L. *et al.* Transgenic mice for intersectional targeting of neural sensors and effectors with high specificity and performance. *Neuron* **85**, 942–958 (2015).
 206. St-Pierre, F. *et al.* High-fidelity optical reporting of neuronal electrical activity with an ultrafast fluorescent voltage sensor. *Nat. Neurosci.* **17**, 884–9 (2014).
 207. Gong, Y., Wagner, M. J., Zhong Li, J. & Schnitzer, M. J. Imaging neural spiking in brain tissue using FRET-opsin protein voltage sensors. *Nat. Commun.* **5**, 3674 (2014).
 208. BORDEN, P. *et al.* Thalamic control of cortical sensory representations. in *Society of Neuroscience Annual Conference* (Society of Neuroscience, 2016).
 209. BORDEN, P. Y. *et al.* Thalamic control of sensory evoked spatiotemporal cortical responses. in *Society of Neuroscience* (Society of Neuroscience, 2017).
 210. McCormick, D. A. & von Krosigk, M. Corticothalamic activation modulates thalamic firing through glutamate ‘metabotropic’ receptors. *Proc. Natl. Acad. Sci.* **89**, 2774–2778 (1992).
 211. Béhuret, S., Deleuze, C. & Bal, T. Corticothalamic Synaptic Noise as a Mechanism for Selective Attention in Thalamic Neurons. *Front. Neural Circuits* **9**, 1–21 (2015).
 212. Hirata, A. & Castro-Alamancos, M. A. Neocortex Network Activation and Deactivation States Controlled by the Thalamus. *J. Neurophysiol.* **103**, 1147–1157 (2010).
 213. Olsen, S. R., Bortone, D. S., Adesnik, H. & Scanziani, M. Gain control by layer six in cortical circuits of vision. *Nature* **483**, 47–52 (2012).
 214. Li, L. & Ebner, F. F. Cortex dynamically modulates responses of thalamic relay neurons through prolonged circuit-level disinhibition in rat thalamus in vivo. *J. Neurophysiol.* **116**, 2368–2382 (2016).
 215. Swadlow, H. A., Bezdudnaya, T. & Gusev, A. G. Spike timing and synaptic dynamics at the awake thalamocortical synapse. *Prog. Brain Res.* **149**, 91–105 (2005).
 216. Stoelzel, C. R., Bereshpolova, Y. & Swadlow, H. a. Stability of thalamocortical synaptic transmission across awake brain states. *J. Neurosci.* **29**, 6851–9 (2009).
 217. Lesica, N. a *et al.* Dynamic encoding of natural luminance sequences by LGN bursts. *PLoS Biol.* **4**, e209 (2006).
 218. McCormick, D. A., McGinley, M. J. & Salkoff, D. B. Brain state dependent activity in the cortex and thalamus. *Curr. Opin. Neurobiol.* **31**, 133–140 (2015).
 219. Boudreau, C. E. & Ferster, D. Short-term depression in thalamocortical synapses of cat primary visual cortex. *J. Neurosci.* **25**, 7179–7190 (2005).
 220. Chung, S., Li, X. & Nelson, S. B. Short-term depression at thalamocortical synapses contributes to rapid adaptation of cortical sensory responses in vivo. *Neuron* **34**, 437–46 (2002).
 221. Murray Sherman, S. Tonic and burst firing: Dual modes of thalamocortical relay. *Trends Neurosci.* **24**, 122–126 (2001).
 222. Guido, W., Lu, S., Vaughan, J. W., Godwin, D. W. & Sherman, S. M. Receiver

- operating characteristic (ROC) analysis of neurons in the cat ' s lateral geniculate nucleus during tonic and burst response mode. 723–741 (1995).
223. Borden, P. Y. *et al.* Genetically expressed voltage sensor ArcLight for imaging large scale cortical activity in the anesthetized and awake mouse. *Neurophotonics* **4**, 031212 (2017).
 224. Wang, Q., Webber, R. M. & Stanley, G. B. Thalamic synchrony and the adaptive gating of information flow to cortex. *Nat. Neurosci.* **13**, 1534–41 (2010).
 225. Ma, Y. *et al.* Wide-field optical mapping of neural activity and brain haemodynamics: considerations and novel approaches. *Philos. Trans. R. Soc. B Biol. Sci.* **371**, 20150360 (2016).
 226. Lustig, B. R., Friedman, R. M., Winberry, J. E., Ebner, F. F. & Roe, A. W. Voltage-sensitive dye imaging reveals shifting spatiotemporal spread of whisker-induced activity in rat barrel cortex. *J. Neurophysiol.* **109**, 2382–92 (2013).
 227. Millard, D. C., Whitmire, C. J., Gollnick, C. A., Rozell, C. J. & Stanley, G. B. Electrical and Optical Activation of Mesoscale Neural Circuits with Implications for Coding. *J. Neurosci.* **35**, 15702–15715 (2015).
 228. Stujenske, J. M., Spellman, T. & Gordon, J. A. Modeling the Spatiotemporal Dynamics of Light and Heat Propagation for InVivo Optogenetics. *Cell Rep.* **12**, 525–534 (2015).
 229. Stark, E., Koos, T. & Buzsaki, G. Diode probes for spatiotemporal optical control of multiple neurons in freely moving animals. *J. Neurophysiol.* **108**, 349–363 (2012).
 230. Zhan, X. J., Cox, C. L. & Sherman, S. M. Dendritic depolarization efficiently attenuates low-threshold calcium spikes in thalamic relay cells. *J. Neurosci.* **20**, 3909–3914 (2000).
 231. Zhan, X. J., Cox, C. L., Rinzel, J. & Sherman, S. M. Current clamp and modeling studies of low-threshold calcium spikes in cells of the cat's lateral geniculate nucleus. *J. Neurophysiol.* **81**, 2360–2373 (1999).
 232. Hoogland, P. V., Welker, E. & Van der Loos, H. Organization of the projections from barrel cortex to thalamus in mice studied with Phaseolus vulgaris-leucoagglutinin and HRP. *Exp. Brain Res.* **68**, 73–87 (1987).
 233. Claus, L. *et al.* Barreloid Borders and Neuronal Activity Shape Panglial Gap Junction-Coupled Networks in the Mouse Thalamus. *Cereb. Cortex* 213–222 (2016). doi:10.1093/cercor/bhw368
 234. Wang, Q., Millard, D. C., Zheng, H. J. V & Stanley, G. B. Voltage-sensitive dye imaging reveals improved topographic activation of cortex in response to manipulation of thalamic microstimulation parameters. *J. Neural Eng.* **9**, 026008 (2012).
 235. Whitmire, C., Wailbinger, C., Liew, Y., Schwarz, C. & Stanley, G. B. State-dependent encoding in the thalamocortical circuit. Modeling feature selectivity in different optogenetically induced thalamic states. in *Society of Neuroscience* (Society for Neuroscience, 2017).
 236. Gücer, G. The effect of sleep upon the transmission of afferent activity in the somatic afferent system. *Exp. Brain Res.* **34**, 287–298 (1979).
 237. Niell, C. M. & Stryker, M. P. Modulation of visual responses by behavioral state in mouse visual cortex. *Neuron* **65**, 472–479 (2011).

238. Massaux, A., Dutrieux, G., Cotillon-Williams, N., Manunta, Y. & Edeline, J.-M. Auditory Thalamus Bursts in Anesthetized and Non-Anesthetized States: Contribution to Functional Properties. *J. Neurophysiol.* **91**, 2117–2134 (2004).
239. Sela, Y., Vyazovskiy, V. V., Cirelli, C., Tononi, G. & Nir, Y. Responses in Rat Core Auditory Cortex are Preserved during Sleep Spindle Oscillations. *Sleep* **39**, 1069–1082 (2016).
240. Issa, E. B. & Wang, X. Sensory Responses during Sleep in Primate Primary and Secondary Auditory Cortex. *J. Neurosci.* **28**, 14467–14480 (2008).
241. Constantinople, C. M. & Bruno, R. M. Effects and mechanisms of wakefulness on local cortical networks. *Neuron* **69**, 1061–8 (2011).
242. Haider, B., Duque, A., Hasenstaub, A. R., Yu, Y. & McCormick, D. A. Enhancement of Visual Responsiveness by Spontaneous Local Network Activity In Vivo. *J. Neurophysiol.* **97**, 4186–4202 (2007).
243. McGinley, M. J., David, S. V. & McCormick, D. A. Cortical Membrane Potential Signature of Optimal States for Sensory Signal Detection. *Neuron* **87**, 179–192 (2015).
244. Hu, H. & Agmon, A. Differential Excitation of Distally versus Proximally Targeting Cortical Interneurons by Unitary Thalamocortical Bursts. *J. Neurosci.* **36**, 6906–6916 (2016).
245. Kalappa, B. I., Brozoski, T. J., Turner, J. G. & Caspary, D. M. Single unit hyperactivity and bursting in the auditory thalamus of awake rats directly correlates with behavioural evidence of tinnitus. *J. Physiol.* **592**, 5065–5078 (2014).
246. Fanselow, E. E., Sameshima, K., Baccala, L. A. & Nicolelis, M. A. Thalamic bursting in rats during different awake behavioral states. *Proc. Natl. Acad. Sci. U. S. A.* **98**, 15330–5 (2001).
247. Waiblinger, C., Whitmire, C. J., Sederberg, A., Stanley, G. B. & Schwarz, C. Primary Tactile Thalamus Spiking Reflects Cognitive Signals. *J. Neurosci.* **38**, 4870–4885 (2018).
248. Petersen, C. C. H. & Crochet, S. Synaptic computation and sensory processing in neocortical layer 2/3. *Neuron* **78**, 28–48 (2013).
249. Otazu, G. H., Tai, L.-H., Yang, Y. & Zador, A. M. Engaging in an auditory task suppresses responses in auditory cortex. *Nat. Neurosci.* **12**, 646–54 (2009).
250. Sherman, S. M. Thalamic relays and cortical functioning. *Prog. Brain Res.* **149**, 107–126 (2005).
251. Bickford, M. E. Thalamic Circuit Diversity: Modulation of the Driver/Modulator Framework. *Front. Neural Circuits* **9**, 86 (2015).
252. Govindaiah, G. & Cox, C. L. Metabotropic Glutamate Receptors Differentially Regulate GABAergic Inhibition in Thalamus. *J. Neurosci.* **26**, 13443–13453 (2006).
253. Lee, J. H., Whittington, M. A. & Kopell, N. J. Top-Down Beta Rhythms Support Selective Attention via Interlaminar Interaction: A Model. *Plos Comput. Biol.* **9**, (2013).
254. Montero, V. M. Attentional activation of the visual thalamic reticular nucleus depends on ‘top-down’ inputs from the primary visual cortex via corticogeniculate pathways. *Brain Res.* **864**, 95–104 (2000).
255. Vaingankar, V., Sanchez Soto, C., Wang, X., Sommer, F. T. & Hirsch, J. a. Neurons in the thalamic reticular nucleus are selective for diverse and complex visual

- features. *Front. Integr. Neurosci.* **6**, 118 (2012).
256. McAlonan, K., Cavanaugh, J. & Wurtz, R. H. Attentional modulation of thalamic reticular neurons. *J. Neurosci.* **26**, 4444–50 (2006).
 257. Hirai, D. *et al.* Shaping somatosensory responses in awake rats: cortical modulation of thalamic neurons. *Brain Struct. Funct.* **223**, 851–872 (2018).
 258. Ortúño, T., Grieve, K. L., Cao, R., Cudeiro, J. & Rivadulla, C. Bursting thalamic responses in awake monkey contribute to visual detection and are modulated by corticofugal feedback. *Front. Behav. Neurosci.* **8**, 198 (2014).
 259. Weyand, T. G., Boudreaux, M. & Guido, W. Burst and Tonic Response Modes in Thalamic Neurons During Sleep and Wakefulness. *J Neurophysiol* **85**, 1107–1118 (2000).
 260. Landisman, C. E. & Connors, B. W. VPM and PoM nuclei of the rat somatosensory thalamus: intrinsic neuronal properties and corticothalamic feedback. *Cereb. Cortex* **17**, 2853–65 (2007).
 261. Bruno, R. M. & Sakmann, B. Cortex {Is} {Driven} by {Weak} but {Synchronously} {Active} {Thalamocortical} {Synapses}. *Science (80-.)*. **312**, 1622–1627 (2006).
 262. Khatri, V., Hartings, J. a & Simons, D. J. Adaptation in thalamic barreloid and cortical barrel neurons to periodic whisker deflections varying in frequency and velocity. *J. Neurophysiol.* **92**, 3244–54 (2004).
 263. Ahissar, E., Sosnik, R. & Haidarliu, S. Transformation from temporal to rate coding in a somatosensory thalamocortical pathway. **406**, (2000).
 264. Yu, C., Derdikman, D., Haidarliu, S. & Ahissar, E. Parallel Thalamic Pathways for Whisking and Touch Signals in the Rat. *PLoS Biol.* **4**, e124 (2006).
 265. Bezdudnaya, T. *et al.* Thalamic burst mode and inattention in the awake LGNd. *Neuron* **49**, 421–432 (2006).
 266. Poulet, J. F. a, Fernandez, L. M. J., Crochet, S. & Petersen, C. C. H. Thalamic control of cortical states. *Nat. Neurosci.* **15**, 370–2 (2012).
 267. Tibshirani, R. Regression Shrinkage and Selection Via the Lasso. *J. R. Stat. Soc. Ser. B* **58**, 267–288 (1996).
 268. Chuong, A. S. *et al.* Noninvasive optical inhibition with a red-shifted microbial rhodopsin. *Nat. Neurosci.* **17**, 1123–1129 (2014).
 269. Mattis, J. *et al.* Principles for applying optogenetic tools derived from direct comparative analysis of microbial opsins. *Nat. Methods* **9**, 159–172 (2012).
 270. Raimondo, J. V., Kay, L., Ellender, T. J. & Akerman, C. J. Optogenetic silencing strategies differ in their effects on inhibitory synaptic transmission. *Nat. Neurosci.* **15**, 1102–1104 (2012).
 271. Ferezou, I. *et al.* Spatiotemporal Dynamics of Cortical Sensorimotor Integration in Behaving Mice. *Neuron* **56**, 907–923 (2007).
 272. Reimer, J. *et al.* Pupil Fluctuations Track Fast Switching of Cortical States during Quiet Wakefulness. *Neuron* **84**, 355–362 (2014).
 273. Zuo, Y., Perkon, I. & Diamond, M. E. Whisking and whisker kinematics during a texture classification task. *Philos. Trans. R. Soc. Lond. B. Biol. Sci.* **366**, 3058–69 (2011).
 274. Weyand, T. G., Boudreaux, M. & Guido, W. Burst and Tonic Response Modes in Thalamic Neurons During Sleep and Wakefulness. *J Neurophysiol* **85**, 1107–1118

- (2000).
275. Castro-Alamancos, M. A. Dynamics of sensory thalamocortical synaptic networks during information processing states. doi:10.1016/j.pneurobio.2004.09.002
 276. Yavorska, I. & Wehr, M. Somatostatin-Expressing Inhibitory Interneurons in Cortical Circuits. *Front. Neural Circuits* **10**, 76 (2016).
 277. Lee, S.-H. S. *et al.* Activation of specific interneurons improves V1 feature selectivity and visual perception. *Nature* **488**, 379–83 (2012).
 278. Naka, A. & Adesnik, H. Inhibitory Circuits in Cortical Layer 5. *Front. Neural Circuits* **10**, 35 (2016).
 279. Abbas, A. I. *et al.* Somatostatin Interneurons Facilitate Hippocampal-Prefrontal Synchrony and Prefrontal Spatial Encoding. *Neuron* **100**, 926–939.e3 (2018).
 280. Hu, H. & Agmon, A. Properties of precise firing synchrony between synaptically coupled cortical interneurons depend on their mode of coupling. *J. Neurophysiol.* **114**, 624–37 (2015).
 281. Hu, H., Ma, Y. & Agmon, A. Submillisecond firing synchrony between different subtypes of cortical interneurons connected chemically but not electrically. *J. Neurosci.* **31**, 3351–61 (2011).
 282. Ollerenshaw, D. R., Zheng, H. J. V., Millard, D. C., Wang, Q. & Stanley, G. B. The Adaptive Trade-Off between Detection and Discrimination in Cortical Representations and Behavior. *Neuron* **81**, 1152–1164 (2014).
 283. Kato, H. K., Gillet, S. N. & Isaacson, J. S. Flexible Sensory Representations in Auditory Cortex Driven by Behavioral Relevance. *Neuron* **88**, 1027–1039 (2015).
 284. Abdelfattah, A. S. *et al.* A Bright and Fast Red Fluorescent Protein Voltage Indicator That Reports Neuronal Activity in Organotypic Brain Slices. *J. Neurosci.* **36**, 2458–72 (2016).
 285. Guido, W. & Sherman, S. M. Response latencies of cells in the cat's lateral geniculate nucleus are less variable during burst than tonic firing. *Vis. Neurosci.* **15**, 231–237 (1998).
 286. Herring, B. E., Xie, Z., Marks, J. & Fox, A. P. Isoflurane inhibits the neurotransmitter release machinery. *J. Neurophysiol.* **102**, 1265–73 (2009).
 287. Raz, A. *et al.* Preferential effect of isoflurane on top-down vs. bottom-up pathways in sensory cortex. *Front. Syst. Neurosci.* **8**, 191 (2014).
 288. Gentet, L. J. *et al.* Unique functional properties of somatostatin-expressing GABAergic neurons in mouse barrel cortex. *Nat. Neurosci.* **15**, 607–612 (2012).
 289. Castro-alamancos, M. A. Different temporal processing of sensory inputs in the rat thalamus during quiescent and information processing states in vivo. 567–578 (2002). doi:10.1013/jphysiol.2001.013283
 290. Heiss, J. E., Katz, Y., Ganmor, E. & Lampl, I. Shift in the balance between excitation and inhibition during sensory adaptation of S1 neurons. *J. Neurosci.* **28**, 13320–30 (2008).
 291. Schiff, M. L. & Reyes, A. D. Characterization of thalamocortical responses of regular-spiking and fast-spiking neurons of the mouse auditory cortex in vitro and in silico. *J. Neurophysiol.* **107**, 1476–1488 (2012).
 292. Lewis, L. D. *et al.* Local cortical dynamics of burst suppression in the anaesthetized brain. *Brain* **136**, 2727–37 (2013).
 293. Stoelzel, C. R., Bereshpolova, Y. & Swadlow, H. A. Stability of Thalamocortical

- Synaptic Transmission across Awake Brain States. *J. Neurosci.* **29**, 6851–6859 (2009).
294. Taniguchi, H. Genetic dissection of GABAergic neural circuits in mouse neocortex. *Front. Cell. Neurosci.* **8**, 8 (2014).
 295. Alonso, J.-M., Usrey, W. M. & Reid, R. C. Precisely correlated firing in cells of the lateral geniculate nucleus. *Nature* **383**, 815–9 (1996).
 296. Bolus, M. F., Willats, A. A., Whitmire, C. J., Rozell, C. J. & Stanley, G. B. Design strategies for dynamic closed-loop optogenetic neurocontrol in vivo. *J. Neural Eng.* **15**, (2018).
 297. Newman, J. P. *et al.* Closed-Loop, Multichannel Experimentation Using the Open-Source NeuroRighter Electrophysiology Platform. *Front. Neural Circuits* **6**, 98 (2012).
 298. Stoy, W. A. *et al.* Robotic navigation to subcortical neural tissue for intracellular electrophysiology in vivo. *J. Neurophysiol.* **118**, 1141–1150 (2017).
 299. Zhao, S. *et al.* Cell type-specific channelrhodopsin-2 transgenic mice for optogenetic dissection of neural circuitry function. *Nat. Methods* **8**, 745–52 (2011).
 300. Lesica, N. a & Stanley, G. B. Encoding of natural scene movies by tonic and burst spikes in the lateral geniculate nucleus. *J. Neurosci.* **24**, 10731–40 (2004).